NORTHWESTERN UNIVERSITY

Chemistry-Climate Dynamics of Warm Habitable Zone Extrasolar Planets

A DISSERTATION

SUBMITTED TO THE GRADUATE SCHOOL
IN PARTIAL FULLFILLMENT OF THE REQUIREMENTS

for the degree

Doctor of Philosphy

Earth and Planetary Sciences

By

Howard Chen

EVANSTON, ILLINOIS

March 2022

Abstract

Rocky exoplanets are indicated to be common in the galaxy. Future instruments including the *James Webb Space Telescope* (JWST), high resolution ground-based spectrographs, and direct imaging missions for under consideration by the 2020 Decadal Survey on Astronomy and Astrophysics are poised to unlock the atmospheres of habitable zone planets orbiting nearby and distant main-sequence stars. However, retrieval and interpretation of observational measurements will require understanding of possible atmospheric compositions, star-planet environmental context, and their consequences on the habitability and detectability of the planet. To inform future instruments, a range of model complexity, architectures, and frameworks have been used. Recently, emerging terrestrial general circulation model (GCM) results argue that planetary rotation can drive changes in heat redistribution, cloud formation, and circulation regimes, potentially influencing chemical transport and the spatial distribution of gaseous species such as atmospheric biosignatures. Observations of neighborhood stars show evidence for flaring events that deviates substantially from their time-averaged spectra over day-to-week time spans. These flares will likely accompany heightened UV radiation and energetic particle precipitation, effects that should be accounted for in single column and global climate models. These newfound importance of atmospheric dynamics and dayside photochemistry, particularly for slowly-rotating planets orbiting low-mass stars, has been hypothesized to have important ramifications for the cumulative and evolving atmospheric compositions, surface habitability, and remote detectability of molecular signals.

In this dissertation, we employ an array of three-dimensional Earth-system models in a series of experiments that seek to self-consistently determine the atmospheric composition and dynamics of extrasolar planets. Specifically, this dissertation utilizes global chemistry-climate models in conjunction with observed data of stellar parameters to explore the habitability and observational prospects of rocky exoplanets orbiting G, K, and M-stars. In Chapter 1, we describe the

motivation, background, and approach that serve as the foundation our work. In Chapter 2, we adapt a chemistry-climate model (CCM) to simulate slowly- and synchronously-rotating planets orbiting systems with masses less than the Sun. Using this newly adapted tool, we confined the degree of spatial heterogeneity of key biosignature compounds and find substantial chemical day-night side contrasts for planets with rotation periods of 60 Earth days. In Chapter 3, we employ a high-top version of the CCM to investigate hypothetical oxygen-rich exoplanets around a variety of M-dwarf spectral types. For planets at the inner edge of the habitable zone, we find that chemical-climate feedback driven by stellar forcing lead to thinning of the ozone layer as the model atmospheres move towards more active M-dwarfs or increasingly wetter climates. Further, the difference between these scenarios will likely manifest in observed atmospheric spectra and could be discriminated by instruments aboard the JWST. In Chapter 4, we apply the same CCM to discovered habitable zone planetary climates, but we use stellar spectra and lightcurves with the inclusion of flare activity as inputs. We find secular and order-of-magnitude variations in the global concentrations of habitability-associated gas-phase species (e.g., nitrogen and hydrogen oxides) over weekly to monthly timescales. In Chapter 5, we expand upon the results of Chapter 3 and explore the consequence of different global oxygenation levels from pO_2 of 0.1% present atmospheric level (PAL) to 10% PAL on the habitability of dry and moist climates. The slow rise of molecular oxygen in Earth's history is a result of oxygenating photosynthesis on a planetary-scale, and our results from this chapter highlight the importance of 3D modeling in evaluating the effects of (exo)planetary evolution. Finally, in Chapter 6, we develop a volatile accretion model based on N-body planetary accretion simulations to trace the origins and sources of key elements (C, N, H) that make up Earth's hydrosphere and atmosphere.

Acknowledgements

It is impossible to list everyone who has supported, encouraged, and challenged me during my PhD. I am greatly in debt to my advisor, Daniel Horton, whose intelligence, meticulousness, and craftsmanship have contributed to the success of my PhD endeavors. His attentiveness and care for the well-being of his students is a quality I hope to emulate.

I have been very lucky to interact with many kind and talented people over the course of my academic career and I owe so many of them thanks: to my AP US History Teacher David Schmus, who inspired me to pursue my passions in the very first place; to my undergraduate mentors, Phil Muirhead, Leslie Rogers, and James Kasting, who have ignited my interest in planetary sciences; to my collaborators Eric T. Wolf, Zhuchang Zhang, and Ravi Kopparapu, who have helped me immensely and offered key scientific ideas that substantially enhanced the quality of my work; to my committee members Fred Rasio, for his strong support and insights, and Donna Jurdy, for our random but informative encounters and chats in the dept; and to all the folks in the Earth and Planetary Sciences and CIERA, including Jiuyuan Wang, Fei Wang, and Vivian Tang. My five plus years of graduate school turned out to be much more enjoyable because of each of you and for that I am eternally grateful. Finally, I thank the National Aeronautics and Space Administration (NASA) for funding the final three years of my graduate career and the first few years of my post doctoral fellowship.

Above all however, I thank my late grandfather, who has taught me the values of hard work and parsimony, which I've tried to implement throughout the course of my science career. This dissertation would not exist without his loving wisdom.

Contents

List of Figures

My parents taught me that the provable, tangible, verifiable things were sacred, that sometimes the most astonishing ideas are clearly profound, but when they get labeled as "facts", we lose sight of their beauty. It doesn't have to be this way. Science is the source of so much insight worthy of ecstatic celebration.

Sasha Sagan

Chapter 1

Introduction

We stand at an important juncture in human history; for the first time we have the capability to perform detail survey and characterization of planets outside the solar system (i.e., extrasolar planets, or exoplanets). Since the first discovery of a transiting exoplanets in 1996, the *Kepler Space Telescope* has revolutionized our knowledge regarding the demographics of planetary systems and simultaneously, has provided us with detailed dossiers of the attributes and histories of potential planetary environments. In recent years, we are gradually moving from planet discovery towards planet characterization with the ultimate goal of understanding the existence and distribution of life in the Universe.

Today, about five thousand exoplanets are known to exist (e.g., Bryson et al. 38, Hsu et al. 147), but our knowledge of these planets and their environments is incomplete. While fundamental physical parameters such as mass, radius, and bulk density are relatively well measured, we know little about the structure and atmospheres of these systems. Critically, understanding the nature of exoplanets and how they form and evolve, particularly for small planets, is needed to help predict and interpret anticipated atmospheric measurements of potentially habitable worlds includ-

ing Kepler-186f, Proxima Centauri b, TRAPPIST-1e, LHS 1140b, and TOI-700d with upcoming ground-based spectrographs and space-borne missions such as the *James Webb Space Telescope* (*JWST*), the European Extremely Large Telescope (E-ELT), the *Large Ultraviolet Optical Infrared Surveyor* (LUVOIR), the Habitable Exoplanet Observatory (HabEx), and the Origins Space Telescope (OST).

In the past decade, extrasolar planet characterization efforts revealed exotic atmospheric compositions and climate patterns. Hot Jupiters, one of the most well examined exoplanet classes, are found to host familiar compounds such as carbon monoxide (CO) and water vapor (H_2O) [207, 228], bolstering the likelihood for such detections in terrestrial worlds. Detection of aluminium oxide (Al_2O_3) and titanium oxide (TiO) and even sulfur (S) imply the occurrence of complex chemistry on these warm gaseous planets [23, 52, 59]. Transit-transmission spectroscopy of sub Neptunes and super Earths found that clouds and hazes have a large impact on the observed spectra by raising the baseline and/or muting certain spectral features [196]. Recently, the field has rapidly pushed towards smaller planets with greater habitability prospects. For example, initial remote reconnaissance of the TRAPPIST-1 system has ruled out high mean-molecular weight atmospheres as the primary composition for TRAPPIST-1e and TRAPPIST-1f [69, 246].

For the next few decades, a primary focus of the astronomy, planetary science, and astrobiolgical communities will be the atmospheric and surface characterization of small and potentially rocky planets. With the imminent launch of the *JWST* and flagship direct imaging missions on the horizon, we will need terrestrial planet models to interpret observations and retrieve planetary characteristics by upcoming observational campaigns. Earlier efforts to quantify the climate, habitability, and observational potential of habitable zone typically rely on conceptual, analytical, or single-column models. In the past decade or so, state-of-the-art numerical models such as the three-dimensional (3D) general circulation models (GCMs) have also been employed (e.g., Eager et al. 86, Kasting et al. 168, Komacek and Abbot 187, Kopparapu 192, Way et al. 348, Wolf et al. 354). However,

terrestrial planet GCMs typically do not include chemical speciation, transport, and interactive reactions that are imperative for detailed habitability and biosignature modeling. To better circumscribe the climate and atmospheres of warm habitable exoplanets, coupled chemistry-climate models are warranted. Below, we describe the need for such an advance in modeling techniques in terrestrial planet studies. In doing so, we motivate the work conducted in this dissertation.

Conventional GCM studies without interactive chemistry assumed atmospheres composed of N_2-CO_2-H_2O, with either ocean-covered or dry surfaces and quiescent stellar spectral energy distributions. However, observational measurements show evidence of stellar flares (and implicitly coronal mass ejections) in the *Kepler* and TESS data (e.g., Howard and Law 146, Seli et al. 307, Tu et al. 334). In many cases, the measured peak flare emissions of typical M-dwarfs are over three orders of magnitude greater than the strongest record solar flare i.e., the Carrington Event [281]. When modeling the 3D atmospheres of small exoplanets, it is thus important to account for the coupled effects of stellar activity [280, 289] as well as the dynamical and chemical responses because both initial perturbation and subsequent feedbacks could determine the ionization rates, energy balance, and production/destruction of gas-phase species.

Previous work has demonstrated inclusion of 3D processes can significantly affect the long-term climate and chemistry of slowly- and synchronously-rotating planets orbiting early K and late M-dwarfs. Strong substellar buoyant updrafts can lead to the formation of optically thick dayside cloud decks, which increases the planetary albedo and lowers the global mean surface temperature [348, 362]. For planets with $P > 25$ days, it has been shown that divergent day-to-night circulation can efficiently transport photochemically and photolytically produced compounds (e.g., O_3) to the nightside and suggest that global simulation of trace molecular species will be important next steps [271, 369], shown to be vital for the chemical composition of gas giant exoplanets [85]. As different photochemical reactions dominate different atmospheric scenarios, identification of specific trace-gas chemistry pathways could serve as observational hallmarks for certain atmospheric or climate

archetypes.

Another motivation for the utilization of 3D coupled CCMs is to improve synergies between different model communities and heritages. For example, an existing challenge is that the model complexities a wide variety of climate predictions. Even for a single planet climate simulation e.g., TRAPPIST-1e, 1D radiative-convective models and 3D GCMs disagree on the surface temperature predicted [91]. Even within GCMs, there exists significant discrepancies between published results. For instance, the LMD, ExoCAM, and MET Office GCM suites disagree on whether a planet transitions through a moist greenhouse phase or transition directly into the runaway greenhouse phase [170, 203]. In the modern Earth climate science community, large GCM ensemble experiments allows researchers to assess this range of and better capturing model uncertainty. Because paleoclimate and exoplanet climate studies typically involve individual institution and/or research groups, such feats are difficult to accomplish [368]. A 3D model simulations that includes self-consistent photochemistry could serve as a gateway between 1D and 3D exoplanet modeling communities.

The dissertation uses Earth-system chemistry-climate models to explore atmospheric and surface scenarios relevant to the past, present, and future of terrestrial exoplanets. In the experiments presented in this dissertation, the National Center for Atmospheric Research (NCAR) Whole Atmosphere Community Climate Model (WACCM) is modified to study hypothetical atmospheres of habitable exoplanets. WACCM is a 3D global CCM that simulates interactions of atmospheric chemistry, radiation, thermodynamics, and dynamics. Unless otherwise stated in the specific chapters, the model utilizes sub-components Community Atmosphere Model v4 (CAM4), the Community Land Model (CLM) 4.0, and a customised thermodynamic ocean model. In addition, it includes an active hydrological cycle and prognostic photochemistry, which takes advantage of version 3 of the Modules for Ozone and Related Chemical Tracers (MOZART) chemical transport model [179]. The final component of WACCM includes a number of improved and expanded

high-top atmospheric physics and chemical components. Processes in the MLT region are based on the thermosphere-ionosphere-mesosphere electrodynamics (TIME) GCM [279]. An important addition employed in this dissertation is the open source convolution neural network (CNN) code. This CNN code was developed by Feinstein et al. [92] with the goal of identifying flaring activity in the TESS data and we have used it to generate flare lightcurves for use in our climate model. Throughout the studies presented in this dissertation, these modeling components are used in various configurations to test the sensitivity of the HZ exoplanet climate to a range of different environmental parameters and boundary conditions.

Each chapter includes a detailed description of these experimental designs and explores a different aspect terrestrial exoplanetary atmospheres. The dissertation is comprised of five main results-based Chapters (2-6), in addition to an introductory Chapter (1) and concluding with a summary Chapter (7). Specifically, Chapters 2- 5 used the modeling tool described above to study the habitability and observability of planets around other stars, while the final chapter present a newly written code to explore the delivery and loss of key hydrospheric ingredients. Chapter 2 investigates the roles of planetary rotation and stellar illumination, as well as the Earth-Sun and planet-star orbital configuration on the distribution and concentration of remotely detectable biosignatures (Chen et al. 2018). These experiments were the first to incorporate a chemistry module MoZart, including 150 trace gas species and reactions, into a terrestrial exoplanet GCM, resulting in a benchmark advance in the exoplanet GCM intercomparison community. Chapter 3 builds on this CCM simulation setup and performed a more comprehensive study into the boundaries of the inner edges of the HZ across a range of stellar spectral types. One important finding is that the ultraviolet (UV) spectral energy distribution is a key parameter in determining the inner edge of the habitable zone, but it is unclear how time-resolved model (Chen et al. 2019). This question is further addressed in Chapter 4, when observed stellar lightcurves and modeled spectra are used as inputs to the CCM presented in Chapter 3. Flare induced variability of the nitrogen- and hydrogen-oxide reservoir

are found to produce potentially observable signatures for next-generation observatories (Chen et al. 2021). In Chapter 5, wet and dry climate scenarios experimented in Chapter 3 are examined with an aim to understand the consequences of different global oxygenation levels on exoplanetary climate, motivated by the biogeochemical evolution of Earth's atmosphere (Chen et al., in prep). In Chapter 6, the formation of early Earth's atmosphere and hydrosphere is investigated with a newly built model of terrestrial planet accretion. This soon to be publically available code is used to investigate the elemental ratios of primitive Earth and trace the origins of carbon, nitrogen, and hydrogen (Chen & Jacobson, submitted).

1.1 Publications and conference abstracts resulting from this dissertation

Refereed Publications

Chen, H., Wolf, E.T., Kopparapu, R., Domagal-Goldman, S. and Horton, D.E., 2018. Biosignature anisotropy modeled on temperate tidally locked M-dwarf planets. *The Astrophysical Journal Letters*, 868(1), p.L6. **(Chapter 2 is adapted from this publication)**

Chen, H., Wolf, E.T., Zhan, Z. and Horton, D.E., 2019. Habitability and spectroscopic observability of warm M-dwarf exoplanets evaluated with a 3D chemistry-climate model. *The Astrophysical Journal*, 886(1), p.16. **(Chapter 3 is adapted from this publication)**

Chen, H., Zhan, Z., Youngblood, A., Wolf, E.T., Feinstein, A.D. and Horton, D.E., 2021. Persistence of flare-driven atmospheric chemistry on rocky habitable zone worlds.*Nature Astronomy*, 5(3), pp.298-310. **(Chapter 4 is adapted from this publication)**

Chen, H., Luo, Yangcheng, and Horton, D.E., Modulation of the Water-Loss Timescales by Planetary Oxygenation Levels, in prep. **(Chapter 5)**

Chen, H. and Jacobson, S. A., C/N and C/H on Earth-like Planets as Outcomes of Impact Loss and Degassing, submitted to EPSL **(Chapter 6 is adapted from this submitted manuscript)**

Conference Abstracts

Chen, H., Horton, D. E., 2021, December. The 3D Effects of Large Stellar Flares on Habitable Zone Planets. In AGU Fall Meeting Abstracts (Vol. 2021, pp. U44B-06).

Chen, H., Luo, Y., Horton, D. E., 2021, December. Caveats for the Water-Loss Limits at the Inner Edge of the Habitable Zone. In AGU Fall Meeting Abstracts (Vol. 2021, pp. P45B-2418).

Chen, H., Jacobson, S. A., 2021, December. Modeling the evolution of mantle and atmospheric elemental abundances on nascent Earth-like planets. In AGU Fall Meeting Abstracts (Vol. 2021, pp. DI35C-0034).

Chen, H., Mendillo, M., Becker, J. and Horton, D.E., 2020, December. On the Ionospheres of Strongly-to Weakly-Oxygenated Terrestrial Exoplanets. In AGU Fall Meeting Abstracts (Vol. 2020, pp. U008-11).

Chen, H., Wolf, E., Zhan, Z. and Horton, D., 2019. M-dwarf Activity Driven 3D Climate and Photochemistry of Inner Habitable Zone Tidally-Locked Planets. AAS/Division for Extreme Solar Systems Abstracts, 51, pp.502-04.

Chen, H., Wolf, E.T., Zhan, Z. and Horton, D.E., 2019, June. Coupled 3D Chemistry-Climate Simulations of Moist Greenhouse Terrestrial Planets: Water-Loss and Spectroscopic Observability. In 2019 Astrobiology Science Conference. AGU.

Chen, H. and Horton, D., 2018, January. Modeled 3-D Biosignatures from the Stratospheres of Proxima Centauri b and M-dwarf Planets. In American Astronomical Society Meeting Abstracts# 231 (Vol. 231, pp. 148-13).

Chapter 2

Biosignature Anisotropy Modeled on Temperate Tidally Locked M-dwarf Planets

2.1 Abstract

[1] A planet's atmospheric constituents (e.g., O_2, O_3, H_2O_v, CO_2, CH_4, and N_2O) can provide clues to its surface habitability, and may offer biosignature targets for remote life detection efforts. The plethora of rocky exoplanets found by recent transit surveys (e.g., the *Kepler* mission) indicates that potentially habitable systems orbiting K- and M-dwarf stars may have very different orbital and atmospheric characteristics than Earth. To assess the physical distribution and observational prospects of various biosignatures and habitability indicators, it is important to understand how they may change under different astrophysical and geophysical configurations, and to simulate

---

[1]Chapter adapted from: Chen, H., Wolf, E.T., Kopparapu, R., Domagal-Goldman, S. and Horton, D.E., 2018. Biosignature anisotropy modeled on temperate tidally locked M-dwarf planets. *The Astrophysical Journal Letters*, 868(1), p.L6.

these changes with models that include feedbacks between different subsystems of a planet's climate. Here we use a three-dimensional (3D) Chemistry-Climate model (CCM) to study the effects of changes in stellar spectral energy distribution (SED), stellar activity, and planetary rotation on Earth-analogs and tidally-locked planets. Our simulations show that, apart from shifts in stellar SEDs and UV radiation, changes in illumination geometry and rotation-induced circulation can influence the global distribution of atmospheric biosignatures. We find that the stratospheric day-to-nightside mixing ratio differences on tidally-locked planets remain low ($< 20\%$) across the majority of the canonical biosignatures. Interestingly however, secondary photosynthetic biosignatures (e.g., C_2H_6S) show much greater ($\sim 67\%$) day-to-nightside differences, and point to regimes in which tidal-locking could have observationally distinguishable effects on phase curve, transit, and secondary eclipse measurements. Overall, this work highlights the potential and promise for 3D CCMs to study the atmospheric properties and habitability of terrestrial worlds.

2.2   Introduction

A promising approach in the hunt for life beyond Earth is through the detection of biosignatures – biologically produced compounds such as O_2, O_3, CH_4, N_2O, and CO_2 – in the atmospheres of terrestrial planets orbiting the putative habitable zones (HZs) of nearby stars [168, 218, 287, 300].

In recent years, the convergence of our ability to detect, confirm, and characterize extrasolar planets has profoundly strengthened the prospects of finding life on other worlds. Consistently improving measurements of stellar mass, radius, and distance allows more accurate constraints on their attending planets [227]. Large-scale observational surveys such as the M-Earth project, TRAPPIST survey, Hungarian Automated Telescope Network (HATNet), Kepler Space Telescope, and Transiting Exoplanet Satellite Survey (TESS) have detected planets in the habitable zones

around these stars [327] and will continue to monitor closer and brighter systems for Earth-sized planets [20]. Simultaneously, follow-up characterization efforts of these confirmed planets were able to resolve atmospheres of much smaller planets than past efforts (e.g., HAT-P-26b; Wakeford et al. 343). Looking ahead, a variety of instruments are being designed with life detection goals in mind. This includes ground-based observatories such as the European Extremely Large Telescope (E-ELT), Giant Magellen Telescope (GMT), and Thirty-Meter Telescope (TMT), as well as space-based missions such as the James Webb Space Telescope (JWST), Large UV/Optical/IR Surveyor (LUVOIR), Origins Space Telescope (OST), and Habitable Exoplanet Imaging Observatory (HabEx). HabEx and LUVOIR in particular would enable characterization of potentially habitable Earth-sized rocky planets in our solar neighborhood (100 parsecs; Batalha et al. 22, Bolcar et al. 34, Mennesson et al. 242).

The recent discoveries of Proxima Centauri b [10] and the TRAPPIST-1 system [106] demonstrate that analyses of small rocky planets are within reach. However, many of these planets orbit extremely close to their host M-type stars (0.02-0.2 AU) and are susceptible to trapping by tidal-forces [325]. Tidally-locked but potentially habitable planets are expected to be common in HZs of low-mass stars ($\sim$15%; Dressing and Charbonneau 84) – which dominate our solar neighborhood stellar population ($\sim$70%; Henry et al. 136). Concurrently, our earliest opportunity for a biosignature search will likely come from the JWST and ground-based extremely large telescopes (E-ELT, GMT, and TMT); these observatories will enable spectroscopic observations of rocky planets around K- and M-type stars. It is therefore likely that our first opportunity to measure atmospheres of rocky worlds will be tidally-locked terrestrial planets around K- or M-dwarf stars.

Characterization of exoplanets primarily involves measuring starlight and terrestrial thermal emissions absorbed by planetary atmospheres as a function of wavelength. For transit spectroscopy, which will be the main tool for obtaining spectra from planets around M-dwarf stars, observations are biased towards atmospheric constituents across the terminators. Therefore, interpreting spectro-

scopic observations requires inferring both the concentration and distribution of detectable gases. Such properties can be predicted by 3D global climate and chemistry-climate models (GCMs and CCMs). GCMs and CCMs are numerical models that employ laws of physics, fluid motion, and in the case of CCMs, chemistry to simulate movements, interactions, and climatic implications of a planet's atmospheric constituents and boundary conditions.

Previous simulations of atmospheres of tidally-locked planets performed with 3D GCMs have demonstrated that habitable states of tidally-locked planets are strong functions of: (*i*) Coriolis force [190, 348, 364], (*ii*) stellar energy distribution (SED) and bolometric stellar flux [191, 351], (*iii*) atmospheric mass [357], and (*iv*) radiative transfer scheme [364]. Despite the ability of GCMs to simulate key climatological factors, as demonstrated by these studies, their foci have primarily been on questions of habitability, rather than the concentrations and distributions of biologically-produced gases and habitability indicators.

To study effects of tidal-locking on atmospheric chemistry and molecular spectroscopic signals, models capable of resolving chemical speciation, reactions, and transport are needed. To date, exoplanet atmospheric photochemical predictions have largely relied on one-dimensional global-mean photochemistry-climate models (e.g., Kasting et al. 166, Meadows et al. 237, Segura et al. 303). These 1D models have been used to simulate synthetic spectra of hypothetical rocky planets under the influence of different host SEDs [274, 285]. However, 1D models employ relatively simple eddy-diffusion parameterizations for vertical transport and do not account for atmospheric dynamics, climate heterogeneities, or 3D geometric effects critical to observations. These factors are important as advection and diffusion can affect concentration, distribution, and ultimately the composition of an atmosphere [306]. In addition to altering photochemistry, as shown by 1D models, shifts in stellar SED can influence atmospheric circulation and climate (e.g., Fujii et al. 99, Shields et al. 310). Atmospheric chemistry and dynamics are thus interactive, and should ideally be simulated using fully-coupled 3D model components.

Here, to better undererstand the observational potential of tidally-locked planets, the integrated effects of atmospheric chemistry, photochemistry, and circulation are considered over the 3D geometry of a planet's atmosphere. In this Letter, we simulate Earth-analogs and tidally-locked planets around M-dwarf stars using a 3D CCM, while seeking to (*i*) elucidate the photochemical nature of Earth-like worlds, (*ii*) demonstrate the utility of 3D CCMs in terrestrial exoplanet studies, (*iii*) and advance model comparison efforts between 3D and 1D research communities.

2.3   Model Description & Experimental Setup

In this study, we employ the Community Atmosphere Model with Chemistry (CAM-chem), a subset of the National Center for Atmospheric Research (NCAR) Community Earth System Model (CESM v.1.2), to investigate atmospheres of Earth-like planets. CAM-chem is a 3D global CCM that simulates interactions of atmospheric chemistry, radiation, thermodynamics, and dynamics (for complete model description see Lamarque et al. [199]). CAM-chem combines the CAM4 atmospheric component with the fully implemented Model for Ozone and Related Chemical Tracers (MOZART) chemical transport model. CAM-chem resolves 97 gas phase species and aerosols linked by 196 chemical and photolytic reactions. CAM, the atmosphere component of the model, has seen wide applications in problems of paleoclimate and exoplanets (e.g., Kopparapu et al. 190, Wolf and Toon 353), whereas CAM-chem has largely been limited to studies of present Earth. All simulations presented were run for 30 Earth years and reported results are averaged over the last 20.

We simulate Earth-analogs and tidally-locked planets and assess the sensitivity of atmospheric biosignatures to three primary variables: (*i*) stellar spectral energy distribution, (*ii*) stellar UV radiation, and (*iii*) planetary rotation period. To simulate Earth-analogs, we use a preindustrial Earth

setup forced by solar spectral irradiance data [202], i.e., apart from the orbital parameters described below, our Earth-analog simulation uses identical boundary and initial conditions to Earth in 1850, prior to anthropogenic influences [326]. These conditions include atmospheric gases N_2 (78% by volume), O_2 (21%), and CO_2 ($2.85\times10^{-2}\%$) [225]. In addition, the model simulates the free-running evolution of H_2O_v and O_3, while CH_4 and N_2O surface fluxes are latitudinally variable (global mean CH_4: 7.23×10^{-7} and N_2O: 2.73×10^{-7} mol mol^{-1}). Throughout the remainder of the paper, we refer to this Earth-Sun simulation as the baseline.
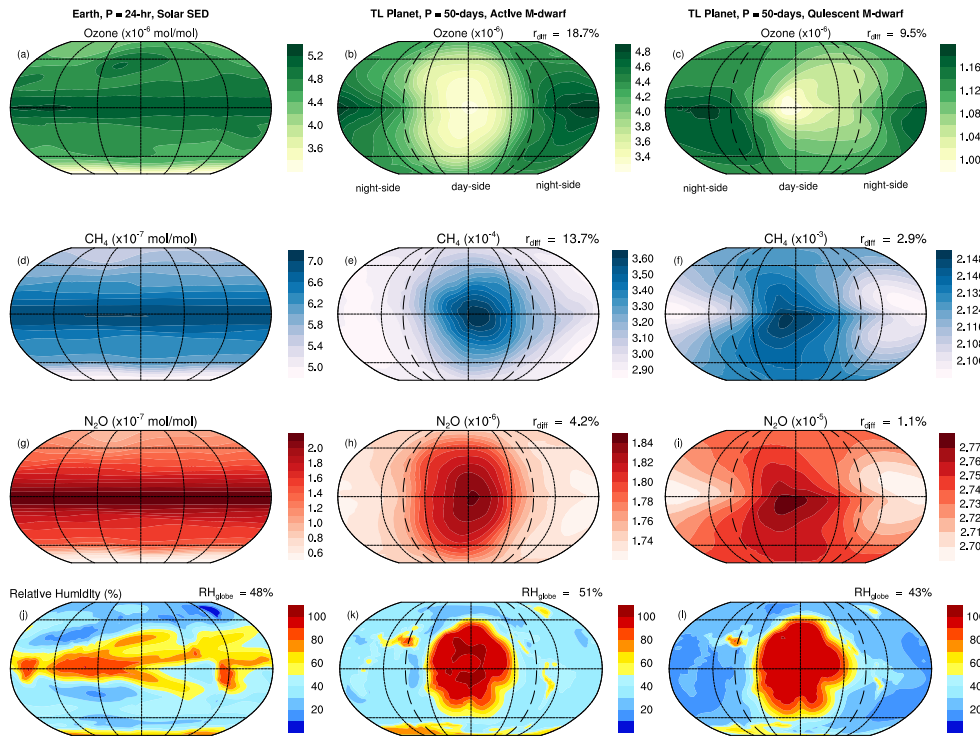
Figure 2.3.1: Global distribution of O_3, CH_4, and N_2O mixing ratios and relative humidity for Earth-like non-tidally-locked ($P = 24$ hr) Solar SED simulations (a, d, g, j) and tidally-locked ($P = 50$ days) active (b, e, h, k) and quiescent (c, f, i, l) M-dwarf SED simulations. Evidence of circulation- and photochemical-induced biosignature anisotropy are apparent. Day-to-nightside mixing ratio contrasts (r_{diff}) for tidally-locked simulations are reported, while relative humidity is averaged across the globe (RH_{globe}). Gas mixing ratios are pressure-weighted vertical averages over the top of the model atmosphere (1-to-100 mb). Relative humidity is reported for the 200 mb pressure surface. Note differences in scaling factors used amongst experiments and constituents. Dashed-lines indicate locations of terminators.

We also modify CAM-chem to simulate tidally-locked planets with initially Earth-like atmospheric compositions forced by M-dwarf SEDs. This SED was obtained from an open-source dataset of an M6V star, Proxima Centauri, compiled by NASA's Virtual Planetary Laboratory (VPL) team and is available at `http://vpl.astro.washington.edu/spectra/stellar/`. We explore two SED-types (active and quiescent) that bracket the endmember ranges of stellar activity. VPL Proxima Cen. data is assumed to be moderately-to-highly active. To construct a quiescent

M-dwarf SED, we swap out UV bands ($\lambda < 500$ nm) of the original Proxima Cen. data with that of a low-activity star (HD114710). For all exo-Earth simulations, we assume tidal-locking (i.e., trapped in 1:1 spin-orbit resonances), with orbital periods of 50 Earth days. While we do not use self-consistent stellar-flux orbital period relationships (e.g., Haqq-Misra et al. 125, Kopparapu et al. 190), the idealized case studied here highlights the value of using CCMs for modeling chemical processes on slowly and synchronously rotating planets.

For both Earth and tidally-locked exoplanet simulations, we set orbital parameters (obliquity, eccentricity, and precession) to zero, such that top-of-atmosphere incident stellar flux is symmetric about the equator. Incident bolometric stellar flux for all simulations is set to 1360 W m^{-2}. The substellar point for all simulations is fixed at (Earth's) $latitude = 0$ and $longitude = 180$, in the Pacific Ocean. Note that other studies (e.g., Lewis et al. 208) have shown that surface type beneath a substellar point can modify water vapor availability, influencing water vapor-induced greenhouse and cloud radiative effects, and possibly atmospheric chemistry.

In all simulations, we assume present Earth's continental configuration, topography, mass, and radius. We use prognostic atmospheric and oceanic components of CESM, as well as prescribed preindustrial land, surface ice, and sea ice components. Horizontal resolution (latitude $\times$ longitude) is set to $1.9 2.5$ $with 26 vertical atmospheric levels and model top of 1 mb$ (~ 50 km). The land model is Community Land Model version 4.0 with non-interactive surface features. The ocean component is a thermodynamic slab model with prescribed heat flux values sourced from dynamical ocean simulations (e.g., Danabasoglu and Gent 65).

Consistent with 1D studies (e.g., Segura et al. 303) and in alignment with our lack of terrestrial exoplanet observations, we assume atmospheric compositions, biological production, and dry deposition rates of gaseous species the same as those of preindustrial Earth. Apart from CH_4 and N_2O, global surface gas flux inputs are based on spatially-explicit preindustrial monthly averages

(e.g., DMS; Kettle and Andreae 176). Due to SED sensitivities, CH_4 and N_2O surface flux boundary conditions are estimated via ancillary CCM simulations that allow for the emergence of stellar SED-dependent flux magnitudes (i.e., WACCM; Neale et al. 252). Emergent SED-consistent N_2O and CH_4 flux estimates are temporally and spatially fixed in active and quiescent M-dwarf simulations at CH_4: 3.5×10^{-4} and 2.3×10^{-3} mol mol^{-1} and N_2O: 2.5×10^{-6} and 3.2×10^{-5} mol mol^{-1}, respectively. Given uncertainties inherent in flux estimates, sensitivity experiment and day-to-nightside mixing ratio comparisons should focus on relative rather than absolute differences.

2.4   Results

Three general observations can be made from our simulated 3D global distributions of O_3, CH_4, N_2O, and DMS on Earth-like and tidally-locked planets (Figures 1 and 4): (*i*) Changes in mixing ratios of O_3, CH_4, and N_2O are primarily due to different levels of stellar UV flux amongst the three SED datasets. (*ii*) Introduction of tidal-locking modifies globally homogeneous gas distributions that characterize Earth-like scenarios. (*iii*) Heterogeneous surface-to-atmosphere flux distributions (e.g., DMS) can influence the resultant mixing ratios of atmospheric constituents.

To facilitate analysis of our results, we define a day-to-nightside mixing (mole) ratio contrast as:

$$r_{\text{diff}} = \frac{r_{\text{day}} - r_{\text{night}}}{r_{\text{globe}}} \tag{2.1}$$

i.e., the relative difference between the two hemispheres, where r_{day} is the dayside hemispheric mixing ratio mean, r_{night} the nightside mean, and r_{globe} the global mean. The degree of anisotropy

is loosely encapsulated in this parameter, which is analogous to the definition used by Koll and Abbot [183] in the context of temperature contrasts. Values of r_{diff} for each respective experiment are shown in Figures 1 and 4 and will be discussed throughout the paper.
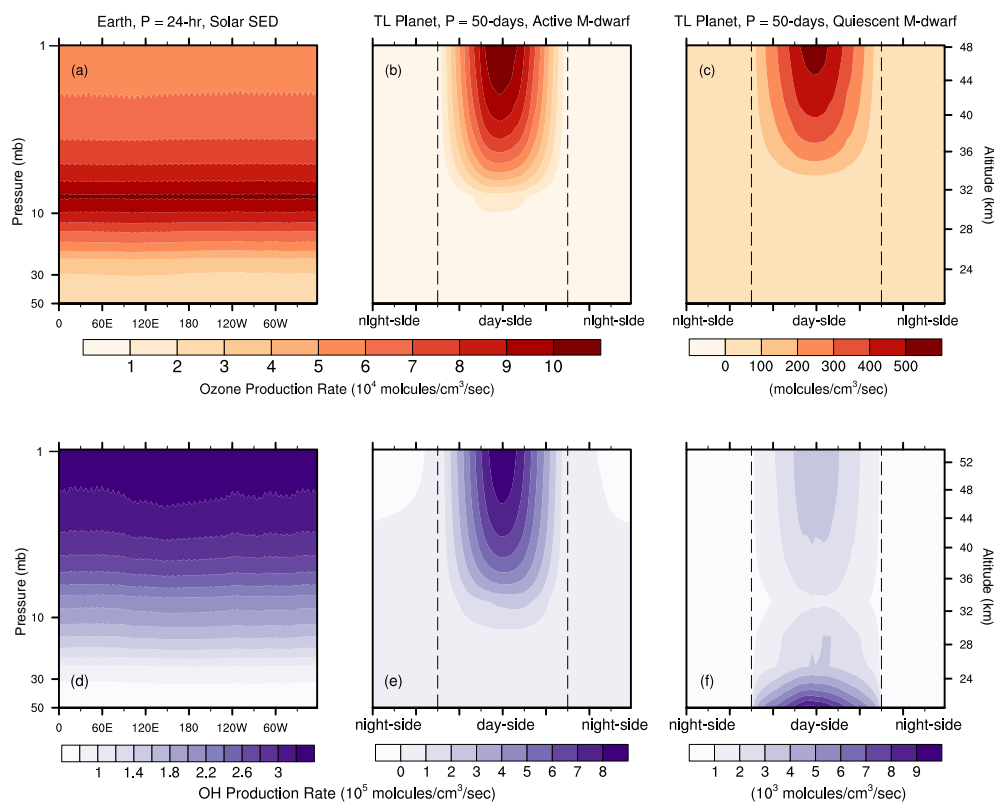
Figure 2.4.1: Stratospheric O_3 and OH production rates as functions of longitude[Stratospheric O_3 and OH production rates as functions of longitude] for Earth-like non-tidally-locked ($P = 24$ hr) Solar SED simulations (a, d) and tidally-locked ($P = 50$ days) M-dwarf SED (b, c, e, f) simulations. Photolytic processes drive ozone and hydroxyl radical production and help to explain many of the observed biosignature gas distributions in Figure 1. Note vertical axis begins at 50 mb ($\sim$20 km). Dashed-lines indicate locations of terminators.

2.4.1 Ozone Distributions, Water Vapor Mixing Ratios, and Temperature Profiles

Ozone production and destruction depend on stellar UV activity, availability of molecular and atomic oxygen, and ambient meteorological conditions (P, T). As our simulated M-dwarf SED is moderately active in the UV bands, our results show similar quantities of ozone between the baseline Earth-Sun and tidally-locked cases (Figures 1a-c). However, the quiescent SED, produces lower ozone concentrations above the tropopause (Figure 3c). These differences reflect specific stellar activity inputs. Quiescent M-dwarfs emit lower UV in the range responsible for ozone production ($160 < \lambda < 240$ nm). Moreover, calculated day-to-nightside mixing ratio differences r_{diff} are higher ($\sim$19%) in the active M-dwarf SED scenario, a result of the more photochemically active substellar hemisphere.

Modulations to ozone concentration have major influences on distributions of other biosignature gases. This is due to substellar hemispheric production of excited state atomic oxygen $O(^1D)$ and constituent families of HO_x. Both $O(^1D)$ and HO_x constituents are reactive radicals important for atmospheric biogenic organo-compounds and hydrocarbons (e.g., CH_4, CH_3, HCL, H_2S).

As ozone is photochemically produced, horizontal advection carries a portion to the nightside as evidenced by its presence in both hemispheres. The lifetime of ozone ($\sim$15 days), in conjunction with day-to-nightside transport, is sufficient enough to sustain some nightside O_3, but not efficient enough to fully mix the atmosphere, allowing day-to-nightside contrast ($\sim$19%; Figure 1b). Conversely, the product $O(^1D)$ shows limited transport effects due to a short lifetime (< 5 secs), reflected in its large r_{diff} value ($\sim$300%; not shown). $O(^1D)$ is rapidly removed by one of R1 or R2 reaction pathways [157]:

$$O(^1D) + H_2O_v \rightarrow 2OH \tag{2.2}$$

$$O(^1D) + M(N_2, O_2) \rightarrow O(^3P) + M \tag{2.3}$$

$$O(^3P) + O_2 + M \rightarrow O_3 + M \tag{2.4}$$
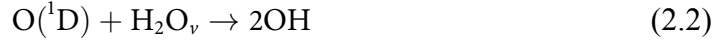
The higher ozone mixing ratios on tidally-locked nightsides is explained by these reaction pathways (Figure 1b-c). Reaction R1, which creates the hydroxyl radical OH, predominantly occurs on the dayside due to the abundance of H_2O_v (Figures 2e-f). In R2, singlet oxygen returns to the triplet ground state, which can then recombine with oxygen to form ozone via R3. Considered together, significant dayside UV ozone destruction and enhanced removal of $O(^1D)$ by water vapor offset higher ozone production rates (Figure 3b), which helps to explain lower dayside ozone mixing ratios (Figure 1b-c).

Interaction of stellar UV photons with O_2 and O_3 can also be seen in vertical temperature profiles. On Earth-like planets, stratospheric temperature is primarily a function of incident UV flux ($200 < \lambda < 310$ nm) due to the role of O_3 absorption of shortwave photons. In our simulations, this feature is apparent in global and hemispherically averaged profiles. Our simulations indicate that upper-stratospheric temperatures increase (and inversions weaken) as UV radiation levels increase; from quiescent SED, to active SED, to the baseline Earth simulation (Figure 3a). Enhanced UV absorption by O_3 and O_2 increase temperatures above the tropopause, reducing the vertical gradient and inversion strength.

We now turn to discussing testability of our 3D model predictions. Based on simulated ozone distributions, the calculated r_{diff} ($\sim 20\%$) is notable but unlikely to be discernible with current ob-

servational capabilities [40]. However, this task may prove viable using future instruments (e.g., Greene et al. 113). Proedrou and Hocke [271] reached a similar conclusion by comparing total column ozone of a tidally-locked Solar SED Earth and found an $\sim23\%$ difference between mean ozone columns during four arbitrary phases due to varying viewing angles.

Compared with 1D model studies, our 3D simulations produce similar ozone mixing ratios. However, we find substantially different Bond albedos, temperature, and water mixing ratio profiles. As a consequence of increased dayside water vapor-induced opacity and substellar clouds on tidally-locked planets, global-mean surface temperatures of both tidally-locked simulations are ~40 K colder than the baseline (Figure 3a), while Bond albedos are substantially higher, in agreement with GCM studies [190, 191, 361]. Colder global (and nightside) temperatures produce lower global water vapor mixing ratios than predicted by 1D models with clear-sky assumptions (i.e., pure water vapor without clouds). Conversely, dayside H_2O_v mixing ratios are greater due to humid updrafts at the substellar point (Figures 1j-l). Curiously, the quiescent M-dwarf SED simulation (Figure 1l) has lower global-mean relative humidity than the Earth-analog (Figure 1j) and the active M-dwarf case (Figure 1k). This is due to increased ozone mixing ratios and degree of UV absorption, which limit the photolysis of H_2O_v, in the more active SED simulations. Hence counterintuitively, more dayside H_2O_v destruction is experienced by the simulation under lower UV radiation. Such behaviors exemplify the value of CCM simulations, in which capturing feedbacks between 3D dynamical processes, solar forcing, and atmospheric chemistry is critical.

2.4.2 Types I and II Biosignatures: 3D CH_4 and N_2O Abundances

CH_4 and N_2O are important biosignatures produced by a myriad of bacterial metabolic pathways [73, 298]. In Figures 1d-f, we show modeled CH_4 distributions. High CH_4 mixing ratios for planets
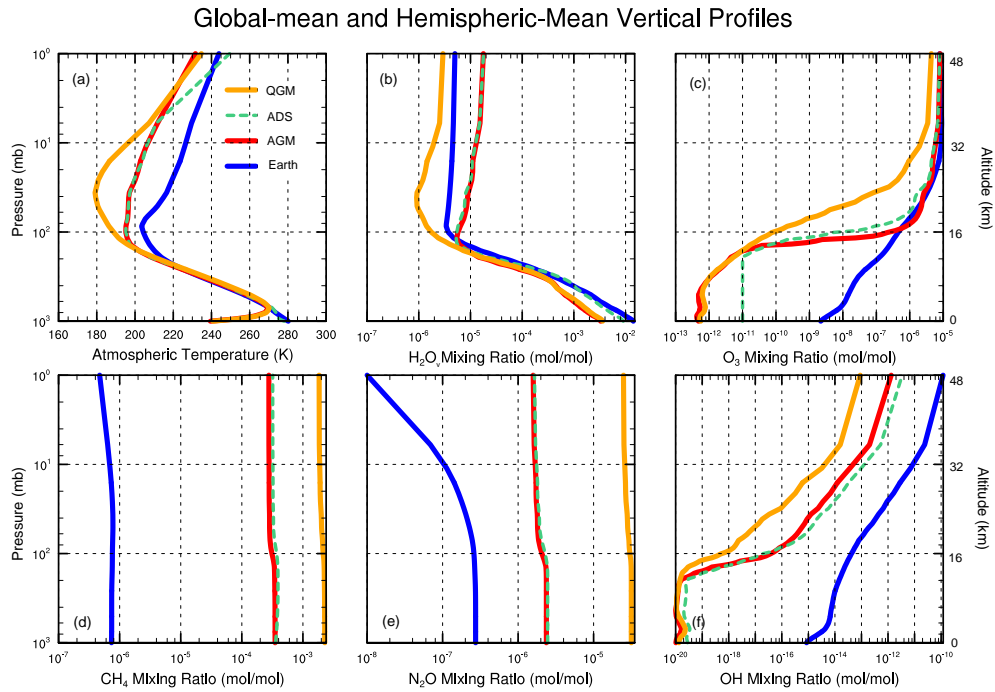
Figure 2.4.2: Vertical profiles of global-mean temperature (a) and mixing ratios of various gas phase species (b, c, d, e, f). QGM (quiescent global-mean) denotes global-mean values from simulations forced by a quiescent M-dwarf SED, AGM (active global-mean) denotes those forced by an active M-dwarf SED, and ADS (active day-side) denotes dayside-mean values from simulations forced by an active M-dwarf SED. Note axes are log-scaled and begin at planetary surfaces ($\sim$1000 mb).

orbiting quiet M-dwarfs were first noted by Segura et al. [303] using a 1D model, caused by reduced photochemical removal by reaction with OH:

$$CH_4 + OH \rightarrow CH_3 + H_2O \tag{2.5}$$

In our 3D CCM, we find similar global mean CH_4 increases in tidally-locked simulations (Figures 1e-f). However, active and quiescent simulations have low CH_4 r_{diff} values (13.7% and 2.9%,

respectively). Low r_{diff} values are explained by a mixture of competing processes. First, upwelling in tidally-locked simulations occurs exclusively below the substellar point, as evidenced by upper-tropospheric moisture patterns (Figures 1j-l). Compared to the baseline, tidally-locked meridional overturning circulation is strengthened, which brings greater moisture aloft. This, in conjunction with the dayside abundance of OH, removes CH_4 via R4. Increased dayside OH production (Figures 2e-f) is a consequence of abundant $O(^1D)$ and H_2O_v (R1), both of which are sparse on the nightside. These processes combine to limit dayside CH_4 and produce lower r_{diff} values than expected.

N_2O is primarily destroyed by UV photons ($\lambda < 220$ nm) and photo-oxidation by reactions with stratospheric $O(^1D)$ (Figure 1g-i). Hence predicted N_2O concentrations around active M-dwarfs are lesser than those with quiescent SEDs. For both active and quiescent SED simulations, higher concentrations within the substellar hemisphere are found (Figures 1h-i), similar to CH_4 behavior.

Interestingly, simulations forced by the active SED have greater stratospheric r_{diff} (CH_4: 13.7% and N_2O: 6.9%; Figures 1e-h) than those forced by quiescent SEDs (CH_4: 2.9% and N_2O: 1.1%; Figures 1f-i). Higher r_{diff} values for active SED cases is somewhat counterintuitive as one might expect that enhanced photolytic destruction on planets around active M-dwarfs should suppress day-to-nightside contrasts. However, simulations forced by active SEDs have more isothermal atmospheres (i.e., weaker temperature inversions; Figure 3a), which promote vertical mixing of surface gases above the tropopause, contributing to higher r_{diff} values.

2.4.3 Effects of Surface Fluxes on Atmospheric Distribution: Case of Dimethyl Sulfide

On tidally-locked planets, phototrophs are unlikely to emit biogenic gases globally (i.e., the assumption for all biosignature gases considered thus far); rather, photosynthetically-derived emissions are
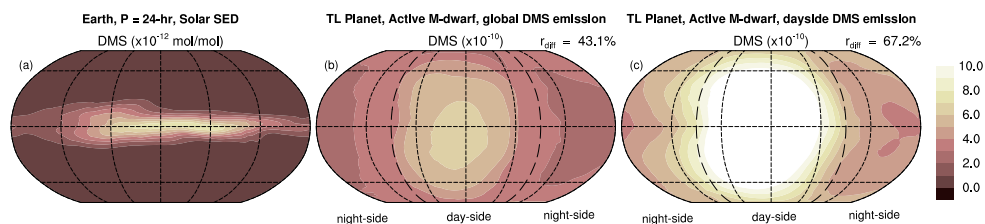
Figure 2.4.3: Global distribution of photosynthetic biosignature dimethyl sulfide (DMS, $(CH_3)_2S$) for Earth-like non-tidally-locked ($P = 24$ hr) Solar SED simulations (a), tidally-locked ($P = 50$ days) active M-dwarf SED simulations with a global DMS flux assumption (b), and tidally-locked with a dayside DMS flux assumption (c). Day-to-nightside mixing ratio differences (r_{diff}) for the tidally-locked simulations are reported. Phototrophs are assumed to be only present on the permanently lit day-side in panel (c), which results in an enhanced stratospheric day-to-nightside mixing ratio contrast. Dashed-lines indicate locations of terminators.

likely to be restricted to the dayside. To see how a biosignature gas (e.g., DMS; C_2H_6S) may behave on a tidally-locked planet, we conduct three experiments, each with a different DMS flux distribution assumption, i.e., Earth-like, tidally-locked with global DMS flux, and tidally-locked with dayside DMS flux (Figure 4). We find that global DMS emissions result in substantially lower r_{diff} values ($\sim$0% and $\sim$33%; Figures 4a-b) compared to a strictly dayside DMS emission assumption ($\sim$67%; Figure 4c). The larger value of r_{diff} in the latter simulation is due to the relatively short lifetime of DMS [181].

Similar to the above DMS behavior, a potential consequence of tidal-locking is the relegation of CH_4 and N_2O production to a single hemisphere, i.e., processes of methanogenesis and denitrification favor anaerobic conditions and may be disfavored on photosynthetic oxygen-producing daysides. Spatially-variable surface to atmosphere flux distributions of CH_4 and N_2O therefore could exhibit higher r_{diff} than the values predicted here (10%; Figures 1e-f and 1h-i).

2.5 Discussion

Here we discuss possible areas of future advancement, as well as the observational relevance of this study.

In this CCM study, we find that factors that determine biosignature concentration and distribution on a habitable tidally-locked planet are species dependent. For example, ozone mixing ratios are primarily driven by photolytic production and destruction, while ozone distribution and nightside sustenance are controlled by its transport and lifetime. An additional consideration, here demonstrated in our DMS simulations, is the spatial variance of gas fluxes. Given that habitable exoplanets are likely to possess heterogeneous ecologies, whose fluxes will interface with attendant atmospheric structure and circulation patterns, spatially-heterogeneous surface fluxes could have observationally-distinguishable effects on atmospheric spectra. For example, dayside upwelling could facilitate vertical mixing of surface gases into the upper atmosphere (Figure 1e-f), while nightside radiation inversions could trap constituents near the surface, limiting vertical mixing, day-nightside interactions, and potentially observability. These scenarios, in which atmospheric dynamics, photochemistry, surface flux sources, and feedback processes play important roles highlight the utility of 3D CCM simulations. However, due to non-linear interactions and internal atmospheric variability, disentangling drivers of emergent behavior is challenging and will likely require the tools of modern atmospheric and computational science, including Lagrangian tracking of constituents (e.g., Sölch and Kärcher 316), single- and multi-model ensembles (e.g., Kay et al. 173), and statistical analyses focused on detection and attribution (e.g., Diffenbaugh et al. 74, Horton et al. 145).

Despite these challenges, the introduction of 3D CCMs to exoplanet biosignature prediction efforts offers substantial research potential. Future applications are likely to consider a wider va-

riety of Earth-like biospheres, e.g., markedly disparate atmospheres of Earth throughout geologic time [12, 284], and should be expanded to include biologically constrained models and modules [45, 345]. Such applications will facilitate egocentricity avoidance – a commonly acknowledged goal of the field (e.g., Seager et al. 301). Until then, use of default Earth conditions may restrict the relevance of 3D CCM findings to truly Earth-like planets, with similar atmospheric formation histories, ecospheres, and biological signatures resulting from oxygenic photosynthesis [238].

This study demonstrates that fully-coupled CCMs are particularly promising for studies that seek to assess the roles of and feedbacks between different stellar SEDs, biological behaviors, and atmospheric compositions. Such efforts are consistent with recent reviews, discussing aspirational goals and the future of exoplanet biosignature research [45, 345]. Extrasolar astrophysical radiation environments and/or atmospheric conditions may alter biological activity, as life is both photochemically and climatologically mediated. Living organisms are highly receptive toward UV emissions such that UV-B ($290 < \lambda < 320$ nm) photons hinder metabolism, photosynthesis, and thus biological production rates [**?**]. Moreover, due to different climate and redox conditions, for example on anoxic Archean Earth ($\sim$3.0 Ga), hydrocarbons and organosulfur biosignatures (C_2H_6, CH_4, OCS, DMS etc.) could rise to more prominent abundances and hence may be conducive to remote detection [12, 76, 126, 148].

In terms of the potential observational implications of our simulations, our results agree with those of Segura et al. [303], Rauer et al. [274], and Rugheimer et al. [285], i.e., rocky planets orbiting active and quiet M-dwarfs should have deeper absorption depths, particularly for ozone and secondary biosignatures such as methane and nitrous oxide (as seen in transit and emission spectra). This makes habitable zone planets orbiting M-dwarfs favorable targets. 3D predictions from our CCM simulations may be confirmed by remote observations. Phase curve analysis can potentially resolve 3D atmospheric structures of super-Earth and Earth-sized terrestrial planets [195, 322]. For example, thick substellar clouds could appear characteristically for planets with specific spit-orbit

resonances [361].

In terms of biosignature measurements on tidally-locked planets, different longitudinal gradients of gaseous constituents may affect measurements of variation spectra (peak amplitude of the phase curves) extracted from thermal phase curves [308]. As variation spectral signals depend on amplitude-peaks in orbital light curves, there may be added anisotropy due to time-varying longitudinal gas distributions on tidally-locked planets in each orbit (assuming null obliquity, as seen in Figure 1). Compared to non-tidally locked fast rotators (with similar stellar UV activity and orbital period), we predict that more pronounced absorption signals would be seen in variation spectrum on tidally-locked planets, driven by greater difference between maximum and minimum phase amplitudes due to uneven hemispheric gas distributions. Emission spectrum at maximum phase (direct line-of-sight) should correspondingly see similar behavior, at least for a few IR-windows (e.g., between 3-9 μm; Selsis et al. 308). For direct imaging, one possibility is that these features may be more prominent during certain orbital phases. Ozone observability, for example, may decrease during secondary eclipses as the dayside with reduced ozone abundance would be Earth-facing. Radiative transfer models, using our CCM results as inputs, will be needed to quantitatively assess observational prospects of the above.

2.6 Conclusions

This Letter reports numerical simulations using a coupled 3D CCM to explore global distribution of biosignature gases on Earth-like and tidally-locked planets as a function of stellar spectral type, stellar activity, and planetary rotation period. Qualitatively similar to 1D models, we find increased mixing ratios of biogenic compounds (e.g., O_3, CH_4, and N_2O) for both active and inactive M-dwarf

SEDs. These increases are most pronounced for planets around quiet M-dwarfs. Even though the effects of tidal-locking are noticeable in our simulations, they are not yet discernable with current observational techniques, i.e., the primary biosignatures simulated in this work (O_3, CH_4, N_2O) show low (20%) day-to-nightside mixing ratio contrasts. Conversely, simulated day-to-nightside differences of photosynthetic compounds (e.g., DMS) are found to be nearly 70% and underscore the need for heterogeneous 3D realism in modeling biosignatures and their photochemical derivatives. Overall, this study serves as a stepping stone for future applications using 3D CCMs to study the habitability and spectroscopic observability of terrestrial exoplanets.

2.7   Acknowledgements

Chapter 3

Habitability and Spectroscopic Observability of Warm M-dwarf Exoplanets Evaluated with a 3D Chemistry-Climate Model

3.1 Abstract

[1] Planets residing in the circumstellar habitable zones (CHZs) offer the best opportunities to test our theories on life's pervasiveness and its potential complexity. A wide array of upcoming ground- and space-based facilities are aimed at searching for and characterizing these planets and planet candidates. Constraining the precise boundaries of habitability and their observational discriminants is thus critical to maximize our chances at remote life detection. Conventionally, calculations of the

inner edge of the habitable zone (IHZ) have been performed using both 1D radiative-convective models and 3D general circulation models without interactive chemistry. Here we employ a 3D chemistry-climate model (CCM) to evaluate the IHZ boundaries of synchronously-rotating planets around K- and M-dwarf stars. Simulations are conducted for planets with N_2-O_2-H_2O-CO_2 atmospheres around a range of stellar spectral types and self-consistent stellar spectral energy distribution (SED)-orbital period relationships. With the inclusion of interactive chemistry, we find that our runaway and moist greenhouse thresholds are in good agreement with previous work with similar radiative transfer schemes. However, around quiescent stars, our prognostic hydrogen mixing ratios are orders of magnitude lower than previous diagnostic estimates, suggesting the need for direct simulations of photochemical processes using CCMs. Around active M-dwarfs, increases in upper atmospheric moisture and photodissociation rates allow hydrogen mixing ratios to approach that of water vapor, leading to elevated water loss efficiency via diffusion-limited escape. Transmission and emission spectra produced using CCM inputs show that both water vapor and ozone features could be detectable by future missions such as the James Webb Space Telescope. Our work indicates that simultaneous constraints on the UV emission of low-mass stars and the orbital properties of their attending planets will be critical to understand the habitability and observability of rocky exoplanets.

3.2   Introduction

For the first time in human history, it is possible to find and characterize nearby rocky and potentially habitable worlds. Recent discoveries of Proxima Centauri b, the TRAPPIST-1 system, and LHS 1140b [9, 75, 106] show that remote examination of small rocky planets is within reach. Terrestrial planets, such as these, are expected to be common ($\sim$15%) in circumstellar habitable zones (CHZs) of low-mass stars [84, 325] $-$ systems that are especially amenable to spectroscopic

observation due to their high transit frequencies, low star-to-planet brightness contrasts, prolonged main sequence lifetimes, and abundance in both the solar neighborhood and the projected *Transiting Exoplanet Survey Satellite (TESS)* sample [19, 136]. In fact, TESS has already found small and Earth-sized planets transiting cool stars (e.g., Dragomir et al. 82, Vanderspek et al. 339). Upcoming characterization efforts by the *James Webb Space Telescope*, ground-based 30-meter extremely large telescopes, and direct imaging missions will likely attempt to detect habitability indicators (e.g., N_2, H_2O_v) and/or biosignatures (O_2, O_3, CH_4, N_2O, CO_2; Sagan et al. 287) on these K- and M-dwarf systems. Indeed, atmospheric characterization of increasingly smaller planets ($R_p 4 R_\oplus$) is already underway (e.g., Benneke et al. 28, 29, Wakeford et al. 343).

Future target selection and characterization efforts will benefit from improved understanding of and constraints on CHZ boundaries. Earliest estimates of the CHZ made use of energy balance models (EBMs) [129], which established the dependence of HZ widths on stellar spectral type. Follow on studies, using 1D radiative-convective models, identified two boundaries of the inner habitable zone: one defined by the onset of a water-enriched stratosphere and another defined by a radiative equilibrium threshold [163, 165]. These early simulations assumed a fully saturated troposphere with a fixed moist adiabatic lapse rate and static clouds. Subsequently, Kasting et al. [168] found that as the absorbed stellar flux increases, the stratosphere moistens and warms significantly which could allow water vapor to efficiently escape to space. Other studies, also using 1D models, provided additional insights, finding for example, that CHZ widths could change according to atmospheric composition and/or atmospheric pressure (e.g., Ramirez and Kaltenegger 272, Vladilo et al. 341, Zsom et al. 377).

In more recent years, idealized and state-of-the-art estimates of the CHZ have utilized 3D general circulation models (GCMs) to place physics-based constraints on CHZ boundaries (e.g., Abe et al. 2, Way et al. 348, Yang et al. 362). GCM predictions improved upon 1D model projections by way of explicit simulation of large-scale circulation and key climate system feedbacks. For in-

stance, incorporation of atmospheric dynamics into models of slowly-rotating planets resulted in climatic behaviors that can only be resolved in 3D, e.g., substellar cloud formation and convergence caused by changes in the Coriolis force [190, 349, 361]. Follow-up studies, using similar GCMs, found that habitable planets around M-dwarf stars have moist stratospheres despite mild global mean surface temperatures (e.g., Fujii et al. 99, Kopparapu et al. 191). These results stood in contrast to previous inverse modeling approaches with 1D radiative-convective models (e.g., Kasting 163), where a surface temperature of 340 K was deemed the threshold for the classical "moist greenhouse" regime.

Despite these advances, exoplanet GCM studies have traditionally not accounted for photochemical and atmospheric chemistry-climate interactions – components recently found by both 1D [194, 209] and 3D models [54] to be critical for habitability and biosignature prediction. The addition of photochemistry to prognostic atmospheric models allows for interactions between high energy photons and gaseous molecules. This often leads to the breaking of molecular bonds and creation of free radicals and ions, which have significant impacts on atmospheric composition and associated habitability. Determination of water loss, in particular, requires knowledge of where water vapor photodissociation occurs in the mesosphere and lower thermosphere (MLT), and is dependent on dynamical, photochemical, and radiative processes. To simulate the speciation, reaction, and transport of various gaseous constituents (e.g., H_2O_v) and their photochemical byproducts (e.g., H, H_2), coupled 3D chemistry-climate models (CCMs) are needed. CCMs are also able to simulate photochemically important species such as ozone, allowing for prognostic assessments of chemistry-climate system feedbacks. As ozone is primarily derived from molecular oxygen, prognostic ozone calculations enable consideration of O_2-rich atmospheres with active oxygenating photosynthesis on the surface. Lastly, the large number of chemical species calculated by CCMs provide a rich tapestry for calculating transmission spectra, compared to the simplified atmospheric compositions generally considered in GCMs.

Earlier climate models of tidally-locked Earth-like planets adopted vertical resolutions of 15-25 layers with equally spaced 30-50 mbar levels [87, 161, 243]. While this setup fully resolved the general structure of the troposphere where the majority of weather takes place [134], it neglected the upper stratosphere and thermosphere. Critically, interactive simulation of photochemistry and atmospheric chemistry requires a high model-top (i.e., a model whose atmosphere reaches into the mid-thermosphere ($\sim$150 km)), as highly energetic photons initially and primarily interact with a planet's upper atmosphere. While most radiatively active species are stable against dissociation in the troposphere, species become vulnerable to photolysis above the tropopause and to photoionization above the stratopause ($\sim$1 mbar) and mesopause ($\sim$10^{-2} mbar). Apart from key dissociative processes in the MLT region, high-top atmospheric dynamics are also important as they influence the transport of gaseous molecules. This is because vertical velocity in the vicinity of the tropopause is not an isolated process, but influenced by momentum sources in the stratosphere and lower thermosphere [143]. Further, mean meridional circulation of the lower stratosphere, which can affect the distribution of chemical tracers, is driven primarily by the drag provided by planetary and gravity wave momentum deposition in the stratosphere and mesosphere [133, 143, 282]. A high model-top is therefore essential to simulate chemical interactions and their associated dynamical processes in the MLT region.

Based on conventional theory, endmembers of habitability are represented by (i) CO_2-rich ice-house climates at the outer edge of the habitable zone (OHZ; e.g., Paradise and Menou 260) and (ii) moist greenhouse climates at the inner edge of the habitable zone (IHZ; e.g., Kopparapu et al. 190). In this study, we use a 3D high-top CCM to investigate the latter regime, namely the moist greenhouse limits of IHZ planets orbiting M-dwarf stars. The paper is organized as follows: In Section 2, we describe our model and experimental setup. In Section 3, we present and analyze our results. Section 4 discusses implications of our results, caveats, and relevance to observations. Finally, Section 5 summarizes key findings, provides concluding remarks, and suggests next step.

3.3   Model Description & Numerical Setup

We employ the National Center for Atmospheric Research (NCAR) Whole Atmosphere Community Climate Model (WACCM) to investigate the putative atmospheres of rocky exoplanets. WACCM is a 3D global CCM that simulates interactions of atmospheric chemistry, radiation, thermodynamics, and dynamics. We set the Community Atmosphere Model v4 (CAM4) as the atmosphere component of WACCM. CAM4 uses native Community Atmospheric Model Radiative Transfer (CAMRT) radiation scheme [177], the Hack scheme for shallow convection [123], the Zhang-McFarlane scheme for deep convection [374], and the Rasch-Kristjansson (RK) scheme for condensation, evaporation and precipitation [375]. For a complete model description see Neale et al. [252] and [229].

WACCM includes an active hydrological cycle and prognostic photochemistry and atmospheric chemistry reaction networks. The chemical model is version 3 of the Modules for Ozone and Related Chemical Tracers (MOZART) chemical transport model [179]. The module resolves 58 gas phase species including neutral and ion constituents linked by 217 chemical and photolytic reactions. The land model is a diagnostic version of the Community Land Model v4 with the 1850 control setup including prescribed surface albedo, surface CO_2, vegetation, and forced cold start. The oceanic component is a 30-meter deep thermodynamic slab model with zero dynamical heat transport and no sea-ice. Even though a fully dynamic ocean is ideal, Yang et al. [365] recently demonstrated that the inclusion of such does not significantly impact the climate of moist greenhouse IHZ planets. Furthermore, the presence of significant North-South oriented continents minimizes the effects of ocean heat transport on tidally locked worlds [72, 365].

WACCM includes a number of improved and expanded high-top atmospheric physics and chemical components. Processes in the MLT region are based on the thermosphere-ionosphere-

mesosphere electrodynamics (TIME) GCM [279]. Key processes included are: neutral and high-top ion chemistry (ion drag, auroral processes, and solar proton events) and their associated heating reactions. In this study, we do not use prognostic ion chemistry (e.g., WACCM-D; Verronen et al. 2016) for the sake of computational efficiency. In terms of atmospheric dynamics, WACCM allows the emergence of gravity waves (important for governing large-scale flow patterns and chemical transport) by orographic sources, convective overturning, or strong velocity shears [252]. As we assume Earth-like topography in all our simulations, orography may also provide a means of direct forcing on planetary scale Rossby waves, which act to increase the asymmetry of atmospheric circulation and turbulent flow (the absence of topography such as on an idealized aquaplanet would minimize this effect and thus induce greater circulation symmetry). Topography also drives gravity waves which deposit energy into the mesosphere, affecting its temperature structure and circulation [21]. Molecular diffusion via gravitational separation of different molecular constituents [18] is an extension to the nominal diffusion parameterization in CAM4. Below 65 km (local minimum in shortwave heating and longwave cooling), WACCM retains CAM4's radiation scheme. Above 65 km, WACCM expands upon both longwave (LW) and shortwave (SW) radiative parameterizations from those of CAM3 and CAM4 [62]. WACCM uses thermodynamic equilibrium (LTE) and non-LTE heating and cooling rates in the extreme ultraviolet (EUV) and infrared (IR) [94]. In the SW (0.05 nm to 100 μm; Lean 201, Solomon and Qian 319), radiative heating and cooling are sourced from photon absorption, as well as photolytic and photochemical reactions.

Earth's atmospheric structure is typically defined using the vertical temperature gradient. In WACCM simulations the atmospheric structure is dependent on the atmospheric gases, planetary rotation period, and bolometric stellar flux − thus the simulated vertical temperature gradient is different from that of Earth. However, to facilitate comparison, we refer to simulated atmospheric layers using the typical pressure levels of Earth's atmosphere: That is, troposphere refers to regions extending from the surface to 200 mbar, the stratosphere 200 mbar to 1 mbar, the mesosphere 1

mbar to 0.001 mbar, and the thermosphere 0.001 mbar to $5-6$ mbar. The latter two layers comprise the so-called MLT region (see Section 1). Specifically, the mesosphere extends from $\sim$1 mbar to the mesopause (roughly the homopause, at $\sim$0.001 mbar), where temperature minima caused by CO_2 radiative cooling are typically found. Above the mesosphere, the thermosphere encompasses the heterosphere zone, in which diffusion plays an increasingly greater role and the chemical composition of the atmosphere varies in accordance with the atomic and molecular mass of each species. This region (i.e., the thermosphere) extends from the mesopause to model-top at pressures of $5.1-6$ hPa ($\sim$145 km). Shifts in atmospheric structure occur and depend on the planetary rotation period and the bolometric stellar flux.

We configure the described model components to simulate the atmospheres of tidally-locked (trapped in 1:1 spin-orbit resonance) planets across a range of stellar spectral energy distributions, bolometric stellar fluxes, and planetary rotation periods. We construct stellar spectral energy distributions (SEDs) using the PHOENIX synthetic spectra code [152] assuming stellar metallicities of [Fe/H] = 0.0, alpha- enhancements of [α/M] = 0.0, surface gravities log g = 4.5, and stellar effective temperatures (T_{eff}) of 2600 K (TRAPPIST- 1-like), 3000 K (Proxima Centauri-like), 3300 K (AD Leo-like), and 4000 K (late K-dwarf). All synthetic stellar SEDs are assumed to be in states of quiescence. The corresponding rotation periods obeys Kepler's 3rd law, as in Kopparapu et al. [190], which is given by:

$$P_{\text{years}} = \left[\left(\frac{L_*/L_\odot}{F_p/F_\oplus} \right)^{3/4} \right] (M_*/M_\odot)^{1/2} \tag{3.1}$$

where $L/L_\odot$ is the stellar luminosity in solar units, $F_p/F_\oplus$ is the incident stellar flux in units of present-Earth flux (1360 W m^{-2}), and $M/M_\odot$ is the stellar mass in solar units.

We set the mass and radius of all our simulations to those of present-day Earth. We set the orbital

parameters (obliquity, eccentricity, and precession) to zero. We use present Earth's continental configuration and topography, which is a reasonable starting point as fully ocean-covered planets are unlikely to support an active climate-stabilizing carbon-silicate cycle and allow build-up of O_2 [1, 212]. We place the substellar point stationary over the Pacific at 180° longitude and turn off the quasi-biennial oscillation forcing in all simulations, as this prescription is based on observations of Earth.

We assume initially Earth-like preindustrial surface concentrations of gases N_2 (0.78 by volume), O_2 (0.21), CH_4 (7.23×10^{-7}), N_2O (2.73×10^{-9}), and CO_2 (2.85×10^{-4}). The existence of an O_2-rich atmosphere implies active oxygenating photosynthesis on the surface[2] H_2O_v and O_3 are spatially and temporally variable gases but are initialized at preindustrial Earth values. The surface atmospheric pressure is 101325 Pa (1013.25 mbar). We use the native broadband radiation model of CAM4 and do not include new absorption coefficients as done in Kopparapu et al. [191] due to the extensive effort required to derive new coefficient values for CH_4, N_2O, and other IR absorbers included in the chemical transport model, which is beyond the scope of this work.

WACCM simulations are run at horizontal resolutions of $1.9^o \times 2.5^o$ (latitude by longitude) with 66 vertical levels, model top of 5.1×10^{-6} hPa (145 km), and a model timestep of 900 seconds. We increase the total stellar flux by intervals of 0.1 $F_p/F_\oplus$ and modify the rotation period according to Equation 1. We follow previous work [190, 362] and assume that the maximum flux for which a planet can maintain thermal equilibrium, i.e., top of atmosphere (TOA) radiation balance, defines the incipient stage of a runaway greenhouse. We refer to climatically-stable (i.e., in thermal equilibrium) simulations as converged simulations, while those that are climatically unstable (i.e., out of thermal equilibrium) are deemed to be in incipient runaway states. With the exception of Figure 1, all converged simulations have been run for 30 Earth years of model time and the results

---

[2]We note that some doubt has been raised as to whether biotic O_2 can build-up on planets around M-dwarfs due to the potential paucity of photosynthetically active radiation [206, 213].

presented here are averaged over the last 10.

Note that our model simulation naming convention follows from simulated stellar flux and effective temperature: *XXFYYT*, where *XX* represents the total stellar flux (relative to the Earth's) and *YY* represents the effective temperature of the host star. For instance, 13F26T represents an experiment in which the stellar flux is set to 1.3 $F_\oplus$ and the host star has an effective temperature of 2600 K.

3.4 Results

We present the first simultaneous 3D investigation of climate and atmospheric chemistry in temperate, moist greenhouse, and incipient runaway greenhouse atmospheres on synchronously-rotating planets. The results section is structured as follows: First, we examine the onset of runaway greenhouse conditions in our simulations. Next, we discuss moist greenhouse conditions and their associated climatic and chemical properties. We then investigate isolated changes in stellar spectral type and bolometric stellar flux. Specifically, we analyze the effects of different stellar spectral types, increased incident stellar flux, and UV radiation on our results. Next, we show prognostic water vapor and hydrogen mixing ratios and discuss new escape rates calculated with interactive chemistry. Lastly, we present simulated atmospheric transmission spectra and secondary eclipse thermal emission spectra using our CCM results as inputs and discuss their observational implications.

3.4.1 Climate Behaviors in Runaway Greenhouse States

Runaway greenhouse states are energetically unstable climate conditions in which the net absorption of stellar radiation exceeds the ability of water vapor rich and thus thermally opaque atmo-
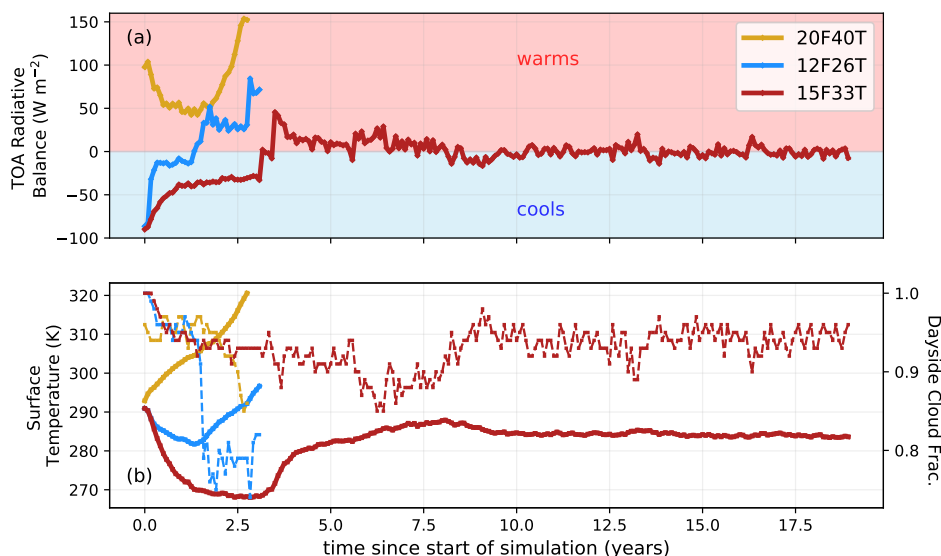
Figure 3.4.1: Temporal evolution of radiative energy balance (a) and surface temperatures (b) of three representative simulations (12F26T, 20F40T, and 15F33T) across model time of 20 Earth years. Simulations 12F26T and 20F40T progress to incipient runaway greenhouse states due to dissipation of substellar clouds and water vapor greenhouse feedbacks, while 15F33T maintains a stable climate by way of the cloud-stabilizing feedback. Dashed curves represent dayside-mean cloud fraction for the specified simulation.

spheres to emit radiation to space, as described by the Simpson-Nakajima limit [251]. A subset of our simulations reaches this runaway threshold, which we define as the innermost boundary of the HZ. We illustrate incipient runaway behavior and contrast it with a climatically-stable case by providing timeseries of TOA radiation balance and surface temperature from three representative simulations, initialized from the same climatic state, i.e., global-mean surface temperature (T_s) of $\sim$291 K (Figure 3.4.1). From this initial state, simulations diverge, largely according to the intensity of stellar flux and cloud development. For example, in the climatically-stable 15F33T simulation (Figure 3.4.1, red curves), the TOA radiation balance begins negative, but stabilizes about zero as the day-side cloud fraction initially decreases, but then oscillates near 95% coverage. This radiation balance allows the global-mean T_s to stabilize at 283 K. In contrast to this climatically

stable pathway, "incipient runaway greenhouse" [355] conditions are simulated for planets at both lower (12F26T) and higher (20F40T) stellar fluxes around late M-dwarf (12F26T) and late K-dwarf (20F40T) stars. In the 20F40T simulation, the planet rapidly transitions into an incipient runaway greenhouse state as the stellar flux is sufficiently high that it causes the collapse of the substellar cloud-albedo shield (Figure 3.4.1, gold curves). No equilibrium T_s is achieved in this simulation. Similarly, in the lower flux 12F26T case (Figure 3.4.1, blue curves), the global-mean T_s does not achieve an equilibrium. Initially global-mean T_s decreases similar to 15F33T, but the higher rotation rate reduces the dayside cloud shield, allowing the TOA radiation imbalance to turn positive, which leads to the incipient stage of a runaway thermal state
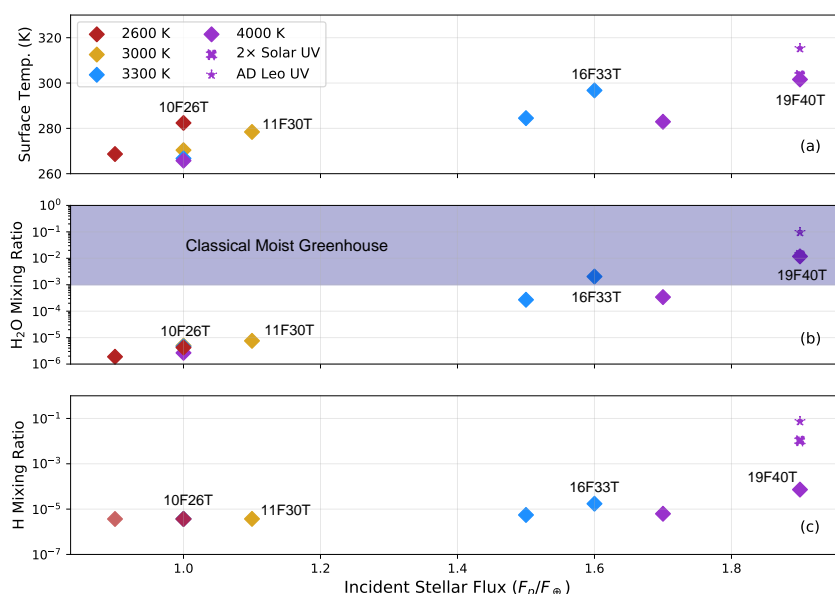
Figure 3.4.2: Simulated global mean surface temperature (a), stratospheric water vapor mixing ratios (mol mol^{-1}) (b), and thermospheric hydrogen mixing ratios (mol mol^{-1}) (c) for all climatically-stable experiments plotted according to stellar spectral type and incident stellar flux. IHZ limit simulations are given alphanumeric labels and blue shading in (b) indicates the classical moist greenhouse regime. Color indicates the effective temperature of the host star. Note overlapping results at $F_p = 1.0F_\oplus$.

3.4.2 Climate and Chemistry near the IHZ: Temperate & Moist Greenhouse States

While runaway greenhouse states delineate the optimistic IHZ, both temperate and moist green-house climates may be situated at or near the IHZ limit. In this study, we are primarily interested in the chemistry and climatic conditions of habitable planets located at the IHZ. To identify this boundary, four host star type simulations were run with incremental ($0.1\ F_p/F_\oplus$) increases in stellar flux. Simulations not pushed into the incipient runaway state described in Section 3.1, i.e., simulations with flux $0.1\ F_p/F_\oplus$ less than runaway conditions, define our "IHZ limit" cohort: 10F26T (temperate), 11F30T (temperate), 16F33T (moist greenhouse), and 19F40T (moist greenhouse). Temperate atmospheres have low, Earth-like stratospheric water vapor content (typically $1-5$ mol mol^{-1}) and global-mean T_s below 285 K. Moist greenhouse atmospheres emerge when the stratospheric H_2O_v mixing ratio are sufficiently high, i.e., $3-3$ mol mol^{-1} such that water-loss via diffusion-limited escape could occur at a geologically significant rate in the thermosphere [163]. If the water-loss is sufficiently slow (i.e., 5 Gyrs), then rapid desiccation of a planet's oceans is prevented and its surfaces can remain habitable.

Amongst our simulations, only IHZ limit climates around early-to-mid M-dwarfs ($T_{\text{eff}} = 3300$ and 4000 K) meet the moist greenhouse criterion (Figure 3.4.2b, 16F33T and 19F40T). Simulations around these stars but with lesser stellar flux, i.e., 15F33T and 17F40T, do not achieve sufficient stratospheric H_2O_v to place them in the moist greenhouse regime (Figure 3.4.2b). Simulations 16F33T and 19F40T have stratospheric H_2O_v mixing ratios of $2.05-3$ and $1.179-2$ mol mol^{-1} respectively, yet their global mean T_s does not exceed 310 K (Figure 2a), which indicates that the surface may be habitable despite the high stratospheric water vapor content. Temperate IHZ limit climates (experiments 10F26T and 11F30T) simulated around late M-dwarfs ($T_{\text{eff}} = 2600$ and 3000 K) do not enter the moist greenhouse regime with incremental ($0.1\ F_p/F_\oplus$) increases in stellar flux (Figure 3.4.2, red and gold). Instead, they abruptly transition into incipient runaway greenhouse

states (e.g., 12F26T; Figure 3.4.1, blue curve). Similar conclusions were reached by Kopparapu et al. [191] using CAM4 with updated H_2O_v absorption coefficients but excluding interactive chemistry.
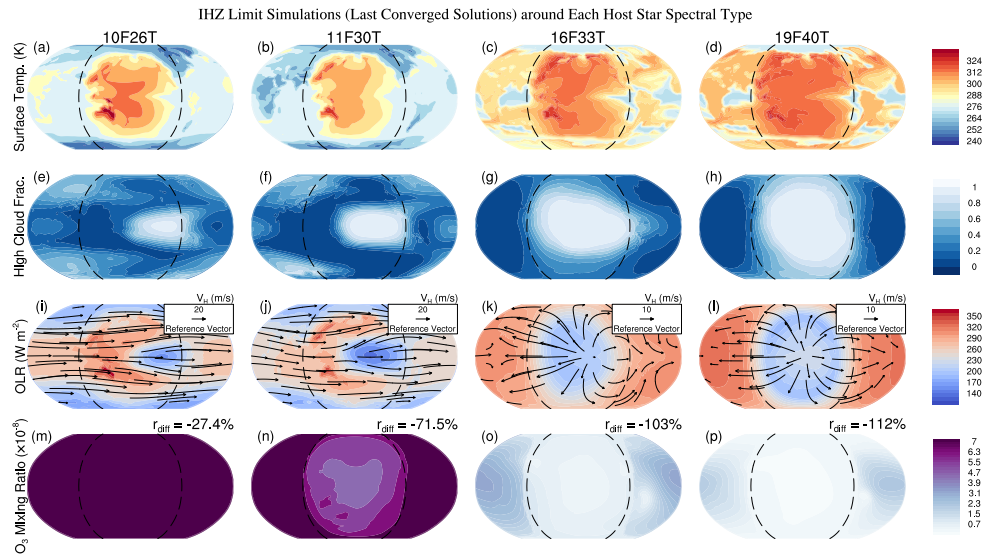
Figure 3.4.3: Simulated global surface temperature (a-d), high cloud fraction (400 to 50 mbar) (e-h), TOA OLR (i-l) and horizontal winds at 100 mbar (i, j) and 10 mbar (k, l), and stratospheric ozone mixing ratios vertically-averaged between 10^{-4} and 100 mbar (m-p) from the IHZ limit simulations around each stellar spectral type. r_{diff} is the value of the day-to-nightside mixing ratio contrast defined in Equation 2. Dashed lines indicate the terminators.

We demonstrate differences in climate and chemistry amongst the IHZ limit simulations across the four host star types by showing contour plots of surface temperature, high cloud fraction, upper atmospheric wind fields, TOA outgoing longwave radiation (OLR), and ozone mixing ratios averaged between 10^{-4} and 100 mbar (Figure 3.4.3). These results exhibit the convolved effects of stellar T_{eff}, incident flux, and planetary rotation, as all three parameters are correlated. Following Chen et al. [54], we define a metric to assess the day-to-nightside gas mixing ratio contrasts:

$$r_{diff} = \frac{r_{day} - r_{night}}{r_{globe}} \qquad (3.2)$$

where r_{day} is the dayside hemispheric mixing ratio mean, r_{night} the nightside mean, and r_{globe} the global mean. The degree of anisotropy is loosely encapsulated in this parameter, which is shown in Figures 3.4.3 and 3.4.8 and will be discussed throughout the paper.

Substantial differences in surface temperature distributions can be found amongst the four IHZ limit simulations. With increasing stellar T_{eff}, day-to-nightside T_s gradients decrease (Figures 3.4.3a-d). This is caused by increased day-to-nightside heat redistribution at higher incident fluxes. Consistent with previous GCM studies that exclude interactive chemistry (e.g., Kopparapu et al. 191), we find that on slowly rotating planets, the weaker Coriolis force allows formation of optically thick substellar cloud decks by way of buoyant updrafts (Figures 3.4.3e-h). In addition, meridional overturning cells expand to higher latitudes when the Rossby radius of deformation approaches the diameter of the planet [71], which decrease the pole-to-equator temperature gradient. These two consequences (i.e., formation of dayside clouds and reduction of temperature gradient) of slow rotation allow planets around early M-dwarfs to maintain habitable climates at higher fluxes.

Atmospheric dynamics regulate cloud patterns, circulation symmetry, and transport of airmasses on a planet. For slowly-rotating cases, substellar OLR is reduced by the high opacity of deep convective cloud decks, which induce a strong warming effect (experiments 16F33T and 19F40T; Figure 3.4.3k-l). As we move from 16F13T, to 11F30T, then to 10F26T, the dynamical state gradually transitions from divergent circulation to one dominated by tropical Rossby waves and zonal jets. The resultant elevated high-to-low latitude momentum transport can be seen in the streamlines and OLR patterns (Figure 3.4.3i-j; see also Gill 105, Matsuno 234), and is likely caused by shear between Kelvin and Rossby waves [311]. Comparing our results to the circulation regimes studied by Haqq-Misra et al. [125], we find that simulations 16F33T and 19F40T are situated in their slow rotating regime (Figure 3.4.3i-j), in which thermally driven radial flows dominate. Simulation 10F26T (Figure 3.4.3i) is consistent with the rapid rotator characterized by strong zonal jet

streams and a weaker substellar rising motion, while 11F30 belongs in the so-called Rhines rotator regime, in which the OLR and radial flows are shifted eastward by the emergence of turbulence (Figure 3.4.3j). For the simulation in latter Rhines rotator regime, the meridional extent of Rossby waves is just under the planetary radius value, thus horizontal flow is a combination of superrotation and thermal-driven circulation (similar in terms of dynamical behavior to the "transition regime" found by Carone et al. 42).

An additional consideration, allowed by the coupling of chemistry and dynamics, is the role of stratospheric circulation in the transportation of airmasses (and thus photochemically produced species and aerosols). Atmospheres around late M-dwarfs (simulations 10F26T and 11F30T) display superrotation that induces standing tropical Rossby waves, thereby confining the majority of the produced ozone near the equator (Figure 3.4.4a and b). Carone et al. [43] explained this by the weakening of the extratropical Rossby wave and reduced efficiency of stratospheric wave breaking; here we confirm their hypothesis by directly accounting for ozone photochemistry and transport. In atmospheres with high circulation symmetry (simulations 16F33T and 19F40T), tropical jets are effectively damped. This leads to increased strength of stratospheric meridional overturning circulations (i.e., a thermally driven version of the Brewer-Dobson circulation) and that of the Walker circulation, which allows equator-to-pole and day-to-nightside dispersal of ozone (Figure 3.4.4c and d). Lastly, ozone day-to-night mixing ratio contrasts (r_{diff}) depend on both chemical (e.g., reaction with OH) and dynamical (e.g., strength of Rossby and Kelvin waves) factors and highlight the interplay between transport, photochemical, and photolytic processes (Figure 3.4.3m-p; see also Chen et al. 54).
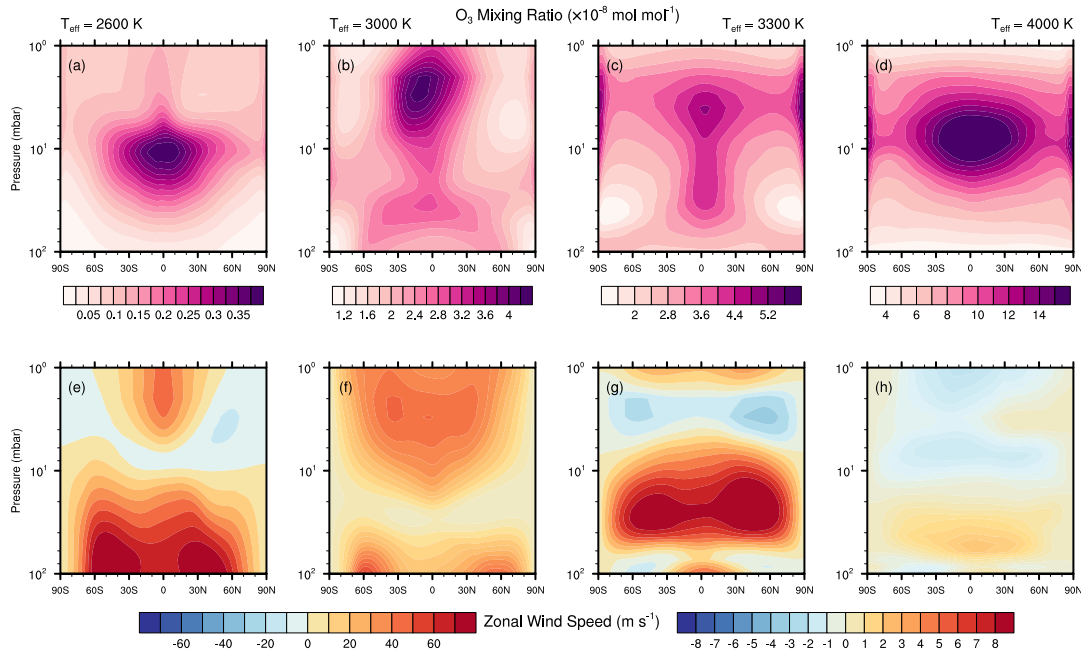
Figure 3.4.4: Zonal mean of ozone mixing ratio around stars with stellar effective temperatures of 2600 K (a), 3000 K (b), 3300 K (c), 4000 K (d) and zonal mean of zonal wind around the same set of stellar T_{eff}s (e, f, g, h). Direct day-night side circulation allows global dispersal of ozone (c, d), whereas strong zonal jets disrupt efficient equator-to-pole zone transport (a, b). Note the different color bar ranges.

3.4.3 Temperate Atmospheres: Effects of Changes in Stellar SED

Host star spectral-type can influence attendant planet atmospheres through changes in stellar T_{eff} and planetary rotation period, as the latter two variables are correlated through Kepler's third law. Our coupled CCM simulations demonstrate that the primary climatic effects of different input stellar SEDs are modulations in greenhouse gas radiative forcing, while photochemistry (e.g., driver of water photolysis) is not substantially impacted.

The red-shifted spectra of low-mass stars have consequences on planetary climate and chemistry by way of an increased water vapor greenhouse effect and reduction in dayside cloud cover (Figure 3.4.5a-c). Specifically, greater IR absorption by atmospheres around stars with $T_{\text{eff}} = 2600$

K and 3000 K increases both atmospheric temperature and the amount of precipitable water, and decrease radiative cooling efficiency aloft (Figure 3.4.5a and b, red curve). Reduction in the efficiency of radiative cooling and dayside cloud fractions lead to the water vapor greenhouse effect offsetting that of cloud albedo, and results in higher T_s for 10F26T compared to simulations around early M-dwarfs (Figure 3.4.5b). Moreover, potential increased concentrations of other greenhouses gases such as CH_4 and N_2O on late M-dwarf planets would also contribute to increased T_s [285, 303].
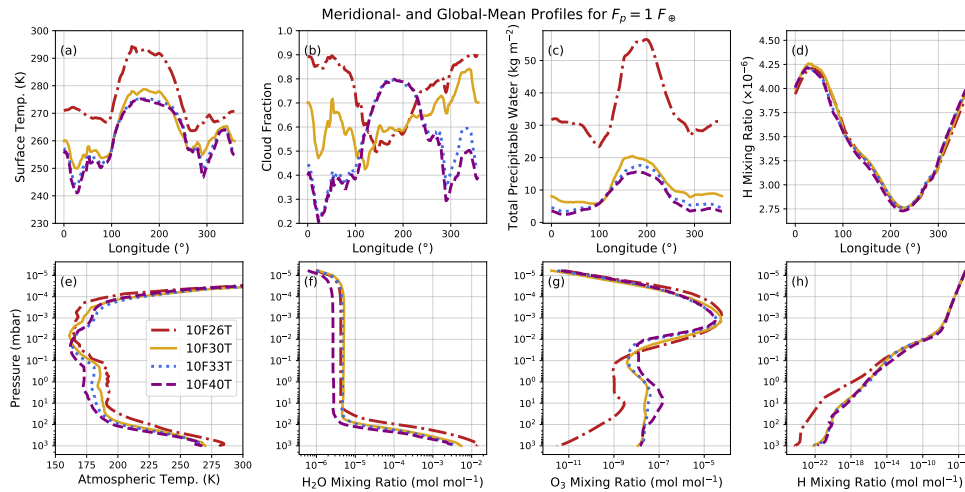
Figure 3.4.5: Zonal profiles of mean meridional surface temperature (a), total cloud fraction (b), vertically-integrated precipitable water (c), model-top H mixing ratios (mol mol^{-1}) (d), and global-mean vertical profiles of atmospheric temperature (e), H_2O_v (f), O_3 (g), and H mixing ratios (mol mol^{-1}) (h). We show simulations around stars with T_{eff} =2600, 3000, 3300, 4000 K but with the same total stellar flux $F_p = 1.0F_\oplus$. In the zonal profiles, the substellar point is over longitude 180°.

Further insight into the effects of different stellar T_{eff} can be observed in the global-mean vertical profiles (Figure 3.4.5e-h). Below 80 km (10^{-2} mbar), atmospheric temperature increases monotonically with decreasing stellar T_{eff} (Figure 3.4.5e). This relationship exists because longwave absorption increases and Rayleigh scattering decreases with the redness of the host star. Above 80 km (10^{-2} mbar), however, the dependence of temperature on stellar T_{eff} is reversed due to the

increasingly important role of O_2 photodissociation by shortwave photons at higher altitudes (Figure 3.4.5e). Both H_2O_v shortwave heating and strength of vertical advection increase with lower T_{eff} due to the higher NIR fluxes. At pressures less than $10^{-4} - 10^{-5}$ mbar, temperatures rise rapidly (Figure 3.4.5e) by way of thermospheric O_2 and O absorption of soft X-ray and EUV, while water vapor mixing ratios decline due to photodissociation to H, H_2, and OH (Figure 3.4.5f).

Ozone photochemistry is modulated by incident UV flux, chemical reaction pathways, and ambient meteorological conditions (P, T). Our predicted ozone mixing ratios above 70 km (10^{-1} mbar) reduce with decreasing stellar T_{eff} (Figure 3.4.5g). Elevated OH production through water vapor photosys leads to greater photochemical removal of O_3 by OH. OH destruction of ozone is maximized near the boundary layer for the 10F26T experiment as increased surface temperatures (due to lower substellar albedos) leads to larger H_2O_v inventories. At pressures less than 10^{-2} mbar, ozone mixing ratios rise as mean free paths between molecules increase dramatically with altitude.

Atmospheric hydrogen is primarily produced from the photolysis of high-altitude water vapor. At temperate conditions, H mixing ratios in both meridional and vertical profiles (Figure 3.4.5d and Figure 3.4.5h) are not substantially impacted by shifts in stellar SED, assuming quiescent stars. This is seen by the fact that all four simulations have close to zero H mixing ratios until $\sim 10^{-3}$ mbar, at which point they rise to $\sim 10^{-7}$ mol mol^{-1} (Figure 3.4.5h). Increased efficiency in water vapor photolysis above the mesosphere ($\sim 10^{-2}$ mbar) is evidenced by the exponential dependence of H mixing ratios on altitude. A transition in H mixing ratios above 80 km (10^{-2} mbar) is caused by the rapid increase in water vapor photolysis rates and hence stronger dependence on pressure altitude. We should point out however, that the seemingly minor effects of stellar T_{eff} stem from our choice of input SED-types. The PHOENIX stellar model data [152] we employed are inactive in the UV and EUV bands, regardless of the spectral type. As many M-dwarfs are active in the Ly-α line fluxes ($115 < \lambda < 310$ nm; France et al. 95), we next explore how changes in these assumptions
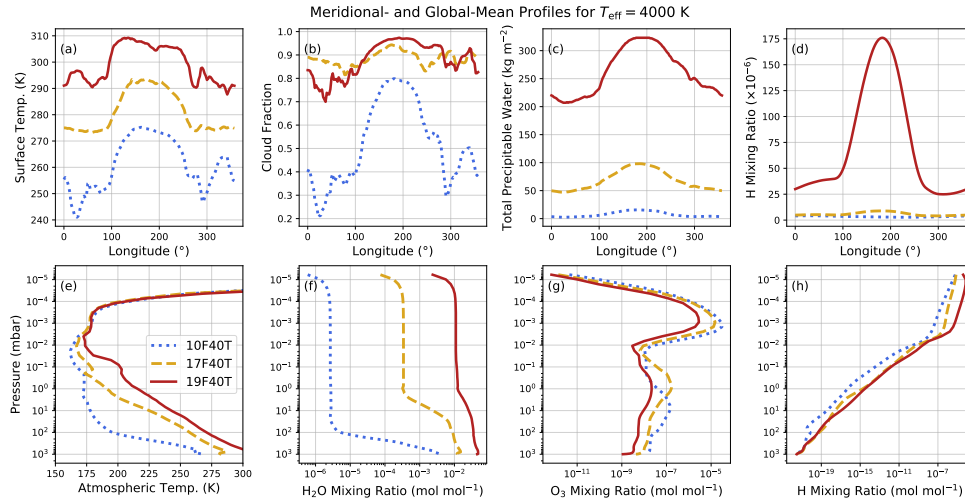
Figure 3.4.6: Zonal profiles of mean meridional surface temperature (a), total cloud fraction (b), vertically-integrated precipitable water (c), model-top H mixing ratios (mol mol^{-1}) (d), and global-mean vertical profiles of atmospheric temperature (e), H_2O_v (f), O_3 (g), and H mixing ratios (h). Simulations use total stellar fluxes $F_p = 1.0, 1.5, 1.8 F_\oplus$ and stellar T_{eff} held fixed at 4000 K. In the zonal profiles, the substellar point is over longitude 180°.

affect our findings (Section 3.5).

3.4.4 Moist Greenhouse Atmospheres: Effects of Increasing Stellar Flux

Increasing stellar flux can affect both climatic and photochemical variables. For instance, we find that both atmospheric temperature and water vapor mixing ratios increase monotonically with increasing incident flux as reported by previous studies (e.g., Kasting et al. 165, 168), whereas photochemically important species and their derivatives such as ozone and hydrogen display non-monotonic behavior.

Water vapor concentrations and surface climate are both strong functions of stellar flux. With increasing stellar flux at fixed stellar T_{eff} (= 4000 K) we find that water vapor quickly becomes a

major constituent from the stratosphere ($\sim$100 mbar) to the thermosphere (5$-$5 mbar). For example, total precipitable water increases by a factor of 5 for every interval change of incident flux (Figure 3.4.6c). However, the corresponding surface temperature rises much more gradually, wherein a change in stellar flux (from experiment 10F40T to 17F40T, or from $F_p = 1.0\ F_\oplus$ to $F_p = 1.6\ F_\oplus$) only causes an average T_s increase of $\sim$20 K in the substellar hemisphere due to stabilizing cloud feedbacks (Figure 3.4.6a).

The rapid rise in water vapor mixing ratios in the upper atmosphere (1 mbar) can be attributed to positive feedbacks between flux, H_2O_v IR heating, and vertical motion. H_2O_v NIR absorption and cloud feedbacks are amplified by increased stellar flux and incident IR. With increased water vapor, the tropospheric lapse rate decreases and the moist convection zone expands. These two shifts lead to displacement of the cold trap to higher altitudes (Figure 3.4.6e) and thus more efficient H_2O_v vertical advection. Greater H_2O_v vertical transport increases its concentration in the upper atmosphere, increasing the strength of greenhouse effect and atmospheric temperature.

While we find considerable increases in H_2O_v mixing ratios in the stratosphere, the increase in surface temperatures is less dramatic. For instance, in experiment 19F40T, the stratospheric water vapor mixing ratio has reached 10^{-2} mol mol^{-1} (Figure 3.4.6f) yet the global-mean surface temperature is still just 300 K (Figure 3.4.6e). This result agrees with previous findings of the so-called habitable moist greenhouse in which the stratosphere becomes highly saturated while the troposphere is stabilized by optically thick clouds [191]. In habitable moist greenhouse states (e.g., 19F40T; Figure 3.4.6e-h), surface habitability, to the first order, depends on the rate of water escape from the upper atmosphere. If water escape is sufficiently slow in these conditions, then insofar as the surface climate remains stable, the planet could host life on a timescale that raises the possibility of remote detection.

Stellar flux can indirectly affect ozone photochemistry via an increase in atmospheric water

vapor dissociation and changes in ambient conditions such as atmospheric temperature. Vertical profiles of ozone show a minimum in the ozone mixing ratio in the highest total incident flux simulation (Figure 3.4.6g, 19F40T, red curve), and a maximum for the simulations receiving the least (Figure 3.4.6g, 10F40T, blue curve). The resultant thinner ozone layer at high fluxes is caused by the increased removal rate via photochemical reactions with dayside HO_x and NO_x (primarily OH and NO species) for simulation 19F40T. Reduction in ozone between the boundary layer and altitude at 5.0 mbar is due to photochemical removal by OH, while the ozone maximum is shifted to 1.0 mbar (Figure 3.4.6g, gold curve), indicating a change in the location of highest gross ozone production rate.

Elevated water vapor mixing ratios lead to more atomic hydrogen via photodissociation. At temperate conditions, the most efficient altitude of water vapor photolysis is at pressure levels less than 10^{-3} mbar, as implied by the H mixing ratio shift (Figure 3.4.6h). With higher incident fluxes however, e.g., 19F40T, the inflection of H mixing ratios change with altitude indicating higher photodissociation efficiencies with height. Notably, we find that our prognostic H mixing ratios are almost never twice the amount of H_2O_v, as assumed in previous studies (e.g., Kasting et al. 167, Kopparapu et al. 189, 191). This suggests that previous climate modeling works on the moist greenhouse state have overestimated water-loss rates. Lesser simulated H mixing ratios are the result of a variety of processes, including the oxidation of H by O_2 and photochemical shielding by O_3, CH_4, and N_2O. In the next section we explore the dependence of photochemistry on stellar UV radiation inputs. With simulated hydrogen, we then provide revised calculations of water loss and estimate the longevity of our exoplanetary oceans.
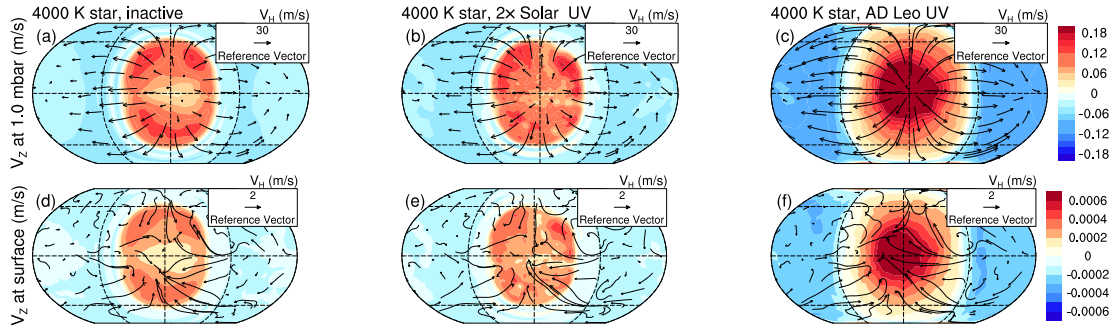
Figure 3.4.7: Simulated global wind velocity fields at 1.0 mbar (a-c) and at the surface (d-f) at three different stellar UV radiation levels. Colored contours present simulated vertical velocities (in the z-direction) at the indicated height while vectors represent the horizontal wind velocities.

3.4.5   Dependence on Stellar UV Activity

Stellar UV radiation can affect atmospheric chemistry, photochemistry, surface habitability, and based on our findings, observability. Here, we investigate the 3D effects of different stellar UV activity assumptions on tidally-locked planets with Earth-like atmospheres. To test the effects of UV radiation we run simulations in which the UV bands ($\lambda < 300$ nm) of the fiducial $T_{\mathrm{eff}} = 4000$ K (experiment 19F40T) star are swapped with those of (a) active VPL AD Leonis data (19FADLeoUV; Segura et al. 303) and (b) UV data obtained by doubling the Solar UV spectrum (19FSolarUV; Lean et al. 202). Active stellar SEDs are joined with the VIS/NIR portion of the spectra beyond 300 nm by linearly merging the last UV datapoint with the first optical ($\lambda > 300$ nm) datapoint in the PHOENIX stellar model. The aim in this section is to test how including UV activity could alter the conclusions in Section 3.1 Only changes in the UV wavelengths of the SEDs are tested as we are primarily interested in the isolated effects of UV photons, rather than those in other wavelengths. Follow-up work will make use of HST + XMM/Chandra-based M dwarf spectra with observed UV bands from France et al. [95], Youngblood et al. [370], and Loyd et al. [219].

UV radiation may drive changes in atmospheric dynamics, in addition to atmospheric chemistry. With changes in our fiducial late K-dwarf ($T_{\text{eff}} = 4000$ K) SED, we find increases in the vertical velocities at the substellar point from 0.10 m s^{-1} (inactive star), to 0.14 m s^{-1} ($2\times$ Solar UV), then to 0.18 m s^{-1} (AD Leo UV; Figure 3.4.7a-c), indicating stronger ascent of substellar updrafts. In addition, horizontal and thus day-to-nightside transport are enhanced as evidenced by the higher wind velocities. While mesospheric (1 mbar) zonally-averaged wind speeds forced by the quiescent M-dwarf are modest $\sim$25 m s^{-1} (Figure 3.4.7a), equatorial winds driven by elevated day-to-nightside temperature gradients can reach as high as 60 m s^{-1} for the simulations forced by the AD Leo UV SED (Figure 3.4.7c). Near-surface winds converge toward the substellar point due to large-scale updrafts in all three cases, but are not significantly altered by changes in UV radiation (Figure 3.4.7d-f).

Global distributions of photochemically important species and their byproducts are also affected by stellar UV activity (Figure 3.4.8). Substellar updrafts (due to radiative heating) of chemical constituents and antistellar downdrafts (due to radiative cooling) should result in higher ozone mixing ratios on the dayside. For the simulations forced by the $2\times$ Solar UV and AD Leo UV SED (Figure 3.4.8b-c), this effect is heightened by increased UV in the wavelengths responsible for ozone production (shortward of 220 nm). In contrast, lower ozone production rates on the quiescent simulation lead to reduced dayside ozone (Figure 3.4.8a).

The amount of dayside OH and H is directly related to the input UV, with chemical transport playing a small role. With a higher UV radiation than that received by the baseline, the OH distributions become increasingly concentric (19FSolarUV: 192% and 19FADLeoUV: 201%; Figure 3.4.8e-f) due to its short lifetime and the greater contribution from water vapor photodissociation. In contrast at higher UV levels, H mixing ratio distributions begin to lose their concentric shapes and reduced r_{diff} (19FSolarUV: 32.9%, and 19FADLeoUV: 28.8%; Figure 3.4.8g-i). These
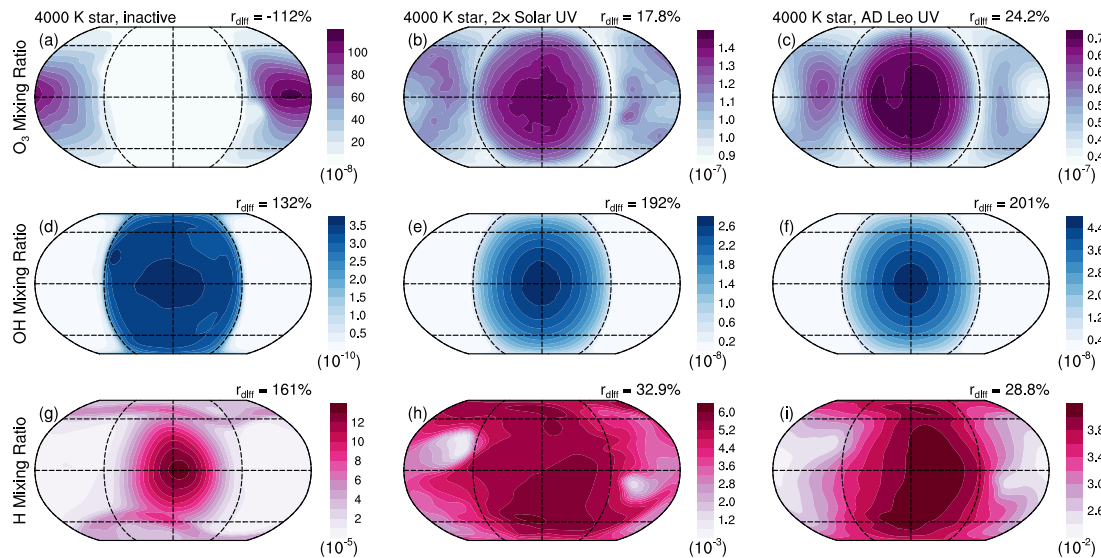
Figure 3.4.8: Simulated global ozone mixing ratio (a), OH mixing ratio (b), and H mixing ratio (mol mol^{-1}) (c) at three different levels of UV radiation: inactive, 2× Solar, and AD Leo. Ozone and OH mixing ratios are vertically averaged (column-weighted) between 10^{-4} and 100 mbar. H mixing ratio values are reported at model-top ($\sim 5 \times 10^{-6}$ mbar). Note that each panel has a unique color bar range.

different responses are explained by the enhanced dispersal of H by atmospheric transport as seen by the slight eastward shift of H mixing ratio distribution in the AD Leo UV case (Figure 3.4.8i). Increased horizontal advection migrates the effects of enhanced dayside photolytic removal, reflected in the decreasing r_{diff} of hydrogen with greater UV input. Note that our inactive stellar SEDs result in more reduced dayside ozone than those reported by Chen et al. [54], which likely stems from the lack of a fully resolved stratosphere-MLT region (e.g., Brewer-Dobson circulation) in the low-top out-of-the-box version of CAM4. These discrepancies in day-to-nightside chemical gradients illustrate the need for model inter-comparisons of exoplanetary climate predictions (e.g., Yang et al. 366).

Unsurprisingly, the three different UV radiation schemes produce atmospheric temperature profiles that are substantially different (Figure 3.4.9a). Elevated incident UV fluxes translate to higher

shortwave heating and thus atmospheric temperatures due to FUV and EUV absorption by atomic and molecular oxygen. A "harder" UV spectrum is also able to penetrate more deeply into the atmosphere.

Apart from different thermal structures, we find orders of magnitude differences in H_2O_v, O_3, and H mixing ratio profiles (Figure 3.4.9b, c, and d)$-$ indicating that stellar activity can have strong ramifications for water loss and atmospheric chemistry for moist greenhouse atmospheres. Enhanced AD Leo EUV and UV induced shortwave heating increases stratospheric and mesospheric (between 100 and 1 mbar) temperatures and water vapor mixing ratios (red curve; Figure 3.4.9a and b). However, the altitude at which photolysis is maximized moves lower due to the more energetic shortwave photons (Figure 3.4.9b). For ozone mixing ratios, production outpaces destruction resulting in a thicker ozone layer for simulations around more active stars (gold and red curves, Figure 3.4.9c), while the upper ozone layers remain desiccated.
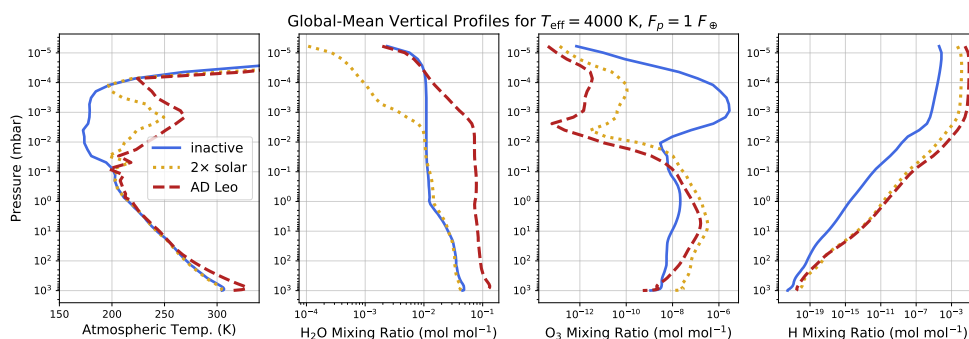
Figure 3.4.9: Global-mean vertical profiles of atmospheric temperature (a), H_2O_v (b), O_3 (c), and H mixing ratios (mol mol^{-1}) (d) at three different levels of UV radiation: inactive, 2× Solar, and AD Leo.

Finally, different input UV assumptions also alter the altitude at which water vapor photolysis is most efficient, which can determine the thermospheric H mixing ratio and hence water escape rate. Without stellar activity, the H mixing ratios remain low $7.27-5$ mol mol^{-1} (red curve, Figure 3.4.9d). With the inclusion of stellar activity, both altered UV simulations are pushed into the

true moist greenhouse regime with H mixing ratios of $1.04-3$ and $7.45-2$ mol mol^{-1} respectively (gold and red curves, Figure 3.4.9d). This implies that although planets around inactive stars may only experience minor water loss, both active Solar and AD Leo SEDs could cause attendant planets to suffer rapid water loss.

Inclusion of stellar UV activity may modify conclusions regarding host star spectral type dependent IHZ boundaries, as moist greenhouse atmospheres around early M-dwarfs ($T_{eff} \sim 4000$K) are more vulnerable to photodissociation than temperate climates around late M-dwarfs ($T_{eff} \sim 2600$ K). With the present simulations, it is challenging to further this possibility as our grid of stellar effective temperature values are rather coarse (i.e., only four T_{eff}s between 2600 and 4000 K).

3.4.6   Prognostic Hydrogen & Ocean Survival Timescales

The ability of a given planet to host a viable habitat is linked to the survivability of its ocean, i.e., the so-called "ocean loss timescale". Conventional estimates of the ocean loss timescale have used 1D climate models and GCMs that rely on prescribed H mixing ratios calculated by doubling their model-top H_2O_v. Here we reassess previous estimates by using directly simulated H mixing ratios and thermospheric temperature profiles drawn from our CCM simulations. We find that our ocean survival timescales are substantially higher than previously published estimates for quiescent stars, and are critically dependent on the stellar activity level. We demonstrate this by estimating water loss rates with Jeans' diffusion-limited escape scheme. While an over-simplification due neglect of hydrodynamics, this first order estimate is typically used to interpret climate model results of moist greenhouse atmospheres (e.g., Kasting et al. 167, Kopparapu et al. 189, 191, Wolf and Toon 353). With our prognostic hydrogen mixing ratios at each stellar T_{eff} and incident flux combination
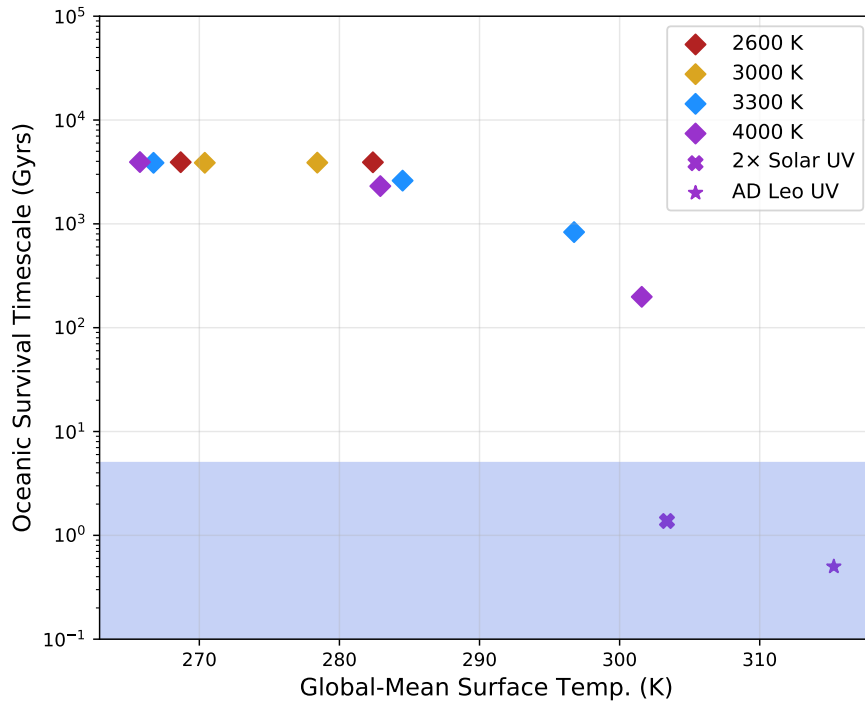
Figure 3.4.10: Ocean survival timescale as a function of stellar T_{eff} (2600, 3000, 3300, 4000 K), UV activity (2× Solar and AD Leo), and their corresponding global-mean T_s. Our results suggest that only simulations around active M-dwarfs enter the classical moist greenhouse regime as defined by Kasting et al. [167]. Blue shading indicates timescales less than the age of the Earth.

(Figure 2), we can calculate new escape rates of hydrogen [151]:

$$\Phi(H) \approx \frac{bQ_{\text{H}}}{H} \tag{3.3}$$

where Q_{H} is thermospheric hydrogen mixing ratio (model top), H is the atmospheric scale height

kt/mg, and b is the binary Brownian diffusion coefficient given by:

$$b = 6.5 \times 10^7 T_{\text{thermo}}^{0.7} \qquad (3.4)$$

where T_{thermo} is the thermospheric temperature of the atmosphere (taken at 100 km altitude).

We find that IHZ planets with Earth-like atmospheric compositions experiencing water loss should be more resilient to desiccation than previously reported. For example, all simulations around inactive stars have ocean survival timescales well above 10 Gyrs (Figure 3.4.10), even for those with H_2O_v mixing ratios above $3-3$ mol mol^{-1} (i.e., classical moist greenhouse). With realistic UV SED however, the oceans are predicted to be lost quickly (< 1 Gyr) via the molecular diffusion of H to space. This result stands in contrast to previous estimates using diagnostic H mixing ratios to calculate the escape rates, finding much shorter ocean loss timescales across all host star spectral types (see e.g., Figure 5 in Kopparapu et al. 191). Clearly, a careful assessment of a star's activity level is critical for determining whether planets around M-dwarfs will lose their oceans to space.

3.5   Discussion

This study builds upon previous efforts to study planets near the IHZ, but with the added complexity of interactive 3D photochemistry and atmospheric chemistry, and by self-consistently simulating the atmosphere into the lower thermosphere ($5-6$ mbar). In comparison with studies that employed self-consistent stellar flux-orbital period relationships, our runaway greenhouse limits are further out (from the respective host stars) than those of Kopparapu et al. [190], but closer in than those of Kopparapu et al. [191] and Bin et al. [33]. For example, Kopparapu et al. [190] found that

the critical flux threshold for thermally stable simulation orbiting a 3000 K star occurs at (F_{crit}) $\sim$1.3$F_{\oplus}$, which is approximately 0.2 $F_{\oplus}$ higher than predicted in this study. This discrepancy may be attributable to (i) the inclusion of ozone and its radiative effects in WACCM and (ii) the presence of non-condensable greenhouse gas species. While Kopparapu et al. [190] include 1 bar of N_2 plus 1 ppm of CO_2, this study includes additional modern Earth-like CH_4 and N_2O concentrations, thus yielding IHZ limits that are further away from the host star in comparison to Kopparapu et al. [190]. Note that both studies use the same radiative transfer scheme, cloud physics, and convection scheme. Simulated climates around stars with higher T_{eff} show much smaller differences stemming from lack of ozone heating and reduced degree of inversion, leading to comparable Bond albedos at the inner edge. However, greater disparities are found between our study and Kopparapu et al. [191]. For example, runaway greenhouse occurs at fluxes (F_{crit}) $\sim$0.35$F_{\oplus}$ higher for simulations across nearly all M-class spectral types. This is explained by the finer spectral resolution in the IR and updated H_2O absorption by Wolf and Toon [352] and Kopparapu et al. [191], which cause the stratosphere to warm and moisten substantially at a much lower stellar flux. Further, the native radiative transfer of CAM4 is shown to be too weak, both in the longwave and shortwave, with respect to water vapor absorption [363]. Differences between previous GCM calculations of the IHZ around Sun-like stars (e.g., CAM4; Wolf and Toon 353 and LMD: Leconte et al. 203) can also be attributed to treatment of moist physics and clouds [366].

Our predictions of water loss and habitability implications show greater divergence from previous GCM studies−an outcome that is not unexpected given different initial atmospheric compositions and the addition of model chemistry. For quiescent stars, model top H mixing ratio predictions (hence water loss rates) presented here are orders of magnitude lower than previous work with simplified atmospheric compositions and without interactive chemistry. Implications of our results are favorable to the survival of surface liquid water for planets around quiescent M-dwarfs. For example, a recent study of the temporal radiation environment of the LHS 1140 system suggests that

the planet receives relatively constant NUV ($177 - 283$ nm) flux $< 2\%$ compared to that of the Earth (Spinelli et al. 2019). Our results suggest that LHS 1140b is likely stable against complete ocean desiccation due to the low UV activity of the host star, which bodes well for its habitability. Note however, that since our WACCM simulations assume a hydrostatic atmosphere, escape of H_2O_v is only roughly approximated. Furthermore, during the pre-main sequence phases of M-dwarfs (< 100 Myr), high amounts of X-ray/EUV irradiation may cause an early desiccation and/or runway greenhouse of planetary atmospheres in the IHZ [222]. Even so, rocky planets around M-dwarfs may still possess active hydrological cycles through acquisition of cometary materials [329] as well as extended deep mantle cycling and the emergence of secondary atmospheres [185]. Despite the super-luminous stages of M-dwarfs, existence of abundant water inventories is shown to be plausible using numerical TTV analysis, for example, in the TRAPPIST-1 system [117]. For this pilot CCM study of the IHZ, we focus on main-sequence stars to be consistent with previous work modeling moist greenhouse states (e.g., Kasting et al. 167, Kopparapu et al. 191). Further study is warranted examining stellar activity levels, including enhanced UV flux, time-dependent stellar flares, and sun-like proton events, and their roles in driving water-loss in habitable planet atmospheres.

Coupled CCMs, such as the one employed here, are advantageous for helping to improve/inform 1D model simulations. Previous work (e.g., Zhang and Showman 376) have shown that the constant vertical diffusion coefficients assumed in 1D models (e.g., Hu et al. 148, Kaltenegger and Sasselov 162) may be invalid for different chemical compounds. Here, we find that the efficiency of global-mean vertical transport is not only species-dependent, but also host star dependent, as the magnitude of meridional overturning circulation and degree of vertical wave mixing are inherently tied to the planetary rotation rate and stellar T_{eff} (Figure 3.4.4), both of which are constrained for synchronously rotating planets. Although a detailed comparison of the full set of our chemical constituent profiles with those of 1D is beyond the scope of this study, our results show that 3D CCMs

could offer a basis to improve prediction of the 1D vertical distribution of photochemically important species (e.g., ozone). This task is especially important in the transition regime (i.e., for planets around stars with $2900 T_{eff} 3400$ K), where stratospheric circulation patterns can shift substantially (i.e., emergence of anti-Brewer-Dobson cells; Carone et al. 43), leading to the further breakdown of a fixed vertical diffusivity assumption by 1D models.

In this study we focus solely on simulations with Earth-like ocean coverage and landmass distributions. However, water inventories vary with accretion and escape history. If a planet is barren (i.e., without a substantial surface liquid water inventory), then moist convection is inhibited and the water vapor greenhouse effect is suppressed. This can result in the delay of a runaway greenhouse [2] and the onset of moist bistability wherein surface water could condense in colder reservoirs [204]. similar effect could occur if the substellar point is located above a large landmass instead of an ocean basin [208]. This has relevance for atmospheric chemistry and habitability as it could suppress substellar moisture, leading to lower production rates of H in the thermosphere (above 10^{-2} mbar) and OH in the stratosphere (between 100 and 1 mbar).

Similarly, we fix our substellar point over an ocean basin and assume circular orbits locked in 1:1 spin-orbit resonance. In reality, the substellar point and stellar zenith angle could be nonstationary [205] and planetary orbits could be eccentric without the stabilizing influence of a gas giant [333]. Nonstationary solar zenith angles could affect atmospheric circulation by modulating efficiency of moist convection, while eccentricity could drive planetary climate by as evidenced by Earth's geological record [144]. However, these considerations are arguably secondary as existence of thermal tides are theoretical in the context of exoplanets and planets in the RV samples that have eccentricity greater than 0.1 are not common [309]. Thus, we believe our simplification of fixed substellar point and perfect circular orbit should be valid for the majority of actual planetary systems.

Apart from surface climate, continued habitability is contingent upon the formation and retention of an ozone layer to shield excessive stellar UV-C ($200 < \lambda < 280$ nm) radiation and energetic particle bombardment. A thin ozone layer is hazardous to DNA due to surface exposure to high doses of UV radiation (e.g, O'Malley-James and Kaltenegger 258). Alternatively, UV radiation may be critical in instigating complex prebiotic chemistry (e.g., Ranjan et al. 273). As our simulations enter the moist greenhouse regime, we find that their atmospheres have orders of magnitude lower ozone mixing ratios than those in temperate climates (Figure 3.4.6g), implying that the UV fluxes reaching the planetary surface may be high and therefore potentially threatening to surface life. Further, we find that both stellar UV activity and efficiency of day-to-nightside ozone transport could control the degree of UV flux penetration on the dayside surface. Thus, future constraints on the width of this "complex life habitable zone" (HZCL; Schwieterman et al. 299) will need to evaluate its dependencies on stellar flux, spectral type, and stellar activity, and will benefit from the use 3D CCMs.

Ultimately, CCM predictions of planetary habitability near the IHZ depend on the water accretion history [?], stellar XUV evolution [222], orbital parameters [178], and the spatial distribution of surface water [182, 348]. These considerations should be investigated in a more extensive CCM-based parameter space study (similar in spirit to e.g., Komacek and Abbot 186) to better understand the climate, chemistries, and habitability potentials of IHZ planets around M-dwarfs.

3.5.1 Observational Implications & Detectability

Follow-up characterization efforts by future instruments will likely target planets around M-dwarfs. To contextualize our CCM results within an observational framework, we calculate transmission spectra, secondary eclipse thermal emission spectra, and their simulated observations using the

Simulated Exoplanet Atmosphere Spectra (SEAS) model (Zhan et al. in revision). SEAS is a radiative transfer code that calculates the attenuation of photons by molecular absorption and Rayleigh/Mie scattering as the photons travel through a hypothetical exoplanet atmosphere. The simulation approach is similar to previous work by Kempton et al. [175] and Miller-Ricci et al. [244]. The molecular absorption cross-section for O_2, H_2O, CO_2, CH_4, O_3, and H are calculated using the HITRAN2016 molecular line-list database [110]. The SEAS transmission spectra are validated through comparison of its simulated Earth transmission spectrum with that of real Earth counterparts measured by the Atmospheric Chemistry Experiment (ACE) data set [32]. For more details on SEAS, please see Section 3.4 of Zhan et al., (in revision).

To compute atmospheric spectra, we use a subset of our CCM results: (i) Earth around the Sun, (ii) tidally-locked planet around an M8V star (10F26T), (iii) tidally-locked planet around a quiescent M2V star (19F40T), and (iv) tidally-locked planet around an active M2V star (19FADLeoUV). These simulations are chosen to illustrate the spectral feature differences between rapidly-rotating planets (10F26T and Earth-Sun) and slowly-rotating planets (19F40T and 19FADLeoUV). These simulations also demonstrate the consequences of different stellar UV activity levels on the spectral shapes: from low (10F26T and 19F40T) to mid (Earth-Sun), to high (19FADLeoUV) UV inputs. Lastly, planets orbiting late K-dwarfs, such as 19F40T, are argued to be at an advantage over those around mid-to-late M-dwarfs for biosignature potential [13, 210, 211], and thus our primary focus on the host stars with T_{eff} of 4000 K.

CCM inputs for the SEAS model include: simulated temperatures and mixing ratios of gaseous constituents (i.e., N_2, CO_2, H_2O_v, O_2, O_3, CH_4, and N_2O), converted to 1D vertical time-averaged profiles. Transmission spectra were generated using the terminator mean values, while the emission spectra used the dayside-mean. SEAS assumes the premise of clouds, rather than using CCM results, in order to facilitate comparison with previous work [135, 249]. For transmission, we explore three scenarios: uniform grey cloud at 10 mbar with 1.0 opacity (or optical depth), uniform

grey cloud at 100 mbar with 0.5 opacity, and no clouds. For thermal emission, we assumed a 50% patchy grey cloud at 10 mbar with 0.5 opacity. These selections are made based on the fact that the atmosphere molecular absorption path length for stellar radiation passing through the rim of the planet atmosphere is $\sim 10\times$ the molecular absorption pathlength for blackbody radiation traveling from the surface of the planet. Parameterized clouds are used rather than CCM simulated clouds, as the former can set an upper/lower bound to our detection threshold and thus facilitate comparison with previous work. For instance, the 10 mbar with 1.0 opacity case mimics that of an "upper atmosphere uniform haze", e.g., Kawashima and Ikoma [171]. Moreover, GCM simulation of clouds remains an active area of research and thus simulated clouds come with inherent uncertainties. In future efforts, we will endeavor to include simulated clouds and their inherent uncertainties from a suite of GCMs into CCM-SEAS.

We validated our simulated Earth atmosphere transmission spectra with measurements of Earth's atmosphere through the ACE program [32] and emission spectra with MODTRAN [31]. Minor differences are due to exclusion of trace gases in the Earth atmosphere with a column average mixing ratio less than 1 ppmv.

Our simulated observations assume that the system is 2 pc from the observer. The planet of consideration is an Earth-sized and Earth mass planet. We also assume the use of a JWST-like, 6.5 m telescope, and with 25% throughput and an approximated noise multiplier of 50% which accounts for potentially unknown stellar variability and/or instrumental effects. While the spectral resolution of JWST is R = 100 at 1 - 5 μm (NIRSpec) and R = 160 at 5 - 12 μm (MIRI), in practice this "high" resolution (as compared to Hubble WFC3) is not prioritized for detection/distinction of H_2O_v and O_3 molecules in exoplanet atmospheres due to the unique and broad spectra features these two molecules have (Zhan, et al. submitted). Therefore, detection can be optimized by using a larger bin width to increase the signal-to-noise ratio (SNR) of the H_2O_v and O_3 molecules at the expense of reducing the resolution just enough to distinguish the molecules in consideration. We

use the empirical formula of:

$$l_n = l_0 \left(\frac{\lambda_n}{\lambda_0} \right)^m \qquad (3.5)$$

where l_0 is 0.1 μm and λ_0 is 1 μm. i.e, the bin width l_n, at $\lambda_n = 10$ μm, is = 1 μm. Note that we neglect the systematic noise of JWST, which is projected to be on the order of $\sim$10 ppm [113]. Implementation of the noise floor into the JWST simulator will slightly weaken our predicted features. Given the planet is at 2 pc and the high stratospheric H_2O concentration however, the H_2O features will likely still be detectable.

We find that the detection of H_2O_v in moist greenhouse atmospheres can be achieved with high SNR confidence using NIRSpec. We also find that O_3 detection at the 9.6 μm window can potentially reach an SNR of 3 using MIRI LRS for planets around active stars (e.g., a Sun-like star or active M-dwarf). For the transmission spectra (Figure 3.5.1[3]), we compare our simulated results with those of Fujii et al. [99] and Kopparapu et al. [191], and find that our CCM-SEAS results are in agreement with the potential of characterizing water vapor features between 2.5 and 8 μm.

Slowly-rotating planets orbiting the IHZ of M2V stars (e.g., 19F40T and 19FADLeoUV) have moist greenhouse atmospheres and higher stratospheric water vapor content (red curves in Figure 5), which raises their signals in comparison to rapidly-rotating planets and stratospherically dry planets (e.g., 10F26T). In a similar vein, detection of water vapor can be achieved at high SNR confidence only for the moist greenhouse case, where H_2O_v is four orders of magnitude more abundant than in the Earth's stratosphere. Detection of water vapor is difficult for an Earth-like atmosphere in transmission as the majority of water vapor is concentrated below the tropopause. Transmission

---

[3]The planet radius is independent of planetary system, and is easier for comparison with other theory work, as ppm depend on planet/star radius ratio.

spectra of IHZ planets generated with 1D models (e.g., Lincowski et al. [209]) do not display these prominent water vapor features as large-scale hydrological circulation processes are not resolved in 1D. We also find that the results of parameterized clouds match those of previous work [321, 344] such that they inhibit detection of molecular features (Figure 3.5.1).

Oxygenated-atmospheres around active stars (i.e., Earth and 19FADLeoUV) should have more pronounced ozone features due to increased ozone production rates compared to their quiescent counterparts. We find that although the H_2O_v features are not significantly altered by stellar UV activity, the O_3 features are. In addition, we test the effects of total integration time (10 hr vs 100 hr) on the predicted observations to explore the "most optimistic" scenario (Figure 11). These integration times translate to 4 to 7 and 40 to 70 transits respectively for a typical M-dwarf system. We find that detectability of the ozone feature is substantially improved with a higher integration time (Figure 3.5.1).

For secondary eclipse thermal emission spectra, we find that the 9.6 μm O_3 feature is located near the emission peak of the planet ($\sim$300 K blackbody). Despite this finding, detection of this feature via secondary eclipse could be challenging for Earth-sized planets near 4000 K stars due to low SNR confidence. Potentially low SNRs are a result of the constraints of JWST's cryogenic lifetime (necessary for mid-IR observations) of 5 years. Further, as the total number of transit hours that can accumulate is less than 100, the maximum achievable SNR confidence given our simulation parameters would be less than 3. For a super-Earth (e.g., $\sim$1.75 $R_\oplus$) or a hotter (but non-habitable) planet around a late M-dwarf star however, secondary eclipse measurements of these features could be achievable [184, 226].

3.6 Conclusion

In this study, we carried out numerical simulations of climate and chemistries of tidally-locked planets with a 3D CCM. Our results show that the maintenance of ozone layers, water photodissociation efficiency, and the onset of moist and incipient runaway greenhouse states depend on the incident stellar flux, stellar spectral-type, and importantly, UV radiation. By directly simulating photochemically important species such as ozone, we find that their abundance and distribution depend on the host star spectral type. The strength of the stratospheric overturning circulation, for example, increases with stellar T_{eff}, leading to higher efficiency in the divergent transport of airmasses and thus photochemically produced species and aerosols.

Critically, we find that only climates around active M-dwarfs enter the classical moist greenhouse regime, wherein hydrogen mixing ratios are sufficiently high such that water loss could evaporate the surface ocean within 5 Gyrs. For those around quiescent M-dwarfs, hydrogen mixing ratios do not exceed that of water vapor. As a consequence, we find that planets orbiting quiescent stars have much longer ocean survival timescales than those around active M-dwarfs. Thus, our results suggest that improved constraints on the UV activity of low-mass stars will be critical in understanding the long-term habitability of future discovered exoplanets (e.g., in the TESS sample; Günther et al. 121).

Stellar UV radiation has pronounced effects on atmospheric circulation and chemistry. Our 3D CCM simulations show that vertical and horizontal winds in the upper atmosphere ($\sim$1 mbar) are strengthened with higher UV fluxes. Global distributions of O_3, OH, and H are the result of long-term averaged tradeoffs between dynamical, photolytic, and photochemical processes−resulting in substantially different day-to-nightside contrasts with incident UV radiation. Thus, coupling dynamics and photochemistry will be necessary to better understand the spatial distributions and

temporal variability (e.g., Olson et al. 255) of biogenic compounds and their byproducts.

Using a radiative transfer model with our CCM results as inputs, we show that detecting prominent water vapor and ozone features on M-dwarf planets during primary transits is possible by future instruments such as the JWST [25]. However, secondary eclipse observations are more challenging due to the predicted low SNR confidence.

3.7 Acknowledgements

Figure 3.5.1: Simulated atmosphere transmission spectra of synchronously-rotating planets around M-stars and an Earth-like fast rotator around a Sun-like star (P = 24 hrs), showing apparent planet radius and transit depth as a function of wavelength (μm). Simulated input data from CCM (i.e., experiments 10F26T, 19F40T, and 19FADLeoUV) are spatially averaged across the terminators. We explore three cloud assumptions: cloudless (top and bottom panels), uniform grey cloud at 100 mbar with 0.5 opacity (second panel), and uniform grey cloud at 10 mbar with 1.0 opacity (third panel). Also shown are simulated JWST observation with 1σ uncertainty bar (black) at two integration times: 10 hr (first three panels) and 100 hr (bottom panel). The simulated observation assumes the planet to be 2 pc away from the observer, and the bin width of the telescope to be 1 μm at wavelength of 10 μm.

Chapter 4

Persistence of Flare Driven Atmospheric Chemistry on Rocky Habitable Zone Worlds

4.1   Abstract

[1] Low-mass stars show evidence of vigorous magnetic activity in the form of large flares and coronal mass ejections. Such space weather events may have important ramifications for the habitability and observational fingerprints of exoplanetary atmospheres. Here, using a suite of three-dimensional coupled chemistry-climate model (CCM) simulations, we explore effects of time-dependent stellar activity on rocky planet atmospheres orbiting G-, K-, and M-dwarf stars. We employ observed data from the MUSCLES campaign and *Transiting Exoplanet Satellite Survey* and test a range of rotation period, magnetic field strength, and flare frequency assumptions. We find that recurring flares drive K- and M-dwarf planet atmospheres into chemical equilibria that

---

[1]Chapter adapted from: Chen, H., Zhan, Z., Youngblood, A., Wolf, E.T., Feinstein, A.D. and Horton, D.E., 2021. Persistence of flare-driven atmospheric chemistry on rocky habitable zone worlds.*Nature Astronomy*, 5(3), pp.298-310.

substantially deviate from their pre-flare regimes, whereas G-dwarf planet atmospheres quickly return to their baseline states. Interestingly, simulated O_2-poor and O_2-rich atmospheres experiencing flares produce similar mesospheric nitric oxide abundances, suggesting that stellar flares can highlight otherwise undetectable chemical species. Applying a radiative transfer model to our CCM results, we find that flare-driven transmission features of bio-indicating species, such as nitrogen dioxide, nitrous oxide, and nitric acid, show particular promise for detection by future instruments.

4.2 Introduction

In recent years, large-scale observational campaigns such as the *Kepler Space Telescope* [36] indicate that rocky planets are common [39, 147, 192, 250]. A handful of these systems are known to reside within the circumstellar habitable zones (HZs) of their host stars [167, 168] and are amenable to atmospheric spectroscopic measurements (for example, Kepler-186, Kepler-452, Proxima Centauri, TRAPPIST-1, LHS-1140, and TOI-700). On-going Transiting Exoplanet Satellite Survey (TESS) operations [278] will discover many closer and brighter planetary systems, offering more terrestrial exoplanets for follow-up mass measurements and atmospheric characterization efforts [17, 63]. However, interpretation of remotely sensed atmospheric data will require making sense of a planet's signals in context, i.e., understanding interactions of atmospheric chemistry, physics, dynamics, and thermodynamics, within the space weather environment and electromagnetic radiation regime. For instance, strong stellar chromospheric activity from low-mass stars could influence attendant atmospheres via the dissociation, excitation, and ionization processes associated with space weather events [214, 290] – leading to substantial alteration of planetary atmospheres and chemical signatures [5]. Modulation of atmospheric chemistry can have a critical influence on the bulk atmospheric composition [24, 330], atmospheric dynamics [328], surface radiation dosage [14, 360], and detectability of atmospheric species [4].

Stellar activity – which includes stellar flares, coronal mass ejections (CMEs), and stellar proton events (SPEs) – has a profound influence on a planet's habitability, primarily via its influence on atmospheric ozone. Stellar flares are rapid (minutes to days) releases of coronal magnetic energy accompanied by bursts of electromagnetic radiation and accelerated ionized particle fluences. Previous work has shown that while a single large flare (e.g., AD Leonis Great Flare with UV-optical energy of $E \sim 10^{34}$ erg; [130]) does not substantially affect an Earth-like planet's habitability [304], repeated secular flaring and CMEs, by way of UV emissions ($\lambda < 350$ nm) and SPEs ($E > 100$ MeV), could destroy a planet's ozone layer within a few Earth-years [332]. With the exception of the strongest flaring scenarios, time-independent models have predicted that initially Earth-like atmospheres should retain appreciable amounts of ozone that could efficiently filter out incident UV-B and UV-C radiation [114]. However, this conclusion stands in contrast with that of time-resolved models, in which nearly 90% of the stratospheric ozone column could be eroded, even with conservative assumptions in flare magnitude and frequency [332].

In addition to stellar flares' considerable influence on ozone, flares are likely to have observationally-relevant effects on planetary atmospheres [340]. Remote detection of biological processes, or equivalently, the measure of thermodynamic chemical disequilibrium [198, 298], is linked to atmospheric chemistry, brightness temperature, and stellar variability. In the search for signals of life, detection of either biosignatures, i.e., atmospheric constituents that are the direct result of life processes [73, 298], or bio-indicators, i.e., the photochemical derivatives of biosignatures, is sought. High magnitude stellar flares may trigger disequilibrium chemistry and generate bio-indicating species through photo-excitation, photo-dissociation, and/or strong mixing. For example, it has been hypothesized that enhanced accumulation of nitric acid (HNO3) in a biologically active atmosphere experiencing flares could serve as a bio-indicator, as purely abiotic concentrations of HNO3 in anoxic conditions should be low [293, 324]. Abiotic nitric oxide (NO) and nitrogen dioxide (NO_2) production in O_2-depleted environments is also not expected to result in substantial

atmospheric accumulation as their production is mediated by collisions between molecular biogenic oxygen and nitrogen. In atmospheres dominated by N_2–O_2–H_2O however, stellar activity could highlight species such as NO, OH, $O_2(^1D)$ and CO_2 to potentially detectable levels [4, 332].

Previous efforts to understand the effects of stellar flares on planetary atmospheres underscore the value of single column climate models. Their efficiency and speed allow for a wide sampling of the planetary parameter space. However, lower-dimensional models do not account for critical three-dimensional (3D) processes, including atmospheric circulation, large-scale mixing, and cloud dynamics – factors that have substantial impact on the climate and chemistry of exoplanets, particularly for slow-rotators orbiting late K-dwarf and early M-dwarf stars [54, 55, 361]. Assessments of stellar chromospheric and coronal activity influences on planetary atmospheres are likewise inherently 3D problems, e.g., the role of a magnetic field, inclusion of dynamical mixing, and illumination geometry. As such, 3D considerations are likely to have crucial consequences on flare influence predictions. Furthermore, the majority of previous exoplanet-flare-habitability studies have used UV observations from a single high magnitude 10^{34} erg superflare (AD Leonis; [14, 130]), that is unlikely to be representative of typical stellar flaring behavior. Incorporating UV flare spectra and lightcurve temporal evolution using more typical flaring behavior may offer new insights into the photochemical characteristics of habitable zone planets [220, 263].

To better understand interactions between flaring stars and their attendant planets, in this study we employ a 3D global Earth System CCM, the Whole Atmosphere Community Climate Model (WACCM; [229]). We simulate nitrogen-dominated rocky exoplanet atmospheres experiencing time-dependent stellar UV activity and proton events around G-, K-, and M-dwarf stars (Extended Data Figure 1-3). Due to i) stationary substellar cloud formation that prevents runaway greenhouse states near the inner edge of the habitable zone [348, 361], ii) decreased ice-albedo feedbacks which inhibit total glaciation near the outer edge of the habitable zone [48, 50, 310], and iii) increased nutrient replenishment via oceanic upwelling [257], previous 3D studies have demonstrated that

slowly- and synchronously-rotating ocean-covered planets have increased habitability potential. With the inclusion of time-dependent stellar flares, the results from this work further the notion that slowly- and synchronously-rotating planets are favorable targets by future instruments.
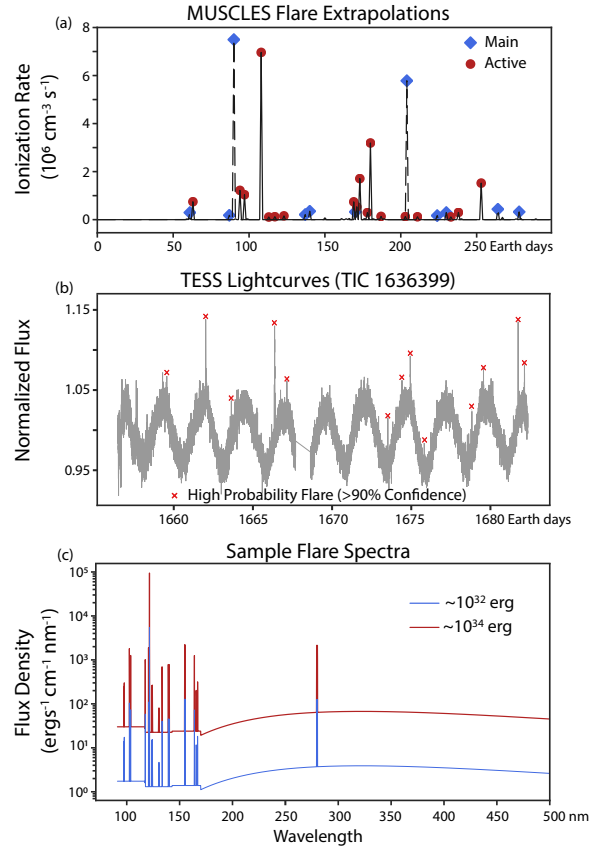
Figure 4.2.1: Observed flare lightcurves and spectra used as inputs for CCM simulations.
a, Flare-driven atmospheric ionization rates produced via power-law extrapolations for large flares ($E > 10^{32}$ erg) from the MUSCLES survey. Data that underpins the main text are denoted by "main", whereas data approaching the activity level of Proxima Centauri are denoted by "active" (See Methods). The dashed black lines connect the 'main' input ionization rates and the solid black line connect those of the 'active'. **b,** Observed TESS lightcurves from TIC 1636399 identified by convolution neural network. **c,** Sample MUSCLES spectra used in model simulations for flares with two different approximate energies during their impulsive phases.

4.3 Numerical Setup

We perform simulations of rocky exoplanetary atmospheres orbiting G-, K-, and M-star archetypes (Sun-like star, HD85512, and TRAPPIST-1). For each planet scenario, we test different oxygena-

tion states, magnetosphere strengths, and stellar activity levels (Extended Data Figure 4.3.1-3). Pre-flare baseline atmospheric compositions are: N_2 (78%), CH_4 (0.701 ppmv), N_2O (0.273 ppmv), and CO_2 (288 ppmv). We focus on three different scenarios: (1) a magnetized rapidly rotating planet around a Sun-like star (which we refer to as "G-star planet"), (2) an unmagnetized slow rotator around HD85512 ("K-star planet"), and (3) a weakly magnetized rapid rotator around TRAPPIST-1 ("M-star planet"). The latter two scenarios assume synchronous-rotation. For each scenario, we simulate the effects of O_2-rich (modern-Earth-like) and O_2-poor (Proterozoic-Earth-like) initial atmospheres. Configurations and boundary conditions were chosen for self-consistency, that is, simulated configurations follow from known physics. For example, greater orbital separations of synchronously-rotating planets around early M-dwarfs imply slower rotation (compared to those around late M-dwarfs). Without rotation induced convection of conducting inner core fluids, i.e., a magnetic dynamo, these planets are unlikely to sustain strong planetary-scale magnetic fields [58]. Thus, while we test the sensitivity of our results to a suite of input parameters and assumptions, the main text presents the most self-consistent simulation scenarios.

Steady-state stellar spectral energy distributions from the 1850 Solar Irradiance spectrum [202], TRAPPIST-1 (M8V; T_{eff} = 2511 K; Wilson et al. in review), and HD 85512 (K6V; T_{eff} = 4715 K; version 2.2; [96] are used as inputs to the CCM. To compute time-dependent activity (Figure 4.2.1), we utilize a Measurements of the Ultraviolet Spectral Characteristics of Low-mass Exoplanetary Systems (MUSCLES) flare generator [220] and observed *TESS* flare data identified by a convolutional neural network [93]. Proton fluence calculations are derived from the above electromagnetic flares [371] and all CCM experiments described are subject to the same stellar activity time series inputs (see Methods and Extended Data Figure 4.3.1-3).

We first report the effects of MUSCLES-derived stellar flares on our self-consistent scenarios. We then explore the effects of observed *TESS* flares, discuss the coupled effects of atmospheric transport, and present results for key flare-modulated chemical species. Next, we compare and

contrast flare-induced differences between O_2-rich versus O_2-poor atmospheres and moist green-house states versus temperate states. Finally, we discuss the observational implications of our results. See the Supplementary Information for the complete simulation setups and input data.
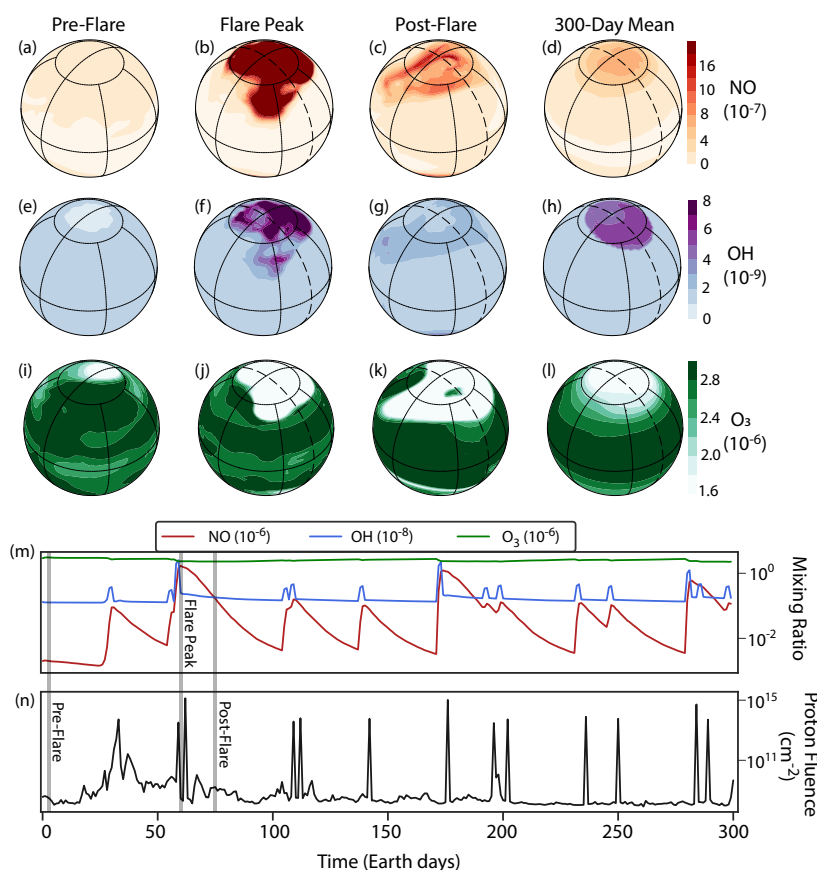
Figure 4.3.1: Spatial and temporal atmospheric effects of repeated stellar flares on a G-star planet. Simulated global time slice distributions of upper atmospheric NO (a-d), OH (e-h), and O_3 (i-l) mixing ratios and their global average time-series (m) that result from exposure to time evolving flare-derived proton fluences (n). The simulated planet rotates around a Sun-like star non-synchronously and has a magnetic field. NO and OH mixing ratios are reported at 0.1 hPa, whereas O_3 mixing ratios are reported at 1.0 hPa. Spherical projections are centered on 40° N latitude and 225° longitude.

4.4   3D Effects of Large Stellar Flares (Results)

We find that strong stellar flares drive dramatic transient and steady-state changes in stratospheric and mesospheric chemistry, particularly in nitrogen and hydrogen oxide reservoirs. Our results show that energetic flares ($E > 10^{33}$ ergs and proton fluence $> 10^{14}$ cm^{-2}) have profound impacts on atmospheric species such as nitric oxide (NO), hydroxide (OH), and ozone (O$_3$) (Figures 2, 3, and Extended Data Figure 4.4.2). On unmagnetized K- and M-star planets in particular, modeled stellar flares modulate the atmospheric concentration of many photochemically important species and ultimately establish new chemical steady-state regimes that substantially deviate from their pre-flare compositions (Figure 4.4.1m and Extended Data Figure 4.4.2m). In contrast, flares do not substantially perturb the atmospheric compositions of magnetized G-star and TESS planets (Figure 4.3.1m; Extended Data Fig. 5).

Simulated mesospheric nitrogen oxides such as NO, derived from reactions initiated by precipitating electrons [156], are orders of magnitude more abundant on K- and M-star planets (Figures 3a-d and Extended Data Figure 4.4.2a-d) than those around G-stars (Figure 4.3.1a-d). This is the combined result of the greater latitudinal extents of proton deposition for weakly or unmagnetized planets (see Methods), steady-state inputs of UV-B spectra, illumination geometries, and planetary circulation regimes.

The circumstellar UV photochemical environment and slow rotation of K- and M-star planets, leads to the persistence of mesospheric NO. NO mixing ratios on our simulated K- and M-star planets do not return to their pre-flare levels after a large flare (Figure 4.4.1m), whereas NO on G-star planets returns to pre-flare levels within < 50 days (Figure 4.3.1m). Enhanced simulated global-mean NO lifetimes on M-star planets are due to lesser emission of UV-B radiation ($280 < \lambda < 315$ nm) by their host stars, which promotes O(^{1}D) formation, reducing an OH sink (as H$_2$O$_v$

+ $O(^1D) = 2OH$). In addition, prolonged NO_x lifetimes on slowly-rotating K-star planets are likely due to thermally driven radial day-to-night advection that transports produced substellar NO_x to the nightside, where it is temporarily stored. Here, daytime nitrogen-hydrogen oxide chemistry, such as $NO + HO_2$ and $NO + NO_2$ photolysis, is averted (see Methods), leading to the time averaged enhancement of NO_x abundances. In contrast, rapid horizontal mixing and higher incident UV-B radiation for planets around G-stars ($P = 24$ hr) leads to more efficient NO_x removal via reaction with ozone and direct titration (Figure 4.3.1a-d).
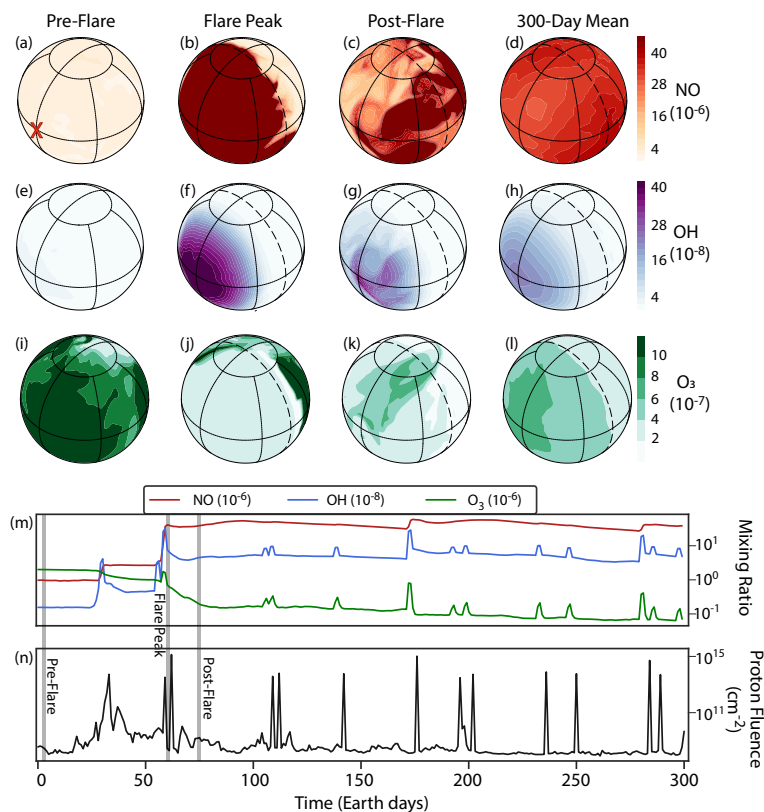
Figure 4.4.1:   Spatial and temporal atmospheric effects of repeated stellar flaring on K-star planet. Simulated global time slice distributions of upper atmospheric NO (a-d), OH (e-h), and O_3 (i-l) mixing ratios and their global average time-series (m) that result from exposure to flares with time-evolving proton fluences (n). The simulated planet rotates around K-star HD85512 synchronously and does not have a magnetic field. NO and OH mixing ratios are reported at 0.1 hPa, whereas O_3 mixing ratios are reported at 1.0 hPa. Spherical projections are centered on 40° N latitude and 225° longitude. Red cross denotes the substellar point.

The presence of water vapor (H_2O_v), a canonical habitability indicator, could signify an active hydrological cycle. Photochemical and photolytic byproducts of H_2O_v such as stratospheric OH and thermospheric H are produced by flare-initiated ion chemistry chains [317]. In our simulations, we find that hydrogen oxide family constituents are particularly sensitive to magnetic field assumptions due to their short lifetimes. Different magnetic field deflection geometries and host star UV spectral energy distributions contribute to different OH mixing ratio distributions (Figure 4.3.1e-h and 3e-h).

During large stellar flares, stratospheric and mesospheric polar OH mixing ratios in the magnetized G-star planet simulation are $\sim 10^{-8}$, but two orders of magnitude greater on the dayside of the unmagnetized K-star planet ($\sim 10^{-6}$).

The existence and persistence of stratospheric ozone in planetary atmospheres is fundamentally important for the protection and development of surface life [305]. Simulated K- and M-star planet atmospheres (Figure 4.4.1a-l and Extended Data Figure 4.4.2a-l) experience greater instantaneous ozone destruction compared to magnetized G-star planets (Figure 4.3.1a-l). In the latter scenario with an Earth-similar magnetosphere, protons are funneled to the polar regions by magnetic field lines, whereas protons directly interact with the dayside atmospheres of the K- and M-star planets, enhancing ozone destruction. These differences are further compounded by redirection of protons to the polar nightside of G-star planets, initiating more sluggish chemical reactions than those that occur in the substellar regions of the unmagnetized planets. Ozone distribution differences between unmagnetized/weakly magnetized K- and M-star planets are due to the more active TRAPPIST-1 spectrum used (compared to that of HD85512), rapid horizontal mixing of chemical species, and strengthened downward transport on M-star planets.

To assess the role of flare frequency on ozone retention, we simulate three flare frequency assumptions (Extended Data Figure 4.4.1). For stellar activity approaching that of an optically-inactive M-dwarf (i.e., with cumulative flare index $\alpha = 0.7$; MUSCLES sample, [220]), the computed total ozone column (see Methods) of the M-star planet gradually transitions to a depleted regime and establishes a new chemical steady-state (Extended Data Figure 4.4.4). For stars with activity levels similar to Proxima Centauri and AD Leo ($\alpha = 0.54$), we find that the ozone column experiences abrupt destruction from ~ 300 Dobson Units (DU) to ~ 106 DU over ~ 200 Earth-days due to rapid erosion by incident stellar protons (Extended Data Figure 4.4.4). Our results could thus be used by observers to tie a measured flare frequency to cumulative effects on a planet's
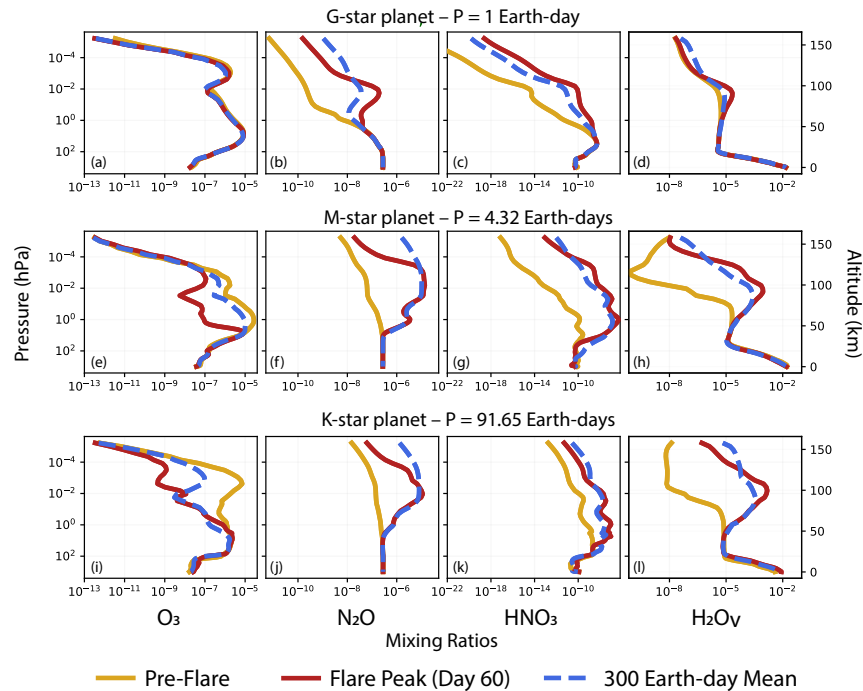
Figure 4.4.2: Global mean vertical profiles of atmospheric species. Simulated mixing ratios of O_3, N_2O, HNO_3, and H_2O_v as a function of pressure and altitude during an initial steady state, the peak of a large flare, and averaged over a 300 Earth-day period. Conditions are shown for an Earth-similar planet around a G-star (a-d), K-star (e-h), and M-star (i-l) that experience flares with proton fluences of $\sim 10^{14.5} cm^{-2}$.

atmosphere.

In addition to modeled flares, we use observed flares from the first *TESS* data release, specifically M-dwarfs TIC 671393 and 1636399 over 20-30 days of observation time (Extended Data Figure 4.3.1. We find that stellar flares from the *TESS* data lead to more subtle changes in the chemical composition of the attendant planets, in comparison with the MUSCLES-based results that use modeled flare lightcurves with extrapolations to higher energies. For instance, simulated mesospheric ozone is halved at the end of the TIC 671393-based simulation (Extended Data Figure 4.4.3), whereas the full 300-day simulation using MUSCLES data results in a 1 to 2 order of magnitude decrease (Figure 4.4.1). The absence of repeated energetic flares and the short time-

frame of the observed TESS data drive lower production rates of NO and UV photolysis of ozone. This conclusion is consistent with analysis of *TESS* across $\sim 24,000$ samples, as very few stars exhibit continuous flares that exceed the 10^{34} erg threshold for ozone depletion [122].

Apart from stellar characteristics, flare influences are also controlled by the interplay between planetary properties, for example, between atmospheric mixing and photochemistry. Fast rotation, ($P < 6$ days) as in the case of our modeled G-star planet scenario, induces standing tropical Rossby waves that disrupt meridional overturning circulation, as opposed to extratropical Rossby waves in the case of the M-star planets and weak planetary waves in the case of the K-star planet. Without rapidly-rotating Earth-like planet deep wave breaking mechanisms or momentum injections into the stratosphere, slow-rotator stratospheric winds are effectively damped and prevent divergent meridional flow and planet-wide chemical transport, leading to confinement of flare induced species in the equatorial regions (Extended Data Figure 7; [43]). However, fast rotation facilitates downward transport of ozone depleting agents such as NO_x into the mid-lower stratosphere (Extended Data Figure 8a). Conversely, slow rotation (i.e., K-star planet) allows NO_x to remain in the mesosphere/thermosphere (Extended Data Figure 8b). The simulated descent of flare-induced species is analogous to the advection of Earth's NO_x-rich airmasses into the stratosphere, driven by the stratospheric polar vortex and large-scale eddies [100]. Thus, while the presence or absence of a planetary magnetic field plays a key role in governing ozone destruction (as polar ozone could be replenished by efficient meridional circulation), our results indicate that slow rotation (i.e., $P > 25$ days for an Earth-sized planet) can help maintain a stable global ozone layer against proton-initiated removal.

The elevated nitrogen and hydrogen oxides discussed above influence the formation and lifetimes of other atmospheric species such as N_2O, CH_4, HNO_3, and H_2O_v, especially for the K- and M-star planet scenarios. Effects on the G-star planet are generally less persistent as seen by lesser 300-day mean deviation from the pre-flare baselines (Figure 4.4.2a-d). For all scenarios, we find

that flaring produces the largest magnitude alteration in nitrous oxide (N_2O), a biosignature (Figure 4.4.2; see Methods). Both HNO_3 and H_2O_v mixing ratios are enhanced on average by two-to-three orders of magnitude and the enhancements are maintained with repeated flaring in the K- and M-star planet scenarios (Figure 4.4.2b-c). In contrast, CH_4 experiences stronger removal via reaction with ion-derived OH during flaring, leading to lower temporal-mean CH_4 mixing ratios (not shown). These results suggest that while biosignatures such as CH_4 are vulnerable to destruction during periods of strong flaring, bio-indicating "beacon of life" species [4] could be prominently highlighted.

Finally, we discuss flare-modulated atmospheric sensitivities of K-dwarf planet non-modern-Earth-similar compositions, including, O_2-poor Proterozoic-like initial conditions and a moist greenhouse state – common hypothetical exoplanetary conditions. These simulations show important departures from the modern-Earth composition baseline. Interestingly, although the Proterozoic-like simulation contains orders of magnitude lower NO concentrations than that of the Earth-like baseline simulation during the pre-flare state, the flare peak NO concentration of the Proterozoic-like simulation approaches that of the latter (Figure 4.4.3b). This indicates that flare-induced NO could serve as potential proxy that are not directly detectable or challenging to observe (e.g., O_2). Repeated flaring in the moist greenhouse (specific humidity $Q_{H2O} > 10^{-3}$) simulation leads to greater OH production and more rapid ozone destruction due to higher humidity than the Earth-like baseline simulation. In addition, in both the temperate and moist greenhouse simulations, the upper atmosphere is pushed into a classical moist greenhouse state [163], despite the temperate simulation having relatively dry surface conditions (Figure 4.4.3c). This suggests that recurring flares via proton events could drive enhanced water loss through diffusion-limited escape even for planets that do not reside at the inner edge of the habitable zone. These putative non-Earth-archetypes demonstrate that flare-driven accumulation of nitrogen and hydrogen oxides could be reliable in-
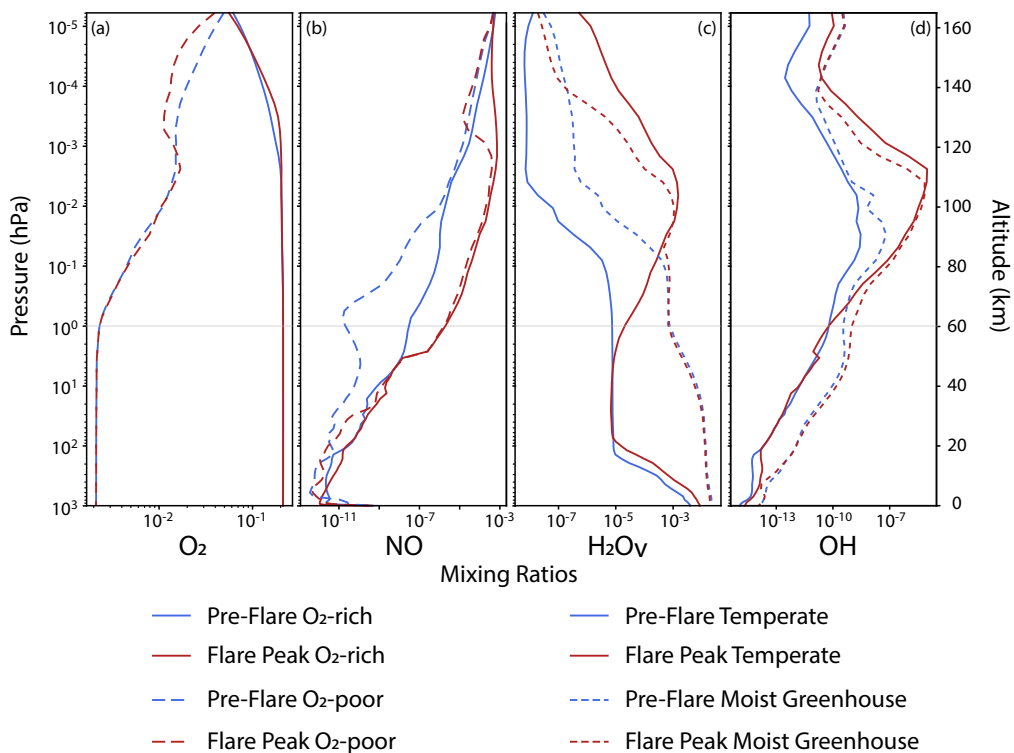
Figure 4.4.3: Global mean vertical profiles of atmospheric species for non-modern-Earth climate archetypes. Simulated mixing ratios of O_2 (a), NO (b), H_2O_v (c), and OH (d) under different climatic conditions. O_2 and NO are reported for simulations with O_2-rich and O_2-poor initial conditions. H_2O_v and OH are shown for two different incident stellar fluxes: temperate (stellar flux $= 1.0\ F_\oplus$) and moist greenhouse (stellar flux $= 1.9\ F_\oplus$). The gray dashed lines denote the approximate transition from the lower atmosphere (stratosphere + troposphere) to the mesosphere and lower thermosphere region.

dicators of an N_2-O_2-H_2O-dominant atmosphere.

4.5   Observational Prospects and Implications (Discussion)

Planetary transmission spectra, using our chemistry-climate model outputs, demonstrate that stellar flaring induces spectral features of habitability indicators and biosignatures (Figure 4.4.4). Here
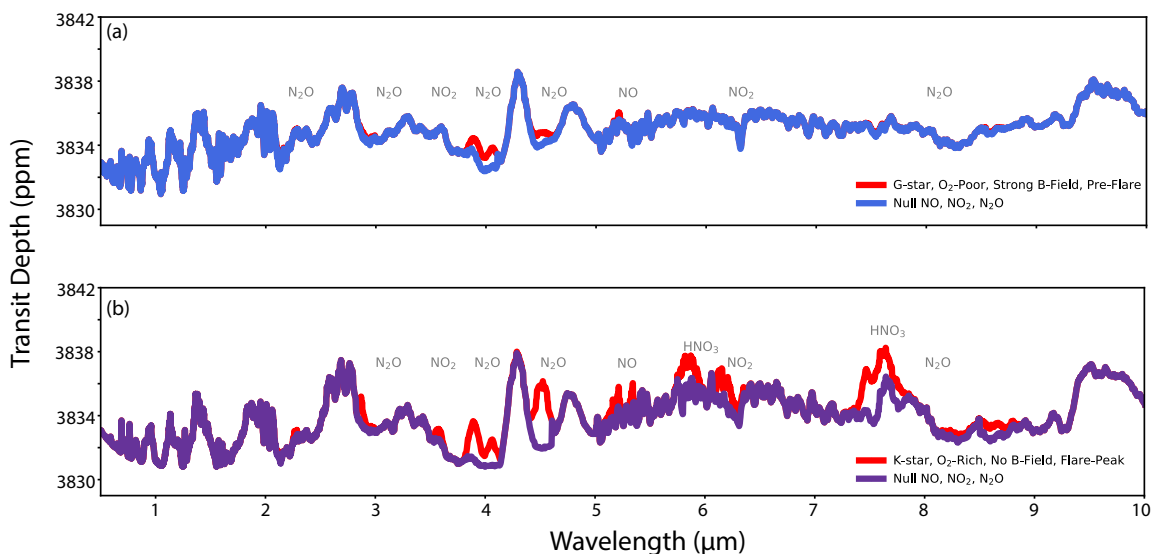
Figure 4.4.4:   Simulated transmission spectra for two end member planetary scenarios. Modeled transit depth as a function of wavelength for simulated atmospheres of a magnetized Earth-like planet around a quiescent G-star without flare activity (a) and an unmagnetized synchronously-rotating planet around an actively flaring K-star (HD85512) (b). We assess the detectability of nitric oxide (NO), nitrous oxide (N_2O), nitrogen dioxide (NO_2), and nitric acid (HNO_3). The red curves contain variable amounts of simulated nitrogen oxide species, whereas the blue and purple curves contain no nitrogen oxides.

we assess the detectability of nitrogen compounds for two endmember atmospheric scenarios from our suite of CCM simulations. Specifically, we compare the transit signals of NO, N_2O, NO_2, and HNO_3 on an O_2-poor magnetized planet orbiting a Sun-like star against those on an O_2-rich unmagnetized planet orbiting a K-dwarf. We find peak absorption depths of 2, 4, 3, and 6 ppm for the respective species in the latter scenario (Figure 4.4.4b). Despite transit depth shifts occurring above the cold trap and thus not muted by clouds [91, 188], differences between pre-flare and flare peak features are less than the predicted noise floor of the James Webb Space Telescope (10-30 ppm; [323]). Moreover, partial overlap of NO and NO_2 features with those of CO_2 and H_2O_v at 4.3 and 5.5 μm obscures their signals. As such, detecting flare-driven biosignature fingerprints on synchronously rotating nitrogen-dominated Earth-sized exoplanets should await the development

of larger telescopes with greater observing power and better instrument noise-floor control (i.e., with the noise-floor pushed to the $\sim$1 $-$ 2 ppm level).

Other simulated spectral features, such as OH and $O_2(^1D)$, are likely only observable during or soon after a large flare, or in a system with a rapid succession of flares during transit measurements. This is due to the species' short chemical lifetimes, relaxation timescales, and rapid zonal mixing on non-synchronously-rotating G-star planets. Transmission features of biosignatures such as CH_4 and O_3 are predicted to be drastically reduced, as they react strongly with nitrogen and hydrogen oxides [324]. Note that these transient features arise primarily from species abundance changes in the mesosphere and lower thermosphere, and not from the stratosphere or troposphere (Figure 4.4.2). This finding is a result of our proton energy spectrum assumption (see Methods). Use of different proton energy spectrum assumptions could alter particle deposition depth, whole-column species abundances, and detectability.

Sudden increases in X-ray and EUV irradiation ($1.0 < \lambda < 100$ nm) – which can energize, ionize, and dehydrate the upper atmosphere [79, 248] – are also associated with CMEs and stellar superflares [67, 364]. Thus, planets around active M-dwarfs may quickly lose their major high mean molecular weight species, while initially volatile rich atmospheres around less active K-dwarfs may be able to survive on geologic timescales [180].

Here, we find that the convolved effects of magnetic field strength, radiation environment, and atmospheric circulation lead to substantial time-averaged (over $\sim$1 Earth year) chemical perturbations on flare-modulated K- and M-star planets. This result underscores the importance of constraining the temporal evolution of the host star spectra and luminosity to assess exoplanetary habitability. While we report the 3D effects of stellar flares on oxidizing atmospheres, strong flares could have other unexpected impacts on atmospheres with reducing conditions. For instance, hydrogen oxide species derived from stellar flares could destroy key anoxic biosignatures such as

methane, dimethyl sulfide, and carbonyl sulfide [77], thereby suppressing their spectroscopic features. However, new ionization rate profiles derived from a prognostic ion chemistry model will be needed to conduct analogous studies in atmospheric compositions dissimilar to Earth's. More speculatively, proton events during hyperflares may reveal the existence of planetary scale magnetic fields by highlighting particular regions of the planet (e.g., the poles; Figure 4.3.1a-d). By identifying nitrogen or hydrogen oxide emitting flux fingerprints during magnetic storms and/or auroral precipitation events, one may be able to determine the geometric extent of exoplanetary magnetospheres.
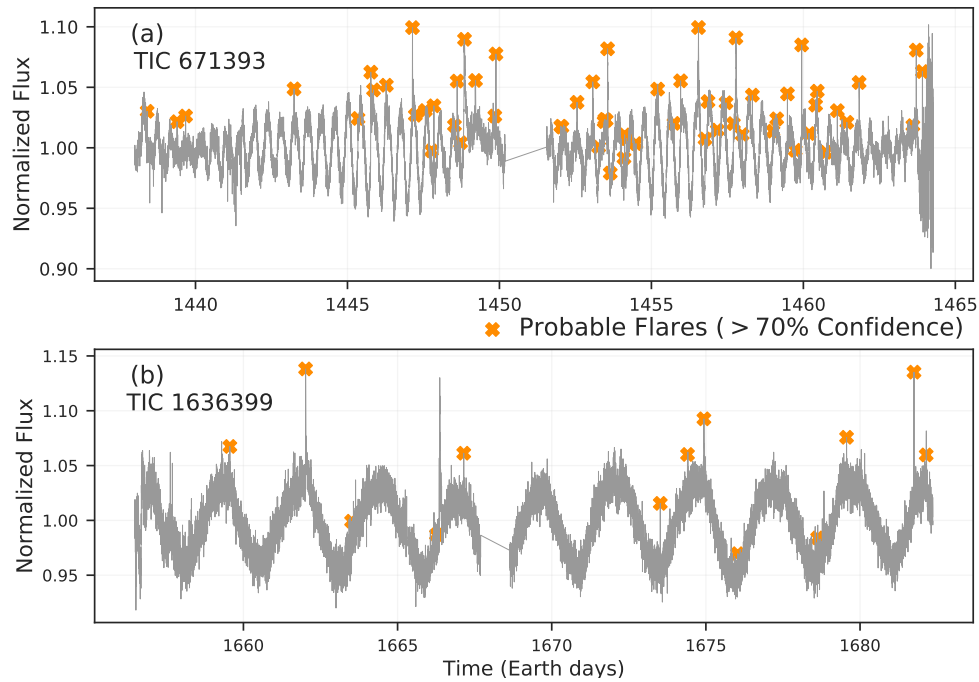
Figure 4.5.2: Timeseries of TESS lightcurves used in this study. The stellar data used are those of TIC 671393 (a) and TIC 1636399 (b), showing identified flares by orange "×"s. Flares are identified by a convolutional neural network algorithm described in Feinstein et al. (2020).
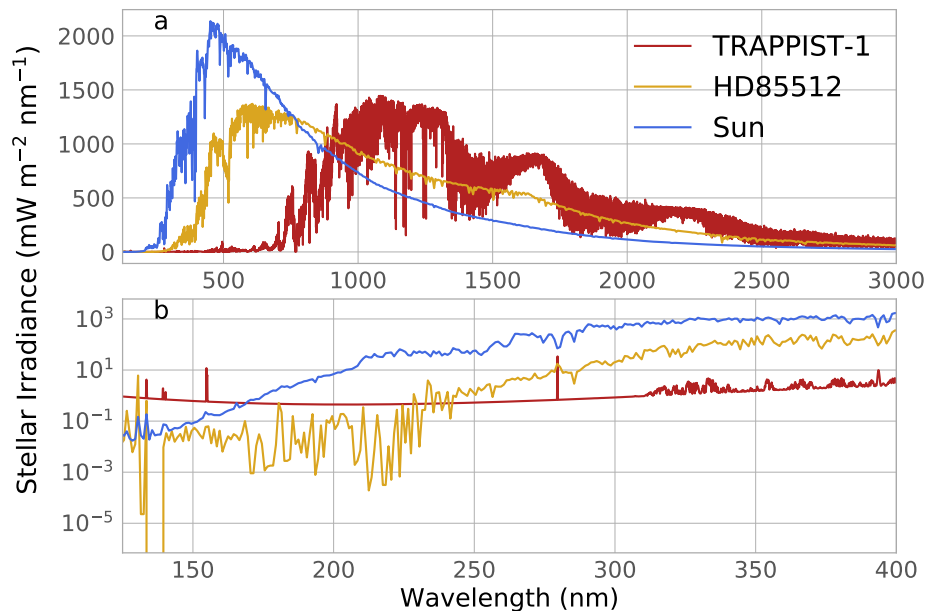
Figure 4.5.1: Input broadband (a) and UV (b) spectral energy distributions for the Sun, HD85512, and TRAPPIST-1. The Sun represents the G-star archetype, HD85512 a K-star, and TRAPPIST-1 a late M-star. We refer to the stellar spectral types these stars represent (G-star, K-star, and M-star) instead of the specific star in the main text and throughout the paper.
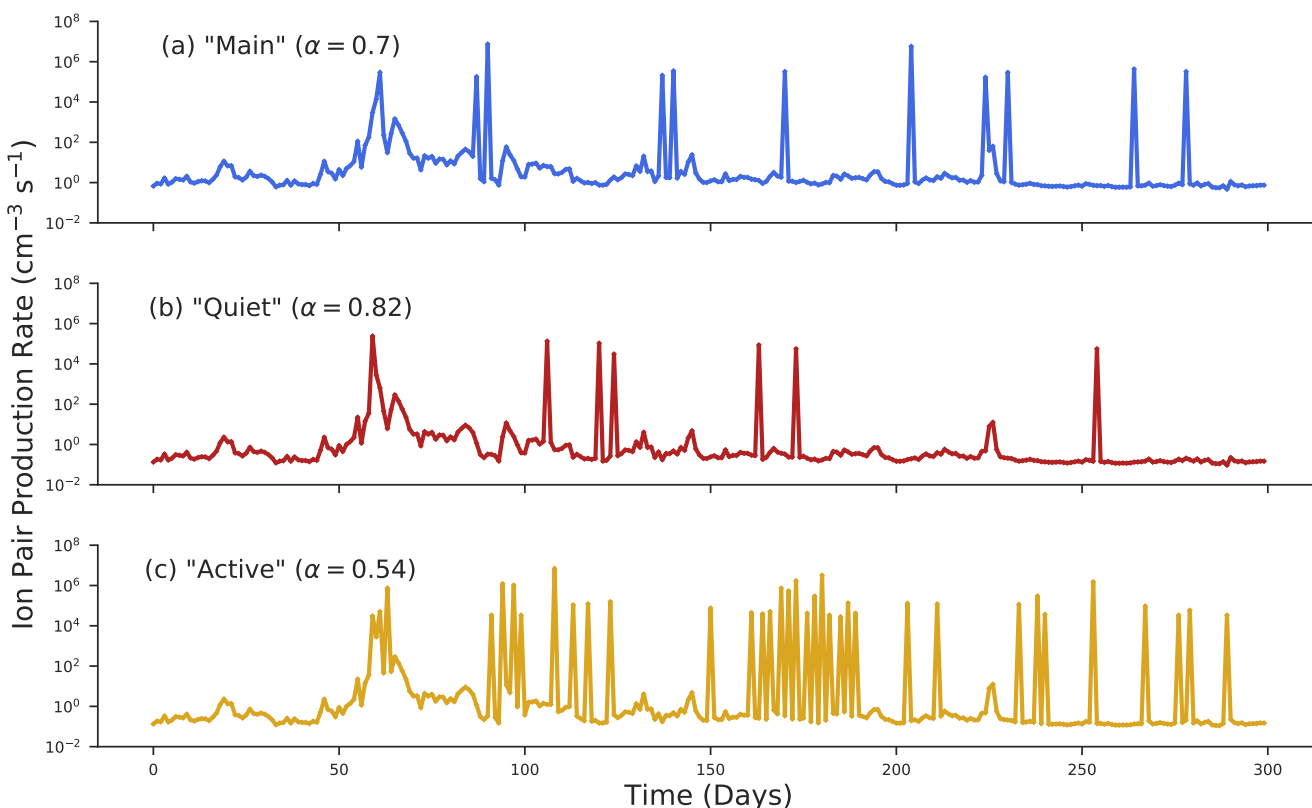
Figure 4.5.3: Three scenarios of vertical-mean ionization rates used as inputs to explore the effects of flare frequency. Three different assumptions are investigated: $\alpha = 0.7, 0.82, 0.54$.

4.6 Methods

The U.S. National Center for Atmospheric Research (NCAR) Whole Atmosphere Community Climate Model (WACCM) was employed to simulate planetary atmospheres. Synthetic and observed flare timeseries and UV spectra are used as inputs to the climate model. Atmospheric transmission and emission spectra are computed using a radiative transfer model with updated molecular line-lists.
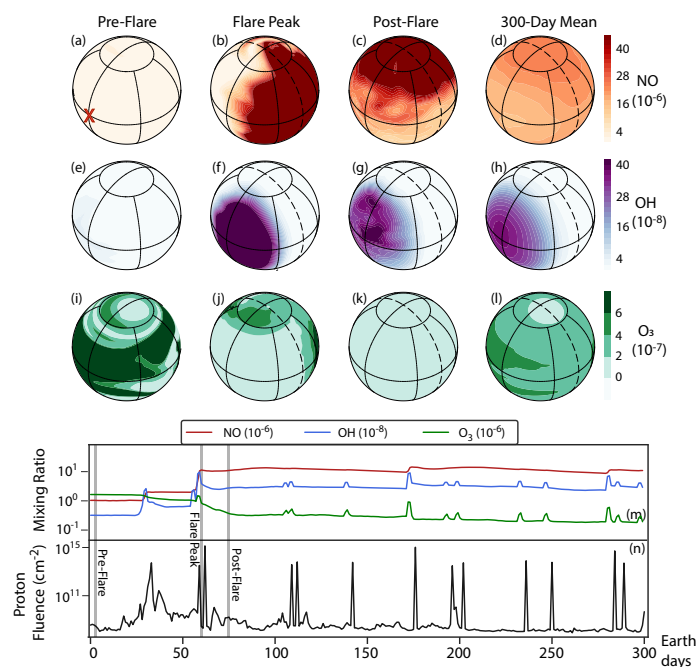
Figure 4.5.4: Spatial and temporal atmospheric effects of repeated stellar flaring on an M-star planet. Simulated global time slice distributions of upper atmospheric NO (a-d), OH (e-h), and O_3 (i-l) concentrations and their global average time-series (m) that result from exposure to flares with time-evolving proton fluences (n). The simulated planet rotates around M-star TRAPPIST-1 synchronously and has a weak magnetic field. and OH mixing ratios are reported at 0.1 hPa, whereas O_3 mixing ratios are reported at 1.0 hPa. Spherical projections are centered on 40° N latitude and 225° longitude. Red cross denotes the substellar point.

4.6.1 Chemistry-Climate Model

To simulate planetary atmospheres, we employ WACCM [229, 252], a high-top version of the Community Earth System Model v1.2, developed by NCAR. The model solves the primitive equations of fluid dynamics and thermodynamics, and includes self-consistent coupling of dynamics, chemistry, radiation, and thermodynamics. We use the Community Atmosphere Model v4 (CAM4) with the following modules: Community Atmospheric Model Radiative Transfer (CAMRT) radiation scheme [375], the Zhang-McFarlane scheme for deep convection [374], and the Hack scheme for
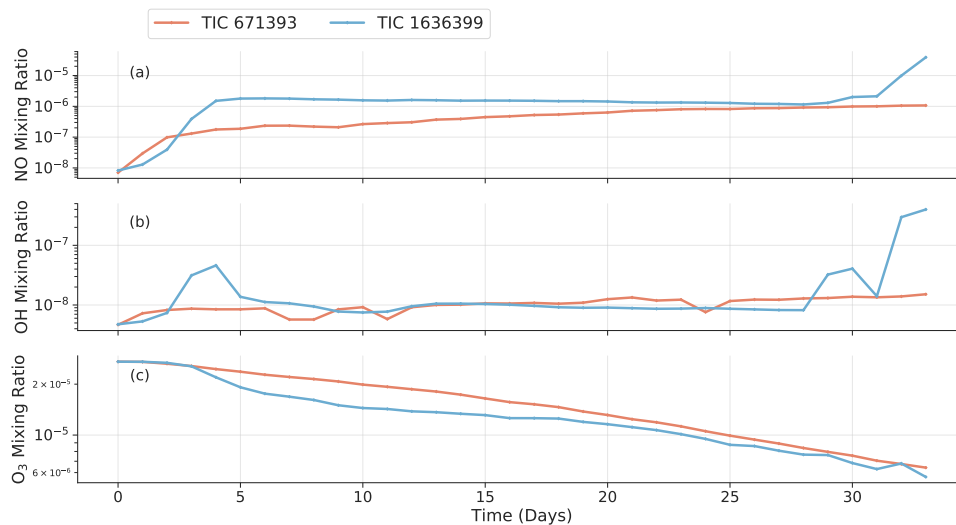
Figure 4.5.5: Temporal evolution of global-mean mixing ratios of NO, OH, and O_3 experiencing *TESS* flares. Result demonstrate that small flares over a short timespan do not substantially affect exoplanetary atmospheres. NO and OH mixing ratios are reported at 0.1 hPa, whereas O_3 mixing ratios are reported at 1.0 hPa.

shallow convection [123]. The chemistry model is version 3 of the Modules for Ozone and Related Chemical Tracers (MOZART) chemical transport model [179], which includes neutral and ionic constituents linked by 217 reactions. All surface gas fluxes are fixed at 1850 pre-industrial values, as industrial emission (e.g., nitrogen oxides; [245]) can affect surface chemistry. Note the small differences between exoplanet chemical model predictions [54, 369], suggesting the need for further model comparison efforts.

The oceanic model is a 30-meter thermodynamic "slab" model with heat diffusion but no advection. The Community Land Model (CLM) v4 is used to model modern Earth continental configurations including pre-industrial surface features (e.g., vegetation, land type, and albedo). Excluding ocean dynamics is appropriate for this study as we are primarily interested in photolytic and ion chemistry, processes that primarily take place above the stratopause. Moreover, ocean heat transport on tidally locked worlds is minimized by the North-South oriented continental configu-
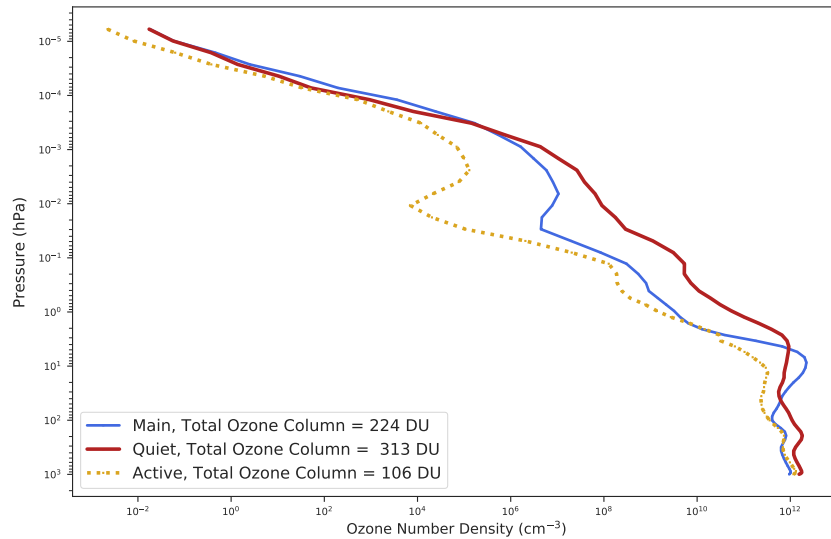
Figure 4.5.6: Global-mean vertical profiles of ozone number density at three different stellar flare frequencies. These results show the cumulative effect (300 Earth days) of repeated stellar flares. Results that assume α approaching those of observed MUSCLES stars ($\alpha = 0.7$) established a new chemical equilibrium, whereas those using values close to very active stars ($\alpha = 0.54$) have their ozone layers rapidly depleted.

ration [50, 367], or by the presence of an equatorial super-continent [288]. 3D climate simulations with a coupled dynamic ocean model of Proxima Centauri b show that an Earth-like continental setup eliminates day-to-night ocean heat transport, and the resulting global climate states are little changed compared to that found using a shallow slab ocean aquaplanet configuration with no dynamic heat transport [72].

We used the finite-volume dynamical core and horizontal resolutions of $1.9^o \times 2.5^o$ (144×96 number of grid cells). The vertical domain extends from the surface at 1013.25 hPa to model-top at 5.1×10^{-6} hPa (145 km) with 66 levels. The vertical resolution is between 0.5-2 km in the troposphere and stratosphere and $\sim$0.5 scale height above the stratosphere. All simulations are integrated for at least 30 Earth years. Each simulation with the inclusion of flares and stellar proton events (SPEs) are then branched off from the final year and run for an additional 300 Earth days.

All simulations adopt a model timestep of 900 seconds (15 minutes).

WACCM is configured to simulate synchronously-rotating planets trapped in 1:1 spin-orbit resonance. For each climate scenario around HD85512 (K6V; [111]) and TRAPPIST-1 (M8V; [297]), the planet is placed at an orbital separation where the total incident TOA stellar flux is equal to that received by present-day Earth. The planetary rotation period is then set according to the stellar mass and luminosity Kepler's 3rd law [190]. In all simulations, the orbital parameters (obliquity, eccentricity, and precession) are set to zero and the planets have 1 Earth-radius and 1 Earth mass. Continental configuration, topography, and surface albedo assume values of present-day Earth. The substellar point is placed over 180° longitude. Earth's quasi-biennial oscillation, which is an observed alternating forcing between easterly and westerly zonal winds, is turned off.

To gauge how different atmospheric compositions respond to stellar activity, we simulate three different scenarios: (i) An "O_2-rich" atmospheric composition (primary focus of the main text), i.e., pre-industrial Earth with N_2 (78% by volume), O_2 (21%), CH_4 (0.701 ppmv), N_2O (0.273 ppmv), and CO_2 (288 ppmv). ii) a Proterozoic-like atmosphere with very low O_2 concentrations (1% Present Atmospheric Level (PAL)) to test the abundance of flare-modulated oxide compounds, though the extent to which O_2 could influence a planet's climate is controversial [262, 270, 342], and (iii) a moist greenhouse atmospheric composition in which the decrease of tropospheric lapse rate and the expansion of the moist convection zones lead to the displacement of the cold trap to higher altitudes. Emergent moist greenhouse conditions are produced following the methodology of previous work [190], where we incrementally increase the incident stellar flux just prior to the onset of the incipient runaway greenhouse phase [355]. The moist greenhouse scenario receives 1.9 times the present Earth's insolation, uses the stellar spectral energy distribution of HD85512, and has global-mean stratospheric H_2O mixing ratio of 1.28×10^{-3}. In all four scenarios, H_2O_v and O_3 are spatially and temporally variable but are initialized at pre-industrial Earth values.

In addition to WACCM's high model top, its radiative transfer scheme includes non-LTE processes allowing for a more realistic assessment of the effects of stellar flares. In the MLT region, radiative transfer and dynamics are based on the thermosphere-ionosphere-mesosphere electrodynamics (TIME) GCM [279]. Key processes included are: neutral and high-top ion chemistry (ion drag, auroral processes, and solar proton events) and their associated heating reactions. Molecular diffusion via gravitational separation of different molecular constituents [18] is an extension to the nominal diffusion parameterization in CAM4. Below 65 km (local minimum in shortwave heating and longwave cooling), WACCM retains CAM4's radiation scheme. Above 65 km, WACCM expands upon both longwave (LW) and shortwave (SW) radiative parameterizations from those of CAM3 and CAM4 [62]. WACCM uses thermodynamic equilibrium (LTE) and non-LTE heating and cooling rates in the extreme ultraviolet (EUV) and infrared (IR) [94]. In the SW (0.05 nm to 100 μm; [201, 319, 347]), radiative heating and cooling are sourced from photon absorption, as well as photolytic and photochemical reactions. The native broadband radiation model of CAM4 is employed and not the newly introduced IR absorption coefficients [191]. Such treatment is appropriate at temperatures $150 < T < 340$ K, which is the primary regime of interest in this study.

4.6.2   Planetary Magnetic Field Assumptions

To test the influence of a gravitational field on the global incident charged particle distribution, we parameterize the presence of planetary-scale magnetic fields as follows:

a) Magnetized Scenario: Protons are injected at polar latitudes ($> 60^o$) across all longitudes, as incident particles are guided by the magnetic field lines to higher latitudes. This means that both the day and nightside receive comparable proton fluences due to the deflection geometry.

b) Weakly or Anomalously Magnetized Scenario: Protons are injected a three different areas, with the assumption that the magnetic field's direction fluctuates wildly and originates from several poles. i) between 30° and 60° latitude, 120° and 240° longitude, ii) between -30° and -60° latitude, 120° and 240° longitude, and iii) between 30° and -30° latitude, 300° and 60° longitude.

c) Unmagnetized Scenario: Protons are directly injected on the substellar hemisphere between 90° and 270° longitude. No magnetic field deflection occurs in this scenario.

In all the above cases, the vertical distribution of ion pair production rate (i.e., the proton spectrum) is based on Earth observations by Michelson Interferometer for Passive Atmospheric Sounding (MIPAS) instrument and the Geostationary Operational Environmental Satellite (GOES)-11 during the October 31st 2003 geomagnetic storm [154, 216]. Calculation of self-consistent particle energy spectra (e.g., [114, 324]) and FUV emissions relationships will be conducted in future work.

4.6.3 Stellar Spectra

Effects of stellar activity across three spectral types are investigated: G, K, and M. For G-star simulations we use an observed and reconstructed solar irradiance spectrum [202]. The input spectrum version is fixed in the year 1850 and no observed irradiance cycle is included. For K- and M-stars, two spectral types that bracket the endmember range of low mass stars were used: i) TRAPPIST-1 (M8V; T_{eff} = 2511 K) data from the Mega-MUSCLES survey (Wilson et al. in review) and ii) HD 85512 (K6V; T_{eff} = 4715 K) stellar SED from the MUSCLES survey (https://archive.stsci.edu/prepds/muscles/; version 2.2; [96, 219, 370]). Both spectra are binned at 1 Angstrom resolution with negative-flux bins removed via iterative-averaging as statistical noise in the low-signal regions and the subtracted background level can result in negative fluxes. Presence of statistical noise in the signal and subtracted background levels necessitates this approach

[96]. Both stellar spectra are constant in time with exception of the FUV and NUV spectra (110-320 nm), which varies with the occurrence of flares (see below). We investigate wavelengths greater than 110 nm, which captures the $Ly - \alpha$ lines and FUV/NUV ranges that affect photochemistry (with peak ionization in the upper stratosphere at 0.1 to 0.01 hPa). Shorter wavelengths are not included for the sake of computational simplicity. But as soft X-ray and EUV wavelengths have peak ionization rates in the thermosphere and the ionosphere, they are unlikely to substantially perturb our conclusions in the stratosphere and mesosphere. One photosphere-only PHOENIX model is used. It assumes stellar metallicities of [Fe/H] = 0.0, alpha- enhancements of [α/M] = 0.0, surface gravity values log g = 4.5. This serves as a benchmark case for a lower-limit flux estimate in the UV regime [152]. In addition, we have benchmarked our M-star planet results against using the high energy TRAPPIST-1 spectrum reconstructed by Peacock et al. [263] and Turbet et al. [337].

While the described stellar SEDs provide steady state spectra of our fiducial stars, assessment of transient stellar emissions requires time-evolving spectra. To compute time-dependent flares, we utilize: i) an open source M-dwarf flare Python module based on a large-scale campaign to characterize stellar FUV evolution [220], and ii) observed stellar flares identified by a convolutional neural network from *TESS* data [93]. Proton fluence calculations are derived from these flares [371]. To isolate the roles of changes in rotation period and magnetic field strength assumptions, all CCM experiments described are subjected to the same stellar flare timeseries inputs (e.g., Figure 4.2.1). Realistically however, the amplitude and frequency of stellar flares correlates with the effective temperature of the host star [41] and the orbital semi-major axis of the planet [114, 304]. While we assume all flares are "direct-hits" upon the attendant planet, future work should employ probabilistic CME impact models to better improve realism of input flare energy and impact frequency [172].

A stochastic flare model based on the Measurements of the Ultraviolet Spectral Characteristics of Low-mass Exoplanetary Systems (MUSCLES) Treasury Survey V [220] is used to generate UV

lightcurves. The MUSCLES Survey (HST observing program 13650) characterized the radiation environment of low-mass stars including the X-ray, XUV, and FUV, and NUV fluxes [96]. The flare model is based on observed data from two stellar populations [220]: the MUSCLE M-dwarf sample and four active stars Proxima Centauri, AD Leo, EV Lac, and AU Mic. Each flare lightcurve is represented by a box car function followed by an exponential decay, simplified from the complex observed behaviors (e.g., multiple, sustained peaks) of flares. This model is used to generate a series of flares with equivalent durations δE drawn from a power-law distribution (typical of observed flares; [131]), where δE is defined by:

$$\delta_E = \int \frac{F_f - F_q}{F_q} dt \tag{4.1}$$

where F_f is the flare flux, F_q is the quiescent flux, and dt is the flare duration.

To get the flare electromagnetic spectra, quiescent UV spectra of each stellar SED are multiplied by the active-to-quiescent flux ratio given by the model (though we note that SPEs are found to be responsible for $\sim$99% of the flare effects; [304, 332]). All flares assume blackbody temperatures of 9000 K, consistent with estimated color temperatures of M-dwarf flares between 7700 and 14000 K [193], though M dwarf flares at much hotter temperatures have been observed [98, 221].

The flare occurrence rate v is given by [220]:

$$v = \mu \left(\frac{\delta_E}{\delta_{\text{ref}}} \right)^{-\alpha} \tag{4.2}$$

where μ is the rate constant, δ_{ref} is the reference equivalent duration value ($\delta_{\text{ref}} = 1000$ s), and α is the power-law index. Three different values of α, 0.82, 0.7, and 0.54 are tested. All synthetic flares are assumed to have equivalent durations between 10^6 and 10^9 seconds. Flares with equivalent

durations of 10^4 secs are close to the largest observed flare [220], so our flares are based on power-law extrapolations. Flares below total energy of 10^{30} ergs and equivalent durations of 10^6 secs are omitted. The choice of equivalent duration range (i.e., between 10^6 and 10^9) also reflects typical equivalent durations of flares observed in the *U* and *Kepler* bands [131, 139].

Apart from utilizing the aforementioned stochastic flares, we use flares observed by the *Transiting Exoplanet Survey Satellite* (*TESS*), which is a five-year photometric survey covering $\sim 80\%$ of the observable sky [278]. Due to the time resolution necessary for observing stellar flares, we chose to search $\sim$100 pre-selected light curves based on their effective temperatures (i.e., between 3000 and 4000 K). The 2-minute light curves are hosted on the Mikulski Archive for Space Telescopes (MAST) and were downloaded using the `lightkurve` package (https://docs.lightkurve.org/). The two objects shown are TIC 671393 and TIC 1636399 where TIC denotes the *TESS* Input Catalog IDs. TIC 671393 has stellar mass of 0.54 $M_\odot$, stellar radius 0.548 $R_\odot$, and effective temperature 3096 K. TIC 1636399 has stellar mass of 0.53 $M_\odot$ stellar radius $0.537 R_\odot$, and effective temperature 3266 K. We identified a total of 61 flares for TIC 671393 over the 25 days of observation time and 21 flares for TIC 1636399 over 24 days.

To ensure completeness in flare energies, we follow the methods of previous work [93] for flare identification. They trained a convolutional neural network (CNN) on a previously created flare catalog [122] and use the CNN as a sliding-box detector, where the "probability" of a data point is part of a flare increases to 1 when a flare is within the sliding-box. As such, we "predict" where flares occur using these models. Flare amplitudes and equivalent durations were calculated by fitting a Gaussian rise and exponential decay profile on a local region of the light curve around the flare. Use of CCN is advantageous as it can identify both large ($\delta > 10^6$ s) and small flares ($\delta < 10^4$ s). While the former is the focus of this study, small flares have important cumulative effects over longer timescales. All code used is part of the open-source `stella` Python package [92].

Previous multi-wavelength observations of stellar activity suggest that optical events can serve as proxies for the initial heating of the chromosphere, as optical flares are found to precede the X-ray, EUV, and UV flares of the impulsive phase [120, 320]. Thus while the *TESS* data do not provide UV spectra, we assume that the UV flare frequencies over the course of > 20 days are qualitatively similar to those in the observed IR and optical. Simulations that use the *TESS* data as inputs assume TRAPPIST-1 steady stellar SED from the Mega-MUSCLES survey (Wilson et al. in review).

Incident charged particles of stellar origin are associated with large flares and CME-like events [14, 109, 313]. While direct observations of energetic particle emissions during CMEs are not available (i.e., only signatures of CMEs are observable; [97]), we follow previous studies by using solar scalings based on near-Earth satellite data. We assume that all of the particles are protons. We compute the expected peak proton fluences from the SiIV energy of stellar flares [371]:

$$\log F_{>10 \text{ MeV}} = 1.20 \log F_{\text{SiIV}} + 3.27 \qquad (4.3)$$

where $F_{>10 \text{ MeV}}$ is the proton fluence. The derived fluences all follow the M-dwarf flare model generated lightcurve shapes/durations. Since there is a linear relationship between the proton flux and production rate of ion pairs [154], we scaled the input ionization rates comparing our estimated proton fluence with that of 2003 Halloween SPE (an order of magnitude lower than the Carrington event in 1710; [154, 216]). The ion pair production rates, provided in the Solar Influence for SPARC (SOLARIS) website (https://solarisheppa.geomar.de/solarprotonfluxes; newly updated in March 2019) and derived from proton flux measurements by GOES 11 instrument, are then applied as daily averages during each flare peak. Daily cadences are appropriate in this pilot study as the cascading NO_x and HO_x reactions are much faster [88] than the flare and model timesteps, but future work should employ higher temporal resolutions to better resolve stellar activity on hourly

timescales (e.g., [266]).

Other methods to calculate ionization rates due to stellar flares or galactic-sourced cosmic rays e.g., the air-shower approach [114], have shown to compare well with the approach taken here and those in prior studies [304]. Note that the majority of stellar and exoplanetary studies uses the same peak size distribution functions from solar events [27, 60]. However, large discrepancies exist between published peak size distributions due to the different underlying physical mechanisms driving these events [138]. Thus the conclusions established from photochemical models, even with the same flare inputs, would likely be contingent upon the specific function used.

4.6.4   Stellar UV and Proton Event Initiated Atmospheric Chemistry

WACCM includes a range of chemical reactions necessary to fully account for the effects of stellar activity. Interaction of UV photons with trace gases typically lead to dissociation via photolysis [157]:

$$H_2O + h\nu(175 < \lambda < 200nm) \rightarrow H + OH \tag{4.4}$$

$$O_3 + h\nu(\lambda < 320nm) \rightarrow O_2 + O(^1D) \tag{4.5}$$
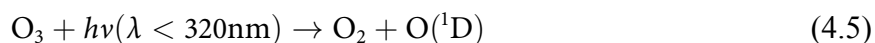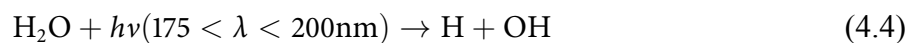
Some important daytime(side) photochemical reactions are [16]:

$$O(^1D) + H_2O \rightarrow 2OH \tag{4.6}$$

$$HO_2 + NO \rightarrow H + NO_2 \tag{4.7}$$

$$NO_2 + h\nu(\lambda < 420\text{nm}) \rightarrow NO + O(^3P) \tag{4.8}$$

Particle precipitation due to SPEs also influence atmospheric chemistry. SPEs produce charged particles (protons and secondary electrons) that causes excitation and subsequent dissociation of ambient gaseous constituents. Ground state and excited state nitrogen are produced via [155, 269]:

$$N_2 + e^- \rightarrow 2N(^4S) + e^- \tag{4.9}$$

or

$$N_2 + e^- \rightarrow 2N(^2D) + e^- \tag{4.10}$$

where e^- represents secondary electrons produced by incident protons. We assume that 1.25 N atoms are produced per ion pair (specifically 0.55 $N(^4S)$ ground state atoms and 0.7 $N(^2D)$ excited state atoms; [269]).

Excited and ground state nitrogen can subsequently produce NO via:

$$N(^2D) + O_2 \rightarrow NO + O(^3P) \tag{4.11}$$

$$N(^2S) + O_2 \rightarrow NO + O(^3P) \tag{4.12}$$

or remove NO via:

$$N(^2S) + NO \rightarrow N_2 + O(^3P) \tag{4.13}$$

Two HO_x species are produced per ion pair. Parameterization of prognostic ionic water cluster reaction networks is done via:

$$H_2O + Ion^+ \rightarrow H + OH + Ion^+ \tag{4.14}$$
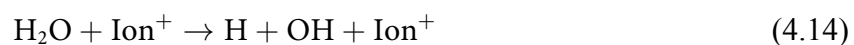
Increase HO_x species lead to catalytic ozone destruction in the stratosphere via [313, 317]:

$$OH + O_3 \rightarrow HO_2 + O_2 \tag{4.15}$$

$$HO_2 + O \rightarrow OH + O_2 \tag{4.16}$$

and the mesosphere via:

$$H + O_3 \rightarrow OH + O_2 \tag{4.17}$$

$$OH + O \rightarrow H + O_2 \tag{4.18}$$

While OH and H are act on on short timescales ($\sim$ hours), the prolonged lifetimes of NO_x species can deplete stratospheric ozone via:

$$NO + O_3 \rightarrow NO_2 + O_2 \tag{4.19}$$

$$NO_2 + O \rightarrow NO + O_2 \tag{4.20}$$

Apart from contributing to ozone loss, enhanced NO and OH during large stellar flares can also modulate the abundance of other important biosignatures and habitability indicators (see e.g., [137, 294]). Example reactions are:

$$N + NO_2 \rightarrow N_2O + O \tag{4.21}$$

$$NO_2 + OH + M \rightarrow HNO_3 + M \tag{4.22}$$

$$CH_4 + OH \rightarrow CH_3 + H_2O \tag{4.23}$$

where NO_2 can be photochemically derived from the cascading N_2 dissociation initiated by SPEs, where OH can come from water vapor photolysis, ion chemistry, and reaction between H_2O +

$O(^1D)$. N_2O can also be produced from the reaction between NO and NH.

4.6.5 Atmospheric Spectroscopy Model

To translate WACCM output into observable predictions, we use the Simulated Exoplanet Atmosphere Spectra (SEAS) model (Zhan et al. in press) to compute atmospheric spectra. SEAS is a radiative transfer code that calculates the attenuation of photons by molecular absorption and Rayleigh/Mie scattering as the photons travel through a hypothetical exoplanet atmosphere. The simulation approach is similar to previous work [175, 244]. The molecular absorption cross-section for O_2, H_2O, CO_2, CH_4, O_3, and H are calculated using the HITRAN2016 molecular line-list database [110]. The SEAS transmission spectra are validated through comparison of its simulated Earth transmission spectrum with that of real Earth counterparts measured by the Atmospheric Chemistry Experiment (ACE) data set [32]. For more details on SEAS, please see Section 3.4 in Zhan et al., (in press).

Mixing ratio contrasts of various gases between the day and nightside are defined as [54]:

$$C_{\text{diff}} = \frac{C_{\text{day}} - C_{\text{night}}}{C_{\text{globe}}} \tag{4.24}$$

where C_{day} is the dayside hemispheric mixing ratio mean, C_{night} the nightside mean, and C_{globe} the global mean. We compute C_{diff} by vertically-averaging the mixing ratios between 1 and 1×10^{-4} hPa.

The column number density of species i is defined as:

$$N_i = \int n_i dz \tag{4.25}$$

where n_i is the volume number density of species i and z is the vertical coordinate. Here, we compute the total ozone column by summing up the volume number density in all 66 levels. The number density of ozone in each level is calculated via:

$$n_{O3} = C_{O3} \frac{N_A P_i}{R T_i} \tag{4.26}$$

where C_{O3} is the mixing ratio of ozone, N_A is the Avogadro's number, R is the gas constant (8.31 J mol^{-1} K^{-1}), and P_i and T_i are the atmospheric pressure and temperature at level i. The total ozone column is typically expressed in Dobson Units (DU). 1 DU = 2.686×10^{20} m^{-2} or 2.686×10^{16} cm^{-2}.

4.6.6 Acknowledgements

Figure 4.5.7: Zonal mean of zonal wind, O_3 mixing ratios, and meridional circulation stream functions for hypothetical O_2-rich planets around a G-star, K-star, and M-star as denoted. Results demonstrate the convolved effects of dynamics and atmospheric chemistry.
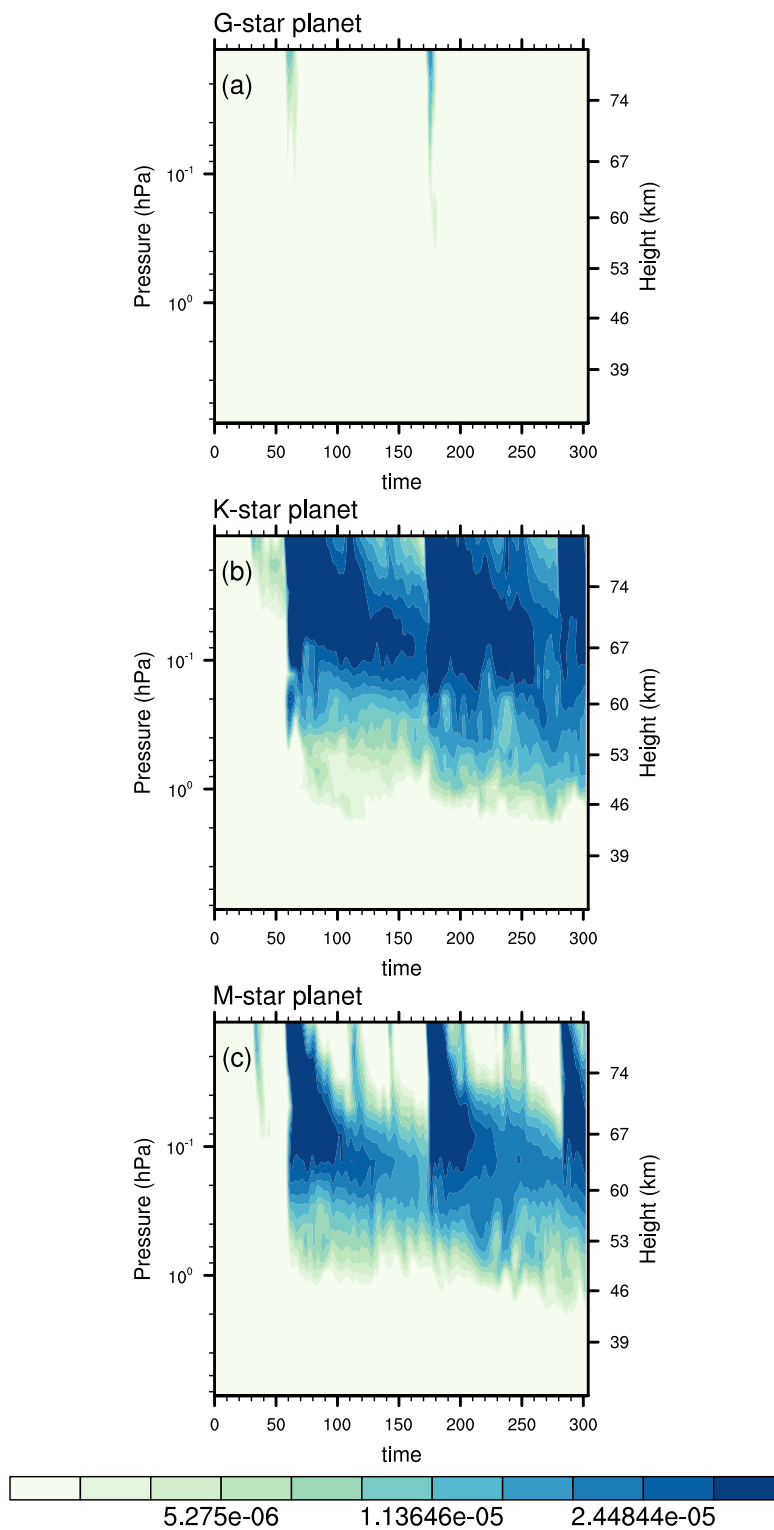
Figure 4.5.8: NO concentration averaged over the poles (latitude$> 65^{\circ}$) as a function of time and pressure for hypothetical O_2-rich planets. The rotation periods of these simulations are 24 hours, 92 Earth days, and 4.32 Earth days around a G-dwarf (a), K-dwarf (b), and M-dwarf (c) star. Note the $\log_{10}$-scale.

Chapter 5

Modulation of Water-Loss Timescales by Planetary Oxygenation Levels

5.1 Abstract

The moist greenhouse "water-loss limit" delineates the pessimistic inner edge of the habitable zone, and depends on the abundance of water vapor in the stratosphere. Previous numerical modeling work has shown that the incident stellar flux needed to reach this limit depends on the surface water distribution, global volatile inventory, atmospheric mean molecular weight, and model dimensionality. Here, we show that these limits are also strongly modulated – by up to 20% – by the oxygenation state of the planet. Using a 3D chemistry climate model, we conducted simulations of rapidly-rotating dry planets and slowly-rotating wet planets at the IHZ edge. We find a positive correlation between the specified O_2 and resultant H_2O mixing ratios, as the CH_4-OH reaction becomes a strong source of stratospheric water vapor in strongly-oxygenated dry atmospheres. On wet and slowly-rotating planets however, we find that the stratospheric water vapor and thermo-

spheric hydrogen mixing ratios change non-monotonically with each increase in oxygenation level. The reduction in O_2 and O absorption of UV fluxes leads to rapid water vapor photodissociation. For these moist greenhouse climates the most oxygen-depleted simulation has the highest rate of atomic hydrogen production and escape, a result that has strong implications for long-term liquid water surface stability.

5.2   Introduction

Near-term and future observatories are poised to characterize terrestrial exoplanetary atmospheres, which may offer clues to their chemistry, geology, and habitability. Within a few months from today, the James Webb Space Telescope (JWST) will launch with a goal of searching for transiting planets around cool stars. Many systems with planets at the inner edge of the habitable zone will be some of the first targets for these future instruments. It is estimated that, during the 10-year cyrogenic lifetime of JWST, it will have an opportunity to observe a total of 63 transits of the TRAPPIST-1e [223]. In addition, in the next 1-2 decades, flagship direct imaging missions, largely offsprings of the Terrestrial Planet Finder (TPF-C), will be primed to search for biosignatures on potentially habitable worlds in a wide range of orbital configurations (e.g., Gaudi et al. 102).

Conventional theory states that the moist greenhouse water-loss limit should be used as the pessimistic inner edge of the habitable zone (IHZ; Kasting 163). Interior to the IHZ, runaway or incipient runaway greenhouse states preclude habitability and planetary surface in this regime are destined to lose the majority of their water inventory. Although climatically stable, moist green-house phases could prompt rapid losses ($\sim$Gyrs) through diffusion-limited escape [167, 353]. This limit is, in essence, determined by the rate of water vapor escape, which is in turn dependent on the rate of water vapor updraft to altitudes where it can be efficiently photodissociated. Because water

vapor concentration at these levels depends on the specific stellar spectral energy distribution, IR heating, and vertical transport, modeling tools such as three dimensional (3D) general circulation models (GCM) can predict H_2O mixing ratios and their feedbacks with surface climate [55, 99].

Previous climate modeling efforts to calculate the inner edge of the habitable zone provided reliable estimates of the span of allowable global water inventory for a planet at a given orbital distance [163, 353]. However, these calculations focused on lifeless planets that had not experienced significant oxygenation instigated by complex metazoans and photosynthetic life. For these life forms, the tolerable P and T conditions are likely much more stringent, leading to a narrower complex life habitable zone (CLHZ; Schwieterman et al. 299. On a planet inhabited by complex life capable of oxygenating photosynthesis, continual habitability is contingent upon the retention of key atmospheric gases such as O_3 [239]. Furthermore, habitability metrics are often influenced by stellar activity processes and atmospheric dynamics, many of which are three-dimensional in nature. Thus, how a planet's atmospheric and chemical constituents, when subjected to stellar and dynamical influences, can vary with different planetary parameters warrants further investigation.

A planet's composition, specifically that of its atmosphere, is crucial in planetary habitability but remains largely an unknown factor, particularly for small planets. Prevailing 3D climate models typically explore paradigm climate archetypes such as Modern Earth, Archean Earth, and Martian/Venusian CO_2-rich atmospheres (e.g., Fauchez et al. 91, in which an equilibrium experiment for each paradigm case is conducted. For instance, targeted planet GCM studies tested the effects of varying CO_2, N_2, and surface partial pressures on their long term averaged surface temperature and observational potential [351, 358]. Using GCM outputs along with a well validated retrieval framework, May et al. [235] showed that different CO_2 partial pressures may lead to ice cloud variability, affecting the observable transmission spectra. Previous exoplanetary GCMs have not assessed the effects of different O_2 partial pressure and concentration, and implicitly, the potential variations in the oxygenation states of young (1-2 Gyr), middle aged (2-4 Gyr), and fully

developed (>5 Gyr) exoplanet ecospheres.

However, the degree of planetary oxygenation is expected to vary amongst terrestrial exoplanets. The inherent stochasticity in planetary accretion/formation outcomes can determine the initial redox state of a protoplanet [292]. Subsequent geophysical and biological evolution such as oxygenating photosynthesis and geochemical feedbacks can further alter the global oxygen budget over $\sim$Gyr timescales [224]. Understanding how different O_2 Levels can affect the stability of temperate climates and observational fingerprints is therefore crucial for upcoming observatories.

Molecular oxygen is a persistent feature of an active biosphere and may indicate the emergence of photosynthetic life (see review by Meadows et al. 239). Our familiarity with O_2 behavior and its significance on biosignature detection substantially increases the likelihood for its successful retrieval and validation in extrasolar environments. However, the associated global consequences of different oxygenation states is less clear and has not been studied for planets around different stellar spectral types. Here, we use a coupled 3D chemistry-climate system model to investigate the effects of different planetary oxygenation levels on the lifetimes of surface liquid water of terrestrial exoplanets. Our study also aids in the delineation of the CLHZ [299], which has only appeared in the literature in the past year and has become increasingly important to investigate.

5.3 Numerical Model & Approach

Using the U.S. National Center for Atmospheric Research (NCAR) Whole Atmosphere Community Climate Model (WACCM), we simulate hypothetical exoplanets with a range of oxygenation and moisture levels. Our numerical setup employs one of WACCM's component set-the F-compset. Specifically, we use the Community Atmosphere Model v4 (CAM4;Collins et al. 62), the Modules

for Ozone and Related Chemical Tracers (MOZART) chemical transport model version 3 [179], but replace the default diagnostic data ocean with a thermodynamic slab ocean with zero prescribed heat transport. For a more detailed description of the out-of-the-box version of the Earth-system model, see Neale et al. [252] and Marsh et al. [229]. In our six template climate scenarios, three different levels of initial oxygen concentration are explored: $10^{-4}, 10^{-2}$, and $1\times$ PAL, encompassing a reasonable span of O_2 level estimates for early Earth, i.e., 2.5 Ga (Proterozoic) to 0 Ga (Phanerozoic). These oxygen concentrations are specified at the start of each simulation and are then allowed to freely evolve. Lower oxygen level climates such as during the Archean and Hadean eras contain too little oxygen for our chemical module computations, as WACCM was originally written for modern Earth research. Calculations of Proterozoic O_2 levels widely disagree [256, 277], as model derived and geochemical records indicate values ranging from 10^{-4} to 10^{-1}PAL [261]. Nonetheless, the estimated O_2 range based on Earth history informs the values chosen by our study.

Other gas species included are N2 (78% by volume), O_2 (21%), CH_4 (0.701 ppmv), N2O (0.273 ppmv), and CO_2 (288 ppmv). The amount of H_2O at any given time is determined by the saturation vapor pressure, whereas the amount of O_3 is determined by photochemical equilibrium established via the Chapman cycle and the smog mechanism. CH_4 and N2O have fixed lower boundary mixing ratios, consistent with measurements of modern Earth [179]. We adopted horizontal resolutions of $1.9^o \times 2.5^o$, corresponding to 144×96 number of grid cells. The vertical domain has 66 levels and extends from 1013.25 hPa to $5.1 \times 10\text{-}6$ hPa (or model top of $\sim$145 km) using hybrid σ coordinates. We set the orbital parameters of all simulated climates (obliquity, eccentricity, and precession) to zero, but kept the planet size, continental configuration, and topography the same as modern Earth. All simulations are integrated for at least 30 Earth years, which is the model time typically needed to achieve top-of-atmosphere (TOA) radiative balance. Unless otherwise stated, all results shown are averaged over the last 10 years.

Stellar spectral energy distributions of a G- and M-dwarf are used to drive the chemistry climate

of the attendant planets. For the G-dwarf, we use a reconstructed irradiance spectrum from the Sun [201], fixed in the year 1850 without the inclusion of solar cycles. For the M-dwarf, we used a reconstructed TRAPPIST-1 spectrum with observed UV wavelengths [350]. The spectrum is binned at 1 Angstrom resolution with negative flux bins removed via iterative averaging as statistical noise in the low-signal regions and the subtracted background level can result in negative fluxes.

We study G-dwarf and M-dwarf planet archetypes orbiting in the inner edge of the habitable zones of their respective star. The G-dwarf planet assumes 24-hr rotation period and receives a stellar flux of 1365 W m^{-2}. The M-dwarf planet is synchronously rotating, i.e., trapped in 1:1 spin-orbit resonance. Planets at the IHZ of M dwarfs orbit at higher rotation periods and allow moist greenhouse atmospheres to remain climatically stable (see also Kopparapu et al. 191. Moist greenhouse climates are characterized by a decrease of tropospheric lapse rate and the weakened efficiency of the cold trap, stemming from the dramatic expansion of the substellar moist convection zones. The naming convention in this study is as follows: Moist greenhouse atmosphere simulations driven by high stellar flux is hereafter denoted as the 'moist climates', and are defined when the stratospheric specific humidity is greater than $\sim 10^{-3}$. Temperate atmosphere simulations with Earth-similar stellar flux have much lower humidities (typically $< 10^{-4}$), and are denoted as the 'dry climates')

Our moist climates are not prescribed but emerge self consistently from the increase in dayside stellar insolation. To produce moist greenhouse atmospheres, we dial up the instellation until the global mean water vapor mixing ratio has reached at least 10^{-3}, but prior to the onset of the incipient runaway greenhouse [355]. For our simulated climates around M-dwarfs, this stellar flux corresponds to 1.9 times Earth's present insolation or 2585 W m^{-2}. For a more detailed description of the numerical model and experimental setup of the tidally-locked planet, refer to Chen et al. [55] and [56].

5.4   Results

Our CCM results, represented by the horizontally averaged, global mean vertical profiles of molecular oxygen, ozone, and water vapor mixing ratios (Figure 5.2.1), show that these atmospheric constituents are strongly modified by the stellar and climate forcing inputs. First, we find that steady-state vertical O_2 profiles are aligned with their initial starting conditions, with the exception of the scenarios with lowest amounts (10^{-4} PAL). However, the O_2 mixing ratios in the moist climates are higher than dry climates due to the weaker UV flux ($100 < \lambda < 280$ nm) of M-dwarfs and hence lower O_2 destruction. Vertical profiles of water vapor mixing ratios primarily depend on surface temperature and relative humidity profile. In the dry and temperate climates, H_2O mixing ratios are on the order of $\sim 10^{-5} - 10^{-6}$. In the moist greenhouse atmosphere, tropospheric H_2O mixing ratios reach between $\sim 10^{-3}$ and $\sim 10 - 2$ (panel b; Figure 5.2.1). Strong and persistent deep convection on the dayside hemisphere maintains this high moisture level by continuously lofting water vapor into the upper atmosphere (see also Kopparapu et al. 191 and Chen et al. 55).

Ozone, an important trace absorber of UV radiation and greenhouse gas, is produced by photochemical dissociation of molecular oxygen. At low O_2 concentrations , namely at 10^{-4} and 10^{-2} PAL, our results show that stratospheric O_3 (at around 1 hPa) has a strong non-linear dependence on O_2 in both dry and moist climates. For instance, as the O_2 levels rise above 10^{-2} PAL, the corresponding increase in O_3 halts. At pressures below the stratosphere (> 1 hPa), O_3 production is limited by OH from reaction between H_2O and $O(^1D)$ and H_2O photodissocation. This result is consistent with previous terrestrial photochemical studies (e.g., Segura et al. 302), where they have found a typical O_2 threshold to establish a robust O_3 layer to be 0.1 bar. As shown by Checlair et al. submitted, this behavior could turn out to be beneficial for observations as O_3 builds up above the temperature minimum cloud deck for water and ice clouds. The moist climates (Figure 5.2.1) however, have a reduced rate of tropospheric O_3 increases as a function of O_2 mixing ratios.

In the mesosphere and lower thermosphere (MLT) region(< 10-1 hPa), O_3 remains low for lower amounts of O_2 for the dry climates, but then rapidly increases when the O_2 level reaches that of the present day (Figure 5.2.1a). For the moist climates, ozone mixing ratios remain low ($\sim 10^{-11}$) at all O_2 initiation levels (Figure 5.2.1b) in part due to enhanced catalytic reactions with upper atmospheric HOx and NOx. In particular, MLT ozone mixing ratios for 10^{-4} and 10^{-2} O_2 levels in the moist climates are comparable as the presence of odd hydrogen radicals increases due to elevated H_2O photodissociation. In the lower mesosphere/upper stratosphere (between 1 and 10^{-2} hPa), only the strongly oxygenated simulation has a sufficient O_2 reservoir to offset the presence of strong moisture and HOx induced removal.

The ocean loss timescale and surface UV flux are often used as important metrics to gauge a planet's habitability potential (see review by Méndez et al. 240). In the preceding description of our sensitivity experiments, we have shown that arbitrary and emergent differences in planetary compositions and thermal structures directly influence and/or feedback onto the model atmospheres at various depths. How might different oxygenation levels affect H_2O retention and ground-level UV dosages? In the following section, we turn to evaluating the long term habitability of our simulated climates using these metrics.

5.4.1   The Dependence of Ocean Lifetime and Global Ozone Column on Oxygen Level

The presence of a hydrosphere is one of the most important requirements for Earth-like life. We calculate water loss rates by adopting a version of the Jeans' diffusion-limited escape. This approach to approximate atmospheric escape, without the need to rely on detailed hydrodynamics (e.g., Tian et al. 331), is typically used to interpret climate model results (e.g., Kasting et al. 167, Wolf and Toon 353). Because we have simulated scenarios with lower amounts of O_2 compared to present

Earth, another question is whether sufficient ozone could be photochemically produced in these hypothetical climates. To answer this, we calculate the global ozone abundance using the total column density formula and compare them with present and ancient Earth.

Our estimates show that the planetary oxygen level can influence the water-loss timescale, namely the time required to remove the entirety of the planet's water reservoir, by modulating the amount of water vapor in the stratosphere. For dry climates, the water loss timescales decrease with decreasing amounts of O_2 (grey curve; Figure 5.3.1), reflecting the increasing amounts of water vapor photoylsis followed by hydrogen escape. For moist cases, conversely, the water loss timescale increases with decreasing O_2 amount (blue curves; Figure 5.3.1). The results suggest that younger and less oxygenated worlds orbiting Sun-like stars are likely farther from the IHZ boundary and thus more resilient to volatile losses.

In all our simulations, the final O_3 columns are directly proportional to the initialized amount of O_2. This is expected as the ozone production depends on concentration of atmospheric O_2 and photons in the UV bands between 170 to 240 nm. However, the change magnitude is different depending on the amount of atmospheric moisture. For dry cases, the global ozone number density decreases only slightly with incremental lowering of O_2 amount (grey curve; Figure 5.4.1). For moist cases, it decreases more drastically with lower O_2. This is due to the increase abundance of odd nitrogen and hydrogen radicals coupled with the elevated consumption rates of atomic oxygen through CO oxidation, thereby limiting O_2 recombination.

Previous work has shown that it is important to quantify whether the surface UV environments are tolerable for potential habitats (e.g., Kozakis et al. 194, Rugheimer et al. 285), especially for planets with lower O_2 fluxes and wet atmospheres in our experiments. In a follow-up work, we will calculate the UVB ($\lambda 280 - 315$ nm) and UVC ($\lambda 200 - 280$ nm) fluxes at the surface to gauge the efficiency of photochemically produced ozone layer in filtering UV radiation.

5.5 Discussion & Conclusions

In this Letter, we focused on the biosignature molecular oxygen (O_2), bio-1indicator ozone (O_3), and habitability indicator water vapor (H_2O). Changes in these species are assessed in context of different degrees of oxygenation and incident flux, drawing from stages throughout Earth history and self-consistent stellar flux orbital period relationships. Oxygen is a long recognized biosignature (e.g., Meadows et al. 239, Owen et al. 259, Sagan et al. 287, Schwieterman et al. 298).

One caveat relevant for our results is that detection of molecular oxygen on HZ exoplanets may not be robust signatures of biological activity. This is because of elevated abiotic oxygenation caused by the extremely luminous pre main sequence (PMS) phase of cool stars [222, 330]. For CO_2-rich atmospheres in particular, collision recombination can form O_2 from atomic oxygen as results of CO_2 photolysis [127]. In contrast, as the PMS of G-dwarfs and Sun-like stars emit much less high energy photons, our simulated dry climates around G-dwarfs will less likely experience large-scale desiccation, and hence reduce the likelihood for a potential false positive detection of O_2. IHZ dry climates around Sun-like stars are also advantageous in this regard as G-stars have lower FUV fluxes, higher MUV/NUV fluxes, and thus lower FUV/NUV ratios compared to M-stars, which suppresses excessive abiotic O_2 buildup on their IHZ planets [101, 127]. In the context of observations, this means that Sun-like stellar systems are favorable targets for biosignature and habitability indicator searches. Coincidentally, these are some of the prime targets for future direct imaging missions such as HabEx and LUVIOR, in part due to the larger inner working angles (IWAs) of these systems. Our study establishes a relationship between oxygen species and H_2O abundances, specifically between rate of water vapor loss and resultant global O_3 amount. Understanding this relationship is crucial for nitrogen dominated atmospheres as the total water inventory on a planet can help interpret future O_3 and O_2 observations. In particular, it has been argued that the presence of water (usually in the form of condensate clouds, atmospheric gas, and/or ocean basins) can

help confirm or rule out O_2 false positive scenarios associated with water-loss or photochemistry in water-poor atmospheres. However, H_2O alone only indicates the potential presence of an ocean, so caution will be needed when interpreting its signal. Additionally, the potential to detect H_2O on terrestrial exoplanets with near-term instruments such as JWST has been debated. Chen et al. [54] computed the spectral for planets orbiting M-dwarfs with a wide range of effective temperatures using 3D model inputs and predicted that up to 70 transits will be needed to identify water vapor features ($\sim$5.6μm). If the hypothetical planet is situated only 5 pc away from Earth, then only 4-10 transits are needed. Other studies [188, 323] that used prognostic GCM cloud inputs found that it will be challenging to detect H_2O due to the effects of water and ice clouds flattening the spectral lines.

Our results also have implications for observing near-term targets such as the TRAPPIST-1 system, specifically regarding the detectability of its water and oxygen species. Bolmont et al. [35] predicted that planets in the system can possess a large water inventory even for high FUV to NUV stellar flux ratios and rapid H_2O photodissociation rates. This conclusion is consistent with the results of Grimm et al. [118] where they found a present volatile rich composition. While planets e, f, and g all lie in the HZ, TRAPPIST-1e could potentially be situated in the moist greenhouse regime, depending on the amount of greenhouse gases present [336, 351]. The other two planets (f and g) likely have dry climates as they require a higher partial pressure of greenhouse gas (e.g., CO_2 and H_2O) to sustain surface liquid water [336]. Owing to the high FUV/NUV of TRAPPIST-1, abiotic accumulation of oxygen and ozone is highly likely for TRAPPIST-1e (assuming a CO_2-H_2O-rich composition), particularly if the planet has a saturated atmosphere. Therefore our results suggest that if TRAPPIST-1e is in a moist greenhouse state, then detection of O_2 or O_3 cannot be used as definite bioindicators (e.g., [127]. Because of the weak UVB and UVA ($\lambda > 215$ nm) emission of M-dwarfs compared to G-dwarfs, biosignature gases such as methane and nitrous oxide have enhanced lifetimes in moist and/or steam atmospheres, i.e., IHZ climate simulation around the M-

dwarf star [303, 358]. Moving forward, accounting for these changes in atmospheric biomarker abundance as a function of stellar spectral type and activity level will be important when modeling planetary atmospheres with varying oxygenation levels.

Moist NIR-driven greenhouses and water dominated worlds orbiting cool and/or old stars will be the first few exoplanetary atmospheres accessible with JWST. Understanding moist greenhouse and steam dominated runaway greenhouse by modeling and observational means could provide unparalleled windows into the nature extrasolar worlds such as TOI-1266c [128]. In the future, the observations of these atmospheric archetypes with vary ing oxygenation levels will aid in larger planet sample size analyses, particularly in the context of biosignature false positives and their galactic wide distribution (e.g., Checlair et al. 51).

Using coupled 3D models of terrestrial chemistry climate, we show that the degree of planetary oxygenation can influence stratospheric moisture and the global mean ozone column density. For dry stratospheres (e.g., IHZ planets around G-dwarfs), continuous planetary oxygenation leads to more rapid water-loss on geologic timescales due to enhanced methane oxidation. For wet stratospheres (e.g., IHZ planets around early mid M-dwarfs), the prevalence of HO_x and NO_x chemistry lead to highly non-linear effects on water vapor and ozone column abundances. With atmospheric constituents such as O_3 and H_2O being potentially ideal targets for future observatories closely studying extrasolar environments, our study highlights the need for modeling of photochemical reactions, climate feedbacks, and accurate stellar UV spectral characterizations.
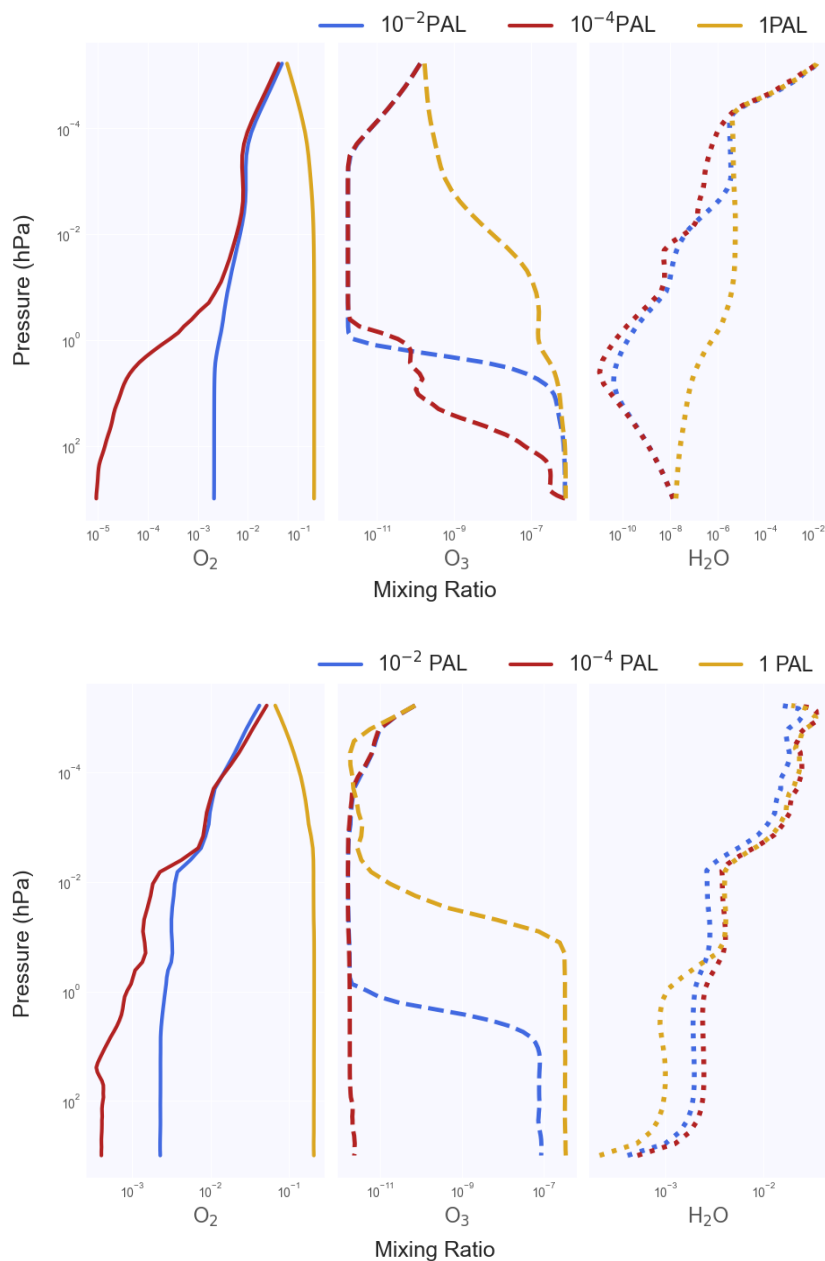
Figure 5.2.1: Vertical profiles of molecular oxygen, ozone, and water vapor for dry climates (planets orbiting G-dwarf's inner edge of the habitable zone; a) and wet climates (planets orbiting M-dwarf's inner edge of the habitable zone; b). Feedback cycles between H_2, O_2, O_3 promote non-linear effects, indicating the importance of coupled dynamics to atmospheric chemistry when modeling highly saturated atmospheres.
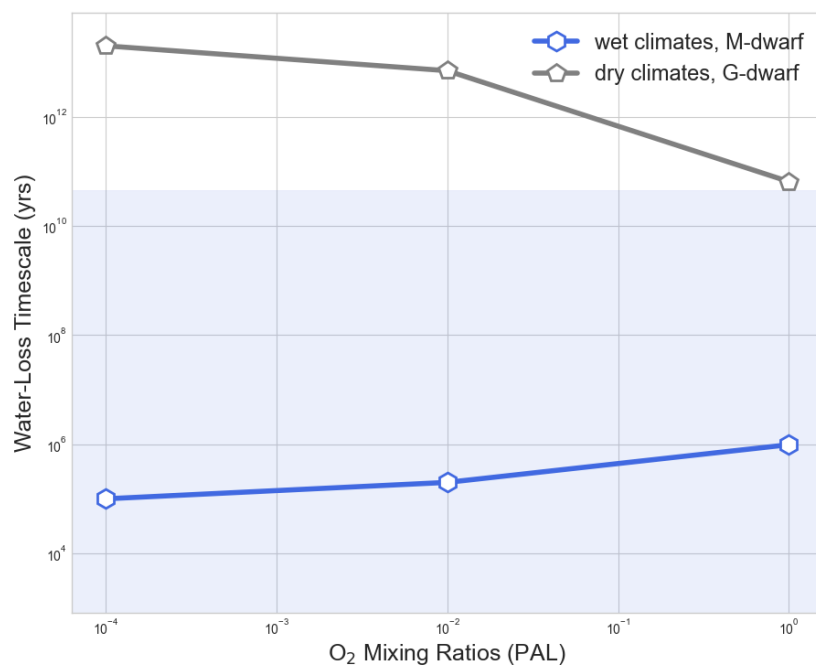
Figure 5.3.1: Water-loss timescale, calculated from the stratospheric (1.0 mbar) water vapor mixing ratios, as a function of global oxygen mixing ratio and climate state. Blue shading denotes the classical Kasting moist greenhouse regime. With the same stellar activity level, the resultant orders of magnitude changes in the water-loss timescales are produced by variations in oxygenation level and amount of air moisture.
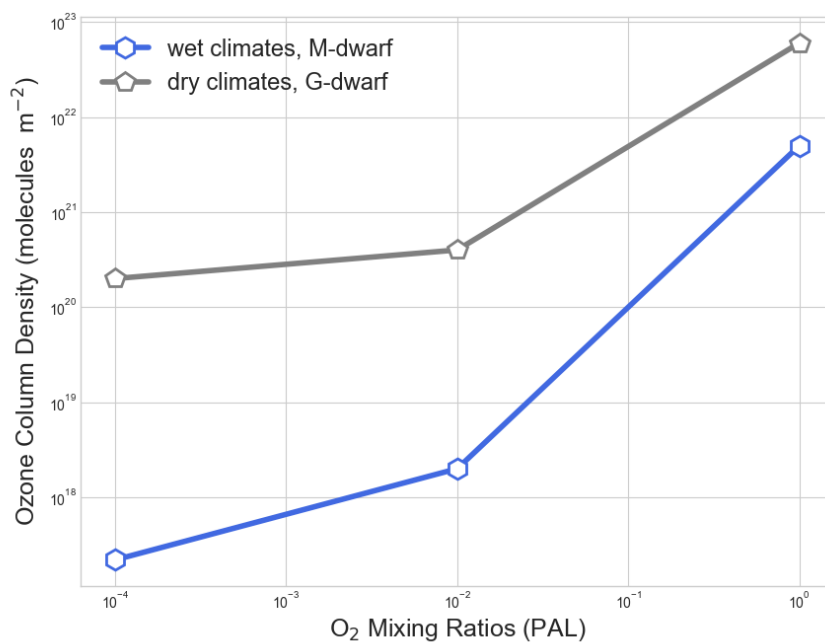
Figure 5.4.1: Global-mean ozone column as a function of global oxygen mixing ratio and climate state. Our results show that the global abundance of ozone not only depends on UV spectra, photosynthetic processes, biogeochemical feedbacks, but also the specific global atmospheric state (e.g., desert versus water worlds, and dry versus wet climates).

Chapter 6

Impact Induced Atmosphere-Mantle Exchange Controls the Volatile Elemental Ratios on Primitive Earth-like Planets

6.1 Abstract

Chondritic materials are thought to have delivered crucial atmospheric and hydrospheric elements such as carbon (C), nitrogen (N), and hydrogen (H) onto primitive Earth. However, recent measurements highlight the significant elemental ratio discrepancies between terrestrial parent bodies and the supposed planet building blocks. Here we present a volatile evolution model during the assembly of Earth and Earth-like planets. Our model includes impact losses, atmosphere-mantle exchange, and time dependent effects of accretion and outgassing calculated from dynamical modeling outcomes. Exploring a wide range of planetesimal properties (i.e., size and composition) as well as impact history informed by N-body accretion simulations, we find that while the degree

of CNH fractionation has inherent stochasticity, the evolution of C/N and C/H ratios can be traced back to certain properties of the protoplanet and projectiles. Interestingly, the majority of our Earth-like planets acquire superchondritic final C/N ratios, implying that the volatile elemental ratios on terrestrial planets are driven by the complex interplay between delivery, atmospheric ablation, and mantle degassing.

6.2 Introduction

The timing and sources for the acquisition of Earth's major volatiles from pre-Solar nebular gases laid the foundation for the planet's geology, atmosphere, and habitability [169, 230]. While Earth itself was accreted by materials from a mixture of chondritic sources and planetary precursors [83, 231, 247], Earth's abundance and composition are incompatible with the originally volatile-rich disk materials from which it was built [124], suggesting that these materials have undergone significant thermal alteration, transfer, and/or differentiation prior to or during accretion. One or a combination of these processes are needed to explain the depletion of Earth's noble gas abundances (by a factor of 40 relative to CI carbonaceous chondrites), and the depletion C and N (by a factor of $\sim$1000; Lodders 215). Hence how Earth has acquired and retained key moderately volatiles (C, N, H) and extremely volatile (noble gas) ingredients during planet formation is a complex problem involving interactions between the impactors and the parent body, as well as between the their principal reservoirs (i.e, mantle, crust, and fluid envelopes).

The formation of Earth and the terrestrial planets of our Solar Sytem involves the collection of $\sim 10^{12}$ meter- and kilometer-sized building blocks on the order of $\sim 40 - 100$ Myr [47, 159]. Strong radial mixing during late-stage accretion is predicted when the local density of planetesimals and embryos becomes comparable [46, 253, 276]. During these intense mixing episodes, proto-planets

accreted scattered embryos and planetesimals and the feeding zones can reach up to several AUs [275]. The accretion of these planetesimals led to the development of embryos that are comparable to their isolation masses [132, 153]. Embryo merging events via giant giants eventually formed Earth and Venus and potentially contributed to the volatile inventories of both planets. However, isotopic constraints show that that Earth's water matches carbonaceous chondrites, which originate from the outer asteroid belt and further out [247]. In order for Earth to have achieved its present volatile (i.e., water) abundances, planetary embryos must thought to have experienced intense bombardment by carbon and water-rich CI chondrite-like bodies from the outer asteroid region early in their evolution stages. As such, the final composition of the inner planets is heavily dependant on the prescribed initial composition distribution (as well as the configuration of Jupiter and Saturn) [46, 253, 276, 346]. Furthermore, if scattering by the inward and outward migration of Jupiter is efficient (e.g., the Grand Tack Paradigm), then a number of volatile-rich asteroids from the trans-Saturn region could have collided with the inner terrestrial planets [254]. Thus to understand the consequence of both both impact loss and delivery as well as volatile transfer across sub components of the BSE and the core, a time-marching model that includes stochastic accretion and feedback effects between reservoirs is needed.

The accretion of atmophile elements (i.e., gas-phase species typically found in the atmosphere) is not a simple summation of individual building block materials. Escape and exchange mechanisms between and within the interacting/colliding bodies can be non-trivial and understanding them requires experimental constraints and theoretical models of accretion and differentiation processes. For instance, high energy photon driven hydrodynamic escape is thought to have removed light atmospheric species such as H and He in the ancient Venusian atmosphere (e.g., Erkaev et al. 90, Kasting and Pollack 164), resulting in the observed isotopic fractionation [78, 119]. Impacts can also drive atmospheric loss to space; all major planetary bodies in the Solar System have suffered intense bombardments during and after accretion [3, 7, 291, 296]. Core forming metals could

also have removed a substantial fraction of carbon from the bulk silicate Earth (BSE) [356]

Astrophysical models of solar system and extrasolar planets typically treat the planet with a single volatile reservoir (gaseous super-Earths; Chen and Rogers 53, Valencia et al. 338). True planets are clearly more complicated than this simplistic, vanilla structure. On terrestrial planets, extremely volatile (e,.g., true atmophiles such as noble gases) and moderately volatiles (C, N, H, S) can reside in multiple reservoirs–the atmosphere (or the hydrosphere), the mantle, and even the core, as many of them are strong lithophiles and siderophiles. Surface interactions with the primordial liquid mantle (e.g., degassing and ingassing) have also shown to be important to the thermal evolution and retention of terrestrial atmospheres [15, 116]. As terrestrial planets formed as molten or partially molten states [318] the vertical distribution of volatiles between the shallow mantle and atmosphere hold clues to the initial phases of planetary growth [89, 372]. Further, the development of thick steam atmospheres, expected during large impacts, could lead to enhanced ingassing of volatiles into the deep interior of nascent Earth and/or the formation of global-scale primordial oceans [233, 372].

Understanding the volatile abundance and composition on proto-worlds will require understanding not only the properties of the impactors but also the effect of each impact on the planet embryo's mantle and atmosphere. Due to the chaotic nature of planetary interactions however, the cumulative volatile delivery to a planet varies with the initial configuration and mass distribution of the system. To account for planetesimal accretion, the usual approach is to assume a constant impact flux based on inferred impact history (e.g., Matsui and Abe 233, Zahnle et al. 372). While such a "fixed-flux" approach has been widely applied, they neglect the stochasticity inherent to accretion processes. N-body planetary accretion simulations demonstrate that with similar initial conditions, two simulations can result in very different accretion histories [46]. More recent work has applied a statistical model of stochastic bombardment to study the formation of Earth's proto-atmosphere during late veneer (1-100 Myr; Sinclair et al. 312), and application to earlier epochs

$(100 - 10^6 \text{yr})$ during the earlier stages of planetary formation.

To date, only a handful of studies attempted to integrate mantle chemistry calculations and N-body simulations (e.g., Rubie et al. [283]) and to our knowledge, no study has integrated atmosphere-mantle exchange with N-body dynamical outcomes. Particularly, *i)* modern models of core-mantle, metal-silicate differentiation model do not include impact escape and, *ii)* studies of atmospheric escape do not interact with chemical evolution and account for stochastic impact events derived from N-body accretion scenarios. Importantly, as the consequence of each impact depends on the evolution of the underlying volatile inventory and the state of the overlain atmosphere, a model that incorporates coupled/interactive effects is needed. In this paper, we make such a contribution by introducing an atmosphere-mantle volatile evolution model of nascent Earth.

6.2.1 The Chemical Composition of Nascent Earth

Today, the cycling of major volatile species such as carbon dioxide, nitrogen, and water through our planet's interior and surface strongly influences its present-day geochemistry, long-term surface climate, and the stability of the biosphere [236, 314]. Carbon concentration in the mantle is estimated to be 2×10^{19} kg [44]. The global nitrogen budget is estimated to be 8×10^{18} kg [108]. Finally, the estimated mantle water content is about 200 ppm, but Marty [230] have posited that up to 90% of water are contained in the mantle which may contain at least an ocean mass worth of H_2O. In addition to absolute concentrations, elemental ratios (e.g., C/N, C/H, C/S Hirschmann 140) can offer insights into fractionation events because they are often associated with specific flux pathways and cosmochemical sources that hold clues to their origin and history.

The C/N values of the interstellar medium, the early nebula, comets, and various types of chondrites differ substantially (i.e., from $\sim$5 to $\sim$200), suggesting that the initial nebular imprint, dif-

ferentiation, thermal metamorphism, outgassing, and atmospheric escape could have all influenced the eventual C/N of the parent body [57, 66, 230, 335]. In the bulk silicate Earth (BSE), nitrogen and carbon are depleted relative to other major volatiles [30, 230], as well as to extreme volatiles such as noble gases [232]. In particular, the modern BSE is found to have superchondritic C/N, which is counter-intuitive as core formation should substantially reduce the BSE's C/N due to the more siderophile nature of C [64]. Note that H is much less siderophilic compared to C and N, which could plausibly explain the subchondritic C/H ratio in the BSE [66]. Lastly, recent work suggests that the C/S value in the BSE could be the result of open-system silicate melting and and carbon loss [141]. Any satisfactory mechanism must not only simultaneously explain all three degrees of elemental fractionation, but also involve the differential removal of C, N, and H relative to the noble gases [124].

6.3   Model Setup

We built an analytical model of atmophile accretion to compute the volatile species evolution as a function of growing Earths and Earth-like planets. Integrated with N-body dynamical simulations, our model includes three reservoirs (atmosphere, mantle, core) and calculates the temporal evolution of C, N, and H amounts as a function of the growing planet. The model accounts for impact degassing/ingassing, atmospheric ablation, and core-mantle-atmosphere equilibration. By modeling how these processes affect the compositions of the interacting bodies for every impact, we track and store the changing volatile content in the reservoirs as the accretion advances. The model is publicly available at `https://github.com/hwchen1996/volatileproject` and we summarize the model components below. A more detail description, including the mathematical formalisms, can be found in the Supplementary Information.

6.3.1 Model Processes and Components

As the assemblage of terrestrial planets is inextricably related to the formation of the volatile inventory, a variety of source/sinks and their associated processes should ideally be considered in an integrated model. These processes include:

- initial composition of solids,

- dynamical evolution and impact history,

- metal-silicate-gas exchange, and

- host star activity and radiation environment.

Each component of our model design addresses one or more of the above process, with an overall goal of assessing impact-induced effects on the volatile content evolution on planetary building blocks. Volatile delivery via impacts may contribute to the global inventory by simply devolatilizing their materials onto the planetary surfaces [373]. Degassing from the deep planetary interior may also supply additional gas to the atmosphere. Ingassing and impacts induced ablation could remove significant amount gases from the atmospheric reservoir, and any species not removed could then be distributed within the planet according to their partition and solubility constants. Calculating both retention and loss processes, as well as potential coupled and feedback effects, is critical to backtrack and predict the volatile abundances on terrestrial planets. In this work, these physical processed are incorporated by modeling:

- Stochastic impact history: The outputs from a suite of N-body simulations based on the Grand Tack Paradigm [158, 346] are used by our volatile growth model. The individual embryo mass and embryo-to-planetesimal ratios were varied.

- Volatile composition of cosmochemical sources: Chondritic materials (enstatite chondrites, ordinary chondrites, carbonaceous chondrites) are assigned volatile fraction values based on their initial heliocentric distances.

- Accretion of planetesimals: Drawing the asteroidal size distribution, accretion of super-planetesimals from the N-body simulations are broken down into smaller, true planetesimals.

- Atmospheric impact erosion: Effects of both giants impacts and planetesimals are approximated using the non-local escape prescription of Schlichting et al. [295].

- Mantle degassing and ingassing: The formation of magma oceans promotes volatile transfer between the mantle and atmosphere. We use Henrian solubilities (e.g., Hirschmann 140) to calculate the mass exchanged during each impact event. One important aspect of this model is that the volatiles dissolved in the mantle are determined solely by the mass of the overlying atmosphere.

- Core formation: During core formation, metals and highly siderophile elements such as carbon are segregated to the core. We use the prescription from Deguen et al. [70] to calculate mantle-core equilibration of carbon.

Ultimately, this model seeks to *(i)* document the accretion histories of volatiles elements (N, C, H) and their gaseous phases (e.g., N_2, CO_2, H_2O), and *(ii)* explicitly quantity their movements across planetary reservoirs. With the above inclusions, the potential complexity of gain/loss events via their dependencies on the composition and timing of the accreted materials can be evaluated.
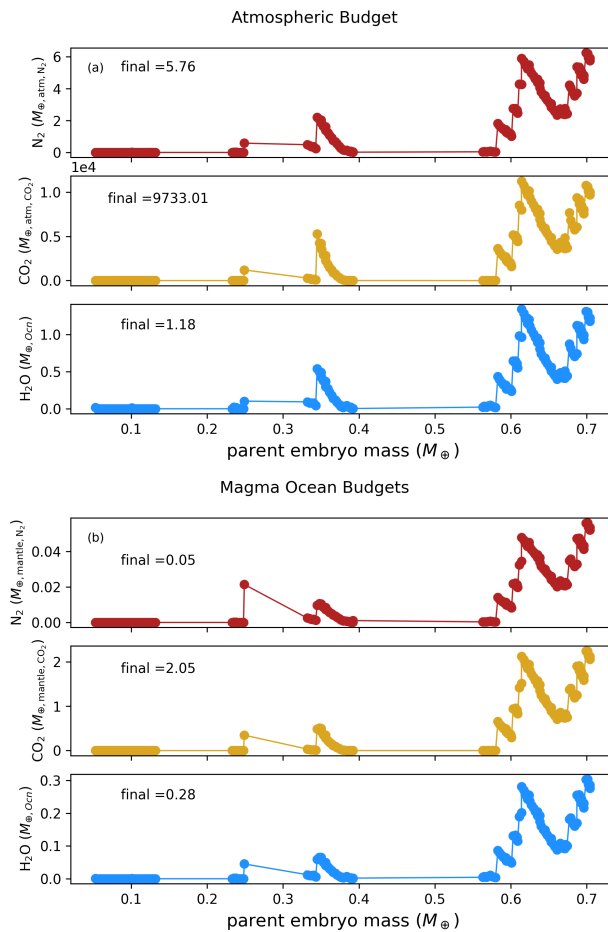
Figure 6.3.1: Time evolution of N_2, H_2O, and CO_2 in the atmosphere and mantle as an Earth-like planet grows, normalized by their respective present-day values. These results correspond to the reference case.

6.4   Results

Using the model described above, we study the volatile growth histories of Earth-like planets by investigating variety of assumptions in initial conditions, impactor composition, impactor population, and accretion history. In particular, we examine the fractionation of CNH elemental species and identify the key processes driving their resultant compositions.
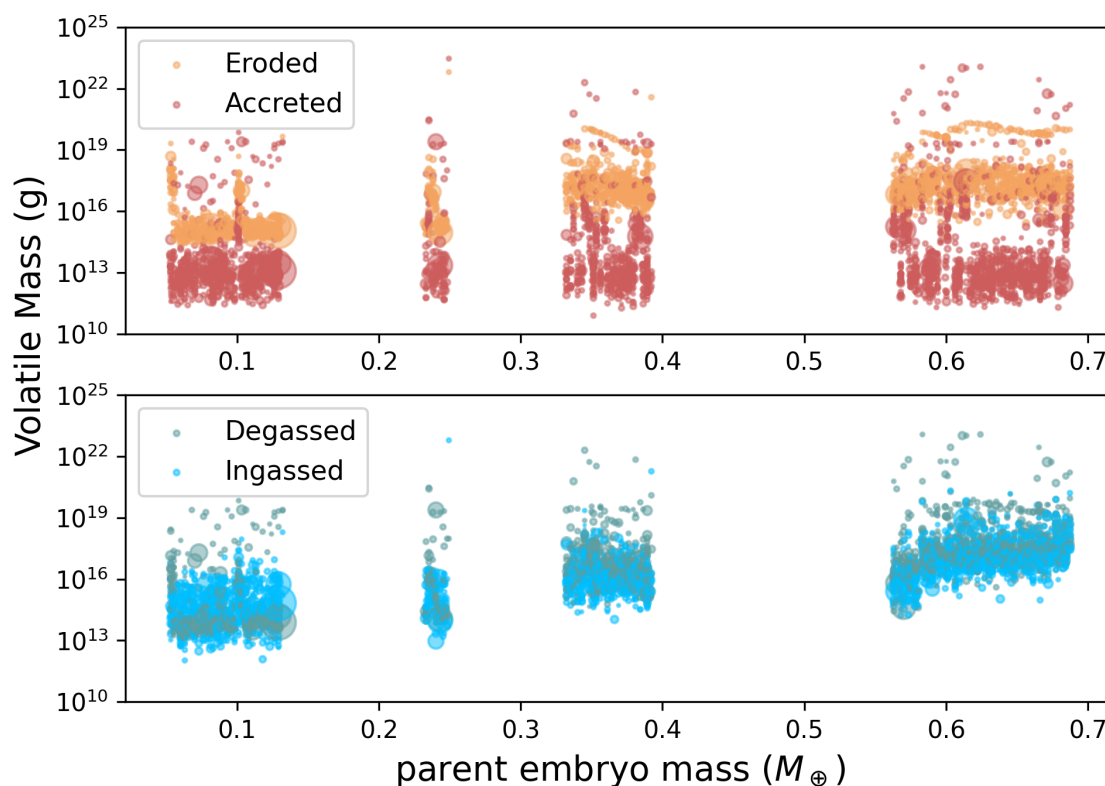
Figure 6.3.2: Volatile mass accreted/eroded (a) and mass degassed/ingassed (b) with a growing Earth. We randomly draw one out of 10^4 planetesimals and document the volatile mass transferred during each impact event. Marker size denotes impactor radius.

6.4.1 Co-evolution of the Atmosphere and Mantle Reservoirs

As the model uses N-body dynamical results as inputs, our approach naturally accounts for both planetesimal and giant impacts, as well as their instantaneous, time-averaged, and cumulative effects on volatile accretion. Figure 6.3.1a shows how the abundances of atmospheric N_2, CO_2, and H_2O change with time reservoir. A few broad observations can be made for the atmospheric abundances (panel a). First, the spikes and dips (i.e., sudden changes in species abundances) are caused by delivery, escape, and degassing. Impact of a large embryo and accretions of volatile-rich planetesimals are primarily responsible for the observed spikes, while successive low mass plan-
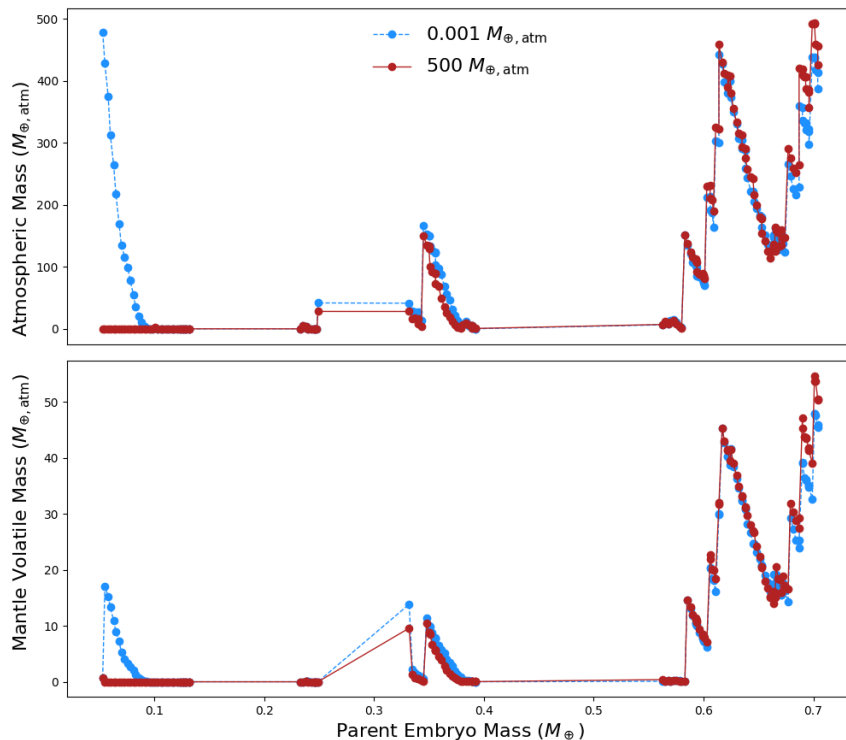
Figure 6.3.3: Time evolution of atmospheric gas with a growing Earth. Two tracks are shown: one model began with accretion seed of $0.001\ M_{\oplus,\mathrm{atm}}$ of gas in the mantle and the other $10^4\ M_{\oplus,\mathrm{atm}}$. Interestingly, they rapidly converge when the planet is only $\sim 0.2 M_{\oplus}$, indicating the existence of one or more equilibrium states that could determine the final properties of a given planet.

etesimal impacts cause the dips in atmospheric mass via efficient impact erosion. Second, volatile gain becomes more pronounced later in time, as seen by the over three times increase in bulk volatile abundance. During the later stages of accretion (when the parent body reaches $\sim 0.7\ M_{\oplus}$), preplanetary materials that originated from beyond 3 AU are being accreted based on the outputs of the N-body accretion simulations. Third, the final atmospheric abundances of N_2 and H_2O all match present Earth well. The large amounts of calculated H_2O is consistent with the formation of a primitive steam atmosphere. Our final surface atmospheric pressure (~ 400 bar for reference case roughly agree with atmospheric evolution (e.g., Zahnle et al. 372) and magma ocean models (e.g., Elkins-Tanton 89). The agreement of CO_2 abundance between our results and that of modern Earth

is poorer, an unsurprising outcome as carbonate crustal block formation is thought to have drawn down massive amounts of atmospheric CO_2 that led to present-day magma ocean lids [315].
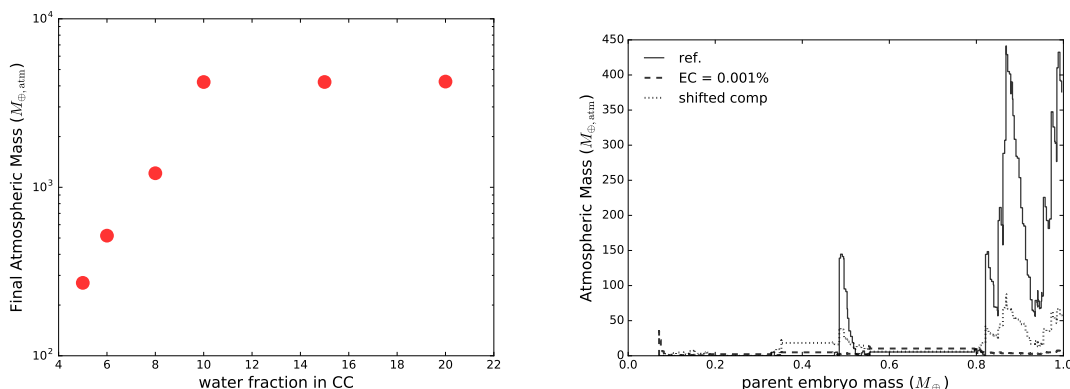
Figure 6.4.1: Sensitivities of atmospheric mass to changes in projectile composition. Here we show the effects of different composition assumptions. In Panel (a), we vary the CC water fraction between 5 and 20%. Other gases assumed in CCs are fixed at the reference value. In Panel (b), we show how Earth grows with a flat EC composition and a different composition step function (Equation 9).

The mantle volatile changes similarly to the atmospheric volatiles as a function of time. Yet volatiles in the model mantle are, in almost all cases, less abundant compared to those in the atmosphere (Figure 6.3.1b). For example, water content in the mantle is slightly lower that on the atmosphere and that of modern Earth's ocean, but is comparable to previously equilibration models (see e.g., Elkins-Tanton 89). The final carbon abundance is strikingly similar to that of modern Earth. Mantle nitrogen is lower relative to but within an order of magnitude of measured nitrogen budget [160].

Variability in volatile content is directly linked to exchange rates between core-mantle-atmosphere-space. Figure 6.3.2 shows the total volatile amount eroded (lost), accreted (added), degassed, and ingassed per impact of the reference Earth case. From panel (a), it can be seen that loss events are generally higher and more frequent compared to accretion events. In the rarer scenarios in which

volatile accreted dominates, they are usually a few orders of magnitude greater than the volatile lost. These events are caused by larger-sized planetesimals (and in some cases giant impacts), as they are less efficient in removing surface volatiles. As we will see in Section 6.3.4, different size distribution of the impactors can cause the ablation-delivery relationship to vary, especially during the later stages of accretion. From panel (b), we see that degassing is almost always greater than ingassing, as the latter only occurs during giant impacts that devolatilize directly onto the magma ocean. At later times, when the protoplanet reaches $\sim$0.6 $M_\oplus$, degassing almost completely dominates,

Our model shows that the long-term accretion of volatiles is independent of the initial starting condition (Figure 6.3.3). The parent body of the red and blue curves have different initial volatile inventory: 0.001 $M_{\oplus,\text{atm}}$ and $\sim$500 $M_{\oplus,\text{atm}}$ respectively, with everything else held equal. When the parent-body embryo (in this case, an Earth-like planet) is at $\sim$0.2$M_\oplus$ however, the two evolution tracks converge and remain qualitatively the same throughout. This behavior implies that there exists certain equilibrium regimes that can established depending on the the properties of the target, its impact history, and the composition of the projectiles. We explore the sensitivity of our model to these assumptions in the following sections.

6.4.2 Importance of Planetesimal Compositions

To explore a reasonable spectrum of chondrite chemical compositions, we perform additional simulations involving changes in: 1) volatile-fraction of enstatite and carbonaceous chondrites, 2) location of step function cut-offs.

Figure 6.4.1a shows results where CC water fraction is varied between 5 and 20%. The ref-
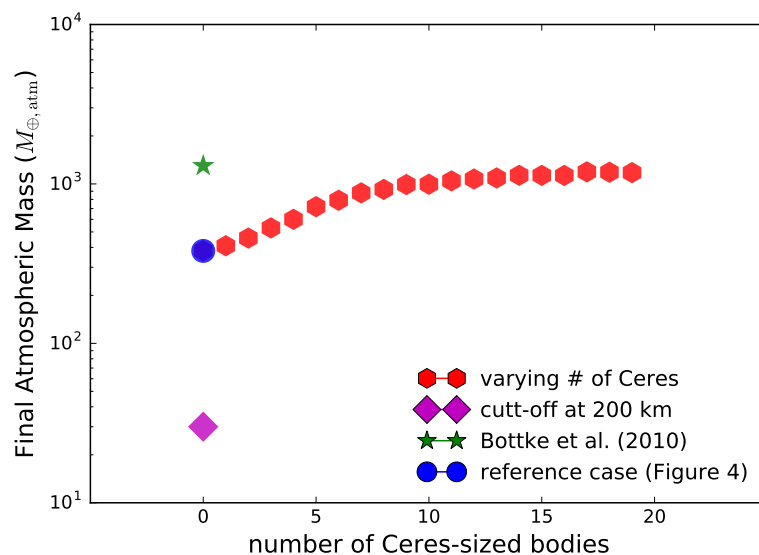
Figure 6.4.2: Final atmospheric compositions mass versus planetesimal size, with shape and color indicating the assumed PSD. The labels in the x-axis correspond to the number of Ceres-sized body in the distribution. For hexagons, each assumed successive PSD contains one more Ceres-sized object. The diamond represents a PSD that is capped at 200 km. The star represents a PSD characterized by massive projectiles (between 1000 and 3000 km in diameter) as proposed by Bottke et al. [37]. Blue circle denotes the reference case, which happens to most accurately match the properties of present Earth (Figure 6.3.1)

erence 5% value roughly reproduces an atmospheric pressure value predicted by other models, as noted earlier (e.g., Zahnle et al. 372). Unsurprisingly, the higher water content assumed, the more massive the final steam atmosphere becomes. As the CC fraction is raised to $\sim$20%, the final atmospheric masses markedly flattens out at about 4000 $M_{\oplus,atm}$.

In Figure 6.4.1b, three runs along with the reference case (solid line) are shown. First, the step
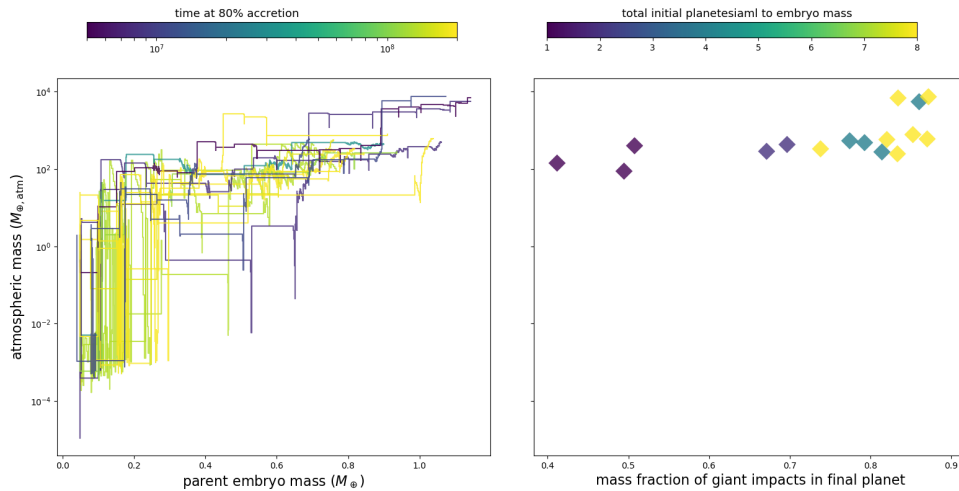
Figure 6.4.3: Atmospheric growth from a suite of N-body simulations to demonstrate the effects of accretion history. Panel (a) shows atmospheric growth histories using all 18 N-body simulations. In panel (b), we show the dependence of final atmospheric mass (when the proto-planet reaches $1\,M_\oplus$) on the carbonaceous chondrite fraction in the final planet and the total initial embryo mass in the simulation. Blue circle denotes the reference case, which happens to most accurately match the properties of present Earth (Figure 6.3.1).

function assumption in Equation 1 is modified to the following:

$$
\chi_{\mathrm{pl}} = \begin{cases} \mathrm{E-type} & \text{for } a < 1.5 \\[2mm] \mathrm{S-type} & \text{for } 1.5 < a < 3.5 \\[2mm] \mathrm{C-type} & \text{for } a \geq 3.5 \end{cases} \tag{6.1}
$$

where the bold denotes the changes made from Equation 1. With these shifts, we have effectively expanded the heliocentric width for ordinary chondrites, while reducing the width for enstatite and carbonaceous chondrites. The results for this simulation is indicated by the dotted curve. The other curve (dashed) represents the assumption of a pure EC composition "flat" distribution (i.e., homogeneous accretion). Both runs resulted in lower atmospheric pressures than the reference case. This outcome illustrates the key role of CCs (planetesimals from greater orbital radii) in

determining volatile abundances. Although some amount of enstatite chondrite is replaced with the more volatile-rich S-type, the amount of CCs accreted when the parent embryo is $\sim 0.8 M_\oplus$ is significantly reduced. It is interesting to note that before $M_{parent} \sim 0.5\ M_{\oplus,atm}$, the reference case is never the highest in atmospheric mass despite having the highest final value. Several explanations may be behind this behavior. First is the dependency of mass-loss efficiency on mean molecular weight μ of the atmosphere through dependency on the scale height ($r_{cap} \propto (H_{tar} R_{tar})^{1/2} \propto 1/\mu$). Second, before the parent body reaches $\sim 0.5\ M_{\oplus,atm}$, volatile-rich body collisions are infrequent, and thus net atmospheric gain is largely controlled by impact loss and remains low.
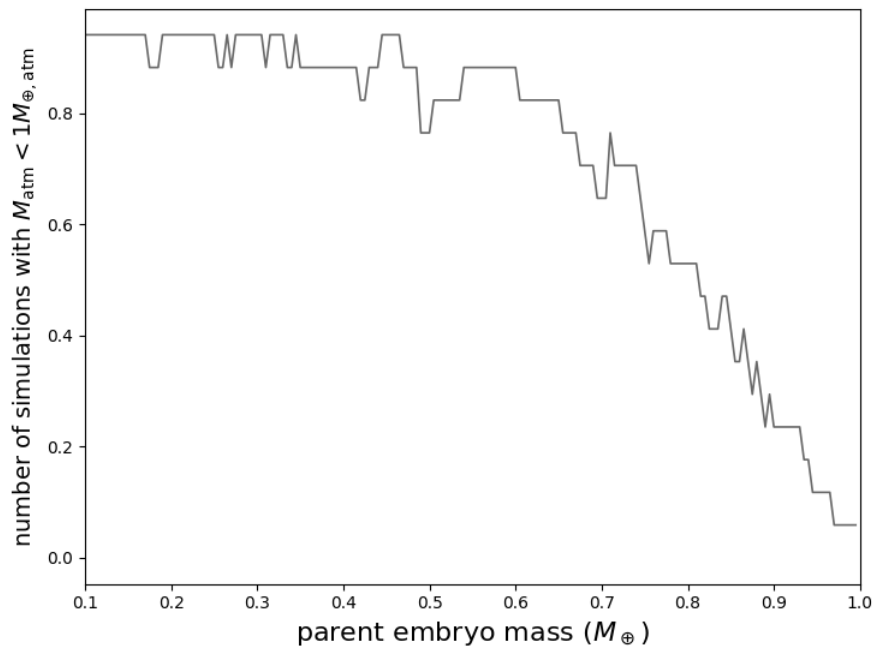
Figure 6.4.4: Fraction of simulations with atmospheric masses less than 1 $M_{\oplus,atm}$ as a function of the parent body mass. A total of 18 N-Body simulations was performed, each with different ratios of total planetesimal mass to embryo mass and individual embryo mass. We find that the number of simulations with $< 1 M_{\oplus,atm}$ decreases with time, suggesting enhanced efficiency of volatiles gain in the later stages of accretion.

6.4.3 Influence of Planetesimal Distribution Assumptions

In the reference simulation cases, we have drawn from the asteroid-belt population to determine the sizes of each planetesimal. Here we test the effects of varying planetesimal size distribution (PSD) assumptions. We perform two modifications to our current planetesimal population–a) including additional Ceres-sized objects, the largest asteroid, and b) capping the upper limit of the size distribution at 200 km in radius, c) adding more giant bodies between 500 and 1500 km in radius, mimicking the size distribution used by Bottke et al. [37].

The results of these changes to the PSD are shown in Figure 6.4.2. From the red circles, we see that the addition of Ceres-sized ($\sim$500 km) bodies results in increased atmospheric mass. This is due to the more dominant contribution of small planetesimals to the total mass-loss history (Figure 6.3.2). With more large Ceres-sized bodies in the distribution, fewer planetesimals with $r_{\mathrm{pl}} \sim r_{\min} \sim \left(3\rho_{\mathrm{surf}}/\rho_{\mathrm{pl}}\right)^{1/3} H_{\mathrm{tar}}$ make up each super-planetesimal. In the case of the Bottke et al. [37] PSD, we find that the result is similar to adding several (between 15-20) Ceres-sized bodies to the asteroid population, namely a substantial increase in the final volatile mass. This result indicates that a distribution with a longer tail than the nominal asteroid population is unrealistic as the assumption produces extreme atmospheric pressures.

Conversely, without any planetesimals greater than 200 km, the final atmospheric mass is dictated by sub-10 km projectile impact escape. This leads to a suppression of atmospheric growth (to $\sim$30 bar).
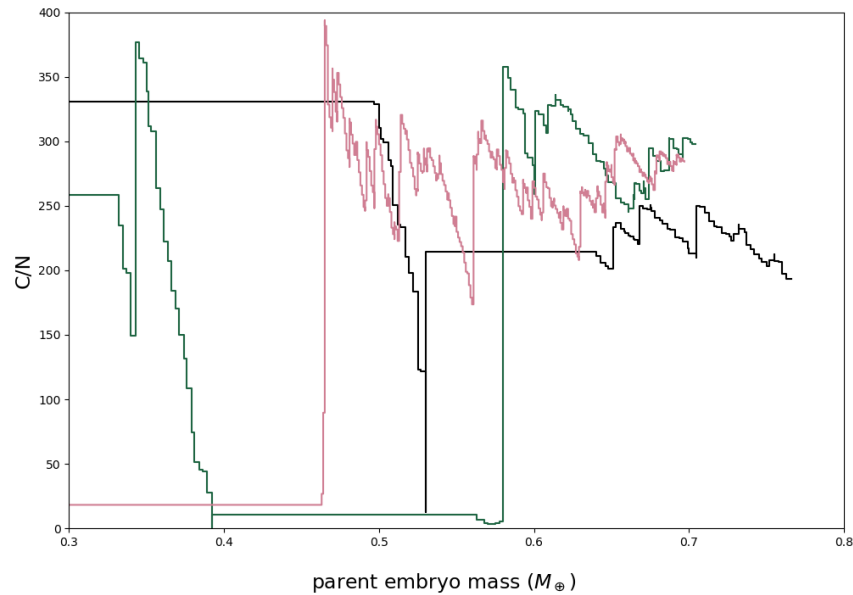
Figure 6.4.5: Sample temporal evolution of C/N ratio of the parent body, showing that the superchondritic C/N arises from the preferential atmospheric loss and mantle degassing of nitrogen over carbon.

6.4.4 Trends in Multiple N-body Simulations: Effects of Accretion History

We test the effects of accretion history on our results using outputs from a suite of N-body accretion simulations. In each N-body simulation, the only changes are the total planetesimal to embryo ratios and the individual embryo mass.

The outcomes of these 18 different N-body simulations are displayed in Figure 6.4.3. In Panel (a), we show the time evolution of ten selected N-body simulation results. Due to the different initial N-body simulation conditions, each growth curve follows a distinct track. However, embryos that reach 80% of its final mass in a shorter period of time have typically more massive atmospheres during accretion. This is seen by the fact that none of the simulations with accretion time $\sim$10 Myr drop below 30 $M_{\oplus,\text{atm}}$ after $M_p > 0.35\,M_{\oplus}$. In Panel (b), only the final atmospheric masses are shown

(as a function of total mass of CC in final assemblage) for each simulation. Some dependence on the total CC accreted can be seen. This is because CCs are very abundant in volatiles, so the more that is contained within a planet simulation the more volatile-rich it will become, assuming the same amount of volatile-loss. As CC accretion fractions $> 5\%$, final atmospheric masses begin to plateau at close to 1000 $M_{\oplus,atm}$. There is also a slight dependence on the initial planetesimal to embryo mass ratio, as seen by the clustering of colors for simulations with higher planetesimal to embryo masses.

Figure 6.4.3 demonstrates that impact history matters in determining the final atmospheric mass and composition, but are there any identifiable trends across these results? We now turn to evaluating atmospheric growth properties of the ensemble. To do this, we record the atmospheric mass for each simulation at each timestep and determine if the value lower than 1 $M_{\oplus,atm}$. As shown in Figure 6.4.4, fluctuations in the number of simulations with light atmospheres occur due to the competitive between impact erosion and delivery. The general trend however is that the number of simulations with low atmospheric masses decreases as the accretion proceeds, suggesting that our protoplanets experience a more pronounced net volatile gain at the later stages of accretion. We find that the majority of our results are consistent with early predictions by Zahnle et al. [372], namely our mean surface atmospheric pressure typically fall between $\sim 200 - 400$ bar.

6.4.5   C/N Ratios as a Natural Consequence of Accretion Processes

Our time-dependent model, integrated with N-body accretion outputs, show that superchondritic BSE C/N is an emergent property of planet formation. All our volatile growth result in high C/N relative to the chondrites. Note that our source chondrites are assumed to have C/N 10 to 25, depending on the heliocentric distance of origin. Figure 6.4.5 shows that all three simulation results
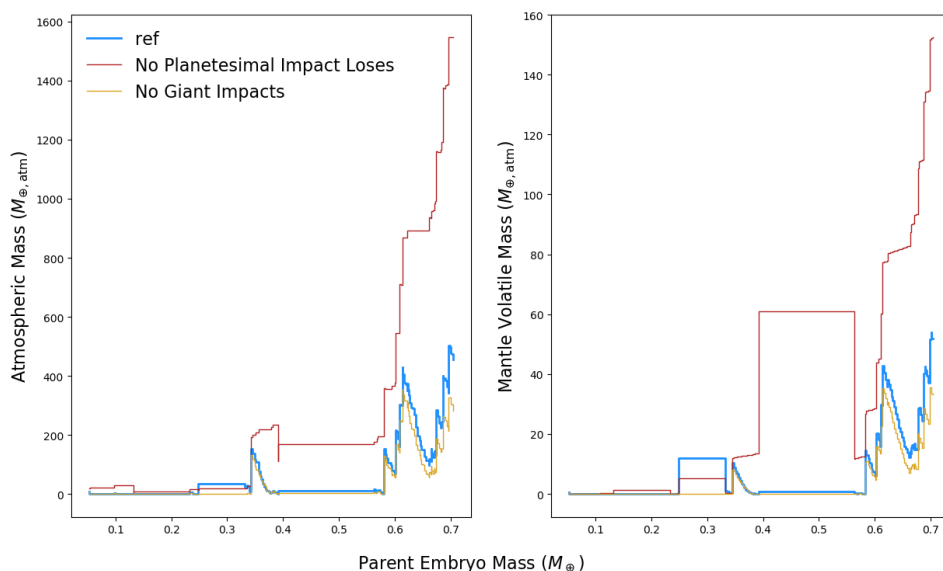
Figure 6.4.6: Time evolution of atmosphere and mantle volatile inventory as an Earth-like planet grows, normalized by their respective present-day values. Each panels include results a) without the effects of planetesimal impact erosion (red), b) without the effects of giant impacts (gold), and c) with both erosion and giant impacts (blue).

in high final BSE C/N (the C/N ratio of the atmosphere is typically subchondritic though). The rise in C/Ns occur almost immediately after the first impact bombardments and only briefly return to their initial (chondritic) values in one of the three cases shown.

To examine the role of impacts in affecting the final C, N, H abundances, we test additional model scenarios without the inclusion of giant embryos and impact erosion by planetesimals. We find that the neglect of giant impacts still lead to high C/N, yet ignoring planetesimal impact escape, in nearly all cases, lead to similar or lower C/N ratios as the impactors themselves (Figure 6.4.7), implying that both loses to space and the subsequent mantle-atmosphere exchange are necessary to produce the superchondritic C/N. Furthermore, in the scenario without the inclusion of impact loses, the final atmospheric mass is much elevated (in excess of $\sim 1500 M_{\oplus, atm}$; Figure 6.4.6). As discussed in Section 3.2, such a large primitive atmosphere is not realistic as it would be challenging

for hydrodynamic and impact erosion to reduce the atmosphere mass to the present-day value. In contrast, ignoring giant impact slightly reduces the final atmospheric mass, indicating that giant impacts play a volatile-delivery rather than volatile-depletion role.

Our results indicate that the synergistic effects of impact erosion and degassing lead to superchondritic BSE C/N ratios. To more quantitatively illustrate the magnitude of each potentially competing process, Figure 6.3.2b shows that the continuous mantle degassing of nitrogen over carbon during the later stages of accretion results. N is less solubility in the magma ocean compared to C. Hence, mantle nitrogen is more rapidly drawn out (relative to carbon) as evidenced by the enhanced degassing rates. On the other hand, the higher escape rates of CO_2 is somewhat misleading due to the higher delivery rate of carbon via CI chondrites, thus creating atmospheres richer in CO_2.
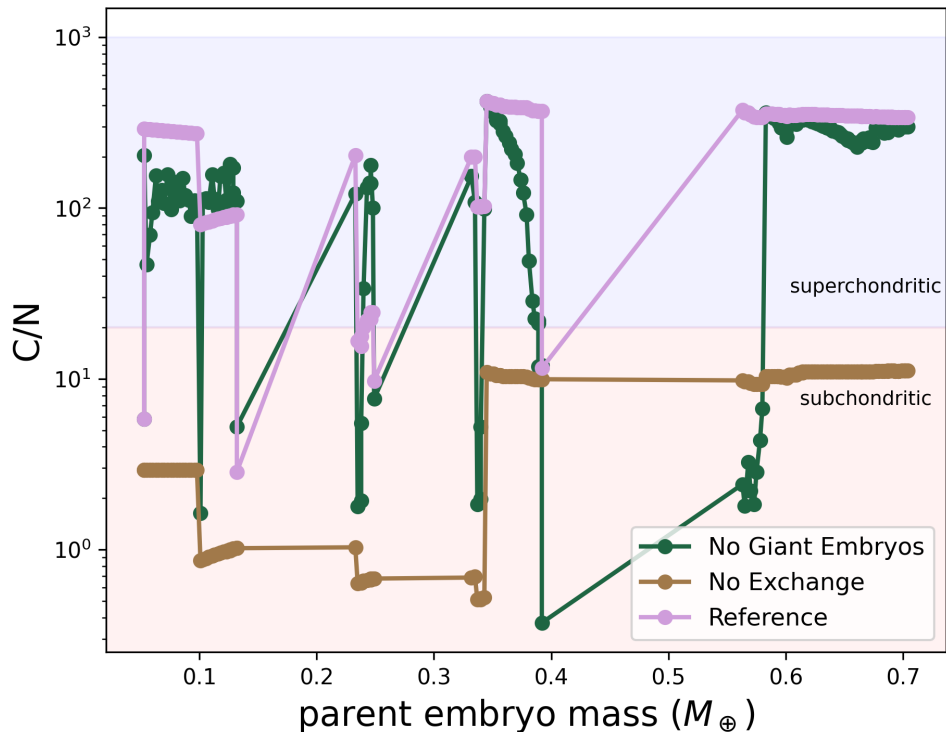
Figure 6.4.7: Time evolution of C:N ratio as an Earth-like planet grows. Different assumptions are represented by different colors.

6.5   Discussion

6.5.1   The Elemental Ratio Conundrum

On Earth, both extremely and moderately volatiles are depleted relative to CI chondrites and other planetary precursors, but the isotopic signatures of the BSE point to an inner solar system asteroidal origin [8, 124], ruling out CV- and E-type-chondrites as major volatile sources. Previous work show that admitting a small amount of cometary materials allows the noble gas proportions to match that of the Earth [124]. However, data from 67P/Churyumov-Gerasimenko suggests minimal cometary

contribution to the bulk of present day Earth [26]. Furthermore, the added materials does not resolve the severe fractionation of moderately volatile species (C, N, H, S) on Earth. In fact, no known Earth reservoir signature perfectly associate with any known chondrites, primitive nor processed.

To resolve this apparent conundrum in elemental composition between Earth and the putative planetary precursors, recent work found that differentiation of preplanetary bodies could transfer carbon to cores during the small solid body processes [141], a channel that could explain both the chondritic C/S and subchondritic C/H. The origin for the observed BSE C/N is likely to be less straightforward, however, as the C/N values of the interstellar medium, the early nebula, comets, and various types of chondrites differ substantially (i.e., from $\sim$5 to $\sim$200; Bergin et al. 30). Interestingly, ordinary chondrites have a diversity of C/N values, a subset of which approach the BSE C/N. Once again, this does not mean that ordinary chondrites are the primary constituent of Earth, as their isotopic signatures do not agree. But it does suggest that one or a combination of metamorphic alteration processes are at work, resulting in the observed range of inherited C/Ns.

Previous work has shown that core formation is more likely to raise rather than reduce the BSE C/N due to the strong siderophile nature of carbon [64, 140], and the similar mantle C and N behaviors [116]. In particular, Hirschmann [140] argued that the draw down of carbon to the core is exceedingly efficient to such an extent that even significant removal of N cannot counteract the reduction of C/N. In another study, Grewal et al. [115] tested different volatile fractions for their giant impactor and found that superchondritic C/N could arise during the merging of a differentiated embryo with an E-type-chondritic composition[1]. However, the majority of these studies assumed static single-stage single-reservoir magma oceans. While we adopt a similar mantle plus an overlying atmosphere interior model, the inclusion of stochastic accretion allows the investigation of chaotic processes and the competition between volatile delivery and escape. One key feature of

---

[1]Note that they found that the atmosphere could also become N-rich if an S-rich core can be achieved, making N_2 less soluble in the MO.

our results is that the predicted final C and N inventories do not hinge on the assumed composition of the preplanetary materials; superchondritic mantle C/N is found regardless of the details of the dynamical history and volatile fraction of the planetesimals. Hence both impact induced degassing and accretion of a late veneer (i.e., differentiated materials) may play roles in elevated the BSE C/N [30].

Our study highlight the key role of time-dependent impact losses in driving the elemental composition of nascent worlds. Our results favor a scenario more consistent with the those posited by Bergin et al. [30] and Tucker and Mukhopadhyay [335]. In particularly however, Bergin et al. [30] argued that during very reduced conditions, the atmosphere can be CO_2-dominated and the nitrogen can be sequestrated as metals, thereby creating high BSE C/N. However, this suggestion neglected the continual effects of impact erosion. During the later stages of accretion, our work shows that rapid loss of nitrogen in oxidizing (rather than reducing) conditions should eventually lead to an elevated mantle C/N.

Because elemental fractionate in accordance with their solubility coefficients, and the solubilities depend on the melt composition (and therefore the bulk planetary composition), the calculated C/N will vary with the planet in question. A future study will study the elemental compositions of Venus and Mars and their extrasolar counterparts, where life-relevant ingredients may be commonplace. Indeed, detection of circumstellar materials (e.g., "exo-Kuiper-belts") around white dwarf has shown the prevalence of key element such as C, N, O, S [359]. An important caveat when considering other planets is that the mantle-atmosphere elemental partitioning behaviors could also be highly P- and T-dependant [232], pointing to the need for further laboratory constraints.

6.5.2 Volatile Sinks: What Dominates?

During planetary accretion, volatiles transfer from the original nebular component to the various reservoirs on a planetary body. Much of these are then lost during further planetary processing. Core formation, MO crystallization, and parent body metamorphism and partial differentiation, for example, incur significant losses for moderate volatiles [64], noble gases [232], and even highly siderophile elements such as carbon [141]. Here, we find that the dominant loss process is impact erosion, particularly in later stages of accretion during high influxes of volatile-rich planetesimals.

Giant impacts are thought to substantially influence the global volatile inventory of forming worlds [103, 104, 115, 174]. This study suggests that giant impacts do not play as of an important role as previously suggested; excluding the effects of giant impacts only led to a $\sim 20\%$ change in the final atmospheric mass (Figure 6.4.6). By randomly sampling planetesimal sizes from modified versions of the asteroid-belt distribution, we find that the occasional accretion of large (km) planetesimals acts as the key controls of the final volatile abundance. More specifically, planetesimals masses drawing from an asteroid-belt-like distribution best fits the outcomes in this study. In turn, our results strongly disfavors the PSDs with many large sized bodies, e.g., one posited by Bottke et al. [37]. This is because the increased stochastic arrival of large-sizes bodies increases the total mass of the atmosphere by more than two orders of magnitude. This result is consistent with the earlier predictions of De Niem et al. [68], where they found that large and slow impactors are particularly important for the final atmospheric mass.

Hydrodynamic atmospheric escape approximated with the energy-limited formalism does not substantially contribute to volatile loss. However, recent work has found that the energy-limited approximation have been over/under-estimate the mass loss rate by over two orders of magnitude [197], and thus explicit simulations of (magneto-)hydrodynamics should ideally be incorporated.

Furthermore, energetic astrophysical event such as stellar flares and coronal mass ejections may enhance stratosphere/mesospheric atmospheric moisture [56] and potentially lead to the long-term dehydration of the upper atmosphere in young systems [80, 112]. Hence solar (stellar) activity is implied to dramatically impact on evolved (exo-)planetary atmospheres, but their effects on early volatile growth warrants further numerical quantification.

6.5.3 Model Limitations & Future Problems

This study aims at constraining the time dependent growth and loss of major gaseous species that constitutes modern Earth's atmosphere (N_2, H_2O, CO_2), but did not include extremely volatile noble gases (Ne, Ar, Kr, Xe). Noble gases are advantageous due to their high ionization energies, reflecting their low chemical reactivity. They also tend to almost always remain in the gaseous phase, making them the most important atmophiles. These properties makes noble gases exceptional as tracers for the origin and history of fluids (see e.g., Pepin 265, Porcelli et al. 268, Tucker and Mukhopadhyay 335).

The Ne/He system is exceptional because whereas many noble gases Ar, Kr, Xe are vulnerable to recycling in planetary interiors, He and Ne are recycles only in minor quantities (e.g., Holland and Ballentine 142). Mid-ocean ridge basalts (MORB), ocean island basalts (OIB), have significantly different $^3He/^{22}Ne$ compared to the nebular component. Several possible explanations have been suggested. Plate tectonics, for one, could recycle and fractionate these gases in the interior. Tucker and Mukhopadhyay [335] on the other hand explained this discrepancy by episodes of MO degassing driven by giant impacts, leaving the primitive MO elementally fractionated. As pointed by Schlichting et al. [295] however, impacts large enough to completely strip the atmosphere most certainly will generate large-scale melting. The lack of geochemical evidence for global magma oceans is problematic for the giant impact argument. The $^{30}Ar/N$ of the BSE and

CV (and CO) chondrites are also enhanced compared to CI-CM chondrites. Another possibility for the observed depletion stem from the variable thermal threshold of the gas-bearing hosts [232], as noble gas-bearing (and often more refractory) materials are affected at higher temperature than nitrogen-bearing ones. When in contact with high temperatures then, nitrogen can be more easily liberated and subsequently lost from the less refractory organics. In a future study, we will build off the model developed here to quantify the volatile retention rates of different host phases.

To allow our present model to calculate atmosphere and mantle oxidation chemistry, two major modifications are needed. First, we will need to add more "boxes" to the mantle reservoir (e.g., Porcelli and Wasserburg 267). While a good approximation, typical mantle-core and mantle-atmosphere equilibration do not involve the whole the MO, with the equilibrium pressure loosely dependent on the impactor mass [11]. Second, physical mixing and transport can fractionate different noble gas isotopes. To account for noble gas isotopes, we will need to implement a chemical fractionation model and adopt the formalism borrowed from Pepin [264]. Apart from C, N, and H, we will include noble gases He, Ne, Ar, Kr, Xe and stable isotopes (e.g., ^{3}He, ^{22}Ne, ^{38}Ar, ^{40}Ar, ^{129}Xe).

Oxygen fugacity (f_{o2}), a crucial parameter, regulates the partitioning of siderophile, lithophile, and atmophiles. In this work, we used fixed (but species-dependent) Henrian solubility coefficients to calculate the distribution of gases in the mantle versus the atmosphere. The influence of evolving redox conditions on our results is uncertain, but many effects will need to be incorporated. First, Earth-like planets originate in highly reduced conditions and begin to oxidize when H_2O-bearing materials are being accreted [283], hence there is a need to understand the extent to which these materials could raise the oxidation state of proto-Earth. Second, compared to small planetesimal accretion, large impacts equilibrate at higher pressures and are able to influence a planet's deep interior. In addition to oxidation via H_2O dissociation and H_2 release, segregation of metallic iron and Fe^{3+} to the core can strongly oxidize the upper mantle [11], which could facilitate the outgassing

of oxidized species. The effects on mantle and atmospheric oxidation, particularly during large impacts, will need to be evaluated with self-consistent calculations of f_{o2} evolution and its effect on volatile abundance and equilibration. This effort is especially important as similar intrinsic oxidation states to Earth, Mars, and Venus has been observed in other planetary systems [81], suggesting that oxidizing process operating in rocky planets and their precursors is universal.

6.6   Conclusions

In this paper, we built an end-to-end model of planetary volatile growth by bringing together important processes including impact erosion, mantle-atmosphere equilibration, and stochastic accretion. Despite the obvious simplifications in calculating impact and exchange processes, we were able to elucidate several aspects of volatile evolution on primitive Earth-like proto-planets. The main take-aways from this work are:

- A volatile growth model with the inclusion of impact delivery and loses can roughly reproduce the atmosphere and mantle reservoir masses of present-day Earth.

- Impactor properties, not the primordial condition of the proto-atmosphere, determine the growth histories of volatiles.

- Models constrain carbonaceous chondrite water abundances to $\sim 1 - 5\%$ by mass.

- Models constrain planetesimal building block size distribution to one similar with the asteroid belt population. Our calculations precludes a distribution with a longer tail dominated by more massive planetesimals > 1000 km as this assumption results in massive atmospheres in excess of 1000 bars.

- A suite of N-body accretion simulations, integrated with our model, highlight the wide range of potential volatile inventory for planets with Earth-similar ($0.7 - 1.1\,M_\oplus$) masses and orbital semi-major axes.

- Superchondritic C/N ratio on bulk silicate Earth is the time dependent result of impact-induced atmospheric loss and subsequent mantle degassing. Based on our model, the elevated MO C/N ratios is robust to different impact histories and initial planetesimal/embryo masses.

I do not know what I may appear to the world, but to myself I seem to have been only like a boy playing on the seashore, and diverting myself in now and then finding a smoother pebble or a prettier shell than ordinary, whilst the great ocean of truth lay all undiscovered before me

Isaac Newton

Chapter 7

Summary, Conclusions, & Future Work

The chapters presented in this dissertation represent advances in numerical modeling techniques of rocky extrasolar planets, with Earth-similar mass and radius. These studies provided a greater understanding of planetary habitability beyond Earth, as well as facilitated the surge in model intercomparison efforts of exotic climate systems. This concluding section describes advantages of a CCM-based modeling approach to the study of HZ exoplanets, summarize the results produced from the dissertation chapters, and offer possible research avenues for the future.

Numerical modeling of exoplanetary systems provide a powerful tool for understanding processes related to planetary climate and planetary atmospheres at a fundamental level. Because the same physical and chemical laws operate on other planetary bodies across the Universe, a deeper grasp of the climatic and chemical phase space extremes will aid in our understanding of possible life-bearing oases beyond Earth, including Venus, Mars, and extrasolar worlds orbiting the liquid water habitable zones around distant stars. However, simple conceptual and single-column models often do not resolve complex and dynamical processes that govern the Earth and planetary systems. On planets orbiting late M-dwarfs, the slowed planetary rotation by tidal forces, altered input stel-

lar spectra energy, and the hypothetical magnetically active circumstellar environments, introduce factors to the system that are advantageous for 3D GCM-perspective studies. These 3D CCMs are a sub-type of GCMs, thus share the majority of their limitations, among them their parameterization schemes, sub-grid scale processes representations, accuracy of their boundary conditions, and realism of their initial conditions, but the results of 3D Earth-system modeling studies often suggest complexities in the climate system not considered in analytical, energy-balance, and single-column climate models. Beyond new climatic complexities, GCM-based studies can also examine conceptual hypotheses within the confines of geochemical data of Earth's history. For example, in chapter five, we motivate our CCM experiments with inferences made on Earth's Proterozoic and Paleozoic oxygen levels. While no fully characterized rocky exoplanets thus far exist, using state-of-the-science modeling tools within a theoretically rigorous framework, we can make the most realistic and possibly testable predictions regarding their chemistry, dynamics, and habitability.

The major dissertation achievements are: (1) the implementation of an originally Earth-based high-top chemistry-climate model to study slowly- and synchronously-rotating exoplanets and the determination that varying planetary rotation periods causes day-night contrasts of trace biosignature gases less than 30%, (2) the observational constraints for planets orbiting close to the inner edge of the habitable zones of cool stars, along with the amount of ozone that is needed to support surface habitability through the filtering of UVC photons, (3) the finding that time-dependent stellar flares could perturb atmospheric compositions to such an extend that they deviate drastically from their non-flare-influenced counterparts, while promoting amplifications of key nitrogen oxide spectral features, (4) the realization that the degree of global oxygenation by biological-means can be introduced as another stress test in the evolutionary narratives of habitable dry and moist climates, and lastly, (5) the development of an independent model to predict the initial conditions of Earth's atmosphere and hydrosphere during planetary accretion. The paper and studies produced as a direct result of this dissertation have galvanized new research avenues. Some examples of these

questions are:

To what extend do very low O_2 concentration assumptions no longer hold? The lowest O_2 concentration we have experimented on in this dissertation is 10^{-4} PAL. How low can we push the chemical scheme originally designed for Earth-based research? At what point would we have to introduce new chemical speciation networks and reaction rates suitable for oxygen-poor conditions?

What are the effects of prognostic/simulated water clouds on observations? Our current model simulates cloud ice amount (kg/kg), cloud liquid amount (kg/kg), effective ice particle radius (μm), liquid drop radius (μm), and cloud cover for two cloud-types: water ice clouds and water liquid clouds. Is it feasible to incorporate these prognostic variables into mapping the full 3D emission and reflected light spectra? How would the inclusion of self-consistent 3D cloud coverage influence detectability for future observatories?

How could the inclusion of photochemical haze affect the yield of planetary habitability and spectra? Apart from water and carbon dioxide clouds, photochemical haze, often composed of C, H, O, N, and S elements, is expected to be ubiquitous on anoxic worlds i.e., Titan and the early Earth [12]. How would the haze-chemistry-climate modeling affect current predictions of planetary habitability? What are some observational discriminant of photochemical haze and what can they tell us about the atmospheres of extrasolar planets?

My plan to tackle some of these research question is as follows:

First, I will borrow subroutines from cousin model `ExoCam`, which incorporates chemical data and modules suitable for present day O_2 rich and low O_2 concentrations down to 1% PAL, but currently does not possess the anoxic chemistry needed to simulate the vast array of anticipated atmospheric archetypes that will be imaged by near term and future observatories. I will then implement important anoxic photochemical equations, including H_2SO_4 aerosols, S_8 aerosols, and

hydrocarbon hazes, into WACCM. This effort will likely require the development and implementation of new radiative and reducing chemical schemes [149, 150], including new treatments of reactions, photolytic/photochemical reactions, surface emission, dry/wet deposition, and thermal escape of low mean molecular weight species. Some of the results produced here will serve as a follow-up study to Chapter 5 of the dissertation.

Importantly, `ExoRT` [354, 355], a publicly available radiative transfer code designed for 3D climate models, is already set up to do anoxic atmospheres, pure CO_2 atmospheres, and H_2-rich atmospheres, hence first I will link WACCM's chemical modules to `ExoRT`. Note that `ExoRT` is already fully coupled to `ExoCAM`, a branch of CESM and close cousin to WACCM. Thus, efforts to couple this new radiation scheme to WACCM will be relatively straightforward. One anticipated difficulty however, is the upper atmospheric components, e.g., mesosphere, ionosphere, and thermosphere regions (above ~ 0.05 hPa) which will require non-LTE radiation adjustments.

As aforementioned, photochemical haze is expected to be ubiquitous on anoxic worlds i.e., Titan and the early Earth [12, 286]. As a follow-up to my disseration, I plan to develop chemistry upgrades to the code that would allow for the self-consistent production of model photochemical haze made of C, H, O, N, and S elements. For instance, the Community Aerosol and Radiation Model for Atmospheres (CARMA), which is already on the trunk of CESM, is state-of-the-art microphysical model that has already been successfully used here to simulate the evolution of fractal aggregate hazes in an CAM-Titan GCM [200], albeit without self-consistent chemical production rates (Figure 4). I will thus begin investigation of aerosol and haze formation by simulating Titan-like exoplanets around M-dwarfs (e.g., Checlair et al. 49, Lora et al. 217) incorporating both prognostic photochemical production rates and with state-of-the-art microphysics.

In our current model, uncertainties with regards to stellar X-ray and EUV flux influences are attributed to the lack of model upper atmospheres and prognostic ion chemistry. To investigate

terrestrial exoplanetary ionospheres around cool stars, I will first employ WACCM-X, a model originally developed for Earth-based research, to study early Earth orbiting a young Sun. I will upgrade model capabilities to include extreme Joule heating and ion chemistry at high T, conditions to be expected for planets around active hosts such as M-dwarfs [6]. In particular, I will coupled the CCM with models available at the GSFC Community Coordinated Modeling Center. Constrasting the ionospheric composition between oxygenated, weakly oxic, and anoxic worlds could reveal important underlying atmospheric/geologic properties [241].

Previous work showed that realistic, self-consistent simulation of stellar variability influences on the planetary space weather environment (e.g., coupling between dynamic pressure and magnetospheric geometry) is critical for modeling the temporal evolution of HZ high- and low-mean molecular weight atmospheres [56, 61]. While our models are currently unable to directly simulate the fully coupled stellar wind-planetary magnetospheric processes, I will borrow formalisms from previous work to provide close estimations. First, I will begin with parameterized magnetospheres, e.g., methods used by Chen et al. [56]. Then, I will investigate the impact of magnetosphere-ionosphere couplings by including an interactive model, e.g., [107].

One of the next steps is to apply these upgrades to anoxic planets, as the precise chemical pathway and degree of chemical alteration depend on the assumed oxidization state of the atmosphere. For instance, anoxic atmospheres lack persistent oxygen-derived ozone and large scale height ionospheres with fully ionized atomic oxygen, and thus may experience higher rates of atmospheric erosion and chemical modulation.

In short, the future is murky, but ripe for exploration. Thanks for reading! -Howard

Bibliography

[1] D. S. Abbot, N. B. Cowan, and F. J. Ciesla. Indication of Insensitivity of Planetary Weathering Behavior and Habitable Zone to Surface Land Fraction. *The Astrophysical Journal*, 756:178, September 2012. doi: 10.1088/0004-637X/756/2/178.

[2] Y. Abe, A. Abe-Ouchi, N. H. Sleep, and K. J. Zahnle. Habitable Zone Limits for Dry Planets. *Astrobiology*, 11:443–460, June 2011. doi: 10.1089/ast.2010.0545.

[3] T. J. Ahrens. Impact erosion of terrestrial planetary atmospheres. *Annual Review of Earth and Planetary Sciences*, 21:525–555, 1993. doi: 10.1146/annurev.ea.21.050193.002521.

[4] V. S. Airapetian, C. H. Jackman, M. Mlynczak, W. Danchi, and L. Hunt. Atmospheric Beacons of Life from Exoplanets Around G and K Stars. *Scientific Reports*, 7:14141, November 2017. doi: 10.1038/s41598-017-14192-4.

[5] V. S. Airapetian, R. Barnes, O. Cohen, G. A. Collinson, W. C. Danchi, C. F. Dong, A. D. Del Genio, K. France, K. Garcia-Sage, A. Glocer, N. Gopalswamy, J. L. Grenfell, G. Gronoff, M. G"udel, K. Herbst, W. G. Henning, C. H. Jackman, M. Jin, C. P. Johnstone, L. Kaltenegger, C. D. Kay, K. Kobayashi, W. Kuang, G. Li, B. J. Lynch, T. L"uftinger, TJ. G. Luhmann, H. Maehara, M. G. Mlynczak, Y. Notsu, R. M. Ramirez, S. Rugheimer, M. Scheucher, J. E. Schlieder, K. Shibata, C. Sousa-Silva, V. Stamenkovi'c, R. J. Strangeway, A. V. Usmanov, P. Vergados, O. P. Verkhoglyadova, A. A. Vidotto, M. Voytek, M. J. Way, G. P. Zank, and Y. Yamashiki. Impact of Space Weather on Climate and Habitability of Terrestrial Type Exoplanets. *arXiv e-prints*, art. arXiv:1905.05093, May 2019.

[6] V. S. Airapetian, R. Barnes, O. Cohen, G. A. Collinson, W. C. Danchi, C. F. Dong, A. D. Del Genio, K. France, K. Garcia-Sage, A. Glocer, N. Gopalswamy, J. L. Grenfell, G. Gronoff, M. Güdel, K. Herbst, W. G. Henning, C. H. Jackman, M. Jin, C. P. Johnstone, L. Kaltenegger, C. D. Kay, K. Kobayashi, W. Kuang, G. Li, B. J. Lynch, T. Lüftinger, J. G. Luhmann, H. Maehara, M. G. Mlynczak, Y. Notsu, R. A. Osten, R. M. Ramirez, S. Rugheimer, M. Scheucher, J. E. Schlieder, K. Shibata, C. Sousa-Silva, V. Stamenković, R. J. Strangeway, A. V. Usmanov, P. Vergados, O. P. Verkhoglyadova, A. A. Vidotto, M. Voytek, M. J. Way, G. P. Zank, and Y. Yamashiki. Impact of space weather on climate and habitability

of terrestrial-type exoplanets. *International Journal of Astrobiology*, 19(2):136–194, April 2020. doi: 10.1017/S1473550419000132.

[7] Francis Albarède. Volatile accretion history of the terrestrial planets and dynamic implications. *Nature*, 461(7268):1227–1233, October 2009. doi: 10.1038/nature08477.

[8] CM O'D Alexander, R Bowden, ML Fogel, KT Howard, CDK Herd, and LR Nittler. The provenances of asteroids, and their contributions to the volatile inventories of the terrestrial planets. *Science*, 337(6095):721–723, 2012.

[9] G. Anglada-Escudé, P. J. Amado, J. Barnes, Z. M. Berdiñas, R. P. Butler, G. A. L. Coleman, I. de La Cueva, S. Dreizler, M. Endl, B. Giesers, S. V. Jeffers, J. S. Jenkins, H. R. A. Jones, M. Kiraga, M. Kürster, M. J. López-González, C. J. Marvin, N. Morales, J. Morin, R. P. Nelson, J. L. Ortiz, A. Ofir, S.-J. Paardekooper, A. Reiners, E. Rodríguez, C. Rodríguez-López, L. F. Sarmiento, J. P. Strachan, Y. Tsapras, M. Tuomi, and M. Zechmeister. A terrestrial planet candidate in a temperate orbit around Proxima Centauri. *Nature*, 536:437–440, August 2016. doi: 10.1038/nature19106.

[10] Guillem Anglada-Escudé, Pedro J Amado, John Barnes, Zaira M Berdiñas, R Paul Butler, Gavin AL Coleman, Ignacio de La Cueva, Stefan Dreizler, Michael Endl, Benjamin Giesers, et al. A terrestrial planet candidate in a temperate orbit around proxima centauri. *Nature*, 536(7617):437–440, 2016.

[11] Katherine Armstrong, Daniel J Frost, Catherine A McCammon, David C Rubie, and Tiziana Boffa Ballaran. Deep magma ocean formation set the oxidation state of earth's mantle. *Science*, 365(6456):903–906, 2019.

[12] G. Arney, S. D. Domagal-Goldman, V. S. Meadows, E. T. Wolf, E. Schwieterman, B. Charnay, M. Claire, E. Hébrard, and M. G. Trainer. The Pale Orange Dot: The Spectrum and Habitability of Hazy Archean Earth. *Astrobiology*, 16:873–899, November 2016. doi: 10.1089/ast.2015.1422.

[13] G. N. Arney. The K Dwarf Advantage for Biosignatures on Directly Imaged Exoplanets. *The Astrophysical Journal Letters*, 873:L7, March 2019. doi: 10.3847/2041-8213/ab0651.

[14] Dimitra Atri. Modelling Stellar Proton Event-Induced Particle Radiation Dose on Close-in Exoplanets. *Monthly Notices of the Royal Astronomical Society*, 465(1):L34–L38, February 2017. doi: 10.1093/mnrasl/slw199.

[15] Guillaume Avice and Bernard Marty. Perspectives on atmospheric evolution from noble gas and nitrogen isotopes on earth, mars & venus. *Space Science Reviews*, 216(3):1–18, 2020.

[16] S Ball. Atmospheric chemistry at night. *ECG Environmental Briefs*, (3), 2014.

[17] Sarah Ballard. Predicted Number, Multiplicity, and Orbital Dynamics of TESS M-dwarf Exoplanets. *The Astronomical Journal*, 157(3):113, March 2019. doi: 10.3847/1538-3881/aaf477.

[18] PM Banks and G Kockarts. Aeronomy, vol. b, chap. 15, 1973.

[19] T. Barclay, J. Pepper, and E. V. Quintana. A Revised Exoplanet Yield from the Transiting Exoplanet Survey Satellite (TESS). *The Astrophysical Journal Supplement Series*, 239:2, November 2018. doi: 10.3847/1538-4365/aae3e9.

[20] T. Barclay, J. Pepper, and E. V. Quintana. A Revised Exoplanet Yield from the Transiting Exoplanet Survey Satellite (TESS). *ArXiv e-prints*, April 2018.

[21] CG Bardeen, OB Toon, EJ Jensen, ME Hervig, CE Randall, S Benze, DR Marsh, and A Merkel. Numerical simulations of the three-dimensional distribution of polar mesospheric clouds and comparisons with cloud imaging and particle size (cips) experiment and the solar occultation for ice experiment (sofie) observations. *Journal of Geophysical Research: Atmospheres*, 115(D10), 2010.

[22] N. E. Batalha, N. K. Lewis, M. R. Line, J. Valenti, and K. Stevenson. Strategies for Constraining the Atmospheres of Temperate Terrestrial Planets with JWST. *The Astrophysical Journal Letters*, 856:L34, April 2018. doi: 10.3847/2041-8213/aab896.

[23] Claire Baxter, Jean-Michel Désert, Shang-Min Tsai, Kamen O. Todorov, Jacob L. Bean, Drake Deming, Vivien Parmentier, Jonathan J. Fortney, Michael Line, Daniel Thorngren, Raymond T. Pierrehumbert, Adam Burrows, and Adam P. Showman. Evidence for disequilibrium chemistry from vertical mixing in hot Jupiter atmospheres. A comprehensive survey of transiting close-in gas giant exoplanets with warm-Spitzer/IRAC. *Astronomy & Astrophysics*, 648:A127, April 2021. doi: 10.1051/0004-6361/202039708.

[24] Juliette Becker, Elena Gallo, Edmund Hodges-Kluck, Fred C. Adams, and Rory Barnes. A Coupled Analysis of Atmospheric Mass Loss and Tidal Evolution in XUV Irradiated Exoplanets: The TRAPPIST-1 Case Study. *The Astronomical Journal*, 159(6):275, June 2020. doi: 10.3847/1538-3881/ab8fb0.

[25] C. Beichman, B. Benneke, H. Knutson, R. Smith, P.-O. Lagage, C. Dressing, D. Latham, J. Lunine, S. Birkmann, P. Ferruit, G. Giardino, E. Kempton, S. Carey, J. Krick, P. D. Deroo, A. Mandell, M. E. Ressler, A. Shporer, M. Swain, G. Vasisht, G. Ricker, J. Bouwman, I. Crossfield, T. Greene, S. Howell, J. Christiansen, D. Ciardi, M. Clampin, M. Greenhouse, A. Sozzetti, P. Goudfrooij, D. Hines, T. Keyes, J. Lee, P. McCullough, M. Robberto, J. Stansberry, J. Valenti, M. Rieke, G. Rieke, J. Fortney, J. Bean, L. Kreidberg, D. Ehrenreich, D. Deming, L. Albert, R. Doyon, and D. Sing. Observations of Transiting Exoplanets with the James Webb Space Telescope (JWST). , 126:1134, December 2014. doi: 10.1086/679566.

[26] David V Bekaert, Michael W Broadley, and Bernard Marty. The origin and fate of volatile elements on earth revisited in light of noble gas data obtained from comet 67p/churyumov-gerasimenko. *Scientific reports*, 10(1):1–18, 2020.

[27] A. Belov, H. Garcia, V. Kurt, H. Mavromichalaki, and M. Gerontidou. Proton Enhancements and Their Relation to the X-Ray Flares During the Three Last Solar Cycles. *Solar Physics*, 229(1):135–159, Jun 2005. doi: 10.1007/s11207-005-4721-3.

[28] B. Benneke, H. A. Knutson, J. Lothringer, I. J. M. Crossfield, J. I. Moses, C. Morley, L. Kreidberg, B. J. Fulton, D. Dragomir, A. W. Howard, I. Wong, J.-M. Désert, P. R. McCullough, E. M.-R. Kempton, J. Fortney, R. Gilliland, D. Deming, and J. Kammer. A sub-Neptune exoplanet with a low-metallicity methane-depleted atmosphere and Mie-scattering clouds. *Nature Astronomy*, July 2019. doi: 10.1038/s41550-019-0800-5.

[29] Björn Benneke, Ian Wong, Caroline Piaulet, Heather A. Knutson, Ian J. M. Crossfield, Joshua Lothringer, Caroline V. Morley, Peter Gao, Thomas P. Greene, Courtney Dressing, Diana Dragomir, Andrew W. Howard, Peter R. McCullough, Eliza M. R. Kempton Jonathan J. Fortney, and Jonathan Fraine. Water Vapor on the Habitable-Zone Exoplanet K2-18b. *arXiv e-prints*, art. arXiv:1909.04642, Sep 2019.

[30] Edwin A. Bergin, Geoffrey A. Blake, Fred Ciesla, Marc M. Hirschmann, and Jie Li. Tracing the ingredients for a habitable earth from interstellar space through planet formation. *Proceedings of the National Academy of Science*, 112(29):8965–8970, July 2015. doi: 10.1073/pnas.1500954112.

[31] A. Berk, P. Conforti, R. Kennett, T. Perkins, F. Hawes, and J. van den Bosch. MODTRAN6: a major upgrade of the MODTRAN radiative transfer code. In *Algorithms and Technologies for Multispectral, Hyperspectral, and Ultraspectral Imagery XX*, volume 9088 of *Proceedeings of SPIE*, page 90880H, June 2014. doi: 10.1117/12.2050433.

[32] Peter F Bernath, Charles Thomas McElroy, MC Abrams, Christopher D Boone, Mike Butler, Claude Camy-Peyret, Michel Carleer, Cathy Clerbaux, P-F Coheur, Réginald Colin, et al. Atmospheric chemistry experiment (ace): mission overview. *Geophysical Research Letters*, 32(15), 2005.

[33] J. Bin, F. Tian, and L. Liu. New inner boundaries of the habitable zones around M dwarfs. *Earth and Planetary Science Letters*, 492:121–129, June 2018. doi: 10.1016/j.epsl.2018.04.003.

[34] M. R. Bolcar, L. Feinberg, K. France, B. J. Rauscher, D. Redding, and D. Schiminovich. Initial technology assessment for the Large-Aperture UV-Optical-Infrared (LUVOIR) mission concept study. In *Space Telescopes and Instrumentation 2016: Optical, Infrared, and Millimeter Wave*, volume 9904 of *Proceedeings of SPIE*, page 99040J, July 2016. doi: 10.1117/12.2230769.

[35] E. Bolmont, F. Selsis, J. E. Owen, I. Ribas, S. N. Raymond, J. Leconte, and M. Gillon. Water loss from terrestrial planets orbiting ultracool dwarfs: implications for the planets of TRAPPIST-1. *Monthly Notices of the Royal Astronomical Society*, 464:3728–3741, January 2017. doi: 10.1093/mnras/stw2578.

[36] William J. Borucki, David Koch, Gibor Basri, Natalie Batalha, Timothy Brown, Douglas Caldwell, John Caldwell, Jørgen Christensen-Dalsgaard, William D. Cochran, Edna DeVore, Edward W. Dunham, Andrea K. Dupree, Thomas N. Gautier, John C. Geary, Ronald Gilliland, Alan Gould, Steve B. Howell, Jon M. Jenkins, Yoji Kondo, David W. Latham, Geoffrey W. Marcy, Søren Meibom, Hans Kjeldsen, Jack J. Lissauer, David G. Monet, David Morrison, Dimitar Sasselov, Jill Tarter, Alan Boss, Don Brownlee, Toby Owen, Derek Buzasi, David Charbonneau, Laurance Doyle, Jonathan Fortney, Eric B. Ford, Matthew J. Holman, Sara Seager, Jason H. Steffen, William F. Welsh, Jason Rowe, Howard Anderson, Lars Buchhave, David Ciardi, Lucianne Walkowicz, William Sherry, Elliott Horch, Howard Isaacson, Mark E. Everett, Debra Fischer, Guillermo Torres, John Asher Johnson, Michael Endl, Phillip MacQueen, Stephen T. Bryson, Jessie Dotson, Michael Haas, Jeffrey Kolodziejczak, Jeffrey Van Cleve, Hema Chandrasekaran, Joseph D. Twicken, Elisa V. Quintana, Bruce D. Clarke, Christopher Allen, Jie Li, Haley Wu, Peter Tenenbaum, Ekaterina Verner, Frederick Bruhweiler, Jason Barnes, and Andrej Prsa. Kepler Planet-Detection Mission: Introduction and First Results. *Science*, 327(5968):977, February 2010. doi: 10.1126/science.1185402.

[37] W. F. Bottke, R. J. Walker, J. M. D. Day, D. Nesvorny, and L. Elkins-Tanton. Stochastic Late Accretion to Earth, the Moon, and Mars. *Science*, 330:1527, December 2010. doi: 10.1126/science.1196874.

[38] Steve Bryson, Michelle Kunimoto, Ravi K Kopparapu, Jeffrey L Coughlin, William J Borucki, David Koch, Victor Silva Aguirre, Christopher Allen, Geert Barentsen, Natalie M Batalha, et al. The occurrence of rocky habitable-zone planets around solar-like stars from kepler data. *The Astronomical Journal*, 161(1):36, 2020.

[39] Steve Bryson, Michelle Kunimoto, Ravi K. Kopparapu, Jeffrey L. Coughlin, William J. Borucki, David Koch, Victor Silva Aguirre, Christopher Allen, Geert Barentsen, Natalie M. Batalha, Travis Berger, Alan Boss, Lars A. Buchhave, Christopher J. Burke, Douglas A. Caldwell, Jennifer R. Campbell, Joseph Catanzarite, Hema Chandrasekaran, William J. Chaplin, Jessie L. Christiansen, Jørgen Christensen-Dalsgaard, David R. Ciardi, Bruce D. Clarke, William D. Cochran, Jessie L. Dotson, Laurance R. Doyle, Eduardo Seperuelo Duarte, Edward W. Dunham, Andrea K. Dupree, Michael Endl, James L. Fanson, Eric B. Ford, Maura Fujieh, III Gautier, Thomas N., John C. Geary, Ronald L. Gilliland, Forrest R. Girouard, Alan Gould, Michael R. Haas, Christopher E. Henze, Matthew J. Holman, Andrew W. Howard, Steve B. Howell, Daniel Huber, Roger C. Hunter, Jon M. Jenkins, Hans Kjeldsen, Jeffery Kolodziejczak, Kipp Larson, David W. Latham, Jie Li, Savita Mathur, Søren Meibom, Chris Middour, Robert L. Morris, Timothy D. Morton, Fergal Mullally, Susan E. Mullally, David Pletcher, Andrej Prsa, Samuel N. Quinn, Elisa V. Quintana, Darin Ragozzine, Solange V. Ramirez, Dwight T. Sanderfer, Dimitar Sasselov, Shawn E. Seader, Megan Shabram, Avi Shporer, Jeffrey C. Smith, Jason H. Steffen, Martin Still, Guillermo Torres, John Troeltzsch, Joseph D. Twicken, Akm Kamal Uddin, Jeffrey E. Van Cleve, Janice Voss, Lauren M. Weiss, William F. Welsh, Bill Wohler, and Khadeejah A. Zamudio. The

Occurrence of Rocky Habitable-zone Planets around Solar-like Stars from Kepler Data. ,
161(1):36, January 2021. doi: 10.3847/1538-3881/abc418.

[40] A. S. Burrows. Spectra as windows into exoplanet atmospheres. *Proceedings of the National Academy of Science*, 111:12601–12609, September 2014. doi: 10.1073/pnas.1304208111.

[41] S. Candelaresi, A. Hillier, H. Maehara, A. Brand enburg, and K. Shibata. Superflare Occurrence and Energies on G-, K-, and M-type Dwarfs. *The Astrophysical Journal*, 792(1):67, Sep 2014. doi: 10.1088/0004-637X/792/1/67.

[42] L. Carone, R. Keppens, and L. Decin. Connecting the dots - II. Phase changes in the climate dynamics of tidally locked terrestrial exoplanets. *Monthly Notices of the Royal Astronomical Society*, 453:2412–2437, November 2015. doi: 10.1093/mnras/stv1752.

[43] L. Carone, R. Keppens, L. Decin, and T. Henning. Stratosphere circulation on tidally locked ExoEarths. *Monthly Notices of the Royal Astronomical Society*, 473:4672–4685, February 2018. doi: 10.1093/mnras/stx2732.

[44] Pierre Cartigny, Françoise Pineau, Cyril Aubaud, and Marc Javoy. Towards a consistent mantle carbon flux estimate: Insights from volatile systematics (h2o/ce, δd, co2/nb) in the north atlantic mantle (14 n and 34 n). *Earth and Planetary Science Letters*, 265(3-4):672–685, 2008.

[45] D. C. Catling, J. Krissansen-Totton, N. Y. Kiang, D. Crisp, T. D. Robinson, S. DasSarma, A. J. Rushby, A. Del Genio, W. Bains, and S. Domagal-Goldman. Exoplanet Biosignatures: A Framework for Their Assessment. *Astrobiology*, 18:709–738, June 2018. doi: 10.1089/ast.2017.1737.

[46] J. E. Chambers. Making More Terrestrial Planets. *Icarus*, 152:205–224, August 2001. doi: 10.1006/icar.2001.6639.

[47] J. E. Chambers. Planetary accretion in the inner Solar System. *Earth and Planetary Science Letters*, 223:241–252, July 2004. doi: 10.1016/j.epsl.2004.04.031.

[48] J. Checlair, K. Menou, and D. S. Abbot. No Snowball on Habitable Tidally Locked Planets. *The Astrophysical Journal*, 845:132, August 2017. doi: 10.3847/1538-4357/aa80e1.

[49] Jade Checlair, Christopher P. McKay, and Hiroshi Imanaka. Titan-like exoplanets: Variations in geometric albedo and effective transit height with haze production rate. *Planetary & Space Sciences*, 129:1–12, September 2016. doi: 10.1016/j.pss.2016.03.012.

[50] Jade H. Checlair, Stephanie L. Olson, Malte F. Jansen, and Dorian S. Abbot. No Snowball on Habitable Tidally Locked Planets with a Dynamic Ocean. *The Astrophysical Journal Letters*, 884(2):L46, Oct 2019. doi: 10.3847/2041-8213/ab487d.

[51] Jade H. Checlair, Geronimo L. Villanueva, Benjamin P. C. Hayworth, Stephanie L. Olson, Thaddeus D. Komacek, Tyler D. Robinson, Predrag Popović, Huanzhou Yang, and Dorian S. Abbot. Probing the Capability of Future Direct-imaging Missions to Spectrally Constrain the Frequency of Earth-like Planets. , 161(3):150, March 2021. doi: 10.3847/1538-3881/abdb36.

[52] Guo Chen, Enric Pallé, Hannu Parviainen, Felipe Murgas, and Fei Yan. Evidence for TiO in the Atmosphere of the Hot Jupiter HAT-P-65 b. *The Astrophysical Journal Letters*, 913(1): L16, May 2021. doi: 10.3847/2041-8213/abfbe1.

[53] H. Chen and L. A. Rogers. Evolutionary Analysis of Gaseous Sub-Neptune-mass Planets with MESA. *The Astrophysical Journal*, 831:180, November 2016. doi: 10.3847/0004-637X/831/2/180.

[54] H. Chen, J. C. Forbes, and A. Loeb. Habitable Evaporated Cores and the Occurrence of Panspermia Near the Galactic Center. *The Astrophysical Journal Letters*, 855:L1, March 2018. doi: 10.3847/2041-8213/aaab46.

[55] Howard Chen, Eric T. Wolf, Zhuchang Zhan, and Daniel E. Horton. Habitability and Spectroscopic Observability of Warm M-dwarf Exoplanets Evaluated with a 3D Chemistry-Climate Model. *The Astrophysical Journal*, 886(1):16, Nov 2019. doi: 10.3847/1538-4357/ab4f7e.

[56] Howard Chen, Zhuchang Zhan, Allison Youngblood, Eric T Wolf, Adina D Feinstein, and Daniel E Horton. Persistence of flare-driven atmospheric chemistry on rocky habitable zone worlds. *Nature Astronomy*, 5(3):298–310, 2021.

[57] Han Chi, Rajdeep Dasgupta, Megan S. Duncan, and Nobumichi Shimizu. Partitioning of carbon between Fe-rich alloy melt and silicate melt in a magma ocean - Implications for the abundance and origin of volatiles in Earth, Mars, and the Moon. *Geochimica et Cosmochimica Acta*, 139:447–471, August 2014. doi: 10.1016/j.gca.2014.04.046.

[58] Ulrich R. Christensen, Volkmar Holzwarth, and Ansgar Reiners. Energy Flux Determines Magnetic Field Strength of Planets and Stars. *Nature*, 457(7226):167–169, January 2009. doi: 10.1038/nature07626.

[59] Katy L. Chubb, Michiel Min, Yui Kawashima, Christiane Helling, and Ingo Waldmann. Aluminium oxide in the atmosphere of hot Jupiter WASP-43b. *Astronomy & Astrophysics*, 639:A3, July 2020. doi: 10.1051/0004-6361/201937267.

[60] E. W. Cliver, A. G. Ling, A. Belov, and S. Yashiro. Size distributions of solar flares and solar energetic particle events. *The Astrophysical Journal Letters*, 756(2):L29, September 2012. doi: 10.1088/2041-8205/756/2/L29.

[61] Ofer Cohen, C. Garraffo, Sofia-Paraskevi Moschou, Jeremy J. Drake, J. D. Alvarado-Gómez, Alex Glocer, and Federico Fraschetti. The Space Environment and Atmospheric

Joule Heating of the Habitable Zone Exoplanet TOI 700 d. *The Astrophysical Journal*, 897 (1):101, July 2020. doi: 10.3847/1538-4357/ab9637.

[62] William D Collins, Cecilia M Bitz, Maurice L Blackmon, Gordon B Bonan, Christopher S Bretherton, James A Carton, Ping Chang, Scott C Doney, James J Hack, Thomas B Henderson, et al. The community climate system model version 3 (ccsm3). *Journal of Climate*, 19 (11):2122–2143, 2006.

[63] Paul A. Dalba, Stephen R. Kane, Thomas Barclay, Jacob L. Bean, Tiago L. Campante, Joshua Pepper, Darin Ragozzine, and Margaret C. Turnbull. Predicted Yield of Transits of Known Radial Velocity Exoplanets from the TESS Primary and Extended Missions. *Publications of the Astronomical Society of the Pacific*, 131(997):034401, March 2019. doi: 10.1088/1538-3873/aaf183.

[64] Celia Dalou, Marc M Hirschmann, Anette von der Handt, Jed Mosenfelder, and Lora S Armstrong. Nitrogen and carbon fractionation during core–mantle differentiation at shallow depth. *Earth and Planetary Science Letters*, 458:141–151, 2017.

[65] Gokhan Danabasoglu and Peter R Gent. Equilibrium climate sensitivity: Is it accurate to use a slab ocean model? *Journal of Climate*, 22(9):2494–2499, 2009.

[66] Rajdeep Dasgupta, Han Chi, Nobumichi Shimizu, Antonio S. Buono, and David Walker. Carbon solution and partitioning between metallic and silicate melts in a shallow magma ocean: Implications for the origin and distribution of terrestrial carbon. *Geochimica et Cosmochimica Acta*, 102:191–212, February 2013. doi: 10.1016/j.gca.2012.10.011.

[67] James R. A. Davenport. The Kepler Catalog of Stellar Flares. *The Astrophysical Journal*, 829(1):23, September 2016. doi: 10.3847/0004-637X/829/1/23.

[68] D De Niem, E Kührt, A Morbidelli, and U Motschmann. Atmospheric erosion and replenishment induced by impacts upon the earth and mars during a heavy bombardment. *Icarus*, 221(2):495–507, 2012.

[69] Julien de Wit, Hannah R. Wakeford, Nikole K. Lewis, Laetitia Delrez, Michaël Gillon, Frank Selsis, Jérémy Leconte, Brice-Olivier Demory, Emeline Bolmont, Vincent Bourrier, Adam J. Burgasser, Simon Grimm, Emmanuël Jehin, Susan M. Lederer, James E. Owen, Vlada Stamenković, and Amaury H. M. J. Triaud. Atmospheric reconnaissance of the habitable-zone Earth-sized planets orbiting TRAPPIST-1. *Nature Astronomy*, 2:214–219, March 2018. doi: 10.1038/s41550-017-0374-z.

[70] Renaud Deguen, Peter Olson, and Philippe Cardin. Experiments on turbulent metal-silicate mixing in a magma ocean. *Earth and Planetary Science Letters*, 310(3-4):303–313, 2011.

[71] A. D. del Genio, W. Zhou, and T. P. Eichler. Equatorial superrotation in a slowly rotating GCM - Implications for Titan and Venus. *Icarus*, 101:1–17, January 1993. doi: 10.1006/icar.1993.1001.

[72] A. D. Del Genio, M. J. Way, D. S. Amundsen, I. Aleinov, M. Kelley, N. Y. Kiang, and T. L. Clune. Habitable Climate Scenarios for Proxima Centauri b with a Dynamic Ocean. *Astrobiology*, 19:99–125, January 2019. doi: 10.1089/ast.2017.1760.

[73] D. J. Des Marais, M. O. Harwit, K. W. Jucks, J. F. Kasting, D. N. C. Lin, J. I. Lunine, J. Schneider, S. Seager, W. A. Traub, and N. J. Woolf. Remote Sensing of Planetary Properties and Biosignatures on Extrasolar Terrestrial Planets. *Astrobiology*, 2:153–181, June 2002. doi: 10.1089/15311070260192246.

[74] Noah S Diffenbaugh, Deepti Singh, Justin S Mankin, Daniel E Horton, Daniel L Swain, Danielle Touma, Allison Charland, Yunjie Liu, Matz Haugen, Michael Tsiang, et al. Quantifying the influence of global warming on unprecedented extreme climate events. *Proceedings of the National Academy of Sciences*, 114(19):4881–4886, 2017.

[75] J. A. Dittmann, J. M. Irwin, D. Charbonneau, X. Bonfils, N. Astudillo-Defru, R. D. Haywood, Z. K. Berta-Thompson, E. R. Newton, J. E. Rodriguez, J. G. Winters, T.-G. Tan, J.-M. Almenara, F. Bouchy, X. Delfosse, T. Forveille, C. Lovis, F. Murgas, F. Pepe, N. C. Santos, S. Udry, A. Wünsche, G. A. Esquerdo, D. W. Latham, and C. D. Dressing. A temperate rocky super-Earth transiting a nearby cool star. *Nature*, 544:333–336, April 2017. doi: 10.1038/nature22055.

[76] S. D. Domagal-Goldman, V. S. Meadows, M. W. Claire, and J. F. Kasting. Using Biogenic Sulfur Gases as Remotely Detectable Biosignatures on Anoxic Planets. *Astrobiology*, 11: 419–441, June 2011. doi: 10.1089/ast.2010.0509.

[77] Shawn D. Domagal-Goldman, Victoria S. Meadows, Mark W. Claire, and James F. Kasting. Using Biogenic Sulfur Gases as Remotely Detectable Biosignatures on Anoxic Planets. *Astrobiology*, 11(5):419–441, June 2011. doi: 10.1089/ast.2010.0509.

[78] T. M. Donahue, J. H. Hoffman, R. R. Hodges, and A. J. Watson. Venus Was Wet: A Measurement of the Ratio of Deuterium to Hydrogen. *Science*, 216(4546):630–633, May 1982. doi: 10.1126/science.216.4546.630.

[79] Chuanfei Dong, Zhenguang Huang, Manasvi Lingam, Gábor Tóth, Tamas Gombosi, and Amitava Bhattacharjee. The Dehydration of Water Worlds via Atmospheric Losses. *The Astrophysical Journall*, 847(1):L4, September 2017. doi: 10.3847/2041-8213/aa8a60.

[80] Chuanfei Dong, Zhenguang Huang, Manasvi Lingam, Gábor Tóth, Tamas Gombosi, and Amitava Bhattacharjee. The dehydration of water worlds via atmospheric losses. *The Astrophysical Journal Letters*, 847(1):L4, 2017.

[81] Alexandra E Doyle, Edward D Young, Beth Klein, Ben Zuckerman, and Hilke E Schlichting. Oxygen fugacities of extrasolar rocks: evidence for an earth-like geochemistry of exoplanets. *Science*, 366(6463):356–359, 2019.

[82] D. Dragomir, J. Teske, M. N. Günther, D. Ségransan, J. A. Burt, C. X. Huang, A. Vanderburg, E. Matthews, X. Dumusque, K. G. Stassun, J. Pepper, G. R. Ricker, R. Vanderspek, D. W. Latham, S. Seager, J. N. Winn, J. M. Jenkins, T. Beatty, F. Bouchy, T. M. Brown, R. P. Butler, D. R. Ciardi, J. D. Crane, J. D. Eastman, L. Fossati, J. Francis, B. J. Fulton, B. S. Gaudi, R. F. Goeke, D. James, T. C. Klaus, R. B. Kuhn, C. Lovis, M. B. Lund, S. McDermott, M. Paegert, F. Pepe, J. E. Rodriguez, L. Sha, S. A. Shectman, A. Shporer, R. J. Siverd, A. Garcia Soto, D. J. Stevens, J. D. Twicken, S. Udry, S. Villanueva, Jr., S. X. Wang, B. Wohler, X. Yao, and Z. Zhan. TESS Delivers Its First Earth-sized Planet and a Warm Sub-Neptune. *The Astrophysical Journal Letters*, 875:L7, April 2019. doi: 10.3847/2041-8213/ab12ed.

[83] M. J. Drake and K. Righter. Determining the composition of the Earth. *Nature*, 416:39–44, March 2002. doi: 10.1038/416039a.

[84] C. D. Dressing and D. Charbonneau. The Occurrence of Potentially Habitable Planets Orbiting M Dwarfs Estimated from the Full Kepler Dataset and an Empirical Measurement of the Detection Sensitivity. *The Astrophysical Journal*, 807:45, July 2015. doi: 10.1088/0004-637X/807/1/45.

[85] Benjamin Drummond, Eric Hébrard, Nathan J. Mayne, Olivia Venot, Robert J. Ridgway, Quentin Changeat, Shang-Min Tsai, James Manners, Pascal Tremblin, Nathan Luke Abraham, David Sing, and Krisztian Kohary. Implications of three-dimensional chemical transport in hot Jupiter atmospheres: Results from a consistently coupled chemistry-radiation-hydrodynamics model. *Astronomy & Astrophysics*, 636:A68, April 2020. doi: 10.1051/0004-6361/201937153.

[86] Jake K. Eager, David J. Reichelt, Nathan J. Mayne, F. Hugo Lambert, Denis E. Sergeev, Robert J. Ridgway, James Manners, Ian A. Boutle, Timothy M. Lenton, and Krisztian Kohary. Implications of different stellar spectra for the climate of tidally locked Earth-like exoplanets. *Astronomy & Astrophysics*, 639:A99, July 2020. doi: 10.1051/0004-6361/202038089.

[87] A. Edson, S. Lee, P. Bannon, J. F. Kasting, and D. Pollard. Atmospheric circulations of terrestrial planets orbiting low-mass stars. *Icarus*, 212:1–13, March 2011. doi: 10.1016/j.icarus.2010.11.023.

[88] Larissa M. Ejzak, Adrian L. Melott, Mikhail V. Medvedev, and Brian C. Thomas. Terrestrial Consequences of Spectral and Temporal Variability in Ionizing Photon Events. *The Astrophyiscal Journal*, 654(1):373–384, January 2007. doi: 10.1086/509106.

[89] L. T. Elkins-Tanton. Linked magma ocean solidification and atmospheric growth for Earth and Mars. *Earth and Planetary Science Letters*, 271:181–191, July 2008. doi: 10.1016/j.epsl.2008.03.062.

[90] N. V. Erkaev, H. Lammer, L. T. Elkins-Tanton, A. Stökl, P. Odert, E. Marcq, E. A. Dorfi, K. G. Kislyakova, Y. N. Kulikov, M. Leitzinger, and M. Güdel. Escape of the martian

protoatmosphere and initial water inventory. *Planet. Space Sci.*, 98:106–119, August 2014. doi: 10.1016/j.pss.2013.09.008.

[91] Thomas J. Fauchez, Martin Turbet, Geronimo L. Villanueva, Eric T. Wolf, Giada Arney, Ravi K. Kopparapu, Andrew Lincowski, Avi Mandell, Julien de Wit, Daria Pidhorodetska, Shawn D. Domagal-Goldman, and Kevin B. Stevenson. Impact of Clouds and Hazes on the Simulated JWST Transmission Spectra of Habitable Zone Planets in the TRAPPIST-1 System. *The Astrophysical Journal*, 887(2):194, December 2019. doi: 10.3847/1538-4357/ab5862.

[92] Adina Feinstein, Benjamin Montet, and Megan Ansdell. stella: Convolutional Neural Networks for Flare Identification in TESS. *The Journal of Open Source Software*, 5(52):2347, August 2020. doi: 10.21105/joss.02347.

[93] Adina D. Feinstein, Benjamin T. Montet, Megan Ansdell, Brian Nord, Jacob L. Bean, Maximilian N. Günther, Michael A. Gully-Santiago, and Joshua E. Schlieder. Flare Statistics for Young Stars from a Convolutional Neural Network Analysis of *TESS* Data. *arXiv e-prints*, art. arXiv:2005.07710, May 2020.

[94] VI Fomichev, J-P Blanchet, and DS Turner. Matrix parameterization of the 15 μm co2band cooling in the middle and upper atmosphere for variable co2concentration. *Journal of Geophysical Research: Atmospheres*, 103(D10):11505–11528, 1998.

[95] K. France, C. S. Froning, J. L. Linsky, A. Roberge, J. T. Stocke, F. Tian, R. Bushinsky, J.-M. Désert, P. Mauas, M. Vieytes, and L. M. Walkowicz. The Ultraviolet Radiation Environment around M dwarf Exoplanet Host Stars. *The Astrophysical Journal*, 763:149, February 2013. doi: 10.1088/0004-637X/763/2/149.

[96] K. France, R. O. P. Loyd, A. Youngblood, A. Brown, P. C. Schneider, S. L. Hawley, C. S. Froning, J. L. Linsky, A. Roberge, A. P. Buccino, J. R. A. Davenport, J. M. Fontenla, L. Kaltenegger, A. F. Kowalski, P. J. D. Mauas, Y. Miguel, S. Redfield, S. Rugheimer, F. Tian, M. C. Vieytes, L. M. Walkowicz, and K. L. Weisenburger. The MUSCLES Treasury Survey. I. Motivation and Overview. *The Astrophysical Journal*, 820:89, April 2016. doi: 10.3847/0004-637X/820/2/89.

[97] E. Franciosini, R. Pallavicini, and G. Tagliaferri. BeppoSAX observation of a large long-duration X-ray flare from UX Arietis. *Astronomy & Astrophysics*, 375:196–204, Aug 2001. doi: 10.1051/0004-6361:20010830.

[98] Cynthia S. Froning, Adam Kowalski, Kevin France, R. O. Parke Loyd, P. Christian Schneider, Allison Youngblood, David Wilson, Alexander Brown, Zachory Berta-Thompson, J. Sebastian Pineda, Jeffrey Linsky, Sarah Rugheimer, and Yamila Miguel. A Hot Ultraviolet Flare on the M Dwarf Star GJ 674. *The Astrophysical Journall*, 871(2):L26, February 2019. doi: 10.3847/2041-8213/aaffcd.

[99] Y. Fujii, A. D. Del Genio, and D. S. Amundsen. NIR-driven Moist Upper Atmospheres of Synchronously Rotating Temperate Terrestrial Exoplanets. *The Astrophysical Journal*, 848: 100, October 2017. doi: 10.3847/1538-4357/aa8955.

[100] B Funke, M López-Puertas, S Gil-López, T Von Clarmann, GP Stiller, H Fischer, and S Kellmann. Downward transport of upper atmospheric nox into the polar stratosphere and lower mesosphere during the antarctic 2003 and arctic 2002/2003 winters. *Journal of Geophysical Research: Atmospheres*, 110(D24), 2005.

[101] Peter Gao, Renyu Hu, Tyler D. Robinson, Cheng Li, and Yuk L. Yung. Stability of CO2 Atmospheres on Desiccated M Dwarf Exoplanets. *The Astrophysical Journal*, 806(2):249, June 2015. doi: 10.1088/0004-637X/806/2/249.

[102] B. Scott Gaudi, Sara Seager, Bertrand Mennesson, Alina Kiessling, Keith Warfield, Kerri Cahoy, John T. Clarke, Shawn Domagal-Goldman, Lee Feinberg, Olivier Guyon, Jeremy Kasdin, Dimitri Mawet, Peter Plavchan, Tyler Robinson, Leslie Rogers, Paul Scowen, Rachel Somerville, Karl Stapelfeldt, Christopher Stark, Daniel Stern, Margaret Turnbull, Rashied Amini, Gary Kuan, Stefan Martin, Rhonda Morgan, David Redding, H. Philip Stahl, Ryan Webb, Oscar Alvarez-Salazar, William L. Arnold, Manan Arya, Bala Balasubramanian, Mike Baysinger, Ray Bell, Chris Below, Jonathan Benson, Lindsey Blais, Jeff Booth, Robert Bourgeois, Case Bradford, Alden Brewer, Thomas Brooks, Eric Cady, Mary Caldwell, Rob Calvet, Steven Carr, Derek Chan, Velibor Cormarkovic, Keith Coste, Charlie Cox, Rolf Danner, Jacqueline Davis, Larry Dewell, Lisa Dorsett, Daniel Dunn, Matthew East, Michael Effinger, Ron Eng, Greg Freebury, Jay Garcia, Jonathan Gaskin, Suzan Greene, John Hennessy, Evan Hilgemann, Brad Hood, Wolfgang Holota, Scott Howe, Pei Huang, Tony Hull, Ron Hunt, Kevin Hurd, Sandra Johnson, Andrew Kissil, Brent Knight, Daniel Kolenz, Oliver Kraus, John Krist, Mary Li, Doug Lisman, Milan Mandic, John Mann, Luis Marchen, Colleen Marrese-Reading, Jonathan McCready, Jim McGown, Jessica Missun, Andrew Miyaguchi, Bradley Moore, Bijan Nemati, Shouleh Nikzad, Joel Nissen, Megan Novicki, Todd Perrine, Claudia Pineda, Otto Polanco, Dustin Putnam, Atif Qureshi, Michael Richards, A. J. Eldorado Riggs, Michael Rodgers, Mike Rud, Navtej Saini, Dan Scalisi, Dan Scharf, Kevin Schulz, Gene Serabyn, Norbert Sigrist, Glory Sikkia, Andrew Singleton, Stuart Shaklan, Scott Smith, Bart Southerd, Mark Stahl, John Steeves, Brian Sturges, Chris Sullivan, Hao Tang, Neil Taras, Jonathan Tesch, Melissa Therrell, Howard Tseng, Marty Valente, David Van Buren, Juan Villalvazo, Steve Warwick, David Webb, Thomas Westerhoff, Rush Wofford, Gordon Wu, Jahning Woo, Milana Wood, John Ziemer, Giada Arney, Jay Anderson, Jesús Maíz-Apellániz, James Bartlett, Ruslan Belikov, Eduardo Bendek, Brad Cenko, Ewan Douglas, Shannon Dulz, Chris Evans, Virginie Faramaz, Y. Katherina Feng, Harry Ferguson, Kate Follette, Saavik Ford, Miriam García, Marla Geha, Dawn Gelino, Ylva Götberg, Sergi Hildebrandt, Renyu Hu, Knud Jahnke, Grant Kennedy, Laura Kreidberg, Andrea Isella, Eric Lopez, Franck Marchis, Lucas Macri, Mark Marley, William Matzko, Johan Mazoyer, Stephan McCandliss, Tiffany Meshkat, Christoph Mordasini, Patrick Morris, Eric Nielsen, Patrick Newman, Erik Petigura, Marc Postman, Amy Reines, Aki Roberge, Ian

Roederer, Garreth Ruane, Edouard Schwieterman, Dan Sirbu, Christopher Spalding, Harry Teplitz, Jason Tumlinson, Neal Turner, Jessica Werk, Aida Wofford, Mark Wyatt, Amber Young, and Rob Zellem. The Habitable Exoplanet Observatory (HabEx) Mission Concept Study Final Report. *arXiv e-prints*, art. arXiv:2001.06683, January 2020.

[103] H. Genda and Y. Abe. Survival of a proto-atmosphere through the stage of giant impacts: the mechanical aspects. *Icarus*, 164:149–162, July 2003. doi: 10.1016/S0019-1035(03)00101-5.

[104] H. Genda and Y. Abe. Enhanced atmospheric loss on protoplanets at the giant impact phase in the presence of oceans. *Nature*, 433:842–844, February 2005. doi: 10.1038/nature03360.

[105] Adrian E Gill. Some simple solutions for heat-induced tropical circulation. *Quarterly Journal of the Royal Meteorological Society*, 106(449):447–462, 1980.

[106] M. Gillon, A. H. M. J. Triaud, B.-O. Demory, E. Jehin, E. Agol, K. M. Deck, S. M. Lederer, J. de Wit, A. Burdanov, J. G. Ingalls, E. Bolmont, J. Leconte, S. N. Raymond, F. Selsis, M. Turbet, K. Barkaoui, A. Burgasser, M. R. Burleigh, S. J. Carey, A. Chaushev, C. M. Copperwheat, L. Delrez, C. S. Fernandes, D. L. Holdsworth, E. J. Kotze, V. Van Grootel, Y. Almleaky, Z. Benkhaldoun, P. Magain, and D. Queloz. Seven temperate terrestrial planets around the nearby ultracool dwarf star TRAPPIST-1. *Nature*, 542:456–460, February 2017. doi: 10.1038/nature21360.

[107] A. Glocer, G. Tóth, T. Gombosi, and D. Welling. Modeling ionospheric outflows and their impact on the magnetosphere, initial results. *Journal of Geophysical Research (Space Physics)*, 114(A5):A05216, May 2009. doi: 10.1029/2009JA014053.

[108] Colin Goldblatt, Mark W Claire, Timothy M Lenton, Adrian J Matthews, Andrew J Watson, and Kevin J Zahnle. Nitrogen-enhanced greenhouse warming on early earth. *Nature Geoscience*, 2(12):891–896, 2009.

[109] N. Gopalswamy, H. Xie, S. Yashiro, S. Akiyama, P. Mäkelä, and I. G. Usoskin. Properties of Ground Level Enhancement Events and the Associated Solar Eruptions During Solar Cycle 23. *Space Science Reviews*, 171(1-4):23–60, October 2012. doi: 10.1007/s11214-012-9890-4.

[110] Iouli E Gordon, Laurence S Rothman, Christian Hill, Roman V Kochanov, Y Tan, Peter F Bernath, Manfred Birk, V Boudon, Alain Campargue, KV Chance, et al. The hitran2016 molecular spectroscopic database. *Journal of Quantitative Spectroscopy and Radiative Transfer*, 203:3–69, 2017.

[111] R. O. Gray, C. J. Corbally, R. F. Garrison, M. T. McFadden, E. J. Bubar, C. E. McGahee, A. A. O'Donoghue, and E. R. Knox. Contributions to the Nearby Stars (NStars) Project: Spectroscopy of Stars Earlier than M0 within 40 pc-The Southern Sample. *The Astronomical Journal*, 132(1):161–170, July 2006. doi: 10.1086/504637.

[112] James Green, Scott Boardsen, and Chuanfei Dong. Magnetospheres of terrestrial exoplanets and exomoons: Implications for habitability and detection. *The Astrophysical Journal Letters*, 907(2):L45, 2021.

[113] T. P. Greene, M. R. Line, C. Montero, J. J. Fortney, J. Lustig-Yaeger, and K. Luther. Characterizing Transiting Exoplanet Atmospheres with JWST. *The Astrophysical Journal*, 817: 17, January 2016. doi: 10.3847/0004-637X/817/1/17.

[114] John Lee Grenfell, Jean-Mathias Grießmeier, Philip von Paris, A. Beate C. Patzer, Helmut Lammer, Barbara Stracke, Stefanie Gebauer, Franz Schreier, and Heike Rauer. Response of Atmospheric Biomarkers to NOx-Induced Photochemistry Generated by Stellar Cosmic Rays for Earth-like Planets in the Habitable Zone of M Dwarf Stars. *Astrobiology*, 12:1109–1122, Dec 2012. doi: 10.1089/ast.2011.0682.

[115] Damanveer S. Grewal, Rajdeep Dasgupta, Chenguang Sun, Kyusei Tsuno, and Gelu Costin. Delivery of carbon, nitrogen, and sulfur to the silicate Earth by a giant impact. *Science Advances*, 5(1):eaau3669, January 2019. doi: 10.1126/sciadv.aau3669.

[116] Damanveer S Grewal, Rajdeep Dasgupta, and Alexandra Farnell. The speciation of carbon, nitrogen, and water in magma oceans and its effect on volatile partitioning between major reservoirs of the solar system rocky bodies. *Geochimica et Cosmochimica Acta*, 280:281–301, 2020.

[117] S. L. Grimm, B.-O. Demory, M. Gillon, C. Dorn, E. Agol, A. Burdanov, L. Delrez, M. Sestovic, A. H. M. J. Triaud, M. Turbet, É. Bolmont, A. Caldas, J. de Wit, E. Jehin, J. Leconte, S. N. Raymond, V. Van Grootel, A. J. Burgasser, S. Carey, D. Fabrycky, K. Heng, D. M. Hernandez, J. G. Ingalls, S. Lederer, F. Selsis, and D. Queloz. The nature of the TRAPPIST-1 exoplanets. *Astronomy & Astrophysics*, 613:A68, May 2018. doi: 10.1051/0004-6361/201732233.

[118] Simon L. Grimm, Brice-Olivier Demory, Michaël Gillon, Caroline Dorn, Eric Agol, Artem Burdanov, Laetitia Delrez, Marko Sestovic, Amaury H. M. J. Triaud, Martin Turbet, Émeline Bolmont, Anthony Caldas, Julien de Wit, Emmanuël Jehin, Jérémy Leconte, Sean N. Raymond, Valérie Van Grootel, Adam J. Burgasser, Sean Carey, Daniel Fabrycky, Kevin Heng, David M. Hernandez, James G. Ingalls, Susan Lederer, Franck Selsis, and Didier Queloz. The nature of the TRAPPIST-1 exoplanets. *Astronomy & Astrophysics*, 613:A68, May 2018. doi: 10.1051/0004-6361/201732233.

[119] D. H. Grinspoon. Was Venus Wet? Deuterium Reconsidered. *Science*, 238(4834):1702–1704, December 1987. doi: 10.1126/science.238.4834.1702.

[120] M. Güdel, M. Audard, F. Reale, S. L. Skinner, and J. L. Linsky. Flares from small to large: X-ray spectroscopy of Proxima Centauri with XMM-Newton. *Astronomy & Astrophysics*, 416:713–732, March 2004. doi: 10.1051/0004-6361:20031471.

[121] M. N. Günther, Z. Zhan, S. Seager, P. B. Rimmer, S. Ranjan, K. G. Stassun, R. J. Oelkers, T. Daylan, E. Newton, E. Gillen, S. Rappaport, G. R. Ricker, D. W. Latham, J. N. Winn, J. M. Jenkins, A. Glidden, M. Fausnaugh, A. M. Levine, J. A. Dittmann, S. N. Quinn, A. Krishnamurthy, and E. B. Ting. Stellar Flares from the First Tess Data Release: Exploring a New Sample of M-dwarfs. *arXiv e-prints*, January 2019.

[122] Maximilian N. Günther, Zhuchang Zhan, Sara Seager, Paul B. Rimmer, Sukrit Ranjan, Keivan G. Stassun, Ryan J. Oelkers, Tansu Daylan, Elisabeth Newton, Martti H. Kristiansen, Katalin Olah, Edward Gillen, Saul Rappaport, George R. Ricker, Roland K. Vanderspek, David W. Latham, Joshua N. Winn, Jon M. Jenkins, Ana Glidden, Michael Fausnaugh, Alan M. Levine, Jason A. Dittmann, Samuel N. Quinn, Akshata Krishnamurthy, and Eric B. Ting. Stellar Flares from the First TESS Data Release: Exploring a New Sample of M Dwarfs. *The Astronomical Journal*, 159(2):60, February 2020. doi: 10.3847/1538-3881/ab5d3a.

[123] J. J. Hack. Parameterization of moist convection in the National Center for Atmospheric Research community climate model (CCM2). , 99:5551–5568, March 1994. doi: 10.1029/93JD03478.

[124] Alex N. Halliday. The origins of volatiles in the terrestrial planets. *Geochimica et Cosmochimica Acta*, 105:146–171, March 2013. doi: 10.1016/j.gca.2012.11.015.

[125] J. Haqq-Misra, E. T. Wolf, M. Joshi, X. Zhang, and R. K. Kopparapu. Demarcating Circulation Regimes of Synchronously Rotating Terrestrial Planets within the Habitable Zone. *The Astrophysical Journal*, 852:67, January 2018. doi: 10.3847/1538-4357/aa9f1f.

[126] J. D. Haqq-Misra, S. D. Domagal-Goldman, P. J. Kasting, and J. F. Kasting. A Revised, Hazy Methane Greenhouse for the Archean Earth. *Astrobiology*, 8:1127–1137, December 2008. doi: 10.1089/ast.2007.0197.

[127] C. E. Harman, E. W. Schwieterman, J. C. Schottelkotte, and J. F. Kasting. Abiotic O_2 Levels on Planets around F, G, K, and M Stars: Possible False Positives for Life? *The Astrophysical Journal*, 812(2):137, October 2015. doi: 10.1088/0004-637X/812/2/137.

[128] C. E. Harman, Ravi Kumar Kopparapu, Guðmundur Stefánsson, Andrea S. J. Lin, Suvrath Mahadevan, Christina Hedges, and Natasha E. Batalha. A Snowball in Hell: The Potential Steam Atmosphere of TOI-1266c. *arXiv e-prints*, art. arXiv:2109.10838, September 2021.

[129] M. H. Hart. Habitable Zones about Main Sequence Stars. *Icarus*, 37:351–357, January 1979. doi: 10.1016/0019-1035(79)90141-6.

[130] Suzanne L. Hawley and Bjorn R. Pettersen. The Great Flare of 1985 April 12 on AD Leonis. *The Astrophysical Journal*, 378:725, September 1991. doi: 10.1086/170474.

[131] Suzanne L. Hawley, James R. A. Davenport, Adam F. Kowalski, John P. Wisniewski, Leslie Hebb, Russell Deitrick, and Eric J. Hilton. Kepler Flares. I. Active and Inactive M Dwarfs. *The Astrophysical Journal*, 797(2):121, December 2014. doi: 10.1088/0004-637X/797/2/121.

[132] Chushiro Hayashi. Structure of the solar nebula, growth and decay of magnetic fields and effects of magnetic and turbulent viscosities on the nebula. *Progress of Theoretical Physics Supplement*, 70:35–53, 1981.

[133] P. H. Haynes, M. E. McIntyre, T. G. Shepherd, C. J. Marks, and K. P. Shine. On the 'Downward Control' of Extratropical Diabatic Circulations by Eddy-Induced Mean Zonal Forces. *Journal of Atmospheric Sciences*, 48:651–680, February 1991. doi: 10.1175/1520-0469(1991) 048<0651:OTCOED>2.0.CO;2.

[134] I. M. Held and M. J. Suarez. A Proposal for the Intercomparison of the Dynamical Cores of Atmospheric General Circulation Models. *Bulletin of the American Meteorological Society*, 75:1825–1830, October 1994. doi: 10.1175/1520-0477(1994)075<1825:APFTIO>2.0.CO;2.

[135] K. Heng. A Cloudiness Index for Transiting Exoplanets Based on the Sodium and Potassium Lines: Tentative Evidence for Hotter Atmospheres Being Less Cloudy at Visible Wavelengths. *The Astrophysical Journal Letters*, 826:L16, July 2016. doi: 10.3847/2041-8205/826/ 1/L16.

[136] T. J. Henry, W.-C. Jao, J. P. Subasavage, T. D. Beaulieu, P. A. Ianna, E. Costa, and R. A. Méndez. The Solar Neighborhood. XVII. Parallax Results from the CTIOPI 0.9 m Program: 20 New Members of the RECONS 10 Parsec Sample. , 132:2360–2371, December 2006. doi: 10.1086/508233.

[137] Konstantin Herbst, John Lee Grenfell, Miriam Sinnhuber, Heike Rauer, Bernd Heber, Saša Banjac, Markus Scheucher, Vanessa Schmidt, Stefanie Gebauer, Ralph Lehmann, and Franz Schreier. A new model suite to determine the influence of cosmic rays on (exo)planetary atmospheric biosignatures. Validation based on modern Earth. *Astronomy & Astrophysics*, 631:A101, November 2019. doi: 10.1051/0004-6361/201935888.

[138] Konstantin Herbst, Athanasios Papaioannou, Saša Banjac, and Bernd Heber. From solar to stellar flare characteristics. On a new peak size distribution for G-, K-, and M-dwarf star flares. *Astronomy & Astrophysics*, 621:A67, Jan 2019. doi: 10.1051/0004-6361/201832789.

[139] Eric J. Hilton. *The Galactic M Dwarf Flare Rate*. PhD thesis, University of Washington, January 2011.

[140] Marc M. Hirschmann. Constraints on the early delivery and fractionation of Earth's major volatiles from C/H, C/N, and C/S ratios. *American Mineralogist*, 101(3):540–553, March 2016. doi: 10.2138/am-2016-5452.

[141] Marc M Hirschmann, Edwin A Bergin, Geoff A Blake, Fred J Ciesla, and Jie Li. Early volatile depletion on planetesimals inferred from c–s systematics of iron meteorite parent bodies. *Proceedings of the National Academy of Sciences*, 118(13), 2021.

[142] G. Holland and C. J. Ballentine. Seawater subduction controls the heavy noble gas composition of the mantle. *Nature*, 441:186–191, May 2006. doi: 10.1038/nature04761.

[143] J. R. Holton, P. H. Haynes, M. E. McIntyre, A. R. Douglass, R. B. Rood, and L. Pfister. Stratosphere-troposphere exchange. *Reviews of Geophysics*, 33:403–439, November 1995. doi: 10.1029/95RG02097.

[144] Daniel E Horton, Christopher J Poulsen, Isabel P Montañez, and William A DiMichele. Eccentricity-paced late paleozoic climate change. *Palaeogeography, Palaeoclimatology, Palaeoecology*, 331:150–161, 2012.

[145] Daniel E Horton, Nathaniel C Johnson, Deepti Singh, Daniel L Swain, Bala Rajaratnam, and Noah S Diffenbaugh. Contribution of changes in atmospheric circulation patterns to extreme temperature trends. *Nature*, 522(7557):465, 2015.

[146] Ward S. Howard and Nicholas M. Law. EvryFlare. IV. Detection of Periodicity in Flare Occurrence from Cool Stars with TESS. *The Astrophysical Journal*, 920(1):42, October 2021. doi: 10.3847/1538-4357/ac142a.

[147] Danley C. Hsu, Eric B. Ford, Darin Ragozzine, and Keir Ashby. Occurrence Rates of Planets Orbiting FGK Stars: Combining Kepler DR25, Gaia DR2, and Bayesian Inference. *The Astronomical Journal*, 158(3):109, September 2019. doi: 10.3847/1538-3881/ab31ab.

[148] R. Hu, S. Seager, and W. Bains. Photochemistry in Terrestrial Exoplanet Atmospheres. I. Photochemistry Model and Benchmark Cases. *The Astrophysical Journal*, 761:166, December 2012. doi: 10.1088/0004-637X/761/2/166.

[149] R. Hu, S. Seager, and W. Bains. Photochemistry in Terrestrial Exoplanet Atmospheres. I. Photochemistry Model and Benchmark Cases. *The Astrophysical Journal*, 761:166, December 2012. doi: 10.1088/0004-637X/761/2/166.

[150] Renyu Hu, Sara Seager, and William Bains. Photochemistry in Terrestrial Exoplanet Atmospheres. II. H_2S and SO_2 Photochemistry in Anoxic Atmospheres. , 769(1):6, May 2013. doi: 10.1088/0004-637X/769/1/6.

[151] D. M. Hunten. The Escape of Light Gases from Planetary Atmospheres. *Journal of Atmospheric Sciences*, 30:1481–1494, November 1973. doi: 10.1175/1520-0469(1973)030<1481: TEOLGF>2.0.CO;2.

[152] T.-O. Husser, S. Wende-von Berg, S. Dreizler, D. Homeier, A. Reiners, T. Barman, and P. H. Hauschildt. A new extensive library of PHOENIX stellar atmospheres and synthetic spectra. *Astronomy & Astrophysics*, 553:A6, May 2013. doi: 10.1051/0004-6361/201219058.

[153] Shigeru Ida and Junichiro Makino. Scattering of planetesimals by a protoplanet: Slowing down of runaway growth. *Icarus*, 106(1):210–227, 1993.

[154] CH Jackman, DR Marsh, FM Vitt, RR Garcia, EL Fleming, GJ Labow, CE Randall, M López-Puertas, B Funke, T von Clarmann, et al. Short-and medium-term atmospheric constituent effects of very large solar proton events. *Atmospheric Chemistry and Physics*, 8 (3):765–785, 2008.

[155] Charles H. Jackman, Matthew T. Deland, Gordon J. Labow, Eric L. Fleming, Debra K. Weisenstein, Malcolm K. W. Ko, Miriam Sinnhuber, and James M. Russell. Neutral Atmospheric Influences of the Solar Proton Events in October-November 2003. *Journal of Geophysical Research (Space Physics)*, 110(A9):A09S27, September 2005. doi: 10.1029/2004JA010888.

[156] Charles H Jackman, Matthew T DeLand, Gordon J Labow, Eric L Fleming, Debra K Weisenstein, Malcolm KW Ko, Miriam Sinnhuber, and James M Russell. Neutral atmospheric influences of the solar proton events in october–november 2003. *Journal of Geophysical Research: Space Physics*, 110(A9), 2005.

[157] Daniel J Jacob. *Introduction to atmospheric chemistry*. Princeton University Press, 1999.

[158] Seth A Jacobson and Alessandro Morbidelli. Lunar and terrestrial planet formation in the grand tack scenario. *Philosophical Transactions of the Royal Society A: Mathematical, Physical and Engineering Sciences*, 372(2024):20130174, 2014.

[159] Seth A Jacobson, Alessandro Morbidelli, Sean N Raymond, David P O'Brien, Kevin J Walsh, and David C Rubie. Highly siderophile elements in earth's mantle as a clock for the moon-forming impact. *Nature*, 508(7494):84–87, 2014.

[160] Ben Johnson and Colin Goldblatt. The nitrogen budget of earth. *Earth-Science Reviews*, 148:150–173, 2015.

[161] M. M. Joshi, R. M. Haberle, and R. T. Reynolds. Simulations of the Atmospheres of Synchronously Rotating Terrestrial Planets Orbiting M Dwarfs: Conditions for Atmospheric Collapse and the Implications for Habitability. *Icarus*, 129:450–465, October 1997. doi: 10.1006/icar.1997.5793.

[162] L. Kaltenegger and D. Sasselov. Detecting Planetary Geochemical Cycles on Exoplanets: Atmospheric Signatures and the Case of SO_2. *The Astrophysical Journal*, 708:1162–1167, January 2010. doi: 10.1088/0004-637X/708/2/1162.

[163] J. F. Kasting. Runaway and moist greenhouse atmospheres and the evolution of earth and Venus. *Icarus*, 74:472–494, June 1988. doi: 10.1016/0019-1035(88)90116-9.

[164] J. F. Kasting and J. B. Pollack. Loss of water from Venus. I - Hydrodynamic escape of hydrogen. *Icarus*, 53:479–508, March 1983. doi: 10.1016/0019-1035(83)90212-9.

[165] J. F. Kasting, J. B. Pollack, and T. P. Ackerman. Response of earth's atmosphere to increases in solar flux and implications for loss of water from Venus. *Icarus*, 57:335–355, March 1984. doi: 10.1016/0019-1035(84)90122-2.

[166] J. F. Kasting, J. B. Pollack, and D. Crisp. Effects of high CO2 levels on surface temperature and atmospheric oxidation state of the early earth. *Journal of Atmospheric Chemistry*, 1: 403–428, 1984. doi: 10.1007/BF00053803.

[167] J. F. Kasting, D. P. Whitmire, and R. T. Reynolds. Habitable Zones around Main Sequence Stars. *Icarus*, 101:108–128, January 1993. doi: 10.1006/icar.1993.1010.

[168] J. F. Kasting, H. Chen, and R. K. Kopparapu. Stratospheric Temperatures and Water Loss from Moist Greenhouse Atmospheres of Earth-like Planets. *The Astrophysical Journal Letters*, 813:L3, November 2015. doi: 10.1088/2041-8205/813/1/L3.

[169] James F Kasting, David Catling, et al. Evolution of a habitable planet. *Annual Review of Astronomy and Astrophysics*, 41(1):429–463, 2003.

[170] James F Kasting, Howard Chen, and Ravi K Kopparapu. Stratospheric temperatures and water loss from moist greenhouse atmospheres of earth-like planets. *The Astrophysical Journal Letters*, 813(1):L3, 2015.

[171] Y. Kawashima and M. Ikoma. Theoretical Transmission Spectra of Exoplanet Atmospheres with Hydrocarbon Haze: Effect of Creation, Growth, and Settling of Haze Particles. I. Model Description and First Results. *The Astrophysical Journal*, 853:7, January 2018. doi: 10.3847/1538-4357/aaa0c5.

[172] Christina Kay, Vladimir S. Airapetian, Theresa Lüftinger, and Oleg Kochukhov. Frequency of Coronal Mass Ejection Impacts with Early Terrestrial Planets and Exoplanets around Active Solar-like Stars. *The Astrophysical Journal Letters*, 886(2):L37, December 2019. doi: 10.3847/2041-8213/ab551f.

[173] JE Kay, C Deser, A Phillips, A Mai, C Hannay, G Strand, JM Arblaster, SC Bates, G Danabasoglu, J Edwards, et al. The community earth system model (cesm) large ensemble project: A community resource for studying climate change in the presence of internal climate variability. *Bulletin of the American Meteorological Society*, 96(8):1333–1349, 2015.

[174] JA Kegerreis, VR Eke, RJ Massey, and LFA Teodoro. Atmospheric erosion by giant impacts onto terrestrial planets. *The Astrophysical Journal*, 897(2):161, 2020.

[175] E. M.-R. Kempton, J. L. Bean, and V. Parmentier. An Observational Diagnostic for Distinguishing between Clouds and Haze in Hot Exoplanet Atmospheres. *The Astrophysical Journal Letters*, 845:L20, August 2017. doi: 10.3847/2041-8213/aa84ac.

[176] AJ Kettle and MO Andreae. Flux of dimethylsulfide from the oceans: A comparison of updated data sets and flux models. *Journal of Geophysical Research: Atmospheres*, 105 (D22):26793–26808, 2000.

[177] JT Kiehl and V Ramanathan. Co2 radiative parameterization used in climate models: Comparison with narrow band models and with laboratory data. *Journal of Geophysical Research: Oceans*, 88(C9):5191–5202, 1983.

[178] C. Kilic, C. C. Raible, and T. F. Stocker. Multiple Climate States of Habitable Exoplanets: The Role of Obliquity and Irradiance. *The Astrophysical Journal*, 844:147, August 2017. doi: 10.3847/1538-4357/aa7a03.

[179] D. E. Kinnison, G. P. Brasseur, S. Walters, R. R. Garcia, D. R. Marsh, F. Sassi, V. L. Harvey, C. E. Randall, L. Emmons, J. F. Lamarque, P. Hess, J. J. Orlando, X. X. Tie, W. Randel, L. L. Pan, A. Gettelman, C. Granier, T. Diehl, U. Niemeier, and A. J. Simmons. Sensitivity of chemical tracers to meteorological parameters in the MOZART-3 chemical transport model. *Journal of Geophysical Research (Atmospheres)*, 112:D20302, October 2007. doi: 10.1029/2006JD007879.

[180] Edwin S. Kite and Megan N. Barnett. Exoplanet secondary atmosphere loss and revival. *Proceedings of the National Academy of Sciences*, 117(31):18264–18271, 2020. ISSN 0027-8424. doi: 10.1073/pnas.2006177117.

[181] Sylvia Kloster, Johann Feichter, Ernst Maier-Reimer, Katharina D Six, Philip Stier, and Patrick Wetzel. Dms cycle in the marine ocean-atmosphere system? a global model study. *Biogeosciences Discussions*, 2(4):1067–1126, 2005.

[182] T. Kodama, A. Nitta, H. Genda, Y. Takao, R. O'ishi, A. Abe-Ouchi, and Y. Abe. Dependence of the Onset of the Runaway Greenhouse Effect on the Latitudinal Surface Water Distribution of Earth-Like Planets. *Journal of Geophysical Research (Planets)*, 123:559–574, February 2018. doi: 10.1002/2017JE005383.

[183] D. D. B. Koll and D. S. Abbot. Temperature Structure and Atmospheric Circulation of Dry Tidally Locked Rocky Exoplanets. *The Astrophysical Journal*, 825:99, July 2016. doi: 10.3847/0004-637X/825/2/99.

[184] D. D. B. Koll, M. Malik, M. Mansfield, E. M.-R. Kempton, E. Kite, D. Abbot, and J. L. Bean. Identifying Candidate Atmospheres on Rocky M dwarf Planets via Eclipse Photometry. *arXiv e-prints*, July 2019.

[185] T. D. Komacek and D. S. Abbot. Effect of Surface-mantle Water Exchange Parameterizations on Exoplanet Ocean Depths. *The Astrophysical Journal*, 832:54, November 2016. doi: 10.3847/0004-637X/832/1/54.

[186] T. D. Komacek and D. S. Abbot. The Atmospheric Circulation and Climate of Terrestrial Planets Orbiting Sun-like and M Dwarf Stars over a Broad Range of Planetary Parameters. *The Astrophysical Journal*, 871:245, February 2019. doi: 10.3847/1538-4357/aafb33.

[187] Thaddeus D. Komacek and Dorian S. Abbot. The Atmospheric Circulation and Climate of Terrestrial Planets Orbiting Sun-like and M Dwarf Stars over a Broad Range of Planetary Parameters. *The Astrophysical Journal*, 871(2):245, February 2019. doi: 10.3847/1538-4357/aafb33.

[188] Thaddeus D. Komacek, Thomas J. Fauchez, Eric T. Wolf, and Dorian S. Abbot. Clouds will Likely Prevent the Detection of Water Vapor in JWST Transmission Spectra of Terrestrial Exoplanets. *The Astrophysical Journal Letters*, 888(2):L20, Jan 2020. doi: 10.3847/2041-8213/ab6200.

[189] R. K. Kopparapu, R. Ramirez, J. F. Kasting, V. Eymet, T. D. Robinson, S. Mahadevan, R. C. Terrien, S. Domagal-Goldman, V. Meadows, and R. Deshpande. Habitable Zones around Main-sequence Stars: New Estimates. *The Astrophysical Journal*, 765:131, March 2013. doi: 10.1088/0004-637X/765/2/131.

[190] R. k. Kopparapu, E. T. Wolf, J. Haqq-Misra, J. Yang, J. F. Kasting, V. Meadows, R. Terrien, and S. Mahadevan. The Inner Edge of the Habitable Zone for Synchronously Rotating Planets around Low-mass Stars Using General Circulation Models. *The Astrophysical Journal*, 819:84, March 2016. doi: 10.3847/0004-637X/819/1/84.

[191] R. k. Kopparapu, E. T. Wolf, G. Arney, N. E. Batalha, J. Haqq-Misra, S. L. Grimm, and K. Heng. Habitable Moist Atmospheres on Terrestrial Planets near the Inner Edge of the Habitable Zone around M Dwarfs. *The Astrophysical Journal*, 845:5, August 2017. doi: 10.3847/1538-4357/aa7cf9.

[192] Ravi Kumar Kopparapu. A Revised Estimate of the Occurrence Rate of Terrestrial Planets in the Habitable Zones around Kepler M-dwarfs. *The Astrophysical Journal Letters*, 767(1): L8, Apr 2013. doi: 10.1088/2041-8205/767/1/L8.

[193] Adam F. Kowalski, Suzanne L. Hawley, John P. Wisniewski, Rachel A. Osten, Eric J. Hilton, Jon A. Holtzman, Sarah J. Schmidt, and James R. A. Davenport. Time-resolved Properties and Global Trends in dMe Flares from Simultaneous Photometry and Spectra. *The Astrophysical Journal Supplement Series*, 207(1):15, Jul 2013. doi: 10.1088/0067-0049/207/1/15.

[194] T. Kozakis, L. Kaltenegger, and D. W. Hoard. UV Surface Environments and Atmospheres of Earth-like Planets Orbiting White Dwarfs. *The Astrophysical Journal*, 862:69, July 2018. doi: 10.3847/1538-4357/aacbc7.

[195] L. Kreidberg and A. Loeb. Prospects for Characterizing the Atmosphere of Proxima Centauri b. *The Astrophysical Journal Letters*, 832:L12, November 2016. doi: 10.3847/2041-8205/832/1/L12.

[196] L. Kreidberg, J. L. Bean, J.-M. Désert, B. Benneke, D. Deming, K. B. Stevenson, S. Seager, Z. Berta-Thompson, A. Seifahrt, and D. Homeier. Clouds in the atmosphere of the super-Earth exoplanet GJ1214b. *Nature*, 505:69–72, January 2014. doi: 10.1038/nature12888.

[197] Andreas F Krenn, Luca Fossati, Daria Kubyshkina, and Helmut Lammer. A critical assessment of the applicability of the energy-limited approximation for estimating exoplanetary mass-loss rates. *arXiv preprint arXiv:2105.05858*, 2021.

[198] Joshua Krissansen-Totton, Stephanie Olson, and David C. Catling. Disequilibrium Biosignatures over Earth History and Implications for Detecting Exoplanet Life. *Science Advances*, 4(1):eaao5747, January 2018. doi: 10.1126/sciadv.aao5747.

[199] J.-F. Lamarque, L. K. Emmons, P. G. Hess, D. E. Kinnison, S. Tilmes, F. Vitt, C. L. Heald, E. A. Holland, P. H. Lauritzen, J. Neu, J. J. Orlando, P. J. Rasch, and G. K. Tyndall. CAM-chem: description and evaluation of interactive atmospheric chemistry in the Community Earth System Model. *Geoscientific Model Development*, 5:369–411, March 2012. doi: 10.5194/gmd-5-369-2012.

[200] Erik J. L. Larson, Owen B. Toon, Robert A. West, and A. James Friedson. Microphysical modeling of Titan's detached haze layer in a 3D GCM. *Icarus*, 254:122–134, July 2015. doi: 10.1016/j.icarus.2015.03.010.

[201] J. Lean. Evolution of the Sun's Spectral Irradiance Since the Maunder Minimum. *Geophysical Research Letters*, 27:2425–2428, August 2000. doi: 10.1029/2000GL000043.

[202] Judith Lean, Juerg Beer, and Raymond Bradley. Reconstruction of solar irradiance since 1610: Implications for climate change. *Geophysical Research Letters*, 22(23):3195–3198, 1995.

[203] J. Leconte, F. Forget, B. Charnay, R. Wordsworth, and A. Pottier. Increased insolation threshold for runaway greenhouse processes on Earth-like planets. *Nature*, 504:268–271, December 2013. doi: 10.1038/nature12827.

[204] J. Leconte, F. Forget, B. Charnay, R. Wordsworth, F. Selsis, E. Millour, and A. Spiga. 3D climate modeling of close-in land planets: Circulation patterns, climate moist bistability, and habitability. *Astronomy & Astrophysics*, 554:A69, June 2013. doi: 10.1051/0004-6361/201321042.

[205] J. Leconte, H. Wu, K. Menou, and N. Murray. Asynchronous rotation of Earth-mass planets in the habitable zone of lower-mass stars. *Science*, 347:632–635, February 2015. doi: 10.1126/science.1258686.

[206] O. R. Lehmer, D. C. Catling, M. N. Parenteau, and T. M. Hoehler. The Productivity of Oxygenic Photosynthesis around Cool, M Dwarf Stars. *The Astrophysical Journal*, 859:171, June 2018. doi: 10.3847/1538-4357/aac104.

[207] N. K. Lewis, H. R. Wakeford, R. J. MacDonald, J. M. Goyal, D. K. Sing, J. Barstow, D. Powell, T. Kataria, I. Mishra, M. S. Marley, N. E. Batalha, J. I. Moses, P. Gao, T. J. Wilson, K. L. Chubb, T. Mikal-Evans, N. Nikolov, N. Pirzkal, J. J. Spake, K. B. Stevenson, J. Valenti, and

X. Zhang. Into the UV: The Atmosphere of the Hot Jupiter HAT-P-41b Revealed. *The Astrophysical Journal Letters*, 902(1):L19, October 2020. doi: 10.3847/2041-8213/abb77f.

[208] N. T. Lewis, F. H. Lambert, I. A. Boutle, N. J. Mayne, J. Manners, and D. M. Acreman. The Influence of a Substellar Continent on the Climate of a Tidally Locked Exoplanet. *The Astrophysical Journal*, 854:171, February 2018. doi: 10.3847/1538-4357/aaad0a.

[209] A. P. Lincowski, V. S. Meadows, D. Crisp, T. D. Robinson, R. Luger, J. Lustig-Yaeger, and G. N. Arney. Evolved Climates and Observational Discriminants for the TRAPPIST-1 Planetary System. *The Astrophysical Journal*, 867:76, November 2018. doi: 10.3847/1538-4357/aae36a.

[210] M. Lingam and A. Loeb. Reduced Diversity of Life around Proxima Centauri and TRAPPIST-1. *The Astrophysical Journal Letters*, 846:L21, September 2017. doi: 10.3847/2041-8213/aa8860.

[211] M. Lingam and A. Loeb. Is life most likely around Sun-like stars? , 5:020, May 2018. doi: 10.1088/1475-7516/2018/05/020.

[212] M. Lingam and A. Loeb. Dependence of Biological Activity on the Surface Water Fraction of Planets. , 157:25, January 2019. doi: 10.3847/1538-3881/aaf420.

[213] M. Lingam and A. Loeb. Photosynthesis on habitable planets around low-mass stars. *Monthly Notices of the Royal Astronomical Society*, 485:5924–5928, June 2019. doi: 10.1093/mnras/stz847.

[214] Jeffrey L. Linsky. Stellar Model Chromospheres and Spectroscopic Diagnostics. *Annual Review of Astronomy and Astrophysics*, 55(1):159–211, August 2017. doi: 10.1146/annurev-astro-091916-055327.

[215] Katharina Lodders. Solar system abundances and condensation temperatures of the elements. *The Astrophysical Journal*, 591(2):1220, 2003.

[216] M. López-Puertas, B. Funke, S. Gil-López, T. von Clarmann, G. P. Stiller, M. Höpfner, S. Kellmann, H. Fischer, and C. H. Jackman. Observation of NO_x enhancement and ozone depletion in the Northern and Southern Hemispheres after the October-November 2003 solar proton events. *Journal of Geophysical Research (Space Physics)*, 110(A9):A09S43, September 2005. doi: 10.1029/2005JA011050.

[217] J. M. Lora, T. Kataria, and P. Gao. Atmospheric Circulation, Chemistry, and Infrared Spectra of Titan-like Exoplanets around Different Stellar Types. *The Astrophysical Journal*, 853:58, January 2018. doi: 10.3847/1538-4357/aaa132.

[218] J. E. Lovelock. Thermodynamics and the Recognition of Alien Biospheres. *Proceedings of the Royal Society of London Series B*, 189:167–180, May 1975. doi: 10.1098/rspb.1975.0051.

[219] R. O. P. Loyd, K. France, A. Youngblood, C. Schneider, A. Brown, R. Hu, J. Linsky, C. S. Froning, S. Redfield, S. Rugheimer, and F. Tian. The MUSCLES Treasury Survey. III. X-Ray to Infrared Spectra of 11 M and K Stars Hosting Planets. *The Astrophysical Journal*, 824:102, June 2016. doi: 10.3847/0004-637X/824/2/102.

[220] R. O. P. Loyd, K. France, A. Youngblood, C. Schneider, A. Brown, R. Hu, A. Segura, J. Linsky, S. Redfield, F. Tian, S. Rugheimer, Y. Miguel, and C. S. Froning. The MUSCLES Treasury Survey. V. FUV Flares on Active and Inactive M Dwarfs. *The Astrophysical Journal*, 867:71, November 2018. doi: 10.3847/1538-4357/aae2bd.

[221] R. O. Park Loyd, Evgenya L. Shkolnik, Adam C. Schneider, Travis S. Barman, Victoria S. Meadows, Isabella Pagano, and Sarah Peacock. HAZMAT. IV. Flares and Superflares on Young M Stars in the Far Ultraviolet. *The Astrophysical Journal*, 867(1):70, Nov 2018. doi: 10.3847/1538-4357/aae2ae.

[222] R. Luger and R. Barnes. Extreme Water Loss and Abiotic O2Buildup on Planets Throughout the Habitable Zones of M Dwarfs. *Astrobiology*, 15:119–143, February 2015. doi: 10.1089/ast.2014.1231.

[223] Jacob Lustig-Yaeger, Victoria S. Meadows, and Andrew P. Lincowski. The Detectability and Characterization of the TRAPPIST-1 Exoplanet Atmospheres with JWST. , 158(1):27, July 2019. doi: 10.3847/1538-3881/ab21e0.

[224] Timothy W Lyons, Christopher T Reinhard, and Noah J Planavsky. The rise of oxygen in earth's early ocean and atmosphere. *Nature*, 506(7488):307–315, 2014.

[225] C MacFarling Meure, D Etheridge, C Trudinger, P Steele, R Langenfelds, T Van Ommen, A Smith, and J Elkins. Law dome co2, ch4 and n2o ice core records extended to 2000 years bp. *Geophysical Research Letters*, 33(14), 2006.

[226] M. Malik, E. M.-R. Kempton, D. D. B. Koll, M. Mansfield, J. L. Bean, and E. Kite. Analyzing Atmospheric Temperature Profiles and Spectra of M dwarf Rocky Planets. *arXiv e-prints*, July 2019.

[227] A. W. Mann, G. A. Feiden, E. Gaidos, T. Boyajian, and K. von Braun. How to Constrain Your M Dwarf: Measuring Effective Temperature, Bolometric Luminosity, Mass, and Radius. *The Astrophysical Journal*, 804:64, May 2015. doi: 10.1088/0004-637X/804/1/64.

[228] Megan Mansfield, Michael R. Line, Jacob L. Bean, Jonathan J. Fortney, Vivien Parmentier, Lindsey Wiser, Eliza M. R. Kempton, Ehsan Gharib-Nezhad, David K. Sing, Mercedes López-Morales, Claire Baxter, Jean-Michel Désert, Mark R. Swain, and Gael M. Roudier. A unique hot Jupiter spectral sequence with evidence for compositional diversity. *Nature Astronomy*, October 2021. doi: 10.1038/s41550-021-01455-4.

[229] D. R. Marsh, M. J. Mills, D. E. Kinnison, J.-F. Lamarque, N. Calvo, and L. M. Polvani. Climate Change from 1850 to 2005 Simulated in CESM1(WACCM). *Journal of Climate*, 26:7372–7391, October 2013. doi: 10.1175/JCLI-D-12-00558.1.

[230] B. Marty. The origins and concentrations of water, carbon, nitrogen and noble gases on Earth. *Earth and Planetary Science Letters*, 313:56–66, January 2012. doi: 10.1016/j.epsl.2011.10.040.

[231] B. Marty, G. Avice, Y. Sano, K. Altwegg, H. Balsiger, M. Hässig, A. Morbidelli, O. Mousis, and M. Rubin. Origins of volatile elements (H, C, N, noble gases) on Earth and Mars in light of recent results from the ROSETTA cometary mission. *Earth and Planetary Science Letters*, 441:91–102, May 2016. doi: 10.1016/j.epsl.2016.02.031.

[232] Bernard Marty, Matthieu Almayrac, Peter H Barry, David V Bekaert, Michael W Broadley, David J Byrne, Christopher J Ballentine, and Antonio Caracausi. An evaluation of the c/n ratio of the mantle from natural co2-rich gas analysis: Geochemical and cosmochemical implications. *Earth and Planetary Science Letters*, 551:116574, 2020.

[233] T. Matsui and Y. Abe. Evolution of an impact-induced atmosphere and magma ocean on the accreting earth. *Nature*, 319:303–305, January 1986. doi: 10.1038/319303a0.

[234] Taroh Matsuno. Quasi-geostrophic motions in the equatorial area. *Journal of the Meteorological Society of Japan. Ser. II*, 44(1):25–43, 1966.

[235] E. M. May, J. Taylor, T. D. Komacek, M. R. Line, and V. Parmentier. Water Ice Cloud Variability and Multi-epoch Transmission Spectra of TRAPPIST-1e. *The Astrophysical Journal Letters*, 911(2):L30, April 2021. doi: 10.3847/2041-8213/abeeff.

[236] Patrick J McGovern and Gerald Schubert. Thermal evolution of the earth: effects of volatile exchange between atmosphere and interior. *Earth and planetary science letters*, 96(1-2): 27–37, 1989.

[237] V. S. Meadows, G. N. Arney, E. W. Schwieterman, J. Lustig-Yaeger, A. P. Lincowski, T. Robinson, S. D. Domagal-Goldman, R. Deitrick, R. K. Barnes, D. P. Fleming, R. Luger, P. E. Driscoll, T. R. Quinn, and D. Crisp. The Habitability of Proxima Centauri b: Environmental States and Observational Discriminants. *Astrobiology*, 18:133–189, February 2018. doi: 10.1089/ast.2016.1589.

[238] V. S. Meadows, C. T. Reinhard, G. N. Arney, M. N. Parenteau, E. W. Schwieterman, S. D. Domagal-Goldman, A. P. Lincowski, K. R. Stapelfeldt, H. Rauer, S. DasSarma, S. Hegde, N. Narita, R. Deitrick, J. Lustig-Yaeger, T. W. Lyons, N. Siegler, and J. L. Grenfell. Exoplanet Biosignatures: Understanding Oxygen as a Biosignature in the Context of Its Environment. *Astrobiology*, 18:630–662, June 2018. doi: 10.1089/ast.2017.1727.

[239] Victoria S. Meadows, Christopher T. Reinhard, Giada N. Arney, Mary N. Parenteau, Edward W. Schwieterman, Shawn D. Domagal-Goldman, Andrew P. Lincowski, Karl R. Stapelfeldt, Heike Rauer, Shiladitya DasSarma, Siddharth Hegde, Norio Narita, Russell Deitrick, Jacob Lustig-Yaeger, Timothy W. Lyons, Nicholas Siegler, and J. Lee Grenfell. Exoplanet Biosignatures: Understanding Oxygen as a Biosignature in the Context of Its Environment. *Astrobiology*, 18(6):630–662, June 2018. doi: 10.1089/ast.2017.1727.

[240] Abel Méndez, Edgard G. Rivera-Valentín, Dirk Schulze-Makuch, Justin Filiberto, Ramses Ramírez, Tana E. Wood, Alfonso Dávila, Chris McKay, Kevin Ortiz Ceballos, Marcos Jusino-Maldonado, Guillermo Nery, René Heller, Paul Byrne, Michael J. Malaska, Erica Nathan, Marta Filipa Simões, André Antunes, Jesús Martínez-Frías, Ludmila Carone, Noam R. Izenberg, Dimitra Atri, Humberto Itic Carvajal Chitty, Priscilla Nowajewski-Barra, Frances Rivera-Hernández, Corine Brown, Kennda Lynch, David Catling, Jorge I. Zuluaga, Juan F. Salazar, Howard Chen, Grizelle González, Madhu Kashyap Jagadeesh, Rory Barnes, Charles S. Cockell, and Jacob Haqq-Misra. Habitability Models for Planetary Sciences. *arXiv e-prints*, art. arXiv:2007.05491, July 2020.

[241] Michael Mendillo, Paul Withers, and Paul A. Dalba. Atomic oxygen ions as ionospheric biomarkers on exoplanets. *Nature Astronomy*, 2:287–291, February 2018. doi: 10.1038/s41550-017-0375-y.

[242] B. Mennesson, S. Gaudi, S. Seager, K. Cahoy, S. Domagal-Goldman, L. Feinberg, O. Guyon, J. Kasdin, C. Marois, D. Mawet, M. Tamura, D. Mouillet, T. Prusti, A. Quirrenbach, T. Robinson, L. Rogers, P. Scowen, R. Somerville, K. Stapelfeldt, D. Stern, M. Still, M. Turnbull, J. Booth, A. Kiessling, G. Kuan, and K. Warfield. The Habitable Exoplanet (HabEx) Imaging Mission: preliminary science drivers and technical requirements. In *Space Telescopes and Instrumentation 2016: Optical, Infrared, and Millimeter Wave*, volume 9904 of *Proceedeings of SPIE*, page 99040L, July 2016. doi: 10.1117/12.2240457.

[243] T. M. Merlis and T. Schneider. Atmospheric dynamics of Earth-like tidally locked aquaplanets. *Journal of Advances in Modeling Earth Systems*, 2:13, December 2010. doi: 10.3894/JAMES.2010.2.13.

[244] E. Miller-Ricci, M. R. Meyer, S. Seager, and L. Elkins-Tanton. On the Emergent Spectra of Hot Protoplanet Collision Afterglows. *The Astrophysical Journal*, 704:770–780, October 2009. doi: 10.1088/0004-637X/704/1/770.

[245] Anastasia Montgomery and Tracey Holloway. Assessing the relationship between satellite-derived no2 and economic growth over the 100 most populous global cities. *Journal of Applied Remote Sensing*, 12(4):042607, 2018.

[246] Sarah E. Moran, Sarah M. Hörst, Natasha E. Batalha, Nikole K. Lewis, and Hannah R. Wakeford. Limits on Clouds and Hazes for the TRAPPIST-1 Planets. , 156(6):252, December 2018. doi: 10.3847/1538-3881/aae83a.

[247] A. Morbidelli, J. Chambers, J. I. Lunine, J. M. Petit, F. Robert, G. B. Valsecchi, and K. E. Cyr. Source regions and time scales for the delivery of water to Earth. *Meteoritics and Planetary Science*, 35:1309–1320, November 2000. doi: 10.1111/j.1945-5100.2000.tb01518.x.

[248] C. Mordasini. Planetary Evolution with Atmospheric Photoevaporation. I. Analytical Derivation and Numerical Study of the Evaporation Balley and Transition from super-Earths to sub-Neptunes. *Astronomy & Astrophysics*, 638:A52, June 2020. doi: 10.1051/0004-6361/201935541.

[249] C. V. Morley, J. J. Fortney, E. M.-R. Kempton, M. S. Marley, C. Visscher, and K. Zahnle. Quantitatively Assessing the Role of Clouds in the Transmission Spectrum of GJ 1214b. *The Astrophysical Journal*, 775:33, September 2013. doi: 10.1088/0004-637X/775/1/33.

[250] Gijs D. Mulders, Ilaria Pascucci, Dániel Apai, and Fred J. Ciesla. The Exoplanet Population Observation Simulator. I. The Inner Edges of Planetary Systems. *The Astronomical Journal*, 156(1):24, July 2018. doi: 10.3847/1538-3881/aac5ea.

[251] Shinichi Nakajima, Yoshi-Yuki Hayashi, and Yutaka Abe. A study on the "runaway greenhouse effect" with a one-dimensional radiative–convective equilibrium model. *Journal of the Atmospheric Sciences*, 49(23):2256–2266, 1992.

[252] Richard B Neale, Chih-Chieh Chen, Andrew Gettelman, Peter H Lauritzen, Sungsu Park, David L Williamson, Andrew J Conley, Rolando Garcia, Doug Kinnison, Jean-Francois Lamarque, et al. Description of the ncar community atmosphere model (cam 5.0). *NCAR Tech. Note NCAR/TN-486+ STR*, 1(1):1–12, 2010.

[253] D. P. O'Brien, A. Morbidelli, and H. F. Levison. Terrestrial planet formation with strong dynamical friction. *Icarus*, 184:39–58, September 2006. doi: 10.1016/j.icarus.2006.04.005.

[254] D. P. O'Brien, K. J. Walsh, A. Morbidelli, S. N. Raymond, and A. M. Mandell. Water delivery and giant impacts in the Grand Tack scenario. *Icarus*, 239:74–84, September 2014. doi: 10.1016/j.icarus.2014.05.009.

[255] S. L. Olson, E. W. Schwieterman, C. T. Reinhard, A. Ridgwell, S. R. Kane, V. S. Meadows, and T. W. Lyons. Atmospheric Seasonality as an Exoplanet Biosignature. *The Astrophysical Journal Letters*, 858:L14, May 2018. doi: 10.3847/2041-8213/aac171.

[256] Stephanie L Olson, Edward W Schwieterman, Christopher T Reinhard, and Timothy W Lyons. Earth: Atmospheric evolution of a habitable planet. *arXiv preprint arXiv:1803.05967*, 2018.

[257] Stephanie L. Olson, Malte Jansen, and Dorian S. Abbot. Oceanographic Considerations for Exoplanet Life Detection. *The Astrophysical Journal*, 895(1):19, May 2020. doi: 10.3847/1538-4357/ab88c9.

[258] J. T. O'Malley-James and L. Kaltenegger. UV surface habitability of the TRAPPIST-1 system. *Monthly Notices of the Royal Astronomical Society*, 469:L26–L30, July 2017. doi: 10.1093/mnrasl/slx047.

[259] T. Owen, A. Bar-Nun, and I. Kleinfeld. Possible cometary origin of heavy noble gases in the atmospheres of Venus, earth, and Mars. *Nature*, 358:43–46, July 1992. doi: 10.1038/358043a0.

[260] A. Paradise and K. Menou. GCM Simulations of Unstable Climates in the Habitable Zone. *The Astrophysical Journal*, 848:33, October 2017. doi: 10.3847/1538-4357/aa8b1c.

[261] AA Pavlov and JF Kasting. Mass-independent fractionation of sulfur isotopes in archean sediments: strong evidence for an anoxic archean atmosphere. *Astrobiology*, 2(1):27–41, 2002.

[262] Rebecca C Payne, Amber V Britt, Howard Chen, James F Kasting, and David C Catling. The response of phanerozoic surface temperature to variations in atmospheric oxygen concentration. *Journal of Geophysical Research: Atmospheres*, 121(17):10–089, 2016.

[263] Sarah Peacock, Travis Barman, Evgenya L. Shkolnik, Peter H. Hauschildt, and E. Baron. Predicting the Extreme Ultraviolet Radiation Environment of Exoplanets around Low-mass Stars: The TRAPPIST-1 System. *The Astrophysical Journal*, 871(2):235, Feb 2019. doi: 10.3847/1538-4357/aaf891.

[264] R. O. Pepin. On the origin and early evolution of terrestrial planet atmospheres and meteoritic volatiles. *Icarus*, 92:2–79, July 1991. doi: 10.1016/0019-1035(91)90036-S.

[265] R. O. Pepin. Evolution of Earth's Noble Gases: Consequences of Assuming Hydrodynamic Loss Driven by Giant Impact. *Icarus*, 126:148–156, March 1997. doi: 10.1006/icar.1996.5639.

[266] Josh Pettit, CE Randall, DR Marsh, CG Bardeen, L Qian, CH Jackman, TN Woods, A Coster, and VL Harvey. Effects of the september 2005 solar flares and solar proton events on the middle atmosphere in waccm. *Journal of Geophysical Research: Space Physics*, 2018.

[267] D. Porcelli and G. J. Wasserburg. Mass transfer of helium, neon, argon, and xenon through a steady-state upper mantle. *Geochimica et Cosmochimica Acta*, 59:4921–4937, December 1995. doi: 10.1016/0016-7037(95)00336-3.

[268] D. Porcelli, D. Woolum, and P. Cassen. Deep Earth rare gases: initial inventories, capture from the solar nebula, and losses during Moon formation. *Earth and Planetary Science Letters*, 193:237–251, November 2001. doi: 10.1016/S0012-821X(01)00493-9.

[269] H. S. Porter, C. H. Jackman, and A. E. S. Green. Efficiencies for production of atomic nitrogen and oxygen by relativistic proton impact in air. *The Journal of Chemical Physics*, 65(1):154–167, July 1976. doi: 10.1063/1.432812.

[270] Christopher J. Poulsen, Clay Tabor, and Joseph D. White. Long-term climate forcing by atmospheric oxygen concentrations. *Science*, 348(6240):1238–1241, June 2015. doi: 10.1126/science.1260670.

[271] E. Proedrou and K. Hocke. Characterising the three-dimensional ozone distribution of a tidally locked Earth-like planet. *Earth, Planets, and Space*, 68:96, June 2016. doi: 10.1186/s40623-016-0461-x.

[272] R. M. Ramirez and L. Kaltenegger. A Volcanic Hydrogen Habitable Zone. *The Astrophysical Journal Letters*, 837:L4, March 2017. doi: 10.3847/2041-8213/aa60c8.

[273] S. Ranjan, R. Wordsworth, and D. D. Sasselov. The Surface UV Environment on Planets Orbiting M Dwarfs: Implications for Prebiotic Chemistry and the Need for Experimental Follow-up. *The Astrophysical Journal*, 843:110, July 2017. doi: 10.3847/1538-4357/aa773e.

[274] H. Rauer, S. Gebauer, P. V. Paris, J. Cabrera, M. Godolt, J. L. Grenfell, A. Belu, F. Selsis, P. Hedelt, and F. Schreier. Potential biosignatures in super-Earth atmospheres. I. Spectral appearance of super-Earths around M dwarfs. *Astronomy & Astrophysics*, 529:A8, May 2011. doi: 10.1051/0004-6361/201014368.

[275] S. N. Raymond, T. Quinn, and J. I. Lunine. High-resolution simulations of the final assembly of Earth-like planets I. Terrestrial accretion and dynamics. *Icarus*, 183:265–282, August 2006. doi: 10.1016/j.icarus.2006.03.011.

[276] S. N. Raymond, D. P. O'Brien, A. Morbidelli, and N. A. Kaib. Building the terrestrial planets: Constrained accretion in the inner Solar System. *Icarus*, 203:644–662, October 2009. doi: 10.1016/j.icarus.2009.05.016.

[277] Christopher T Reinhard, Noah J Planavsky, Benjamin C Gill, Kazumi Ozaki, Leslie J Robbins, Timothy W Lyons, Woodward W Fischer, Chunjiang Wang, Devon B Cole, and Kurt O Konhauser. Evolution of the global phosphorus cycle. *Nature*, 541(7637):386–389, 2017.

[278] G. R. Ricker, J. N. Winn, R. Vanderspek, D. W. Latham, G. Á. Bakos, J. L. Bean, Z. K. Berta-Thompson, T. M. Brown, L. Buchhave, N. R. Butler, R. P. Butler, W. J. Chaplin, D. Charbonneau, J. Christensen-Dalsgaard, M. Clampin, D. Deming, J. Doty, N. De Lee, C. Dressing, E. W. Dunham, M. Endl, F. Fressin, J. Ge, T. Henning, M. J. Holman, A. W. Howard, S. Ida, J. Jenkins, G. Jernigan, J. A. Johnson, L. Kaltenegger, N. Kawai, H. Kjeldsen, G. Laughlin, A. M. Levine, D. Lin, J. J. Lissauer, P. MacQueen, G. Marcy, P. R. McCullough, T. D. Morton, N. Narita, M. Paegert, E. Palle, F. Pepe, J. Pepper, A. Quirrenbach, S. A. Rinehart, D. Sasselov, B. Sato, S. Seager, A. Sozzetti, K. G. Stassun, P. Sullivan, A. Szentgyorgyi, G. Torres, S. Udry, and J. Villasenor. Transiting Exoplanet Survey Satellite (TESS). In *Space Telescopes and Instrumentation 2014: Optical, Infrared, and Millimeter Wave*, volume 9143 of *Proceedings of the SPIE*, page 914320, August 2014. doi: 10.1117/12.2063489.

[279] R. G. Roble and E. C. Ridley. A thermosphere-ionosphere-mesosphere-electrodynamics general circulation model (time-GCM): Equinox solar cycle minimum simulations (30-500 km). *Geophysical Research Letters*, 21:417–420, March 1994. doi: 10.1029/93GL03391.

[280] D. Rodgers-Lee, A. A. Vidotto, and A. L. Mesquita. Charting nearby stellar systems: the intensity of Galactic cosmic rays for a sample of solar-type stars. *Monthly Notices of the Royal Astronomical Society*, 508(4):4696–4704, December 2021. doi: 10.1093/mnras/stab2788.

[281] Romy Rodríguez Martínez, Laura A. Lopez, Benjamin J. Shappee, Sarah J. Schmidt, Tharindu Jayasinghe, Christopher S. Kochanek, Katie Auchettl, and Thomas W. S. Holoien. A Catalog of M-dwarf Flares with ASAS-SN. *The Astrophysical Journal*, 892(2):144, April 2020. doi: 10.3847/1538-4357/ab793a.

[282] D. M. Romps and Z. Kuang. Overshooting convection in tropical cyclones. *Geophysical Research Letters*, 36:L09804, May 2009. doi: 10.1029/2009GL037396.

[283] David C Rubie, Seth A Jacobson, Alessandro Morbidelli, David P O'Brien, Edward D Young, Jellie de Vries, Francis Nimmo, Herbert Palme, and Daniel J Frost. Accretion and differentiation of the terrestrial planets with implications for the compositions of early-formed solar system bodies and accretion of water. *Icarus*, 248:89–108, 2015.

[284] S. Rugheimer and L. Kaltenegger. Spectra of Earth-like Planets through Geological Evolution around FGKM Stars. *The Astrophysical Journal*, 854:19, February 2018. doi: 10.3847/1538-4357/aaa47a.

[285] S. Rugheimer, L. Kaltenegger, A. Segura, J. Linsky, and S. Mohanty. Effect of UV Radiation on the Spectral Fingerprints of Earth-like Planets Orbiting M Stars. *The Astrophysical Journal*, 809:57, August 2015. doi: 10.1088/0004-637X/809/1/57.

[286] C. Sagan and C. Chyba. The early faint sun paradox: Organic shielding of ultraviolet-labile greenhouse gases. *Science*, 276:1217–1221, May 1997. doi: 10.1126/science.276.5316.1217.

[287] C. Sagan, W. R. Thompson, R. Carlson, D. Gurnett, and C. Hord. A search for life on Earth from the Galileo spacecraft. *Nature*, 365:715–721, October 1993. doi: 10.1038/365715a0.

[288] Andrea M. Salazar, Stephanie L. Olson, Thaddeus D. Komacek, Haynes Stephens, and Dorian S. Abbot. The Effect of Substellar Continent Size on Ocean Dynamics of Proxima Centauri b. *The Astrophysical Journal Letters*, 896(1):L16, June 2020. doi: 10.3847/2041-8213/ab94c1.

[289] Evangelia Samara, Spiros Patsourakos, and Manolis K. Georgoulis. A Readily Implemented Atmosphere Sustainability Constraint for Terrestrial Exoplanets Orbiting Magnetically Active Stars. *The Astrophysical Journal Letters*, 909(1):L12, March 2021. doi: 10.3847/2041-8213/abe416.

[290] J. Scalo, L. Kaltenegger, A. G. Segura, M. Fridlund, I. Ribas, Y. N. Kulikov, J. L. Grenfell, H. Rauer, P. Odert, M. Leitzinger, F. Selsis, M. L. Khodachenko, C. Eiroa, J. Kasting, and H. Lammer. M Stars as Targets for Terrestrial Exoplanet Searches And Biosignature Detection. *Astrobiology*, 7:85–166, February 2007. doi: 10.1089/ast.2006.0125.

[291] G. G. Schaber, R. G. Strom, H. J. Moore, L. A. Soderblom, R. L. Kirk, D. J. Chadwick, D. D. Dawson, L. R. Gaddis, J. M. Boyce, and J. Russell. Geology and distribution of impact craters on Venus - What are they telling us? , 97:13, August 1992. doi: 10.1029/92JE01246.

[292] Laura Schaefer and Jr. Fegley, Bruce. Redox States of Initial Atmospheres Outgassed on Rocky Planets and Planetesimals. *The Astrophysical Journal*, 843(2):120, July 2017. doi: 10.3847/1538-4357/aa784f.

[293] M. Scheucher, J. L. Grenfell, F. Wunderlich, M. Godolt, F. Schreier, and H. Rauer. New Insights into Cosmic-Ray-induced Biosignature Chemistry in Earth-like Atmospheres. *The Astrophysical Journal*, 863:6, August 2018. doi: 10.3847/1538-4357/aacf03.

[294] Markus Scheucher, J. L. Grenfell, F. Wunderlich, M. Godolt, F. Schreier, and H. Rauer. New Insights into Cosmic-Ray-induced Biosignature Chemistry in Earth-like Atmospheres. *The Astrophysical Journal*, 863(1):6, Aug 2018. doi: 10.3847/1538-4357/aacf03.

[295] H. E. Schlichting, R. Sari, and A. Yalinewich. Atmospheric mass loss during planet formation: The importance of planetesimal impacts. *Icarus*, 247:81–94, February 2015. doi: 10.1016/j.icarus.2014.09.053.

[296] Hilke E Schlichting and Sujoy Mukhopadhyay. Atmosphere impact losses. *Space Science Reviews*, 214(1):1–31, 2018.

[297] Sarah J. Schmidt, Kelle L. Cruz, Bethany J. Bongiorno, James Liebert, and I. Neill Reid. Activity and Kinematics of Ultracool Dwarfs, Including an Amazing Flare Observation. *The Astronomical Journal*, 133(5):2258–2273, May 2007. doi: 10.1086/512158.

[298] E. W. Schwieterman, N. Y. Kiang, M. N. Parenteau, C. E. Harman, S. DasSarma, T. M. Fisher, G. N. Arney, H. E. Hartnett, C. T. Reinhard, S. L. Olson, V. S. Meadows, C. S. Cockell, S. I. Walker, J. L. Grenfell, S. Hegde, S. Rugheimer, R. Hu, and T. W. Lyons. Exoplanet Biosignatures: A Review of Remotely Detectable Signs of Life. *Astrobiology*, 18:663–708, June 2018. doi: 10.1089/ast.2017.1729.

[299] E. W. Schwieterman, C. T. Reinhard, S. L. Olson, C. E. Harman, and T. W. Lyons. A Limited Habitable Zone for Complex Life. *The Astrophysical Journal*, 878:19, June 2019. doi: 10.3847/1538-4357/ab1d52.

[300] S. Seager, D. Deming, and J. A. Valenti. Transiting Exoplanets with JWST. *Astrophysics and Space Science Proceedings*, 10:123, 2009. doi: 10.1007/978-1-4020-9457-6_5.

[301] S. Seager, W. Bains, and R. Hu. A Biomass-based Model to Estimate the Plausibility of Exoplanet Biosignature Gases. *The Astrophysical Journal*, 775:104, October 2013. doi: 10.1088/0004-637X/775/2/104.

[302] A. Segura, K. Krelove, J. F. Kasting, D. Sommerlatt, V. Meadows, D. Crisp, M. Cohen, and E. Mlawer. Ozone Concentrations and Ultraviolet Fluxes on Earth-Like Planets Around Other Stars. *Astrobiology*, 3:689–708, December 2003. doi: 10.1089/153110703322736024.

[303] A. Segura, J. F. Kasting, V. Meadows, M. Cohen, J. Scalo, D. Crisp, R. A. H. Butler, and G. Tinetti. Biosignatures from Earth-Like Planets Around M Dwarfs. *Astrobiology*, 5:706–725, December 2005. doi: 10.1089/ast.2005.5.706.

[304] A. Segura, L. M. Walkowicz, V. Meadows, J. Kasting, and S. Hawley. The Effect of a Strong Stellar Flare on the Atmospheric Chemistry of an Earth-like Planet Orbiting an M Dwarf. *Astrobiology*, 10:751–771, September 2010. doi: 10.1089/ast.2009.0376.

[305] Antígona Segura. *Star-Planet Interactions and Habitability: Radiative Effects*, page 73. Springer, 2018. doi: 10.1007/978-3-319-55333-7_73.

[306] John H Seinfeld and Spyros N Pandis. *Atmospheric chemistry and physics: from air pollution to climate change*. John Wiley & Sons, 2012.

[307] Bálint Seli, Krisztián Vida, Attila Moór, András Pál, and Katalin Oláh. Activity of TRAPPIST-1 analog stars observed with TESS. *Astronomy & Astrophysics*, 650:A138, June 2021. doi: 10.1051/0004-6361/202040098.

[308] F. Selsis, R. D. Wordsworth, and F. Forget. Thermal phase curves of nontransiting terrestrial exoplanets. I. Characterizing atmospheres. *Astronomy & Astrophysics*, 532:A1, August 2011. doi: 10.1051/0004-6361/201116654.

[309] Y. Shen and E. L. Turner. On the Eccentricity Distribution of Exoplanets from Radial Velocity Surveys. *The Astrophysical Journal*, 685:553–559, September 2008. doi: 10.1086/590548.

[310] A. L. Shields, C. M. Bitz, V. S. Meadows, M. M. Joshi, and T. D. Robinson. Spectrum-driven Planetary Deglaciation due to Increases in Stellar Luminosity. *The Astrophysical Journal Letters*, 785:L9, April 2014. doi: 10.1088/2041-8205/785/1/L9.

[311] A. P. Showman and L. M. Polvani. Equatorial Superrotation on Tidally Locked Exoplanets. *The Astrophysical Journal*, 738:71, September 2011. doi: 10.1088/0004-637X/738/1/71.

[312] Catriona A Sinclair, Mark C Wyatt, Alessandro Morbidelli, and David Nesvornỳ. Evolution of the earth's atmosphere during late veneer accretion. *Monthly Notices of the Royal Astronomical Society*, 499(4):5334–5362, 2020.

[313] M. Sinnhuber, H. Nieder, and N. Wieters. Energetic Particle Precipitation and the Chemistry of the Mesosphere/Lower Thermosphere. *Surveys in Geophysics*, 33(6):1281–1334, November 2012. doi: 10.1007/s10712-012-9201-3.

[314] Norman H Sleep and Kevin Zahnle. Carbon dioxide cycling and implications for climate on ancient earth. *Journal of Geophysical Research: Planets*, 106(E1):1373–1399, 2001.

[315] Norman H Sleep, K Zahnle, and PS Neuhoff. Initiation of clement surface conditions on the earliest earth. *Proceedings of the National Academy of Sciences*, 98(7):3666–3672, 2001.

[316] Ingo Sölch and Bernd Kärcher. A large-eddy model for cirrus clouds with explicit aerosol and ice microphysics and lagrangian ice particle tracking. *Quarterly Journal of the Royal Meteorological Society*, 136(653):2074–2093, 2010.

[317] S. Solomon, D. W. Rusch, J. C. Gerard, G. C. Reid, and P. J. Crutzen. The effect of particle precipitation events on the neutral and ion chemistry of the middle atmosphere: II. Odd hydrogen. *Planetary and Space Science*, 29(8):885–893, Aug 1981. doi: 10.1016/0032-0633(81)90078-7.

[318] S. C. Solomon. Formation, history and energetics of cores in the terrestrial planets. *Physics of the Earth and Planetary Interiors*, 19:168–182, June 1979. doi: 10.1016/0031-9201(79)90081-5.

[319] S. C. Solomon and L. Qian. Solar extreme-ultraviolet irradiance for general circulation models. *Journal of Geophysical Research (Space Physics)*, 110:A10306, October 2005. doi: 10.1029/2005JA011160.

[320] B. Stelzer, J. H. M. M. Schmitt, G. Micela, and C. Liefke. Simultaneous optical and X-ray observations of a giant flare on the ultracool dwarf LP 412-31. *Astronomy & Astrophysics*, 460(2):L35–L38, December 2006. doi: 10.1051/0004-6361:20066488.

[321] K. B. Stevenson. Quantifying and Predicting the Presence of Clouds in Exoplanet Atmospheres. *The Astrophysical Journal Letters*, 817:L16, February 2016. doi: 10.3847/2041-8205/817/2/L16.

[322] K. B. Stevenson, J.-M. Désert, M. R. Line, J. L. Bean, J. J. Fortney, A. P. Showman, T. Kataria, L. Kreidberg, P. R. McCullough, G. W. Henry, D. Charbonneau, A. Burrows, S. Seager, N. Madhusudhan, M. H. Williamson, and D. Homeier. Thermal structure of an exoplanet atmosphere from phase-resolved emission spectroscopy. *Science*, 346:838–841, November 2014. doi: 10.1126/science.1256758.

[323] Gabrielle Suissa, Avi M. Mandell, Eric T. Wolf, Geronimo L. Villanueva, Thomas Fauchez, and Ravi kumar Kopparapu. Dim Prospects for Transmission Spectra of Ocean Earths around M Stars. *The Astrophysical Journal*, 891(1):58, March 2020. doi: 10.3847/1538-4357/ab72f9.

[324] F. Tabataba-Vakili, J. L. Grenfell, J. M. Grießmeier, and H. Rauer. Atmospheric effects of stellar cosmic rays on Earth-like exoplanets orbiting M-dwarfs. *Astronomy & Astrophysics*, 585:A96, Jan 2016. doi: 10.1051/0004-6361/201425602.

[325] J. C. Tarter, P. R. Backus, R. L. Mancinelli, J. M. Aurnou, D. E. Backman, G. S. Basri, A. P. Boss, A. Clarke, D. Deming, L. R. Doyle, E. D. Feigelson, F. Freund, D. H. Grinspoon, R. M. Haberle, S. A. Hauck, II, M. J. Heath, T. J. Henry, J. L. Hollingsworth, M. M. Joshi, S. Kilston, M. C. Liu, E. Meikle, I. N. Reid, L. J. Rothschild, J. Scalo, A. Segura, C. M. Tang, J. M. Tiedje, M. C. Turnbull, L. M. Walkowicz, A. L. Weber, and R. E. Young. A Reappraisal of The Habitability of Planets around M Dwarf Stars. *Astrobiology*, 7:30–65, March 2007. doi: 10.1089/ast.2006.0124.

[326] Karl E Taylor, Ronald J Stouffer, and Gerald A Meehl. An overview of cmip5 and the experiment design. *Bulletin of the American Meteorological Society*, 93(4):485–498, 2012.

[327] S. E. Thompson, J. L. Coughlin, K. Hoffman, F. Mullally, J. L. Christiansen, C. J. Burke, S. Bryson, N. Batalha, M. R. Haas, J. Catanzarite, J. F. Rowe, G. Barentsen, D. A. Caldwell, B. D. Clarke, J. M. Jenkins, J. Li, D. W. Latham, J. J. Lissauer, S. Mathur, R. L. Morris, S. E. Seader, J. C. Smith, T. C. Klaus, J. D. Twicken, J. E. Van Cleve, B. Wohler, R. Akeson, D. R. Ciardi, W. D. Cochran, C. E. Henze, S. B. Howell, D. Huber, A. Prša, S. V. Ramírez, T. D. Morton, T. Barclay, J. R. Campbell, W. J. Chaplin, D. Charbonneau, J. Christensen-Dalsgaard, J. L. Dotson, L. Doyle, E. W. Dunham, A. K. Dupree, E. B. Ford, J. C. Geary, F. R. Girouard, H. Isaacson, H. Kjeldsen, E. V. Quintana, D. Ragozzine, M. Shabram, A. Shporer, V. Silva Aguirre, J. H. Steffen, M. Still, P. Tenenbaum, W. F. Welsh, A. Wolfgang, K. A. Zamudio, D. G. Koch, and W. J. Borucki. Planetary Candidates Observed by Kepler. VIII. A Fully Automated Catalog with Measured Completeness and Reliability Based on Data Release 25. *The Astrophysical Journal Supplement Series*, 235:38, April 2018. doi: 10.3847/1538-4365/aab4f9.

[328] Brentha Thurairajah, Scott M Bailey, and Mark E Hervig. Northern hemisphere summer mesospheric gravity wave response to solar activity from nine years of aim observation. *Journal of Atmospheric and Solar-Terrestrial Physics*, 193:105086, 2019.

[329] F. Tian and S. Ida. Water contents of Earth-mass planets around M dwarfs. *Nature Geoscience*, 8:177–180, March 2015. doi: 10.1038/ngeo2372.

[330] Feng Tian and Shigeru Ida. Water contents of earth-mass planets around m dwarfs. *Nature Geoscience*, 8(3):177–180, 2015.

[331] Feng Tian, James F. Kasting, Han-Li Liu, and Raymond G. Roble. Hydrodynamic planetary thermosphere model: 1. Response of the Earth's thermosphere to extreme solar EUV conditions and the significance of adiabatic cooling. *Journal of Geophysical Research (Planets)*, 113(E5):E05008, May 2008. doi: 10.1029/2007JE002946.

[332] M. A. Tilley, A. Segura, V. Meadows, S. Hawley, and J. Davenport. Modeling Repeated M Dwarf Flaring at an Earth-like Planet in the Habitable Zone: Atmospheric Effects for an Unmagnetized Planet. *Astrobiology*, 19:64–86, January 2019. doi: 10.1089/ast.2017.1794.

[333] K. Tsiganis, R. Gomes, A. Morbidelli, and H. F. Levison. Origin of the orbital architecture of the giant planets of the Solar System. *Nature*, 435:459–461, May 2005. doi: 10.1038/nature03539.

[334] Zuo-Lin Tu, Ming Yang, H. F. Wang, and F. Y. Wang. Superflares, Chromospheric Activities, and Photometric Variabilities of Solar-type Stars from the Second-year Observation of TESS and Spectra of LAMOST. *The Astrophysical Journal Supplement Series*, 253(2):35, April 2021. doi: 10.3847/1538-4365/abda3c.

[335] Jonathan M. Tucker and Sujoy Mukhopadhyay. Evidence for multiple magma ocean outgassing and atmospheric loss episodes from mantle noble gases. *Earth and Planetary Science Letters*, 393:254–265, May 2014. doi: 10.1016/j.epsl.2014.02.050.

[336] Martin Turbet, Emeline Bolmont, Jeremy Leconte, François Forget, Franck Selsis, Gabriel Tobie, Anthony Caldas, Joseph Naar, and Michaël Gillon. Modeling climate diversity, tidal dynamics and the fate of volatiles on TRAPPIST-1 planets. *Astronomy & Astrophysics*, 612: A86, May 2018. doi: 10.1051/0004-6361/201731620.

[337] Martin Turbet, Emeline Bolmont, Vincent Bourrier, Brice-Olivier Demory, Jérémy Leconte, James Owen, and Eric T. Wolf. A Review of Possible Planetary Atmospheres in the TRAPPIST-1 System. , 216(5):100, July 2020. doi: 10.1007/s11214-020-00719-1.

[338] D. Valencia, M. Ikoma, T. Guillot, and N. Nettelmann. Composition and fate of short-period super-Earths. The case of CoRoT-7b. *Astronomy & Astrophysics*, 516:A20, June 2010. doi: 10.1051/0004-6361/200912839.

[339] R. Vanderspek, C. X. Huang, A. Vanderburg, G. R. Ricker, D. W. Latham, S. Seager, J. N. Winn, J. M. Jenkins, J. Burt, J. Dittmann, E. Newton, S. N. Quinn, A. Shporer, D. Charbonneau, J. Irwin, K. Ment, J. G. Winters, K. A. Collins, P. Evans, T. Gan, R. Hart, E. L. N. Jensen, J. Kielkopf, S. Mao, W. Waalkes, F. Bouchy, M. Marmier, L. D. Nielsen, G. Ottoni, F. Pepe, D. Ségransan, S. Udry, T. Henry, L. A. Paredes, H.-S. James, R. H. Hinojosa, M. L. Silverstein, E. Palle, Z. Berta-Thompson, I. Crossfield, M. D. Davies, D. Dragomir, M. Fausnaugh, A. Glidden, J. Pepper, E. H. Morgan, M. Rose, J. D. Twicken, J. N. S. Villaseñor, L. Yu, G. Bakos, J. Bean, L. A. Buchhave, J. Christensen-Dalsgaard, J. L. Christiansen, D. R. Ciardi, M. Clampin, N. De Lee, D. Deming, J. Doty, J. G. Jernigan, L. Kaltenegger, J. J. Lissauer, P. R. McCullough, N. Narita, M. Paegert, A. Pal, S. Rinehart, D. Sasselov, B. Sato, A. Sozzetti, K. G. Stassun, and G. Torres. TESS Discovery of an Ultra-short-period Planet around the Nearby M Dwarf LHS 3844. *The Astrophysical Journal Letters*, 871:L24, February 2019. doi: 10.3847/2041-8213/aafb7a.

[340] O. Venot, M. Rocchetto, S. Carl, A. Roshni Hashim, and L. Decin. Influence of Stellar Flares on the Chemical Composition of Exoplanets and Spectra. *The Astrophysical Journal*, 830: 77, October 2016. doi: 10.3847/0004-637X/830/2/77.

[341] G. Vladilo, G. Murante, L. Silva, A. Provenzale, G. Ferri, and G. Ragazzini. The Habitable Zone of Earth-like Planets with Different Levels of Atmospheric Pressure. *The Astrophysical Journal*, 767:65, April 2013. doi: 10.1088/0004-637X/767/1/65.

[342] David C Wade, Nathan Luke Abraham, Alexander Farnsworth, Paul J Valdes, Fran Bragg, and Alexander T Archibald. Simulating the climate response to atmospheric oxygen variability in the phanerozoic: a focus on the holocene, cretaceous and permian. *Climate of the Past*, 15(4):1463–1483, 2019.

[343] H. R. Wakeford, D. K. Sing, T. Kataria, D. Deming, N. Nikolov, E. D. Lopez, P. Tremblin, D. S. Amundsen, N. K. Lewis, A. M. Mandell, J. J. Fortney, H. Knutson, B. Benneke, and T. M. Evans. HAT-P-26b: A Neptune-mass exoplanet with a well-constrained heavy element abundance. *Science*, 356:628–631, May 2017. doi: 10.1126/science.aah4668.

[344] HR Wakeford, TJ Wilson, KB Stevenson, and NK Lewis. Exoplanet atmosphere forecast: Observers should expect spectroscopic transmission features to be muted to 33%. *arXiv preprint arXiv:1908.10669*, 2019.

[345] S. I. Walker, W. Bains, L. Cronin, S. DasSarma, S. Danielache, S. Domagal-Goldman, B. Kacar, N. Y. Kiang, A. Lenardic, C. T. Reinhard, W. Moore, E. W. Schwieterman, E. L. Shkolnik, and H. B. Smith. Exoplanet Biosignatures: Future Directions. *Astrobiology*, 18: 779–824, June 2018. doi: 10.1089/ast.2017.1738.

[346] K. J. Walsh, A. Morbidelli, S. N. Raymond, D. P. O'Brien, and A. M. Mandell. A low mass for Mars from Jupiter's early gas-driven migration. *Nature*, 475:206–209, July 2011. doi: 10.1038/nature10201.

[347] Y-M Wang, JL Lean, and NR Sheeley Jr. Modeling the sun's magnetic field and irradiance since 1713. *The Astrophysical Journal*, 625(1):522, 2005.

[348] M. J. Way, A. D. Del Genio, N. Y. Kiang, L. E. Sohl, D. H. Grinspoon, I. Aleinov, M. Kelley, and T. Clune. Was Venus the first habitable world of our solar system? *Geophysical Research Letters*, 43:8376–8383, August 2016. doi: 10.1002/2016GL069790.

[349] M. J. Way, A. D. Del Genio, I. Aleinov, T. L. Clune, M. Kelley, and N. Y. Kiang. Climates of Warm Earth-like Planets. I. 3D Model Simulations. *The Astrophysical Journal Supplement Series*, 239:24, December 2018. doi: 10.3847/1538-4365/aae9e1.

[350] David J. Wilson, Cynthia S. Froning, Girish M. Duvvuri, Kevin France, Allison Youngblood, P. Christian Schneider, Zachory Berta-Thompson, Alexander Brown, Andrea P. Buccino, Suzanne Hawley, Jonathan Irwin, Lisa Kaltenegger, Adam Kowalski, Jeffrey Linsky, R. O. Parke Loyd, Yamila Miguel, J. Sebastian Pineda, Seth Redfield, Aki Roberge, Sarah Rugheimer, Feng Tian, and Mariela Vieytes. The Mega-MUSCLES Spectral Energy Distribution of TRAPPIST-1. *The Astrophysical Journal*, 911(1):18, April 2021. doi: 10.3847/1538-4357/abe771.

[351] E. T. Wolf. Assessing the Habitability of the TRAPPIST-1 System Using a 3D Climate Model. *The Astrophysical Journal Letters*, 839:L1, April 2017. doi: 10.3847/2041-8213/aa693a.

[352] E. T. Wolf and O. B. Toon. Hospitable Archean Climates Simulated by a General Circulation Model. *Astrobiology*, 13:656–673, July 2013. doi: 10.1089/ast.2012.0936.

[353] E. T. Wolf and O. B. Toon. The evolution of habitable climates under the brightening Sun. *Journal of Geophysical Research (Atmospheres)*, 120:5775–5794, June 2015. doi: 10.1002/2015JD023302.

[354] E. T. Wolf, A. L. Shields, R. K. Kopparapu, J. Haqq-Misra, and O. B. Toon. Constraints on Climate and Habitability for Earth-like Exoplanets Determined from a General Circulation Model. *The Astrophysical Journal*, 837:107, March 2017. doi: 10.3847/1538-4357/aa5ffc.

[355] E. T. Wolf, R. K. Kopparapu, and J. Haqq-Misra. Simulated Phase-dependent Spectra of Terrestrial Aquaplanets in M Dwarf Systems. *The Astrophysical Journal*, 877:35, May 2019. doi: 10.3847/1538-4357/ab184a.

[356] Bernard J Wood, Michael J Walter, and Jonathan Wade. Accretion of the earth and segregation of its core. *Nature*, 441(7095):825–833, 2006.

[357] R. Wordsworth. Atmospheric Heat Redistribution and Collapse on Tidally Locked Rocky Planets. *The Astrophysical Journal*, 806:180, June 2015. doi: 10.1088/0004-637X/806/2/180.

[358] Fabian Wunderlich, Mareike Godolt, John Lee Grenfell, Steffen Städt, Alexis M. S. Smith, Stefanie Gebauer, Franz Schreier, Pascal Hedelt, and Heike Rauer. Detectability of atmospheric features of Earth-like planets in the habitable zone around M dwarfs. *Astronomy & Astrophysics*, 624:A49, April 2019. doi: 10.1051/0004-6361/201834504.

[359] S Xu, B Zuckerman, P Dufour, ED Young, B Klein, and M Jura. The chemical composition of an extrasolar kuiper-belt-object. *The Astrophysical Journal Letters*, 836(1):L7, 2017.

[360] Yosuke A. Yamashiki, Hiroyuki Maehara, Vladimir Airapetian, Yuta Notsu, Tatsuhiko Sato, Shota Notsu, Ryusuke Kuroki, Keiya Murashima, Hiroaki Sato, Kosuke Namekata, Takanori Sasaki, Thomas B. Scott, Hina Bando, Subaru Nashimoto, Fuka Takagi, Cassandra Ling, Daisaku Nogami, and Kazunari Shibata. Impact of Stellar Superflares on Planetary Habitability. *The Astrophysical Journal*, 881(2):114, August 2019. doi: 10.3847/1538-4357/ab2a71.

[361] J. Yang, N. B. Cowan, and D. S. Abbot. Stabilizing Cloud Feedback Dramatically Expands the Habitable Zone of Tidally Locked Planets. *The Astrophysical Journal Letters*, 771:L45, July 2013. doi: 10.1088/2041-8205/771/2/L45.

[362] J. Yang, G. Boué, D. C. Fabrycky, and D. S. Abbot. Strong Dependence of the Inner Edge of the Habitable Zone on Planetary Rotation Rate. *The Astrophysical Journal Letters*, 787:L2, May 2014. doi: 10.1088/2041-8205/787/1/L2.

[363] J. Yang, J. Leconte, E. T. Wolf, C. Goldblatt, N. Feldl, T. Merlis, Y. Wang, D. D. B. Koll, F. Ding, F. Forget, and D. S. Abbot. Differences in Water Vapor Radiative Transfer among 1D Models Can Significantly Affect the Inner Edge of the Habitable Zone. *The Astrophysical Journal*, 826:222, August 2016. doi: 10.3847/0004-637X/826/2/222.

[364] J. Yang, J. Leconte, E. T. Wolf, C. Goldblatt, N. Feldl, T. Merlis, Y. Wang, D. D. B. Koll, F. Ding, F. Forget, and D. S. Abbot. Differences in Water Vapor Radiative Transfer among 1D Models Can Significantly Affect the Inner Edge of the Habitable Zone. *The Astrophysical Journal*, 826:222, August 2016. doi: 10.3847/0004-637X/826/2/222.

[365] J. Yang, D. S. Abbot, D. D. B. Koll, Y. Hu, and A. P. Showman. Ocean Dynamics and the Inner Edge of the Habitable Zone for Tidally Locked Terrestrial Planets. *The Astrophysical Journal*, 871:29, January 2019. doi: 10.3847/1538-4357/aaf1a8.

[366] J. Yang, J. Leconte, E. T. Wolf, T. Merlis, D. D. B. Koll, F. Forget, and D. S. Abbot. Simulations of Water Vapor and Clouds on Rapidly Rotating and Tidally Locked Planets: A 3D Model Intercomparison. *The Astrophysical Journal*, 875:46, April 2019. doi: 10.3847/1538-4357/ab09f1.

[367] Jun Yang, Dorian S. Abbot, Daniel D. B. Koll, Yongyun Hu, and Adam P. Showman. Ocean Dynamics and the Inner Edge of the Habitable Zone for Tidally Locked Terrestrial Planets. *The Astrophysical Journal*, 871(1):29, January 2019. doi: 10.3847/1538-4357/aaf1a8.

[368] Jun Yang, Jérémy Leconte, Eric T. Wolf, Timothy Merlis, Daniel D. B. Koll, François Forget, and Dorian S. Abbot. Simulations of Water Vapor and Clouds on Rapidly Rotating and Tidally Locked Planets: A 3D Model Intercomparison. *The Astrophysical Journal*, 875(1): 46, April 2019. doi: 10.3847/1538-4357/ab09f1.

[369] Jack S. Yates, Paul I. Palmer, James Manners, Ian Boutle, Krisztian Kohary, Nathan Mayne, and Luke Abraham. Ozone chemistry on tidally locked M dwarf planets. *Monthly Notices of the Royal Astronomical Society*, 492(2):1691–1705, February 2020. doi: 10.1093/mnras/stz3520.

[370] A. Youngblood, K. France, R. O. P. Loyd, J. L. Linsky, S. Redfield, P. C. Schneider, B. E. Wood, A. Brown, C. Froning, Y. Miguel, S. Rugheimer, and L. Walkowicz. The MUSCLES Treasury Survey. II. Intrinsic LYα and Extreme Ultraviolet Spectra of K and M Dwarfs with Exoplanets*. *The Astrophysical Journal*, 824:101, June 2016. doi: 10.3847/0004-637X/824/2/101.

[371] Allison Youngblood, Kevin France, R. O. Parke Loyd, Alexander Brown, James P. Mason, P. Christian Schneider, Matt A. Tilley, Zachory K. Berta-Thompson, Andrea Buccino, Cynthia S. Froning, Suzanne L. Hawley, Jeffrey Linsky, Pablo J. D. Mauas, Seth Redfield, Adam Kowalski, Yamila Miguel, Elisabeth R. Newton, Sarah Rugheimer, Antígona Segura, Aki Roberge, and Mariela Vieytes. The MUThe Astrophysical JournalS Treasury Survey. IV.

Scaling Relations for Ultraviolet, Ca II K, and Energetic Particle Fluxes from M Dwarfs. *The Astrophysical Journal*, 843(1):31, Jul 2017. doi: 10.3847/1538-4357/aa76dd.

[372] K. J. Zahnle, J. F. Kasting, and J. B. Pollack. Evolution of a steam atmosphere during earth's accretion. *Icarus*, 74:62–97, April 1988. doi: 10.1016/0019-1035(88)90031-0.

[373] Kevin Zahnle, Nick Arndt, Charles Cockell, Alex Halliday, Euan Nisbet, Franck Selsis, and Norman H Sleep. Emergence of a habitable planet. *Space Science Reviews*, 129(1-3):35–78, 2007.

[374] Guang J Zhang and Norman A McFarlane. Sensitivity of climate simulations to the parameterization of cumulus convection in the canadian climate centre general circulation model. *Atmosphere-ocean*, 33(3):407–446, 1995.

[375] Minghua Zhang, Wuyin Lin, Christopher S Bretherton, James J Hack, and Phillip J Rasch. A modified formulation of fractional stratiform condensation rate in the ncar community atmospheric model (cam2). *Journal of Geophysical Research: Atmospheres*, 108(D1):ACL–10, 2003.

[376] X. Zhang and A. P. Showman. Global-mean Vertical Tracer Mixing in Planetary Atmospheres. I. Theory and Fast-rotating Planets. *The Astrophysical Journal*, 866:1, October 2018. doi: 10.3847/1538-4357/aada85.

[377] A. Zsom, S. Seager, J. de Wit, and V. Stamenković. Toward the Minimum Inner Edge Distance of the Habitable Zone. *The Astrophysical Journal*, 778:109, December 2013. doi: 10.1088/0004-637X/778/2/109.